LATERAL SPREADING MECHANICS OF COLUMN-SUPPORTED EMBANKMENTS

Zhanyu Huang

Dissertation submitted to the faculty of the Virginia Polytechnic Institute and State University in partial fulfillment of the requirements for the degree of

Doctor of Philosophy
In
Civil Engineering

George M. Filz, Co-chair
Katerina Ziotopoulou, Co-chair
Thomas L. Brandon
Adrian Rodriguez-Marek

September 27, 2019
Blacksburg, Virginia

Keywords:
Column-supported embankment
Lateral spreading
Geosynthetic reinforcement
Failure modes
Three-dimensional numerical analysis

LATERAL SPREADING MECHANICS OF COLUMN-SUPPORTED EMBANKMENTS

Zhanyu Huang

ABSTRACT (ACADEMIC)

Column-supported embankments (CSE) enable accelerated construction on soft soils, high performance, and protection of adjacent facilities. The foundation columns transfer embankment and service loading to a competent stratum at depth such that loading on the soft soil can be reduced. This has the beneficial effects of reducing settlement and lateral displacement, and improving stability. Selection of column type depends on the design load, cost, constructability, etc., although unreinforced concrete columns are commonly used. A load transfer platform (LTP) is often included at the embankment base. This is a layer of coarse-grained fill that may include one or more layers of geosynthetic reinforcement. The LTP improves vertical load transfer to columns by mobilizing the shear strength of the LTP fill and the membrane effect of the geosynthetic. The geosynthetic reinforcement also responds in tension to lateral spreading.

Herein, lateral spreading is defined as the lateral displacements occurring in response to lateral earth pressures in the embankment and foundation. Excessive lateral spreading can lead to bending failure of the concrete columns, tensile failure of the geosynthetic reinforcement, and instability of the system. Design procedures recommend inclusion of geosynthetic reinforcement to mitigate lateral spreading, with assumptions for the lateral thrust distribution, failure mode, and calculation of geosynthetic tensile capacity. The necessity and sufficiency of these assumptions have not been fully validated. In addition, unreinforced concrete columns have low tensile strength and can fail in bending, but recommendations for calculating column bending moments are not available. This research examines the limitations in CSE lateral spreading design with the goal of advancing fundamental understanding of lateral spreading mechanics.

The research was performed using three-dimensional finite difference analyses. Limiting conditions for lateral spreading analysis were identified using case history records, and an undrained-dissipated approach was validated for the numerical analysis of limiting conditions (i.e., undrained end-of-construction and long-term excess pore pressure dissipated). The numerical model was calibrated using a well-documented case history. Additional analyses of the case history were performed to examine the lateral earth pressures in the foundation, column bending moments, and geosynthetic contribution to resisting lateral spreading. A parametric study was conducted to examine the lateral thrust distribution in 128 CSE scenarios. A refined substructure model was adopted for analyzing peak geosynthetic tensions and strains. Lastly, failure analyses were performed to examine the effect of different CSE design parameters on embankment failure height, failure mode, and deformations.

The research produced qualitative and quantitative information about the following: (1) the percent thrust resistance provided by the geosynthetic as a function of its stiffness; (2) the geosynthetic contribution to ultimate and serviceability limit states; (3) the change in lateral thrust distribution throughout the embankment system before and after dissipation of excess pore water pressures; (4) the column-soil interactions involved in embankment failure; and (5) identification of two failure modes in the undrained condition. Design guidance based on these findings is provided.

LATERAL SPREADING MECHANICS OF COLUMN-SUPPORTED EMBANKMENTS

Zhanyu Huang

ABSTRACT (GENERAL AUDIENCE)

Column-supported embankments (CSEs) have been designated by the Federal Highway Administration as a critical technology for new highway alignment projects and widening of existing highways. CSEs enable accelerated construction and high performance in weak soils, which are factors critical to project success. In a CSE, columns are installed in the weak soil, followed by rapid construction of the soil embankment that provides the necessary elevation and foundation for the roadway. The columns transfer most of the embankment and traffic loading to a competent soil stratum at depth. Concrete without steel reinforcement is commonly used to construct the columns, although material selection depends on cost, constructability, expected load, etc. Layers of geosynthetic reinforcement can also be included at the embankment base. The geosynthetics help to transfer loads to the columns and resist excessive movement that could lead to instability. The entire embankment system should be designed for safety and economy.

This research was motivated by uncertainties in design to mitigate lateral spreading. Lateral spreading refers to lateral displacements occurring in response to lateral earth pressures in the embankment and foundation. Excessive lateral spreading can lead to failure of the columns, geosynthetic reinforcement, and the entire embankment system. This research aims to advance fundamental understanding of lateral spreading in CSEs and to re-evaluate current design assumptions. Corresponding design guidance is provided.

ACKNOWLEDGEMENTS

I would like to sincerely thank my advisors, Professor George Filz and Professor Katerina Ziotopoulou, for providing guidance and review. I have learned a lot from them, and much of my personal growth over the last few years can be attributed to their mentorship.

I would also like to thank Professor Adrian Rodriguez-Marek and Professor Thomas Brandon for providing helpful comments, and Dr. Jim Collin for sharing his design experience.

This research was funded by the Center for Geotechnical Practice and Research at Virginia Tech.

TABLE OF CONTENTS

LIST OF FIGURES

LIST OF TABLES

CHAPTER 1. INTRODUCTION

1.1. Description of Column-Supported Embankments

Challenges associated with embankment construction on soft soil include excessive settlement and system instability, which restrict construction rate and affect project economy. Over the last few decades, column-supported embankments (CSEs) have emerged as an alternative technology to staged construction with prefabricated vertical drains for enabling accelerated construction, high performance, and protection of adjacent facilities. In the U.S., CSEs have been designated as a critical technology, with plans for their use in highway alignment projects, widening of existing roadways, and stabilization in special deposits, such as landfills (FHWA 2017). In Europe and Asia, CSEs have been adopted in the construction of railways (Briançon and Simon 2017; Shang et al. 2016; Zanzinger et al. 2002; Zheng et al. 2011; Zhou et al. 2016; Zhuang and Cui 2016).

CSEs are typically constructed when project success is governed by time constraints (Schaefer et al. 2017). In contrast to staged construction, CSEs can be rapidly constructed in one stage without waiting for excess pore water pressures to dissipate. The foundation columns help to transfer embankment and service loading to a competent stratum at depth, thereby reducing loading applied to weak soil strata. This has the potential to reduce construction time, settlement, and lateral spreading of the embankment.

The column type used in CSEs can vary depending on project parameters such as the design loads, constructability, cost, etc. (Schaefer et al. 2017). Column types include aggregate, timber, steel H-section, steel pipe, deep soil mixing, vibro-concrete, precast concrete, etc. (Schaefer et al. 2017). Vibro-concrete columns have been widely used in recent years (Collin, personal communication, 2018). Columns can be end-bearing or floating, where the former is adopted for most CSE applications (SHRP2 2012).

A load transfer platform (LTP) can be included in the CSE design. This is a layer of granular fill that may incorporate one or more layers of geosynthetic reinforcement (Schaefer et al. 2017). As its name suggests, the LTP is designed to improve vertical load transfer. The shear strength of the granular fill contributes to soil arching, and the embedded reinforcements can further enhance load

transfer as they develop tension under vertical loading. Reinforcements also develop tension in response to lateral earth pressures. A CSE schematic is provided in Figure 1-1.

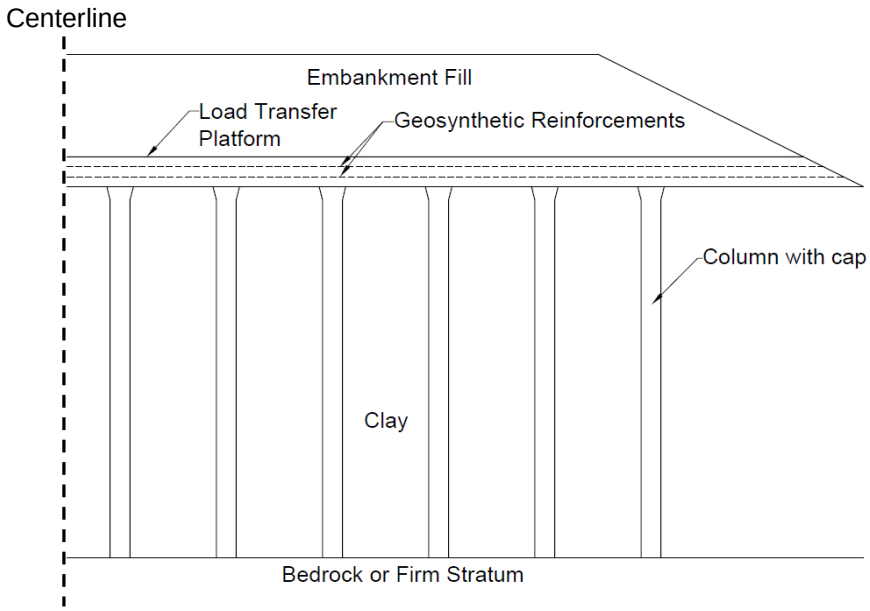

Figure 1-1. Schematic of a typical column-supported embankment.

1.2. Lateral Spreading Design

Performance benefits of CSEs can only be realized with appropriate design for vertical load transfer and stability. A plethora of CSE vertical load transfer research has been conducted in the last few decades, resulting in advancement of design standards around the globe (Sloan et al. 2014; British Standards Institute 2016; van Eekelen and Brugman 2016; Schaefer et al. 2017). However, questions remain regarding design for mitigating lateral spreading. Herein, lateral spreading is defined as the lateral deformations that occur in response to lateral earth pressures in the embankment and foundation soil. If excessive, lateral spreading can lead to geosynthetic tensile failure, column bending failure, and/or system instability.

Schaefer et al. (2017) provide recommendations for CSE design in the U.S. with reference to the British Standard (BSI 2010). A concept that follows BSI (2010) is the design for ultimate and serviceability limit states.

The following ultimate limit states are considered:

1. Pile group capacity – the columns must be designed to carry vertical loads without exceeding capacity;

2. Pile group extent – the column group must have adequate lateral extent to prevent instability at the embankment toe;

3. Vertical load shedding – the foundation and LTP must transfer vertical loads from the embankment to the columns;

4. Lateral sliding – sliding of the embankment fill must be evaluated using lateral force equilibrium;

5. Overall stability – global stability must be evaluated using conventional limit equilibrium stability methods.

The following serviceability limit states are considered:

1. Reinforcement stains – reinforcement strains should be kept under a maximum threshold (typically 5% to 6%) to ensure differential settlements do not manifest at the embankment surface;

2. Foundation settlement – the foundation must be designed to prevent excessive settlement.

Mitigation of lateral spreading is addressed in design via the ultimate limit state of lateral sliding, in which failure is assumed to occur by sliding of the embankment fil over the foundation. Lateral force equilibrium is evaluated. The driving lateral thrust (P_{Lat}) is calculated using Equation 1.1 as a function of the coefficient of active lateral earth pressure (K_a), embankment height (H), unit weight of embankment fill (γ), and service loading (q). The resisting lateral thrust (R_{ls}) is assumed to be provided by the undrained shear strength (s_u) of the foundation soil multiplied by the length beneath the embankment slope (L_s), as shown in Equation 1.2. If the ratio of R_{ls} to P_{Lat} is smaller than 1.5, then geosynthetic reinforcement may be added as an alternative to installing battered piles, under the assumption that vertical unreinforced concrete columns have limited lateral resistance. Whereas BSI (2010) recommends that the columns should be able to resist 10% of the lateral thrust at minimum, Schaefer et al. (2017) do not make any recommendations for the column lateral capacity.

$$P_{Lat} = K_a[\gamma\left(\frac{H^2}{2}\right) + qH] \qquad (1.1)$$

$$R_{ls} = L_s s_u \qquad (1.2)$$

If geosynthetic reinforcement is included in design, then it must have an adequate tensile capacity to resist the coupled effects of vertical load transfer and lateral spreading. This requirement can be met in one of two ways (Schaefer et al. 2017): (1) using a single layer, the design tensile load (T) is calculated as the sum of tensions from vertical and lateral loads (Equation 1.3); or (2) using two layers, one layer carries the tension from only the vertical loading (T_{vert}), and a second layer, with strength greater in the direction perpendicular to the embankment, carries the tension from only the lateral loading (T_{lat} or P_{Lat}), as shown in Equations 1.4 and 1.5. The second approach is recommended because the lateral spreading requirement may exceed the vertical load transfer requirement, and both reinforcement demand and capacity are direction dependent.

$$T = T_{vert} + T_{lat} = T_{vert} + P_{Lat} \qquad (1.3)$$

$$T_1 = T_{vert} \qquad (1.4)$$

$$T_2 = T_{lat} = P_{Lat} \qquad (1.5)$$

The geosynthetic design tensile load should be less than the allowable tensile load (T_{allow}), which is the ultimate tensile strength (T_{ult}) reduced by factors accounting for durability, installation damage, creep, and a safety factor of 1.5 (Equation 1.6).

$$T \leq T_{allow} = \frac{T_{ult}}{RF_{durability} \times RF_{installation\ damage} \times RF_{creep} \times 1.5} \qquad (1.6)$$

1.3. Research Motivation

The design procedure described in Section 1.2 has several limitations, and these motivate the research.

Limitation 1: uncertainty in lateral thrust distribution

Calculation of the driving lateral thrust (P_{Lat}) in Equation 1.1 assumes that lateral spreading occurs with the development of an active condition in the embankment fill. This approach neglects the

increment of lateral earth pressure that develops in the foundation due to the increment of vertical loading applied on the subsoil between columns. The magnitude of foundation earth pressure changes with the development of soil arching and subsoil consolidation, and it has a direct impact on the reinforcement tension and column lateral response. The magnitude of driving lateral thrust is also not well represented by K_a because soil arching results in redistribution of stresses in the embankment. Stress concentration occurs above columns, and stress reduction occurs above the subsoil between columns. Literature review has unveiled no prior investigation on the lateral earth pressures that develop in CSEs. Thus, a focus of the current research is to examine the lateral thrust distribution in CSEs for the purpose of determining driving and resisting lateral loads and whether the geosynthetic should be designed to carry P_{Lat} in its entirety.

Limitation 2: calculation of geosynthetic tension

An incomplete understanding of how the reinforcement responds under the coupling effects of vertical load transfer and lateral spreading limits the procedure for calculating geosynthetic tensile capacity. Investigation of this issue has been limited. Chen et al. (2016) studied the spreading effect on geogrid tension by limiting the subsoil settlement at the end of construction in a full-scale experimental CSE. The subsoil was modeled using water bags, and settlement was limited by controlling drainage of water from the bags. However, the measured geosynthetic tension was very small, possibly due to inadequate reinforcement development length. Effects of lateral displacement on reinforcement tension have also been investigated numerically using a unit cell domain in which lateral springs replaced rollers at boundaries (Yu et al. 2016). Reinforcement loads were found to be larger for the case of spring boundaries compared to the case of roller boundaries. Although these results agree with intuition, further research is necessary to determine the coupling effect of vertical and lateral loads on reinforcement tension. Until then, questions remain regarding whether the current design procedure is appropriate for calculating the required tensile capacity of the geosynthetic reinforcement.

Limitation 3: design of columns under lateral loads

Existing literature suggests that bending failure may be a concern in unreinforced cementitious columns, but guidance for calculating column bending moments is missing from current design procedures. The numerical study reported by Jamsawang et al. (2016) indicates that bending failure

in deep cement mixed (DCM) columns could be more critical than bearing failure and global instability. Centrifuge studies of small-scale CSEs supported by unreinforced cementitious columns beneath the embankment slope found that embankment collapse due to column bending could take precedence over slip circle failure (Kitazume and Maruyama 2006; Kitazume and Maruyama 2007). Chai et al. (2017) formulated a procedure for estimating the maximum bending moment in DCM columns, but the study was limited to area replacement ratios (ARR, ratio of column cross-section area to column tributary area) of 10% – 30%, whereas unreinforced concrete columns are typically installed at lower ARRs of 2.5% to 10% (Collin, personal communication, 2018). Another limitation of the study by Chai et al. (2017) is modeling the DCM columns as linear elastic materials without a failure criterion, such that the columns could not fail in flexural tension or shear. Thus, uncertainties remaining in column design include the bending moments that develop in unreinforced concrete columns and the potential consequences of column bending failure.

Limitation 4: gap in knowledge of failure modes

Failure modes associated with lateral spreading may not be limited to lateral sliding of the embankment fill. Failure could also occur in the foundation if column bending failure or geosynthetic rupture results in an increase in load transfer to the subsoil. This is of particular concern when low column ARRs are used, and the subsoil must carry a substantial portion of the embankment loading. Furthermore, deformations of the reinforcement, columns, and soft soil are interrelated and time-dependent, but the design procedure does not provide guidance about evaluating failure mechanisms that may be critical at different stages of embankment construction and service life. Failure could occur abruptly if the embankment is above the critical height for differential settlement (Demerdash 1996), such that deformations in the foundation may not be reflected at the embankment surface until collapse.

1.4. Research Objectives and Scope

These limitations in CSE lateral spreading design point to a need to advance fundamental understanding of lateral spreading mechanics. This research aims to address the following questions related to CSE lateral spreading design and to provide corresponding design guidance:

1. What is the lateral thrust distribution in the embankment fill, foundation soil, and geosynthetic reinforcement?
2. What is the magnitude of geosynthetic reinforcement tension that develops under the combined effects of lateral spreading and vertical load transfer?
3. What are the magnitudes of bending moments that develop in unreinforced concrete columns at typical ARRs?
4. What are the different failure modes associated with lateral spreading, and what are the consequences of column or geosynthetic failure?

Investigation of these questions used three-dimensional (3D) numerical analyses in the unit cell and half-embankment domains. Three-dimensional analyses are required for investigating stress distribution in a system consisting of isolated columnar elements. The half-embankment domain is appropriate for lateral spreading analysis in symmetric embankments. Analyses were conducted in the commercial finite difference platform, FLAC3D v.5.01 (Itasca 2012). The research consisted of the following tasks:

Task 1: Unit validation studies were conducted. These established the validity of FLAC3D for simulating different aspects of the system response, often through the use of small numerical domains. Examples include validating the stress-deformation response of structural geogrid elements and pile elements (Itasca 2013), the pore pressure and stress-deformation response of different constitutive models under different loading paths, and consolidation deformations calculated using a manual approach for dissipating excess pore pressures.

Task 2: A half-embankment model was calibrated using a well-documented CSE case history, and additional analyses were performed for the case history embankment. Material parameters were calibrated to model the loosening of select embankment zones during the development of soil arching. After model calibration, analyses were performed to investigate the foundation lateral earth pressures, column bending moments, geosynthetic strains, and geosynthetic contribution to reducing lateral spreading.

Task 3: A parametric study totaling 128 scenarios was conducted. The large number of scenarios was used to investigate the lateral thrust distribution in CSEs and to identify conditions under which the geosynthetic makes the greatest contribution to lateral spreading resistance.

Task 4: Peak geosynthetic tensions and strains that develop under the coupled effects of vertical load transfer and lateral spreading were analyzed using substructure analyses. Substructure analyses utilized the unit cell geometry, which allows for greater refinement without the costly computation times associated with a larger numerical domain. Refined zone discretization was required for investigating local strain effects in the geosynthetic.

Task 5: Failure analyses were conducted for eight (8) CSE scenarios for the purpose of investigating failure modes, failure heights, and deformations. In each scenario, the embankment was gradually increased in height until collapse occurred or until a limiting embankment height of 12.8 m (42 ft) was reached.

Task 6: Numerical results were synthesized and design guidance was prepared.

1.5. Dissertation Overview

This dissertation follows a manuscript format, totaling five chapters and three appendices. Chapters 2 to 4 contain manuscripts for publication.

Chapter 2: 3D Numerical Analyses of Lateral Spreading in a Column-Supported Embankment

Huang, Z., Ziotopoulou, K., Filz, G. M. (2019). "3D Numerical Limiting Case Analyses of Lateral Spreading in a Column-Supported Embankment." *ASCE Journal of Geotechnical and Geoenvironmental Engineering*, 145(11), 04019096.

This publication is being reused with permission from ASCE.

Chapter 3: Lateral Thrust Distribution in Column-Supported Embankments for Limiting Cases of Lateral Spreading

Huang, Z., Ziotopoulou, K., Filz, G. M. (2019). "Lateral Thrust Distribution in Column-Supported Embankments for Limiting Cases of Lateral Spreading."

A final version of the manuscript is being prepared for submission to the ASCE Journal of Geotechnical and Geoenvironmental Engineering.

Chapter 4: 3D Numerical Analyses of Column-Supported Embankments: Failures Heights, Failure Modes, and Deformations

Huang, Z., Ziotopoulou, K., Filz, G. M. (2019). "3D Numerical Analyses of Column-Supported Embankments: Failure Heights, Failure Modes, and Performance."

A final version of the manuscript is being prepared for submission to the ASCE Journal of Geotechnical and Geoenvironmental Engineering.

Chapter 5: Summary, Conclusions, and Design Guidance

This chapter contains a summary of key findings and design guidance related to the limitations in CSE design that motivated this research.

Appendix A: Unit Validations

Procedure and results from unit validation studies are documented.

Appendix B: Numerical Predictions of Deformations in Geosynthetic-Reinforced Column-Supported Embankments: Validation of Manual Dissipation of Excess Pore Pressure Approach for Undrained and Drained Analyses

This appendix contains the conference publication documenting the validation studies performed for the undrained-dissipated approach. This two-stage approach was adopted for all numerical analyses performed in the research and involved (1) undrained loading with excess pore pressure generation using an effective stress model and (2) manual dissipation of excess pore pressures and calculation of consolidation deformations. Calculated deformations were validated using benchmark solutions.

Huang, Z., Ziotopoulou, K., Filz, G. M. (2018). "Numerical Predictions of Deformations in Geosynthetic-Reinforced Column-Supported Embankments: Validation of Manual Dissipation of Excess Pore Pressure Approach for Undrained and Drained Analyses." *IFCEE 2018: Innovations in Ground Improvement for Soils, Pavements, and Subgrades*, GSP 296, 327-336.

Appendix C: Substructure Analyses

Substructure analyses were limited by large distortions in zones around column edges and illegal zone geometry. Lessons learned and suggestions for future research are documented in this appendix.

Notation

The following symbols are used in this chapter:

H = embankment height;

K_a = active lateral earth pressure coefficient;

L_s = length of embankment slope;

P_{Lat} = driving lateral load;

q = service load;

RF = reduction factor;

R_{ls} = lateral resistance of foundation soil;

s_u = undrained shear strength of foundation soil;

T = design tensile load in geosynthetic;

T_{allow} = allowable tensile load;

T_{lat} = tensile load from lateral spreading effect;

T_{ult} = ultimate tensile strength;

T_{vert} = tensile load from vertical load transfer effect;

T_1 = design tensile load in the first geosynthetic layer;

T_2 = design tensile load in the second geosynthetic layer; and

γ = unit weight of embankment fill.

References

Briançon, L., and Simon, B. (2017). "Pile-supported embankment over soft soil for a high-speed line." *Geosynthetics International*, 24(3), 293-305.

BSI (Bristish Standards Institution). (2010). *Design of embankments with reinforced soil foundations on poor ground*. BS 8006-1:2010. London: British Standards Institution.

BSI (British Standards Institution). (2016). *Design of embankments with reinforced soil foundations on poor ground*. BS 8006-1:2010+A1:2016. London: British Standards Institution.

Chai, J. C., Shrestha, S., Hino, T., and Uchikoshi, T. (2017). "Predicting bending failure of CDM columns under embankment loading." *Computers and Geotechnics*, 91, 169-178.

Chen, R. P., Wang, Y. W., Ye, X. W., Bian, X. C., and Dong, X. P. (2016). "Tensile force of geogrids embedded in pile-supported reinforced embankment: A full-scale experimental study." *Geotextiles and Geomembranes*, 44(2), 157-169.

Collin, J. G. (2018). Personal Communication.

Demerdash, M. A. (1996). "An experimental study of piled embankments incorporating geosynthetic basal reinforcement." Ph.D. Dissertation, Department of Civil Engineering, University of Newcastle-Upon-Tyne.

Federal Highway Administration (2017). "American Association of State Highway and Transportation Officials (AASHTO) Unites States Department of Transportation Federal Highway Administration (FHWA) 2002 Scanning Project Innovative Technology for Accelerated Construction of Bridge and Embankment Foundations Preliminary Summary Report." <https://www.fhwa.dot.gov/engineering/geotech/research/bescan.cfm#4>. (June, 2017).

Itasca (2012). FLAC3D, version 5.01, Minneapolis, MN.

Itasca (2013). *Structural Elements*, Itasca Consulting Group Inc., Minneapolis, Minnesota.

Jamsawang, P., Yoobanpot, N., Thanasisathit, N., Voottipruex, P., and Jongpradist, P. (2016). "Three-dimensional numerical analysis of a DCM column-supported highway embankment." *Computers and Geotechnics*, 72, 42-56.

Kitazume, M., and Maruyama, K. (2006). "External stability of group column type deep mixing improved ground under embankment loading." *Soils and Foundations*, 46(3), 323-340.

Kitazume, M., and Maruyama, K. (2007). "Internal Stability of Group Column Type Deep Mixing Improved Ground under Embankment Loading." *Soils and Foundations*, 47(3), 437-455.

Schaefer, V. R., Berg, R. R., Collin, J. G., Christopher, B. R., DiMaggio, J. A., Filz, G. M., Bruce, D. A., and Ayala, D. (2017). *Ground Modification Methods Reference Manual - Volume II*. Washington, D. C.: Federal Highway Administration.

Shang, Y., Xu, L., Xu, Y., Li, Y., and Ou, N. (2016). "Field Test Study on a Short Pile-net Composite Foundation over Gravel Clay for High-Speed Railways." *Journal of Engineering Science & Technology Review*, 9(3).

SHRP2 (2012). "Column-Supported Embankments." <http://www.GeoTechTools.org>.

van Eekelen, S. J. M., and Brugman, M. H. A. (2016). *Design guideline basal reinforced piled embankments*. Boca Raton, FL: CRC Press.

Sloan, J. A., Filz, G. M., Collin, J. G., and Kumar, P. (2014). "Column-Supported Embankments: Field Tests and Design Recommendations (2nd Edition)." Virginia Tech Center for Geotechnical Practice and Research, Blacksburg, VA.

Yu, Y., Bathurst, R. J., and Damians, I. P. (2016). "Modified unit cell approach for modelling geosynthetic-reinforced column-supported embankments." *Geotextiles and Geomembranes*, 44(3), 332-343.

Zanzinger, H. and Gartung, E. (2002). "Performance of a geogrid reinforced railway embankment on piles." *7th ICG*, 381-386. Delmas, Gourc, and Girard, eds. Lisse: Swets & Zeilinger.

Zheng, G., Jiang, Y., Han, J., and Liu, Y.-F. (2011). "Performance of Cement-Fly Ash-Gravel Pile-Supported High-Speed Railway Embankments over Soft Marine Clay." *Marine Georesources & Geotechnology*, 29(2), 145-161.

Zhou, M., Liu, H., Chen, Y., and Hu, Y. (2016). "First application of cast-in-place concrete large-diameter pipe (PCC) pile-reinforced railway foundation: a field study." *Canadian Geotechnical Journal*, 53(4), 708-716.

Zhuang, Y., and Cui, X. (2016). "Case Studies of Reinforced Piled High-Speed Railway Embankment over Soft Soils." *International Journal of Geomechanics*, 16(2), 06015005.

CHAPTER 2. 3D NUMERICAL ANALYSES OF LATERAL SPREADING IN A COLUMN-SUPPORTED EMBANKMENT

Zhanyu Huang[1], Katerina Ziotopoulou[2], George M. Filz[3]

[1] Graduate Research Assistant, The Charles E. Via Jr. Department of Civil and Environmental Engineering, Virginia Tech, Blacksburg, USA

[2] Assistant Professor, Department of Civil and Environmental Engineering, University of California, Davis, USA

[3] Professor, The Charles E. Via Jr. Department of Civil and Environmental Engineering, Virginia Tech, Blacksburg, USA

2.1. Abstract

This paper presents three-dimensional numerical analyses of a column-supported embankment case history using the finite difference method. An undrained end-of-construction analysis was followed by a long-term dissipated analysis, in which all excess pore pressures generated in the undrained loading phase were manually dissipated for the calculation of long-term deformations. The two analyses examined limiting cases for lateral spreading, providing results that envelop case history recordings at the end of construction and 125 days after construction, respectively. Numerical calculations were performed for a unit cell and a half-embankment model. Calibration of large-deformation soil arching behavior in the embankment was achieved by reducing the Young's modulus and friction angle of loosened zones whose dimensions were modeled after bench-scale and field-scale tests. Numerical results are in good agreement with case history recordings for vertical load transfer, settlements, and lateral displacements. In addition, numerical results are provided for foundation incremental lateral earth pressure profiles, geogrid strains, column bending moment profiles, and column stresses due to combined effects of bending and axial loading, such that they can be related to the fundamental aspects of lateral spreading resistance. The increment of lateral earth pressures in the foundation soil was largest at the undrained end-of-construction condition, geogrid strains were largest in the long-term dissipated condition, and column bending moments and column tensile stresses were very large in both scenarios. Furthermore, the geogrid contributions to increasing vertical load transfer to the columns and reducing lateral spreading of the embankment were insignificant, likely due to the subgrade support provided by the top coarse-grained fill layer in the foundation.

2.2. Introduction

The column-supported embankment (CSE) technology enables accelerated embankment construction on soft soil and protection of adjacent facilities. In CSEs, columns are installed in the subgrade to transfer embankment loading to a firmer stratum at depth. The vertical load transfer to the columns occurs by soil arching in the embankment fill and differential settlement in the foundation. A load transfer platform (LTP) can be constructed to improve vertical load transfer. The LTP usually consists of coarse granular fill reinforced with one or more layers of geosynthetics. The shear strength of the granular fill contributes to soil arching, and the geosynthetics can further enhance load transfer to columns as they develop tension under vertical loading. Geosynthetics also can be used to resist lateral spreading of the embankment.

With many different components in the system, comprehensive design of column-supported embankments is complex and requires consideration of both vertical load transfer and lateral spreading. Vertical load transfer design includes consideration of column type, column spacing, column size, embankment height, and LTP details such as the number of geosynthetic layers and the geosynthetic strength and stiffness. Vertical load transfer impacts embankment serviceability, and differential settlements occurring at the embankment base must be prevented from manifesting at the embankment surface. Total settlement also is important. Vertical load transfer has been extensively studied, and a number of design procedures are available (Schaefer et al. 2017; BSI 2016; CUR226 2016; Sloan et al. 2014; DGGT 2012).

Compared to vertical load transfer, lateral spreading in CSEs has been less extensively studied, and a number of uncertainties remain in design. Herein, lateral spreading is defined as the lateral deformation of the embankment fill and foundation in response to lateral earth pressures. The current design approach for lateral spreading is to assume that the lateral thrust originates from active lateral earth pressures in the embankment fill and LTP (Schaefer et al. 2017; BSI 2016; Sloan et al. 2014; DGGT 2012). Recommendations for use of geosynthetic reinforcement to resist the lateral thrust include that if one layer of reinforcement is applied, its required tensile capacity is calculated as the sum of the tension developed to resist the lateral thrust and to transfer vertical loads (BSI 2016; DGGT 2012; Schaefer et al. 2017; Sloan et al. 2014). Schaefer et al. (2017) recommended that if two layers of reinforcement are used, one biaxial layer can be designed to carry the tension due to vertical load transfer, and the other uniaxial layer can be designed to carry

the tension due to lateral spreading. Designing the LTP with two layers of geosynthetic reinforcement this way accounts for the direction dependency of the tensile demand.

The preceding lateral spreading analysis has several limitations. First, only the lateral earth pressures in the embankment and LTP are considered, not any lateral earth pressures that develop in the foundation soil due to embankment loading. The foundation earth pressures, which change with the development of soil arching and subsoil consolidation, have a direct impact on the reinforcement tension and column bending moments. Second, the lateral earth pressure in the embankment fill may not be well represented by the active lateral earth pressure because soil arching results in redistribution of stresses throughout the embankment. The lateral stress above columns, where stress concentration occurs, is not equal to the lateral stress above the foundation soil between columns. Third, limited studies have been conducted on the interaction of vertical and lateral loads in the geosynthetic reinforcement (Chen et al. 2016; Yu et al. 2016). Questions remain regarding whether current procedures for calculating the geosynthetic tension are appropriate and conservative. Finally, recommendations for column design in lateral spreading are missing from many CSE design recommendations (Schaefer et al. 2017; Sloan et al. 2014). For concrete columns typically installed at low area replacement ratios (ARR) of 3%-10% (J. G. Collin, personally communication, 2018), there is concern about the bending moments that develop in unreinforced columns and the potential consequences of column bending failure. These gaps in design procedures need to be addressed for safety against lateral spreading and embankment stability.

This study includes the calibration of a unit cell model and a half-embankment model in FLAC3D v.5.01 (Itasca 2012) using a well-documented case history by Liu et al. (2007). The results provide calculated quantities that are fundamental to the evaluation of lateral spreading and are missing from current design procedures: (1) the incremental lateral earth pressures in the foundation, which directly influence column bending moments and geosynthetic tension; and (2) the column bending moments, axial loads, and stresses. Although a number of studies have adopted the Liu et al. (2007) case history for calibration of numerical procedures, none has provided these quantities (Ariyarathne et al. 2013a; Bhasi and Rajagopal 2014; Liu et al. 2007). To the best of the authors' knowledge, this is the first CSE study that presents calculated values of the increment of lateral earth pressure in the foundation soils beneath a CSE.

This study also demonstrates a rational numerical calibration for the large-deformation soil arching behavior in the CSE embankment fill. Small-scale soil arching experiments have been numerically modeled in a number of studies (Girout et al. 2014; Jenck et al. 2007; Moradi and Abbasnejad 2015). Jenck et al. (2009) applied an advanced constitutive model to simulate soil arching in the analyses of embankment case histories. To be more applicable and usable in practice, the procedure for modeling large-deformation behavior presented in this study is a simple alternative to using advanced constitutive relationships. It involves applying calibrated values of Young's modulus (E) and friction angle (φ') in loosened zones in the embankment, with the geometry of the loosened zones based on observations from bench-scale and field-scale tests.

The final distinct feature of this study is the adoption of an undrained (UD)-dissipated (DS) approach for calculating initial undrained distortions, followed by consolidation in a computationally efficient manner. Other CSE numerical studies have adopted undrained analyses (Filz and Navin 2006; Jamsawang et al. 2015; Kitazume and Maruyama 2006; Stewart et al. 2004), fully drained analyses (Han and Gabr 2002; Huang et al. 2005; Jenck et al. 2009; Mahdavi et al. 2016a; Nunez et al. 2013; Stewart et al. 2004; Ye et al. 2017; Yu et al. 2016), or coupled consolidation analyses (Ariyarathne et al. 2013a; Ariyarathne et al. 2013b; Bhasi and Rajagopal 2013; Bhasi and Rajagopal 2014; Bhasi and Rajagopal 2015; Borges and Marques 2011; Huang and Han 2009; Huang and Han 2010; Jamsawang et al. 2016; Liu et al. 2007; Liu and Rowe 2016; Mahdavi et al. 2016; Mahdavi et al. 2016a; Rowe and Liu 2015; Yapage and Liyanapathirana 2014; Yapage et al. 2014; Zheng et al. 2009; Zhuang and Wang 2016). The undrained-dissipated approach was selected to analyze limiting cases of foundation lateral earth pressures and geosynthetic strains.

2.3. Undrained-Dissipated Analyses

Advanced numerical analyses of CSEs should include reasonable representations of soil arching in the embankment fill, strains in the geosynthetic reinforcement, and consolidation of the soft subsoil. A number of studies have adopted the coupled mechanical-fluid approach for this purpose, as previously cited. Although mechanically sound, coupled analyses can be computationally intensive, depending on the constitutive models used, system component properties, and size of the numerical domain.

Evidence from case histories suggest that the analysis of lateral spreading, in terms of soil deformations and geosynthetic strains, may not require a coupled analysis. Case history data have shown that soil arching may not have fully developed by the end of construction, and the subsoil between columns must support more load than if arching had fully developed (Briançon and Simon 2012; Chen et al. 2009; Chen et al. 2013; Habib et al. 2002; Oh and Shin 2007; Shang et al. 2016; Xu et al. 2016; Zhou et al. 2016; Zhuang and Cui 2016). A limiting case can be represented numerically using undrained end-of-construction analysis, where only distortion in the saturated clay layers is permitted, and the subsoil has to support the upper bound of vertical and lateral earth pressures. Case histories with longer recording periods have found that reinforcement strains and foundation lateral deformations can increase after construction (Briançon and Simon 2012; Hong and Hong 2017; Lai et al. 2006; Liu et al. 2012; Shang et al. 2016; Wang et al. 2013; Zhang et al. 2016; Zhou et al. 2016), indicating that the other limiting case for analysis is the consolidated long-term condition.

Instead of a fully coupled analysis, an undrained-dissipated approach using manual dissipation of excess pore pressures can be applied for analyzing the two limiting cases. In this approach, the first stage allows excess pore pressure generation using an effective stress constitutive model during the application of embankment loading. Stresses and deformations are solved for the limiting undrained end-of-construction scenario. The second stage involves manually dissipating the excess pore pressures by returning the total pore pressures to a hydrostatic condition. The change in effective stresses due to dissipation of excess pore pressures results in deformations for the consolidated long-term scenario.

A complete description of the undrained-dissipated approach as well as the FLAC3D numerical procedure for manual dissipation were provided by Huang et al. (2018). Calculated deformations using this approach were validated using two benchmark consolidation examples for various stages of consolidation. Both examples involved monotonic loading, and therefore the manual dissipation method is applicable to the analysis of embankment construction and subsequent consolidation of the subsoil. The method has not been validated for cases of unload-reload. Another limitation of the manual dissipation approach is that it can only calculate deformations associated with known increments of decrease in excess pore pressures, which renders it difficult to apply in cases of intermediate stages of consolidation. The last component of Huang et al. (2018) is the application

of the undrained-dissipated approach in a preliminary unit cell analysis of the Liu et al. (2007) case history. The present study adopted the undrained-dissipated approach for an updated unit cell analysis and a new half-embankment analysis. These new analyses offer greater refinement for calculating the long-term dissipated scenario by using calibrated material parameters for modeling large-deformation response in soil arching. The new half-embankment analysis, with its half-embankment geometry, is also required for lateral spreading analysis.

2.4. Numerical Modeling of Soil Arching

Soil arching was described by Terzaghi (1936) in a trapdoor experiment. The trapdoor apparatus consisted of a boxed enclosure in which a section of the bottom platform could yield to allow differential soil settlement. With this differential settlement, vertical stresses that were uniformly distributed on the platform became increasingly redistributed to parts of the platform that did not yield. A similar stress redistribution occurs in the CSE. As the subsoil consolidates, vertical embankment loads are increasingly transferred to the stiff columns, resulting in stress concentration above the columns and stress reduction above the compressible subsoil between columns. This stress redistribution reduces settlement and allows for accelerated construction. Observations from bench-scale experiments (McGuire 2011) and full-scale test embankments (Sloan 2011) indicate the loosening of fill in the regions of the embankment above the compressible soil that are subject to differential settlement, shear stresses, and reduced normal stresses. BSI (2016) recommends conducting vertical load transfer analyses using large-deformation shear strength parameters. The implication for numerical modeling of soil arching is that it should take into consideration both stress-dependency and large-deformation behaviors.

A limited number of constitutive models has been adopted for the analysis of the trapdoor problem using continuum techniques. The linear elastic-perfectly plastic Mohr-Coulomb failure criterion with non-associated flow rule has been commonly adopted for the study of cohesionless materials in small-scale physical models (Koutsabeloulis and Griffiths 1989; Liang and Zeng 2002; Pardo and Sáez 2014). This constitutive model has also been widely adopted for the analysis of the embankment fill and LTP in CSEs (Ariyarathne et al. 2013b; Bhasi and Rajagopal 2014; Bhasi and Rajagopal 2015; Jung et al. 2016; Liu et al. 2007; Nunez et al. 2013; Stewart et al. 2004; Yu et al. 2016). Stress-dependency has been modeled using the nonlinear hyperbolic elastic Duncan

and Chang (1970) model (Han and Gabr 2002; Jones et al. 1990; Oh and Shin 2007) and the Janbu (1963) formula (Jenck et al. 2009). Jenck et al. (2007) investigated the CJS2 model (Cambou and Jafari 1987) for simulating soil arching in a small-scale LTP, and later applied it in an embankment analysis (Jenck et al. 2009). This is a two-mechanism elastoplastic model with isotropic hardening. For the analysis of granular LTPs in centrifuge tests, Girout et al. (2014) used the Hardening Soil and the Hypoplastic models, though only the latter could account for nonlinear behavior as well as change in density and softening at large strains. Moradi and Abbasnejad (2015) applied a modified Mohr Coulomb model for the validation of experimental trapdoor tests. This model included stress-dependent stiffness elasticity as well as isotropic hardening-softening plasticity. The literature review suggests that very few studies have investigated the effects of different constitutive models on the calculation of arching in general, and even fewer have done so in a CSE model.

In this study, large-deformation behavior in soil arching was modeled in the dissipated analyses by reducing the E and φ' in domed loosened regions above the soil between columns. The geometry of these loosened regions was based on relationships developed from bench-scale experiments conducted by McGuire (2011). The experiments showed that the columns support inverted and truncated cones of embankment fill (Figure 2-1). The fill below the supported cones loosens due to shearing and reductions in normal stress. The tests were performed at different initial densities, and McGuire (2011) found correlations between the inverted cone angle, α, and the friction angle, φ, of the sand embankment fill (Equation 2.1). The upper limit of the loosened regions extended to the critical height, which is the lowest embankment height that does not exhibit differential surface settlements. According to McGuire (2011), the critical height is a function of the column diameter and spacing, and it is 3.3 m for the case history column configuration.

$$\alpha \approx 0.56\,\varphi \quad (2.1)$$

2.5. Description of the Liu et al. (2007) Case History

Liu et al. (2007) documented a CSE constructed in Shanghai, China, and the embankment geometry and site conditions are shown in Figure 2-2. Concrete annulus columns with an outer diameter of 1 m were installed in a 3-m center-to-center square arrangement, which produced an ARR of 8.7%. Column installation involved driving a double-wall casing into the ground, creating

a 120-mm-thick annulus that was concreted during casing withdrawal. The top 0.5 m of the inner soil column was replaced with a concrete plug. Full column installation details were provided by Liu et al. (2007). The LTP consisted of 0.5 m of gravel reinforced with one layer of biaxial polypropylene geogrid (TGGS90-90). Construction took place over a period of 55 days, during which the embankment reached a height of 5.6 m.

Instrumentation and embankment monitoring were reported by Liu et al. (2007) with recording locations shown in Figure 2-2. Instrumentation included 10 earth pressure cells on the foundation soil surface and column head (E1 – E10), 4 surface settlement plates (S1 – S4), 12 subsurface settlement gages (SS) installed every 2 m up to a depth of 24 m, an inclinometer (I1) 1.5 m downstream of the embankment toe, and 2 pore pressure piezometers (P1 and P2). The embankment was monitored for 125 days after construction, and it was reported that the earth pressure cell recordings had stabilized.

2.6. Selection of Material Properties

Material properties and constitutive models followed those selected by Liu et al. (2007), though some modifications were made according to the authors' judgement. Tables 2-1 and 2-2 summarize the soil and structural element material parameters adopted for the analyses, respectively. The selection of the column composite modulus, geogrid properties, foundation compressibility, and large-deformation parameters in soil arching are described subsequently, because these are central to the numerical results discussion. The supplementary file describes the selection of unit weights (γ), Poisson's ratio (v), column-soil interface element properties, geogrid-soil interface properties, and foundation compressibility parameters expanded in greater detail.

The concrete annulus columns were modeled using the composite modulus (E_{col}) matching the axial stiffness, *EA*, and the bending stiffness, *EI*, yielding values of 8.8 GPa and 13 GPa, respectively. The composite modulus cannot match *EA* and *EI* simultaneously, even though matching *EA* is reasonable for vertical load transfer analysis and matching *EI* is reasonable for lateral displacement and column bending moment analysis. Thus, both composite moduli were investigated, because both the vertical and lateral system responses are important to the numerical analysis.

The biaxial geogrid was modeled using FLAC3D structural geogrid elements, which can sustain membrane stress but not bending. The element type was plane stress Constant Strain Triangle, which has three nodes with two translational degrees of freedom per node and rigid attachment in the direction normal to the membrane element (Itasca 2013). The isotropic and orthotropic linear elastic models were investigated, with properties listed in Table 2-2. The isotropic linear elastic model was adopted by Liu et al. (2007) in their numerical analysis of the case history, but it was not considered the most representative of the biaxial geogrid, which has stiffness mainly in orthogonal directions as opposed to the same stiffness in all directions. Thus, analyses also were conducted using orthotropic linear elastic geogrid elements, which had equal stiffness in orthogonal directions, ν of zero (Zhuang and Wang 2015), and shear modulus (G) of 1 kPa. The shear modulus remained an uncertain parameter despite an extensive literature review, and this was the same conclusion reached by Santacruz Reyes (2016). However, the authors judged that G for the orthotropic model should be smaller than for the isotropic model, and to contrast between the two, a low value of 1 kPa was adopted (G = 0 kPa resulted in numerical instability).

Some uncertainty remained in the foundation compressibility parameters, despite being well documented. In the Modified Cam Clay formulation used to characterize the clay and silt layers, elastic and plastic volumetric strain increments are calculated using the preconsolidation pressure (p'_o), recompressibility (κ), and virgin compressibility (λ), as shown in Equations 2.2 and 2.3 (Wood 1990). Liu et al. (2007) conducted numerical analyses of the case history assuming the that entire foundation was normally consolidated, and the calculated lateral displacements exceeded inclinometer measurements by 250%. The authors suspected that the foundation compressibility was overestimated, and thus made reasonable modifications to the foundation preconsolidation pressures and κ, as summarized below.

$$\delta\varepsilon_p^e = \kappa/\nu(\delta p'/p') \qquad (2.2)$$

$$\delta\varepsilon_p^p = (\lambda - \kappa)/\nu(\delta p'_o/p'_o) \qquad (2.3)$$

1) The silty clay was assigned a preconsolidation pressure (σ'_p) increment of 10 kPa above the initial vertical effective stress (σ'_v) based on case history vane shear data.
2) The sandy silt was assigned a σ'_p increment of 500 kPa above the initial σ'_v, as determined from unit cell drained load-share tests. The load-share test involved applying uniform vertical pressures of 674 kPa on the column and 49.5 kPa on the foundation soil, based on

earth pressure cell measurements at E1 to E10 at 125 days after construction (Figure 2-2). Column and subsoil settlements from the load-share test exceeded post-construction recordings when the layer was normally consolidated, but matched recordings when a σ'_p increment of 500 kPa was assigned.

3) Clay layers were assigned κ at a ratio of 0.1 to λ, because calculations exceeded inclinometer data even after increasing preconsolidation pressures. The ratio provided by Liu et al. (2007) is 0.2, which is at the high end of the common range of 0.02 to 0.2 (Terzaghi et al. 1996). Because the recompressibility index is highly sensitive to soil disturbance and testing procedures (Terzaghi et al. 1996), it was impossible to reinterpret without access to original oedometer data or to find justification for the high values. By adopting κ at mid-range of published ratios, lateral displacement calculations for the dissipated and fully drained analyses bracketed end-of-construction inclinometer data. The dissipated analysis calculates undrained distortions and consolidation, so it exceeds the inclinometer data, which reflect some undrained distortion and some consolidation that occurred during construction. The fully drained analysis involves embankment construction without excess pore pressure generation, so it calculates displacements due to consolidation only. Lateral displacements from the fully drained analysis are smaller than those from the dissipated analysis but uncertain in magnitude relative to the end-of-construction inclinometer data. The authors judged that a suitable calibration was provided when the two calculations bracketed the end-of-construction inclinometer data after reducing κ of clays (κ_{clays}).

Large deformation in soil arching produces loosened zones in the embankment whose properties were represented by reduced values of E and φ'. As shown in Figure 2-3, reduced E and φ' were applied to regions in the embankment falling under the shear plane defined by α and up to the critical height. The α value was 16.8° (Equation 2.1). The parameters reduced were E of both the LTP and the embankment fill, and φ' of only the LTP (φ'_{LTP}), because the embankment fill already had a low φ' of 30°. The reduced values were selected based on a dissipated unit cell parametric study conducted separately. As shown in Table 2-3, as E and φ'_{LTP} were simultaneously reduced, the differential settlement increased, the vertical stress on the column decreased, and the vertical stress on the subsoil surface increased. When original (unreduced) values were used in all embankment zones, the differential settlement and vertical stresses on the subsoil were found to

be much smaller than from the drained load-share test in which the embankment load was represented by stresses. This confirmed that the vertical load transfer was affected by the embankment response. The LTP and embankment fill were not as compliant as they should have been, resulting in load transfer to the column that was larger than measured. When E and φ'_{LTP} were reduced to 6 MPa and 30° in the loosened zones, respectively, unit cell dissipated analyses were in good agreement with field measurements at 125 days after construction: differential settlement at subgrade level was measured at 67 mm and calculated at 70 mm; vertical stress on the column top was measured at 674 kPa and calculated at 605 kPa; and vertical stress on the subsoil was measured at 35-58 kPa and calculated at 50-52 kPa. Although combinations of E and φ'_{LTP} other than 6 MPa and 30° could result in the reasonable calibration of stresses and settlements, it was judged that both parameters must simultaneously be reduced for the zones of loosening. Furthermore, reduced values correspond to very loose coarse-grained fill resulting from decreases in normal stress, and the reduced value of φ' should not be interpreted in the same manner as those obtained from tests in which densification occurs prior to failure.

2.7. Geometry and Boundary Conditions

Unit Cell Model

Figure 2-3 shows the unit cell model geometry and discretization. The unit cell model consisted of a square cross-section with edge lengths of 1.5 m, or half the center-to-center column spacing. Rollers were applied on all faces, except the embankment surface, and on all geogrid edges.

Half-Embankment Model

Figure 2-4 shows the half-embankment model discretization and geometry. The half-embankment geometry is applicable to the analysis of a symmetric embankment and allows evaluation of lateral spreading. The model discretization contained a total of 52,454 grid points (locations of displacement calculation) and was adopted because the maximum difference in displacements calculated from a fully drained analysis was 8% compared to that for a model with 39,268 grid points. The foundation lateral extent was set to 4 times the embankment width, as determined by applying an equivalent embankment pressure on the foundation and increasing the lateral extent until displacements converged for both undrained and dissipated analyses.

Boundary conditions in the half-embankment model were similar to those in the unit cell model, with the following exceptions. Pins were applied on the bottom surface to represent the shear resistance likely found at the bottom of the bearing sandy silt layer. The geogrid nodes intersecting the slope were rigidly attached to the LTP, because Liu et al. (2007) described the geogrid as being wrapped and anchored back into the embankment.

2.8. Numerical Procedure

Undrained-dissipated analyses were conducted in FLAC3D version 5.01 (Itasca 2012) for both the unit cell and half-embankment geometries, and a fully drained analysis was conducted for the half-embankment geometry as part of the lateral displacement calibration (previously described). Large-strain mode was adopted so that the geogrid could develop tension under out-of-plane deformation. Numerical procedures for the undrained-dissipated and fully drained analyses are described subsequently.

Undrained-Dissipated

1) In-situ vertical and horizontal stresses were assigned to the foundation. Column zones were initially assigned the same density and stresses as the surrounding soils. Embankment and LTP zones were initially created as null elements.
2) Column installation was modeled by gradually increasing column density and then assigning increased lateral stresses in the foundation soils. The model was solved during density increase, and solved for mechanical equilibrium after increase in lateral stress. The displacements accumulated at this point were very small and were zeroed.
3) Undrained construction involved embankment construction in lifts and excess pore pressure development in the clay and sandy silt layers without drainage. Lift zones that were initially assigned as null elements were changed to Mohr-Coulomb materials, and then their densities were gradually increased, during which the model was solved. The LTP was placed first, in which alternating layers of gravel and geogrid were installed in sequence. Embankment fill construction followed in one lift in the unit cell and in six approximately equal lifts in the half-embankment. The number of lifts in the half-embankment model was determined from a convergence study, in which the lift number was increased until undrained displacements converged.

4) Dissipated long-term analyses were conducted. Because full development of soil arching was expected for the long-term condition, large-deformation parameters were applied from the onset of the dissipated analysis to loosened zones in the embankment fill and LTP (i.e. φ'_{LTP} of 30° and E of 6 MPa), as described previously. Excess pore pressures in the clay and sandy silt layers were manually dissipated in one step according to the method described by Huang et al. (2018). The model was solved for mechanical equilibrium.

Fully Drained

1) Before embankment placement, the numerical procedure was identical to the undrained-dissipated analysis.
2) Embankment construction was similar to that in the undrained analysis but without excess pore pressure development in the foundation. In loosened regions in the embankment, reduced values of E and φ'_{LTP} were adopted after embankment construction, and the model was solved for equilibrium.

2.9. Results and Discussion

Results for undrained-dissipated analyses are provided for three conditions of the geosynthetic reinforcement: isotropic linear elastic, orthotropic linear elastic, and no geogrid. Results for the fully drained analyses using the orthotropic geogrid are also provided in the discussion of lateral displacements. Unless otherwise indicated, results are for $\kappa_{clays} = 0.1\lambda$ and $E_{col} = 8.8$ GPa.

2.9.1. Vertical Load Transfer

Tables 2-4 and 2-5 indicate that for vertical load transfer calculations in the unit cell and the half-embankment, respectively, results for the isotropic (IG), orthotropic (OG), and no geogrid (NG) conditions were very similar. This was true in both undrained and dissipated analyses (i.e. UD and DS). Because excluding the geogrid insignificantly impacted vertical load transfer, using either an isotropic or orthotropic model also was inconsequential.

Compared with recordings at the end of construction, undrained analyses for both the unit cell and half-embankment models produced larger values of vertical stress on the subsoil surface, smaller vertical stress on the column tops, and smaller subsoil and column settlements (UD vs. recordings

in Tables 2-4 and 2-5). This outcome was as expected because embankment construction took 55 days, during which some excess pore pressure dissipation and consolidation occurred, causing more load transfer to the columns and more settlement than represented in the limiting case of the undrained analysis.

Comparing the unit cell (Table 2-4) and half-embankment (Table 2-5) analyses for the undrained condition (UD), more vertical load was transferred to the column top at E9 and E10 in the half-embankment than to the column in the unit cell. This was due to lateral displacements in the half-embankment model, which allowed for more differential settlement and, consequently, more load concentration onto the columns. The half-embankment calculation of vertical stress on the subsoil at E1 to E8 (Table 2-5) was smaller than for the unit cell calculation (Table 2-4), but still larger than recordings, which indicates that the undrained analyses can calculate an upper bound for cases of rapid construction. The over-calculation in the half-embankment model was approximately 50%, which is conservative but reasonable.

Comparing the dissipated analyses (DS) with the undrained analyses (UD) in the unit cell and half-embankment (Tables 2-4 and 2-5), dissipated analyses resulted in an increase in vertical load transfer to columns, a decrease in vertical stress on the subsoil, and an increase in subsoil and column settlements. These occurred in response to the subsoil consolidation and further development of soil arching in the embankment.

Dissipated analyses were in good agreement with recordings at 125 days after construction. For the half-embankment analysis using the orthotropic geogrid (DS, OG in Table 2-5), both κ_{clays} = 0.1λ (reduced) and κ_{clays} = 0.2λ (case history original) produced reasonable agreement with recordings, indicating that the choice to use reduced κ_{clays} at about the mid-range of published ratios to λ was reasonable. Using E_{col} = 8.8 GPa and 13 GPa produced similar results because the relative difference between the two composite column moduli was much smaller than the relative difference between the column and soil moduli. Lastly, the fact that dissipated analyses in both the unit cell and half-embankment (DS in Tables 2-4 and 2-5) were in good agreement with recordings indicates that vertical load transfer was not significantly affected by lateral spreading, because the only difference between the unit cell and half-embankment analyses was lateral displacement.

2.9.2. Lateral Displacements

The measured and calculated lateral displacement profiles at 1.5 m downstream of the embankment toe are illustrated in Figure 2-5. The measured profile was recorded at full embankment height (Liu et al. 2007). Consistent with the comparison by Liu et al. (2007) of foundation lateral displacements at different fill heights, the present study assumed that the displacement profile for the full embankment height was measured near the end of construction and not long after.

As shown in Figure 2-5a, lateral displacement profiles were calculated for the undrained condition, the dissipated condition (i.e. undrained condition followed by excess pore pressure dissipation), and the fully drained condition (i.e. no excess pore pressure development). The undrained and dissipated conditions were analyzed with three cases of geogrid (i.e. isotropic, orthotropic, and no geogrid). The fully drained condition was analyzed with the orthotropic geogrid. The reinforcement conditions had negligible effect on the lateral displacements.

The calculated lateral displacements in increasing order of magnitude were the fully drained, dissipated, and undrained, and the measured profile was in best agreement with the fully drained and dissipated analyses (Figure 2-5a). The dissipated analysis calculated more deformation than did the fully drained analysis because it accounted for undrained distortions. The measured profile was in reasonable agreement with the fully drained and dissipated analyses because consolidation of the foundation soil occurred during actual construction. The undrained analysis calculated larger lateral displacements than did the dissipated analysis because the decrease in volume during consolidation resulted in lateral rebound. When subsoil settlement was limited by the highly effective vertical load transfer to columns, the decrease in soil volume during consolidation occurred both vertically and laterally. Other CSE numerical studies with long-term consolidation also calculated lateral rebound (Huang and Han 2010; Yapage and Liyanapathirana 2014; Yapage et al. 2014). Creep was not modeled, and would have increased calculated long-term displacements if it had been included in the numerical analyses.

The calculated lateral displacement profiles for the fully drained and dissipated analyses were larger than the measured profile in the upper few meters (Figure 2-5a). A reason could be that the coarse-grained fill at the corresponding elevation was stronger than that characterized in the case

history (i.e. E = 7 MPa, φ' = 28°). Without additional data, it is impossible to ascertain the properties of this layer, but it is unlikely that this uncertainty affected the system response because the over-calculation was small (i.e. 5 mm and 14 mm for the fully drained and dissipated analyses, respectively).

Figure 2-5b illustrates the calculated lateral displacement profiles using the different column composite moduli (E_{col}). Results for the different E_{col} were similar, though using E_{col} = 13 GPa produced slightly lower lateral displacements, as was expected given the greater column flexural resistance. The selected values of E_{col} did not significantly affect lateral displacements, vertical load distribution, or settlements, indicating that the system response was not sensitive to the column modulus within this range.

Figure 2-5c illustrates the measured and calculated long-term lateral displacement profiles for κ_{clays} = 0.1λ and 0.2λ. Using κ_{clays} = 0.1λ calculated more reasonable lateral displacements than using κ_{clays} = 0.2λ. Because calculations using κ_{clays} = 0.1λ also resulted in good agreement with measured vertical load distributions and settlements, it was an overall suitable choice for the calibration.

2.9.3. Incremental Lateral Earth Pressures

Figure 2-6 illustrates the foundation incremental lateral earth pressure profiles at the half-embankment centerline for the undrained and dissipated analyses. Incremental lateral earth pressure is defined as the increase in total lateral stress due to loading. Each data point in the profile represents the incremental lateral earth pressure acting in the transverse direction, using the average of values across the longitudinal direction of the 3D domain at a certain depth. Only the profiles calculated using the orthotropic geogrid are illustrated because they were similar for the different geogrid conditions. Because the geogrid condition insignificantly affected vertical load distribution, it also insignificantly affected the foundation lateral earth pressures, because the increment of lateral earth pressure develops in response to the increment of vertical earth pressure.

The undrained analyses resulted in incremental lateral pressures that were greater in magnitude and depth of influence than those of the dissipated analyses. This was expected because the undrained subsoil supported a greater embankment load before consolidation occurred and when soil arching was limited. Following dissipation of excess pore pressures and consolidation, the

foundation lateral earth pressure decreased as greater vertical loads were distributed to the columns by soil arching in the embankment and transfer through shaft resistance. A portion of the dissipated analysis profile was negative, indicating a decrease in lateral stress relative to that at pre-construction. This result is consistent with the lateral rebound that occurred during consolidation, analogous to movement induced by suction.

2.9.4. Column Bending Moments and Maximum Tensile Stresses

Column bending moment profiles are illustrated in Figures 2-7(a and b) for the undrained and dissipated conditions, respectively. These were generated by extracting displacements from the centerline of each column in the half-embankment model and then imposing the displacements on a corresponding FLAC3D pile structural element (Itasca 2013) for the automatic calculation of bending moments. There was insignificant difference in the bending moments calculated for the different geogrid conditions, so the figures are only for the orthotropic geogrid condition. The similarity stems from the insignificant geogrid effect on foundation lateral earth pressures, to which columns respond in bending. The observed trend was that columns increase in bending moments as they increase in distance from the centerline. This was true for both the undrained and dissipated conditions, with the one exception being that the maximum moment in the dissipated condition occurred in column 8 (penultimate) rather than in column 9 (outermost). The column bending moment profiles calculated using the different E_{col} also were compared. Bending moments were larger for E_{col} = 13 GPa because the columns with higher modulus provided greater flexural resistance. These results are consistent with the smaller lateral displacements calculated when using the larger E_{col} (Figure 2-5b).

The bending moments were used to calculate the maximum column tensile stress, which is important for the design of columns weak in tension, such as unreinforced cementious column types. Table 2-6 lists the maximum column tensile stresses (σ_{max}) and the depth at which they were found ($z_{\sigma,max}$), calculated using two methods. The first method calculated the σ_{max} that develops under the combination of bending moments (M_{col}), axial compression (σ_c), and column self-weight (W), using Equation 2.4. Both M_{col} and σ_c were obtained from the pile structural element previously mentioned, and σ_{max} is expressed as tension positive. Results for this first method are listed under the heading "Load combination analysis." The second method approximated σ_{max} by linearly

extrapolating stresses calculated in zones, and results are listed under the heading "Half-embankment analysis." The two methods yielded consistent $z_{\sigma,max}$ and σ_{max}. However, values from the "Load combination analysis" are preferred because they did not involve extrapolation and thus they are used in the following discussion regarding σ_{max}.

$$\sigma_{max} = \frac{M_{col} y}{I} - \sigma_c - \frac{W}{A} \qquad (2.4)$$

Column tensile stresses develop under the combination of flexure and axial compression, and thus the location of maximum tensile stress ($z_{\sigma,max}$) is not necessarily the location of maximum bending moment ($z_{M,max}$). For example, the undrained analysis conducted without a geogrid (UD, NG in Table 2-6) resulted in a maximum M_{col} in column 9 at $z_{M,max}$ of 14m, but a σ_{max} at $z_{\sigma,max}$ of 3.8 m. Another example is in the dissipated analysis conducted without a geogrid (DS, NG in Table 2-6), in which column 8 had a larger M_{col} than column 9, but column 9 had the larger σ_{max} because it was the outermost column and carried least of the embankment loading that can offset flexural tension.

The geogrid condition insignificantly influenced σ_{max} (Table 2-6). This was expected because the geogrid condition insignificantly influenced M_{col} and vertical load distribution. A small discrepancy occurred for the undrained analysis conducted with and without the orthotropic geogrid (UD, OG vs. UD, NG), in which the σ_{max} in column 9 was slightly smaller for the no-geogrid condition. This was due to a local decrease in bending moment at the column depth, and although it is counterintuitive, the difference in σ_{max} is only 2.4%.

Column σ_{max} was calculated for both cases of column composite modulus. The σ_{max} calculated using E_{col} = 13 GPa was higher for both the undrained and dissipated conditions. Because E_{col} insignificantly affected vertical load distribution at the subgrade level and axial compression in the columns (Table 2-5), the larger σ_{max} thus was the result of an increase in M_{col} because columns with the higher modulus provided greater flexural resistance.

The magnitude of σ_{max} was unaffected by the type of analysis with regards to pore pressures, but it could be of concern to unreinforced cementitious columns. The largest σ_{max} occurred in either the undrained or the dissipated condition; σ_{max} was larger in the undrained condition when $\kappa_{clays} = 0.2\lambda$ and larger in the dissipated condition when $\kappa_{clays} = 0.1\lambda$ (Table 2-6). In all scenarios examined,

results suggest that the tensile strength was not exceeded, if typical concrete flexural strengths of 2-3 MPa were considered (ACI 2008). The column ARR was 8.7%, which is at the high end of the typical 3-10%, and the column diameter was 1.0 m, which exceeds the 0.35 m to 0.60 m typically constructed for unreinforced concrete columns for CSE applications in the United States (J.G. Collin, personal communication, 2018). The authors recommend adopting a failure criterion for modeling concrete columns in future numerical investigations, especially in cases in which the column design is less conservative.

2.9.5. Geogrid Strains

Transverse geogrid strain profiles calculated using the orthotropic geogrid for the undrained and dissipated conditions are shown in Figure 2-8. Strains were more critical in the dissipated condition because the geosynthetic increased in vertical deflection during subsoil consolidation. Strains were also higher over the columns than between the columns, and reached maximums above column edges, which is in agreement with other numerical studies (Ariyarathne et al. 2013b; Han and Gabr 2002; Huang and Han 2009; Liu et al. 2007; Zhuang and Wang 2015). Strains found above each column were higher on the downstream side, which likely was due to the influence of lateral spreading. Lastly, strains were higher between the centerline and the crest than near the toe because tension develops through friction at the geogrid-soil interface over a required length.

Table 2-7 provides the maximum geogrid strains calculated from the unit cell and half-embankment analyses, and strains estimated from simplified methods (Filz and Smith 2006; Schaefer et al. 2017). Calculated strains were higher when using an isotropic geogrid model (IG) than when using an orthotropic geogrid (OG). This is because the isotropic geogrid carried more vertical load that was transferred to columns. Calculated strains also were higher for the unit cell analyses than for the half-embankment analyses. This is because the unit cell model adopted a finer discretization, which affected calculation of local strain effects that were found to be highest above column edges. A convergence study using the unit cell geometry and orthotropic geogrid found that calculating the peak strain required a refined discretization of approximately 720 geogrid elements (Figure 2-9). The calculation depended on refinement both in the model cross-section and in the zones above and below the geogrid. The maximum strain that developed under vertical loads converged at 1.23% (Figure 2-9), and this value is close to the 1.7% estimated using

the Filz and Smith (2006) method (Table 2-7). The total strain that develops under the combined effects of vertical load transfer and lateral spreading was estimated at 4.9% (Filz and Smith 2006; Schaefer et al. 2017), which is an increase of 3.2% attributed to lateral spreading. On the other hand, numerical analyses calculated an increase in strain of 0.31% due to lateral spreading. This was calculated as the difference in maximum strains of 0.55% and 0.24% from the half-embankment analysis using an orthotropic geogrid (DS, OG in Table 2-7) and a unit cell analysis with equivalent discretization (Figure 2-9), respectively. These results indicate that although the design recommendation for calculating the geogrid strain appears conservative, it does not account for the ineffectiveness of the geogrid in reducing lateral displacements and earth pressures in this case history.

2.9.6. Geogrid Impacts

A summary of the geogrid impact in the CSE case history is provided based on a comparison of results from undrained-dissipated analyses conducted with and without a geogrid.

1) The geogrid contribution to vertical load transfer to columns in the half-embankment analyses was very limited. This was the case for both the undrained and dissipated conditions, even though the geogrid increased in vertical deflection and tension following subsoil consolidation (i.e. DS, OG vs. DS, NG in Table 2-5).
2) The geogrid decreased lateral displacements 1.5 m downstream of the embankment toe by less than 1.5% (Figure 2-5a).
3) The geogrid insignificantly impacted incremental foundation lateral earth pressures, as expected, given the insignificant improvement in vertical load transfer.
4) The geogrid insignificantly reduced column bending moments and tensile stresses, as expected, given the insignificant change in lateral earth pressures.

The analyses of this case history show that the geogrid did not significantly impact vertical load transfer and lateral spreading, and this is attributed to subgrade support provided by the coarse-grained fill. To demonstrate the effect of subgrade support on geosynthetic contribution to vertical load transfer, undrained-dissipated unit cell analyses were conducted for a case of reduced subgrade support by extending the soft silty clay to the foundation surface. Comparing the geogrid contribution in the dissipated analysis of the modified unit cell with that of the original unit cell

(Table 2-8 versus Table 2-4), the geogrid more effectively reduced the vertical stress on subsoil (18% versus negligible) and the subsoil settlement (14% versus 2%). The increase in geogrid effectiveness in load transfer stems from the higher tensions developed when the geogrid increases in deflection over a more compressible subgrade.

2.10. Summary and Conclusions

Three-dimensional numerical analyses using an undrained-dissipated approach were conducted for a well-documented column-supported embankment (CSE) case history (Liu et al. 2007). Numerical calibration of material parameters was made, first in a unit cell and then in a half-embankment model, such that calculations matched field recordings of vertical load transfer and lateral displacement. An undrained-dissipated approach was adopted because the limiting cases for lateral spreading analysis are undrained end-of-construction and dissipated long-term. The undrained analysis involved development of excess pore pressures in the foundation during embankment construction, and it was followed by the dissipated analysis in which excess pore pressures were manually returned to the hydrostatic condition. The dissipated analysis adopted calibrated values of E and φ' for loosened zones in the embankment fill and load transfer platform that exhibit large-deformation behavior in soil arching. The compressibility of the foundation soil was iteratively adjusted until good agreement between numerical calculations and field recordings of settlements, vertical load distribution, and lateral displacements was obtained. Results were presented in terms incremental lateral earth pressures, column bending moments and tensile stresses, and geosynthetic strains, which are required but missing from current CSE lateral spreading design. The geosynthetic impact was further examined by conducting the analyses using three different geosynthetic conditions (an isotropic linear model, an orthotropic linear model, and excluding the geogrid) and by conducting a modified unit cell analysis with reduced subgrade support.

The numerical analyses provided the following insights into vertical load transfer and lateral spreading in the CSE:

1) Vertical load transfer was not significantly affected by lateral spreading.
2) Undrained end-of-construction analyses calculated conservative but reasonable upper bound vertical stresses on the subsoil.

3) Incremental lateral earth pressures were largest at undrained end-of-construction. With limited settlement, the soft soil supported more load than after subsoil consolidation occurred, resulting in the largest foundation lateral earth pressures at the end of construction.
4) Column tensile stresses could be largest at the undrained end-of-construction or the long-term dissipated condition.
5) Column tensile stresses were largest in the peripheral columns, where lower axial compression offset the tension that developed in flexure.
6) Geogrid strains were more critical in the long-term condition due to subsoil consolidation and geogrid deflection, and were largest above column edges.
7) Subgrade support provided by the coarse-grained fill layer limited geogrid contribution to vertical load transfer.
8) Geogrid contribution to resisting lateral spreading was very limited. Geogrid inclusion insignificantly reduced lateral displacements, incremental lateral earth pressures, and column bending moments.
9) Material property selection was demonstrated to be important for deformation calculations. Modifications to the preconsolidation pressures and recompression affected both settlements and lateral displacements.

Beyond the lessons gained on CSE vertical load transfer and lateral spreading, the authors also recommend the following analyses be conducted for advancing CSE lateral spreading design:

1) Geosynthetic strains resulting from the interaction of the vertical load transfer and lateral spreading effects should be investigated using refined numerical discretizations. The largest strain was found above the column edge, and this is a localized effect that can only be examined through high refinement. This finding also serves as a caution when interpreting geogrid strains in CSE models.
2) The geosynthetic contribution to resisting lateral spreading should be examined for cases of reduced subgrade support, such as when compressible foundation layers extend to the surface and geosynthetic tensions are higher. Effects of additional geosynthetic layers also should be examined.

3) A failure criterion should be adopted for analyzing unreinforced concrete columns in CSE applications. Although the analysis of column tensile stresses suggested that the concrete tensile strength was not exceeded, the area replacement ratio was at the high end of the typical range adopted for concrete columns and the column diameter was larger than what is typically constructed in U.S. practice.

Notation

The following symbols are used in this chapter:

A = area;

c' = effective cohesion;

E = Young's modulus;

E_{col} = composite Young's modulus of column;

e_1 = void ratio at reference pressure;

G = shear modulus;

I = moment of inertia of plane area;

J, J_x, J_y = stiffness (in direction indicated by subscript);

K_0 = coefficient of lateral earth pressure at rest;

M = slope of critical state line;

M_{col} = column bending moment;

p' = mean effective stress;

p'_o = preconsolidation pressure;

p_1 = reference pressure;

W = weight;

y = radial distance from column centerline;

z = depth;

α = angle of shear failure surface from vertical;

γ = unit weight;

$\delta\varepsilon_p^e$ = volumetric elastic strain increment;

$\delta\varepsilon_p^p$ = volumetric plastic strain increment;

$\delta p'$ = change in mean effective stress;

$\delta p'_o$ = change in preconsolidation pressure;

κ = slope of recompression line;

κ_{clays} = slope of recompression line for clays;

λ = slope of virgin compression line;

v, v_x = Poisson's ratio (in direction indicated by subscript);

σ_{max} = maximum tensile stress;

σ_c = axial compressive stress;

σ'_p = preconsolidation pressure;

σ'_v = effective vertical stress;

φ' = effective friction angle;

φ'_{LTP} = effective friction angle of load transfer platform; and

ψ' = effective dilation angle.

References

ACI (American Concrete Institute). (2008). *Building code requirements for structural concrete (ACI 318-08) and commentary*. Farmington Hills, MI: ACI.

Ariyarathne, P., Liyanapathirana, D. S., and Leo, C. J. (2013a). "Comparison of Different Two-Dimensional Idealizations for a Geosynthetic-Reinforced Pile-Supported Embankment." *International Journal of Geomechanics*, 13(6), 754-768.

Ariyarathne, P., Liyanapathirana, D. S., and Leo, C. J. (2013b). "Effect of geosynthetic creep on reinforced pile-supported embankment systems." *Geosynthetics International*, 20(6), 421-435.

Bhasi, A., and Rajagopal, K. (2013). "Numerical investigation of time dependent behavior of geosynthetic reinforced piled embankments." *International Journal of Geotechnical Engineering*, 7(3), 232-240.

Bhasi, A., and Rajagopal, K. (2014). "Geosynthetic-Reinforced Piled Embankments: Comparison of Numerical and Analytical Methods." *International Journal of Geomechanics*, 15(5), 04014074.

Bhasi, A., and Rajagopal, K. (2015). "Numerical study of basal reinforced embankments supported on floating/end bearing piles considering pile–soil interaction." *Geotextiles and Geomembranes*, 43(6), 524-536.

Borges, J. L., and Marques, D. O. (2011). "Geosynthetic-reinforced and jet grout column-supported embankments on soft soils: Numerical analysis and parametric study." *Computers and Geotechnics*, 38(7), 883-896.

Briançon, L., and Simon, B. (2012). "Performance of Pile-Supported Embankment over Soft Soil: Full-Scale Experiment." *Journal of Geotechnical and Geoenvironmental Engineering*, 138(4), 551-561.

BSI (British Standards Institution). (2016). *Design of embankments with reinforced soil foundations on poor ground*. BS 8006-1:2010+A1:2016. London: British Standards Institution.

Cambou, B., and Jafari, K. (1987). "A constitutive model for granular materials based on two plasticity mechanisms." In *Proc., Constitutive Equations for Granular Non-cohesive Soils*, 149-167. Rotterdam, Netherlands: A. A. Balkema.

Chen, R., Xu, Z., Chen, Y., Ling, D., and Zhu, B. (2009). "Field tests on pile-supported embankments over soft ground." *Journal of Geotechnical and Geoenvironmental Engineering*, 136(6), 777-785.

Chen, R. P., Wang, Y. W., Ye, X. W., Bian, X. C., and Dong, X. P. (2016). "Tensile force of geogrids embedded in pile-supported reinforced embankment: A full-scale experimental study." *Geotextiles and Geomembranes*, 44(2), 157-169.

Chen, Y., Qi, C., Xu, H., and Ng, C. W. W. (2013). "Field Test Research on Embankment Supported by Plastic Tube Cast-in-place Concrete Piles." *Geotechnical and Geological Engineering*, 31(4), 1359-1368.

Collin, J. G. (2018). Personal Communication.

DGGT (Deutsche Gesellschaft für Geotechnik). (2012). *Recommendations for Design and Analysis of Earth Structures Using Geosynthetic Reinforcements-EBGEO*. New York: Wiley.

Duncan, J. M., and Chang, C. Y. (1970). "Nonlinear analysis of stress and strain in soils." *Journal of Soil Mechanics & Foundations Div*, 96(5), 1629-1653.

Filz, G. M., and Navin, M. P. (2006). "Stability of Column-Supported Embankments." Virginia Transportation Research Council. Charlottesville, Virgina.

Filz, G. M., and Smith, M. E. (2006). "Design of bridging layers in geosynthetic-reinforced, column-supported embankments." *Report No. VTRC 06-CR12*. Virginia Transportation Research Council. Charlottesville, Virgina.

Girout, R., Blanc, M., Dias, D., and Thorel, L. (2014). "Numerical analysis of a geosynthetic-reinforced piled load transfer platform – Validation on centrifuge test." *Geotextiles and Geomembranes*, 42(5), 525-539.

Habib, H., Brugman, M., and Uijting, B. (2002). "Widening of Road N247 founded on a geogrid reinforced mattress on piles." In *7th Int. Conf. on Geosynthetics*, 369-372. Nice, France: Swets & Zeitlinger.

Han, J., and Gabr, M. A. (2002). "Numerical Analysis of Geosynthetic-Reinforced and Pile-Supported Earth Platforms over Soft Soil." *Journal of Geotechnical and Geoenvironmental Engineering*, 128(1), 44-53.

Hong, W. P., and Hong, S. (2016). "Piled embankment to prevent damage to pipe buried in soft grounds undergoing lateral flow." *Marine Georesources & Geotechnology*, 35(5), 719-729.

Huang, J., and Han, J. (2009). "3D coupled mechanical and hydraulic modeling of a geosynthetic-reinforced deep mixed column-supported embankment." *Geotextiles and Geomembranes*, 27(4), 272-280.

Huang, J., and Han, J. (2010). "Two-dimensional parametric study of geosynthetic-reinforced column-supported embankments by coupled hydraulic and mechanical modeling." *Computers and Geotechnics*, 37(5), 638-648.

Huang, J., Han, J., and Collin, J. G. (2005). "Geogrid-Reinforced Pile-Supported Railway Embankments." *Transportation Research Record: Journal of the Transportation Research Board*, 1936 (1), 221-229.

Huang, Z., Ziotopoulou, K., and Filz, G. M. (2018). "Numerical Predictions of Deformations in Geosynthetic-Reinforced Column-Supported Embankments: Validation of Manual Dissipation of Excess Pore Pressure Approach for Undrained and Drained Analyses." *IFCEE 2018: Innovations in Ground Improvement for Soils, Pavements, and Subgrades, GSP 296*, 327-336.

Itasca. 2012. FLAC3D, version 5.01, Minneapolis, MN.

Itasca (2013). *Structural Elements.* Minneapolis, Minnesota: Itasca Consulting Group Inc.

Jamsawang, P., Voottipruex, P., Boathong, P., Mairaing, W., and Horpibulsuk, S. (2015). "Three-dimensional numerical investigation on lateral movement and factor of safety of slopes stabilized with deep cement mixing column rows." *Engineering Geology*, 188, 159-167

Jamsawang, P., Yoobanpot, N., Thanasisathit, N., Voottipruex, P., and Jongpradist, P. (2016). "Three-dimensional numerical analysis of a DCM column-supported highway embankment." *Computers and Geotechnics*, 72, 42-56.

Janbu, N. (1963). "Soil compressibility as determined by odometer and triaxial tests." *Proceedings of the 2nd European Conference on Soil Mechanics and Foundation Engineering*, 19-25. Essen, Germany: Deutsche Gesellschaft für Erd- und Grundbau.

Jenck, O., Dias, D., and Kastner, R. (2007). "Two-Dimensional Physical and Numerical Modeling of a Pile-Supported Earth Platform over Soft Soil." *Journal of Geotechnical and Geoenvironmental Engineering*, 133(3), 295-305.

Jenck, O., Dias, D., and Kastner, R. (2009). "Three-Dimensional Numerical Modeling of a Piled Embankment." *International Journal of Geomechanics*, 9(3), 102-112.

Jones, C. J. F. P., Lawson, C. R., and Ayres, D. J. (1990). "Geotextile reinforced piled embankments." In *Geotextiles, Geomembranes and Related Products*, 155-160. Rotterdam, Netherlands: Balkema.

Jung, Y. H., Lee, T., Lee, S. H., Lee, I. W., and Kim, T. (2016). "Finite Element Investigation on Patterns of Soil Arching in a Geosynthetics-Reinforced Piled Embankment." *Geotechnical and Structural Engineering Congress 2016*, 329-338. Reston, VA: ASCE.

Kitazume, M., and Maruyama, K. (2006). "External stability of group column type deep mixing improved ground under embankment loading." *Soils and Foundations*, 46(3), 323-340.

Koutsabeloulis, N. C., and Griffiths, D. V. (1989). "Numerical modelling of the trap door problem." *Geotechnique*, 39(1), 77-89.

Lai, Y., Bergado, D., Lorenzo, G., and Duangchan, T. (2006). "Full-scale reinforced embankment on deep jet mixing improved ground." *Proceedings of the Institution of Civil Engineers-Ground Improvement*, 10(4), 153-164.

Liang, R., and Zeng, S. (2002). "Numerical study of soil arching mechanism in drilled shafts for slope stabilization." *Soils and Foundations*, 42(2), 83-92.

Liu, H., Ng, C. W., and Fei, K. (2007). "Performance of a geogrid-reinforced and pile-supported highway embankment over soft clay: case study." *Journal of Geotechnical and Geoenvironmental Engineering*, 133(12), 1483-1493.

Liu, K. W., and Rowe, R. K. (2016). "Performance of reinforced, DMM column-supported embankment considering reinforcement viscosity and subsoil's decreasing hydraulic conductivity." *Computers and Geotechnics*, 71, 147-158.

Liu, S., Du, Y., Yi, Y., and Puppala, A. J. (2012). "Field Investigations on Performance of T-Shaped Deep Mixed Soil Cement Column–Supported Embankments over Soft Ground." *Journal of Geotechnical and Geoenvironmental Engineering*, 138(6), 718-727.

Mahdavi, H., Fatahi, B., Khabbaz, H., Krzeminski, M., Santos, R., and Marix-Evans, M. (2016). "Three-Dimensional Simulation of a Load Transfer Mechanism for Frictional and End Bearing CMC Supported Embankments on Soft Soil." *Geo-China 2016 Advances in Pavement Engineering and Ground Improvement, GSP 258*, 60-67.

Mahdavi, H., Fatahi, B., Khabbaz, H., Vincent, P., and Kelly, R. (2016a). "Comparison of Coupled Flow-deformation and Drained Analyses for Road Embankments on CMC Improved Ground." *Procedia Engineering*, 143, 462-469.

McGuire, M. P. (2011). "Critical Height and Surface Deformation of CSE." Ph.D. Dissertation, Department of Civil and Environmental Engineering, Virginia Polytechnic Institute and State University.

Moradi, G., and Abbasnejad, A. (2015). "Experimental and numerical investigation of arching effect in sand using modified Mohr Coulomb." *Geomechanics and Engineering*, 8(6), 829-844.

Nunez, M. A., Briançon, L., and Dias, D. (2013). "Analyses of a pile-supported embankment over soft clay: Full-scale experiment, analytical and numerical approaches." *Engineering Geology*, 153, 53-67.

Oh, Y. I., and Shin, E. C. (2007). "Reinforcement and Arching Effect of Geogrid-Reinforced and Pile-Supported Embankment on Marine Soft Ground." *Marine Georesources & Geotechnology*, 25(2), 97-118.

Pardo, G. S., and Sáez, E. (2014). "Experimental and numerical study of arching soil effect in coarse sand." *Computers and Geotechnics*, 57(Supplement C), 75-84.

Rowe, R. K., and Liu, K.-W. (2015). "Three-dimensional finite element modelling of a full-scale geosynthetic-reinforced, pile-supported embankment." *Canadian Geotechnical Journal*, 52(12), 2041-2054.

Santacruz Reyes, K. J. (2016). "Geosynthetic Reinforced Soil: Numerical and Mathematical Analysis of Laboratory Triaxial Compression Tests." Ph.D. Dissertation, Department of Civil and Environmental Engineering, Virginia Polytechnic Institute and State University.

Schaefer, V. R., Berg, R. R., Collin, J. G., Christopher, B. R., DiMaggio, J. A., Filz, G. M., Bruce, D. A., and Ayala, D. (2017). *Ground Modification Methods Reference Manual - Volume II*. Washington, D. C.: Federal Highway Administration.

Shang, Y., Xu, L., Xu, Y., Li, Y., and Ou, N. (2016). "Field Test Study on a Short Pile-net Composite Foundation over Gravel Clay for High-Speed Railways." *Journal of Engineering Science & Technology Review*, 9(3).

Sloan, J. A. (2011). "Column-Supported Embankments: Full-Scale Tests and Design Recommendations." Ph.D. Dissertation, Department of Civil and Environmental Engineering, Virginia Polytechnic Institute and State University.

Sloan, J. A., Filz, G. M., Collin, J. G., and Kumar, P. (2014). *Column-Supported Embankments: Field Tests and Design Recommendations*. 2nd Edition. Virginia Tech Center for Geotechnical Practice and Research, Blacksburg, Virginia.

Stewart, M. E., Navin, M. P., and Filz, G. M. (2004). "Analysis of a Column-Supported Test Embankment at the I-95/Route 1 Interchange." *Geotechnical Engineering for Transportation Projects, GSP 126*.

Terzaghi, K. (1936). "Stress distribution in dry and saturated sand above a yielding trapdoor." In *Proc. International Conference of Soil Mechanics*, Harvard University, Cambridge.

Terzaghi, K., Peck, R. B., and Mesri, G. (1996). *Soil Mechanics in Engineering Practice*. New York: Wiley.

van Eekelen, S. J. M., and Brugman, M. H. A. (2016). *Design guideline basal reinforced piled embankments*. Boca Raton, FL: CRC Press.

Wang, Y. M., Song, W. M., Zou, C., and Yang, K. (2013). "Field tests on performance of geosynthetic-reinforced and pile-supported embankment in highway expansion project." *Global View of Engineering Geology and the Environment*, 287-292. London: Taylor & Francis Group.

Wood, D. M. (1990). *Soil Behaviour and Critical State Soil Mechanics*. Cambridge: Cambridge University Press.

Xu, C., Song, S., and Han, J. (2016). "Scaled model tests on influence factors of full geosynthetic-reinforced pile-supported embankments." *Geosynthetics International*, 23(2), 140-153.

Yapage, N. N. S., and Liyanapathirana, D. S. (2014). "A parametric study of geosynthetic-reinforced column-supported embankments." *Geosynthetics International*, 21(3), 213-232.

Yapage, N. N. S., Liyanapathirana, D. S., Kelly, R. B., Poulos, H. G., and Leo, C. J. (2014). "Numerical Modeling of an Embankment over Soft Ground Improved with Deep Cement Mixed Columns: Case History." *Journal of Geotechnical and Geoenvironmental Engineering*, 140(11), 04014062.

Ye, G., Cai, Y., and Zhang, Z. (2017). "Numerical study on load transfer effect of Stiffened Deep Mixed column-supported embankment over soft soil." *KSCE Journal of Civil Engineering*, 21(3), 703-714.

Yu, Y., Bathurst, R. J., and Damians, I. P. (2016). "Modified unit cell approach for modelling geosynthetic-reinforced column-supported embankments." *Geotextiles and Geomembranes*, 44(3), 332-343.

Zhang, J., Zheng, J., Zhao, D., and Chen, S. (2016). "Field study on performance of new technique of geosynthetic-reinforced and pile-supported embankment at bridge approach." *Science China Technological Sciences*, 59(1), 162-174.

Zheng, J. J., Chen, B. G., Lu, Y. E., Abusharar, S. W., and Yin, J. H. (2009). "The performance of an embankment on soft ground reinforced with geosynthetics and pile walls." *Geosynthetics International*, 16(3), 173-182.

Zhou, M., Liu, H., Chen, Y., and Hu, Y. (2016). "First application of cast-in-place concrete large-diameter pipe (PCC) pile-reinforced railway foundation: a field study." *Canadian Geotechnical Journal*, 53(4), 708-716.

Zhuang, Y., and Cui, X. (2016). "Case Studies of Reinforced Piled High-Speed Railway Embankment over Soft Soils." *International Journal of Geomechanics*, 16(2), 06015005.

Zhuang, Y., and Wang, K. Y. (2015). "Three-dimensional behavior of biaxial geogrid in a piled embankment: numerical investigation." *Canadian Geotechnical Journal*, 52(10), 1629-1635.

Zhuang, Y., and Wang, K. Y. (2016). "Finite-Element Analysis on the Effect of Subsoil in Reinforced Piled Embankments and Comparison with Theoretical Method Predictions." *International Journal of Geomechanics*, 16(5), 04016011.

Tables

Table 2-1. Soil material parameters adopted for analyses

Material	γ (kN/m^3)	Model	φ' (deg)	c' (kPa)	ψ' (deg)	E (MPa)	ν	K_0	λ	κ	M	e_1	σ'_p (kPa)
Embankment Fill	18.3	MC	30	10	0	20, 6[a]	0.34						
LTP Gravel	21.0	MC	40, 30[a]	10	0	20, 6[a]	0.27						
Coarse-Grained Fill	20.0	MC	28	15	0	7	0.35						
Silty Clay	19.8	MCC					0.36	0.56	0.06	0.006[b], 0.012[c]	1.20	0.87	σ'_v +10
Soft Silty Clay	17.2	MCC					0.37	0.59	0.15	0.015[b], 0.03[c]	0.95	1.87	σ'_v
Medium Silty Clay	20.2	MCC					0.35	0.54	0.05	0.005[b], 0.01[c]	1.10	0.83	σ'_v
Sandy Silt	19.8	MCC					0.40	0.92	0.03	0.005	1.28	0.82	σ'_v +500

Note: MC = Mohr-Coulomb; MCC = Modified Cam Clay; e_1 was calculated at p_1 of 1 kPa and resulting in-situ void ratios provided agreement with measured water contents.

[a] Reduced values adopted for loosened zones in the embankment for dissipated and fully drained analyses.

[b] $\kappa_{clays} = 0.1\lambda$.

[c] $\kappa_{clays} = 0.2\lambda$ (after Liu et al. 2007).

Table 2-2. Structural element material parameters adopted for analyses

Material	γ (kN/m^3)	Model	E (GPa)	v	J (kN/m)	J_x (kN/m)	J_y (kN/m)	v_x	G (kPa)
Column	20.5	ILE	8.8[a], 13[b]	0.2					
Geogrid	0	ILE		0.3	1180				
		OLE				1180	1180	0.0	1

Note: ILE = Isotropic Linear Elastic; OLE = Orthotropic Linear Elastic.
[a] Composite modulus matching axial stiffness, *EA*.
[b] Composite modulus matching bending stiffness, *EI*.

Table 2-3. Influence of softening on differential settlement (between column top and subsoil surface), vertical stress on column, and vertical stress on subsoil surface in unit cell dissipated analyses

Softening Parameters				
E (MPa)	φ'_{LTP} (deg)	Differential settlement (mm)	Vertical stress on column (kPa)	Vertical stress on subsoil surface (kPa)
20[a]	40[a]	45	663	42-43
16	40	49	654	44-45
12	35	55	644	45-46
8	35	62	619	48-50
6[b]	30[b]	70	605	50-52
4	30	79	575	53-55

Note: Calculated values are for $\kappa_{clays} = 0.1\lambda$ and $E_{col} = 8.8$ GPa.
[a] Original parameters (i.e. embankment fill and LTP not softened).
[b] Reduced parameters adopted for loosened zones in the embankment for dissipated and fully drained analyses.

Table 2-4. Comparison between Liu et al. (2007) case history recordings and corresponding unit cell calculations

	Vertical stress (kPa)		Settlement (mm)	
Case of Comparison	Subsoil surface at E1 to E8	Column top at E9 and E10	Subsoil at S3	Column at S4
End of construction				
Recordings	31-56	552-584	63	14
UD, IG	77	295	13	2
UD, OG	77	295	13	2
UD, NG	77	295	13	2
125 days after construction				
Recordings	35-58	674	87	19
DS, IG	50-52	608	90	21
DS, OG	50-52	605	91	21
DS, NG	50-52	595	93	21

Note: UD = undrained; DS = dissipated; IG = isotropic geogrid; OG = orthotropic geogrid; NG = no geogrid; calculated values are for $\kappa_{clays} = 0.1\lambda$ and $E_{col} = 8.8$ GPa; locations shown in Figure 2-2.

Table 2-5. Comparison between Liu et al. (2007) case history recordings and corresponding half-embankment calculations

Case of Comparison	Vertical Stress (kPa)		Settlement (mm)			
	Subsoil surface at E1 to E8	Column top at E9 and E10	Subsoil at S2	Subsoil at S3	Column at S1	Column at S4
End of construction						
Recordings	31-56	552-584	45	63	8	14
UD, IG	62-68	456	24-25	27-29	5	8
UD, OG						
$\kappa_{clays} = 0.1\lambda$, E_{col} = 8.8 GPa	62-68	456	24-25	27-29	5	8
$\kappa_{clays} = 0.2\lambda$, E_{col} = 8.8 GPa	56-68	495	31-32	35-37	6	9
$\kappa_{clays} = 0.1\lambda$, E_{col} = 13 GPa	62-67	459	24-25	27-29	5	8
UD, NG	62-68	456	24-25	27-29	5	8
125 days after construction						
Recordings	35-58	674	65	87	14	19
DS, IG	41-52	660	62-64	81-84	13	20
DS, OG						
$\kappa_{clays} = 0.1\lambda$, E_{col} = 8.8 GPa	41-52	659	62-64	82-84	13	20
$\kappa_{clays} = 0.2\lambda$, E_{col} = 8.8 GPa	36-52	684	70-72	92-94	14	20
$\kappa_{clays} = 0.1\lambda$, E_{col} = 13 GPa	41-52	660	62-64	81-83	12	19
DS, NG	41-52	659	63-64	82-84	13	20

Note: UD = undrained; DS = dissipated; IG = isotropic geogrid; OG = orthotropic geogrid; NG = no geogrid; calculated values are for $\kappa_{clays} = 0.1\lambda$ and E_{col} = 8.8 GPa unless otherwise indicated; locations shown in Figure 2-2.

Table 2-6. Calculated maximum column tensile stress

		Load combination analysis				Half-embankment analysis	
Analysis	Column	$z_{M,\,max}$ (m)	M_{col} (kNm)	$z_{\sigma,\,max}$ (m)	σ_{max} (kPa)	$z_{\sigma,\,max}$ (m)	σ_{max} (kPa)
UD, OG							
$\kappa_{clays} = 0.1\lambda$, E_{col} = 8.8 GPa	9	14	77	3.8	541	3.6	482
$\kappa_{clays} = 0.2\lambda$, E_{col} = 8.8 GPa	9	3.8	102	3.8	925	3.6	873
$\kappa_{clays} = 0.1\lambda$, E_{col} = 13 GPa	9	14	91	14	598	12.7	592
UD, NG	9	14	78	3.8	528	3.6	481
DS, OG							
$\kappa_{clays} = 0.1\lambda$, E_{col} = 8.8 GPa	9	7.6	112	7.6	702	7.4	706
$\kappa_{clays} = 0.2\lambda$, E_{col} = 8.8 GPa	9	8.8	125	8.4	765	8.6	789
$\kappa_{clays} = 0.1\lambda$, E_{col} = 13 GPa	9	7.6	141	7.6	983	7.4	1010
DS, NG	8	7.2	127	7.2	535	7.0	519
	9	7.6	114	7.6	714	7.4	717

Note: UD = undrained; DS = dissipated; OG = orthotropic geogrid; NG = no geogrid; calculations used $\kappa_{clays} = 0.1\lambda$ and E_{col} = 8.8 GPa, unless otherwise indicated; column 8 is the penultimate column and column 9 is the outermost column.

Table 2-7. Comparison of maximum geogrid strain: numerical vs. simplified procedures

Analysis	Maximum geogrid strain (%)
Unit Cell	
DS, IG	1.8
DS, OG	1.1
Half Embankment	
DS, IG	0.67
DS, OG	0.55
Vertical load transfer (Filz and Smith 2006)	1.7
Vertical load transfer + lateral spreading as function of active lateral earth pressure of fill and LTP (Filz and Smith 2006; Schaefer et al. 2017)	4.9

Note: DS = dissipated; IG = isotropic geogrid; OG = orthotropic geogrid; calculated values are for $\kappa_{clays} = 0.1\lambda$ and E_{col} = 8.8 GPa.

Table 2-8. Unit cell vertical load transfer calculations with soft silty clay layer extended to foundation surface

	Vertical stress (kPa)		Settlement (mm)	
Case of Comparison	Subsoil surface	Column top	Subsoil	Column
DS, OG	21-24	846	202	22
DS, NG	27-28	839	236	22

Note: DS = dissipated; OG = orthotropic geogrid; NG = no geogrid; calculated values are for $\kappa_{clays} = 0.1\lambda$ and E_{col} = 8.8 GPa.

Figures

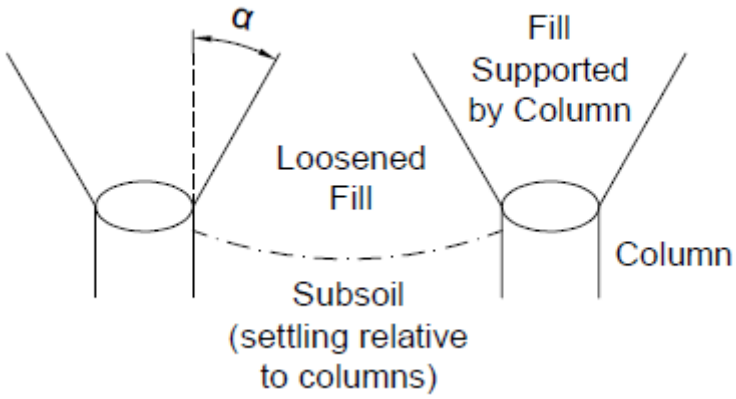

Figure 2-1. Supported and loosened zones in a column-supported embankment (data from McGuire 2011).

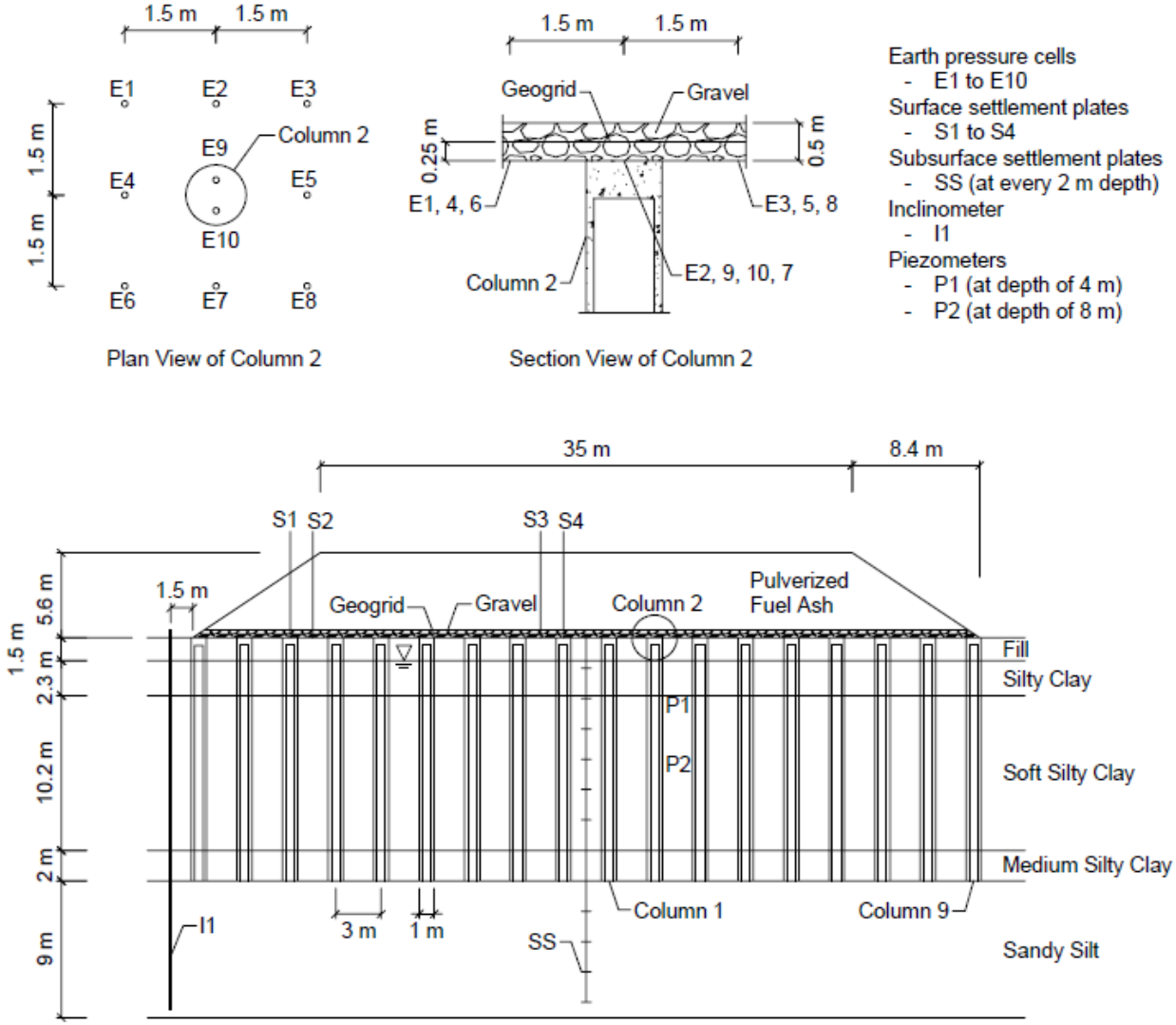

Figure 2-2. Embankment cross section and instrumentation (Reprinted from Liu et al. 2007, with permission from ASCE).

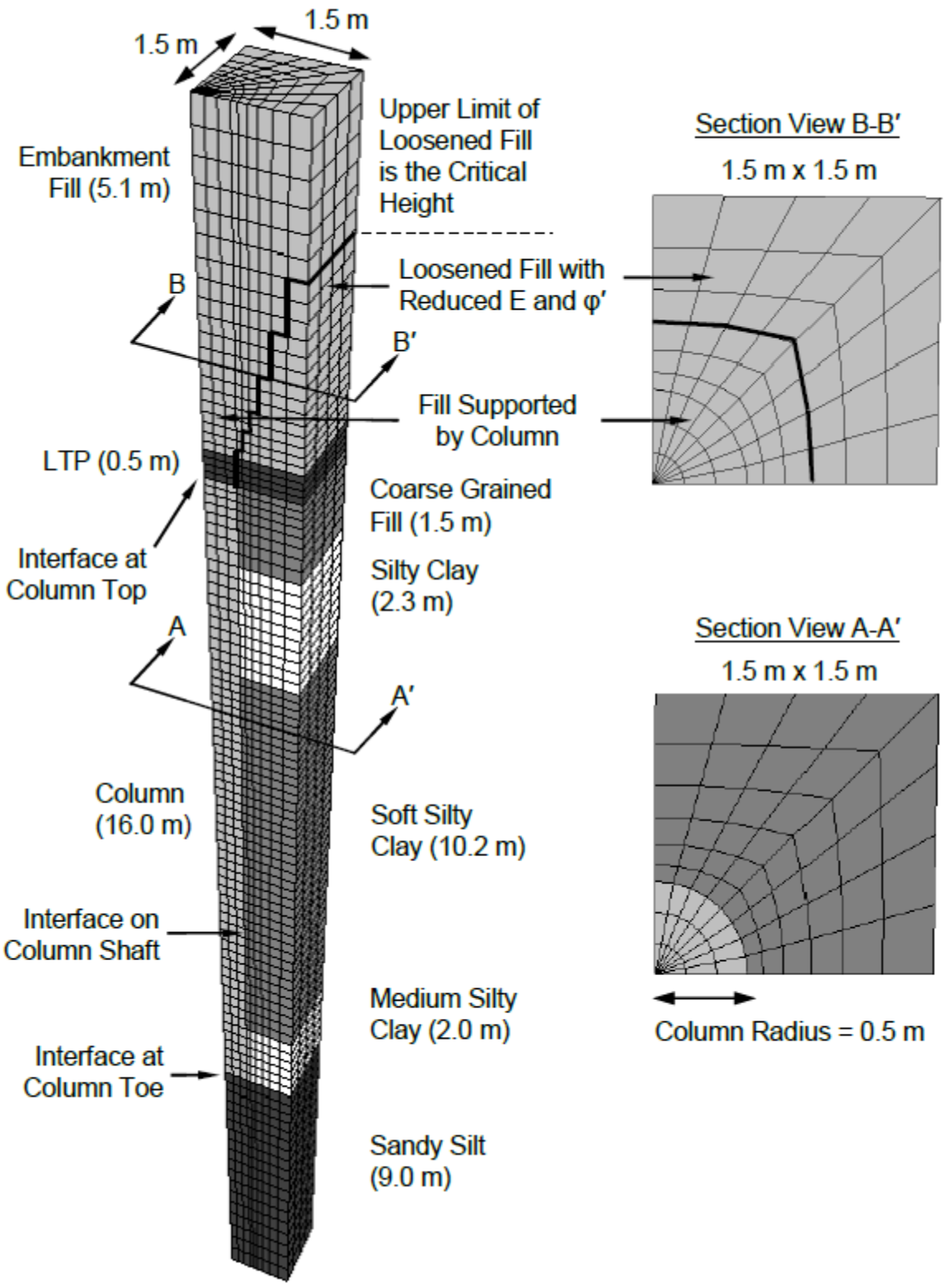

Figure 2-3. Unit cell geometry and discretization.

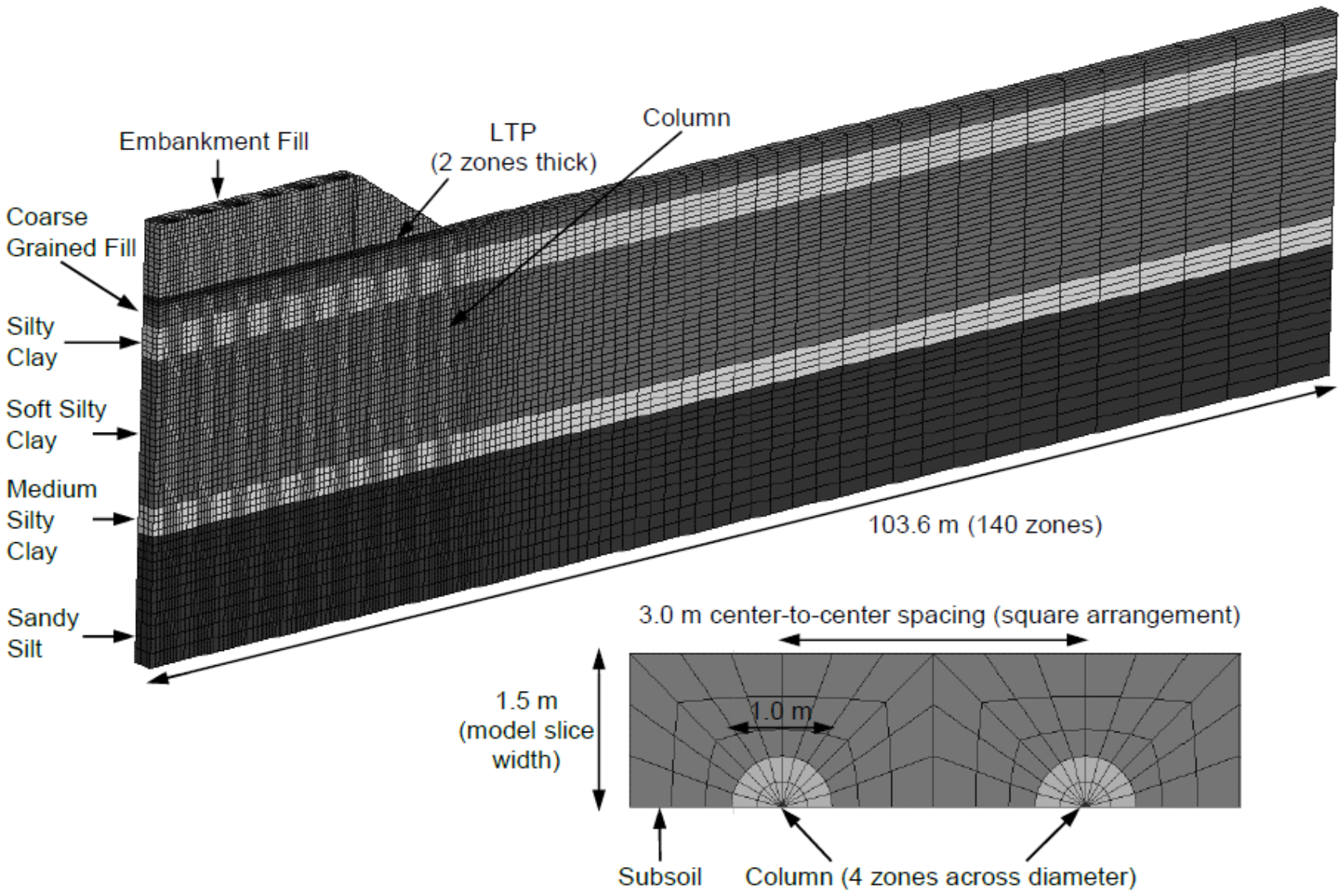

Figure 2-4. Half-embankment model geometry and discretization.

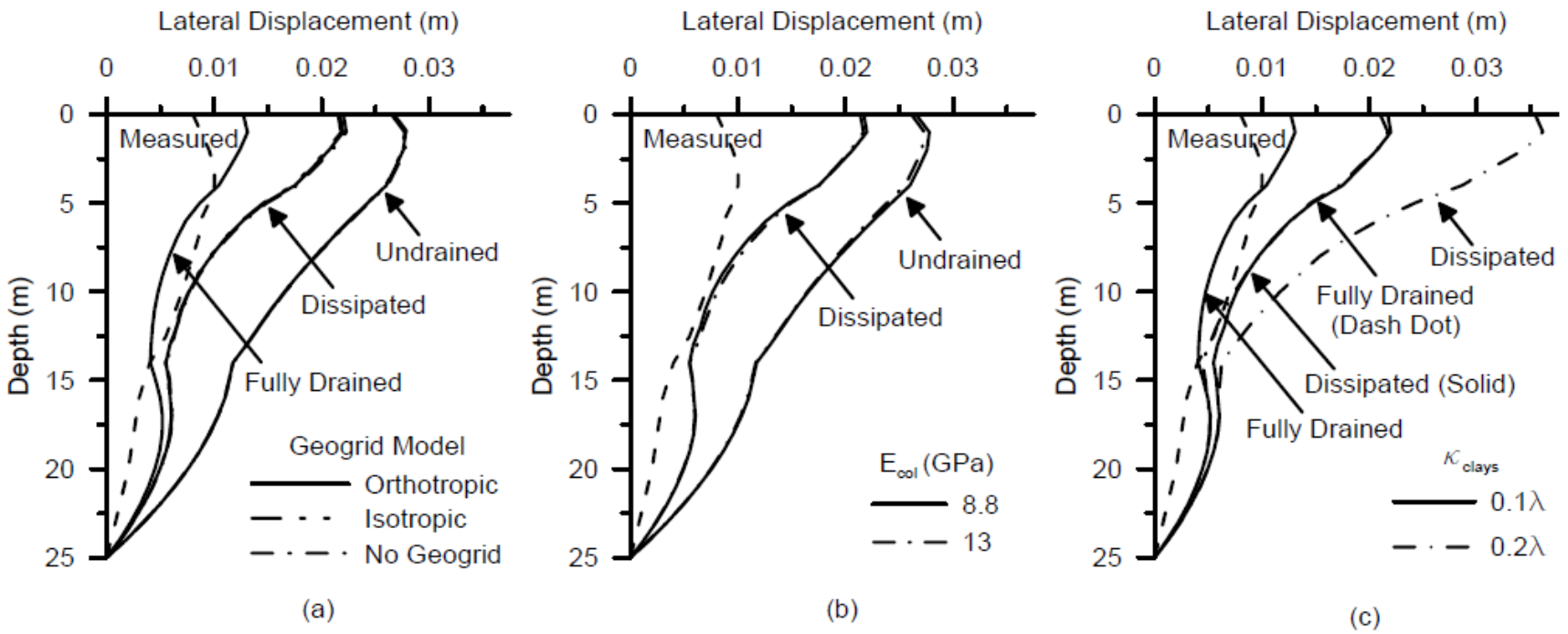

Figure 2-5. Comparison of measured and calculated foundation lateral displacement profiles at 1.5 m downstream of embankment toe for different a) geogrid conditions; b) E_{col}; and c) κ_{clays}. Calculations used orthotropic geogrid, E_{col} = 8.8 GPa, and $\kappa_{clays} = 0.1\lambda$, unless otherwise indicated.

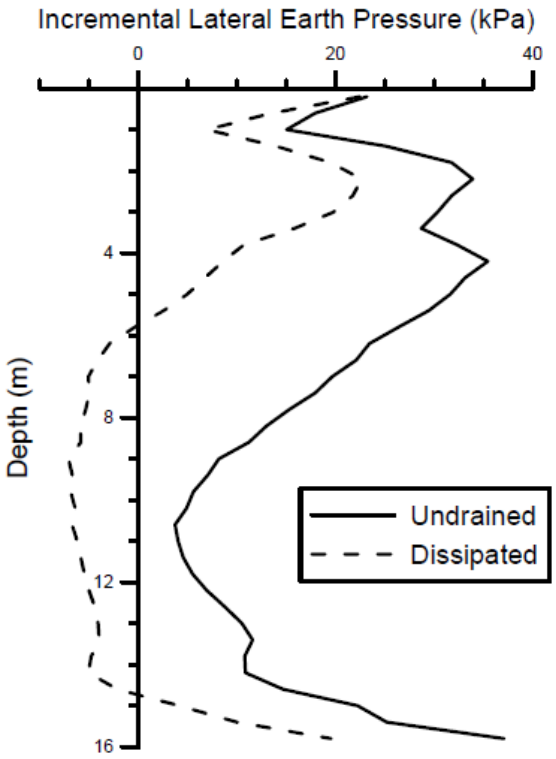

Figure 2-6. Incremental foundation lateral earth pressure at centerline (calculated using orthotropic geogrid, $\kappa_{clays} = 0.1\lambda$, and $E_{col} = 8.8$ GPa).

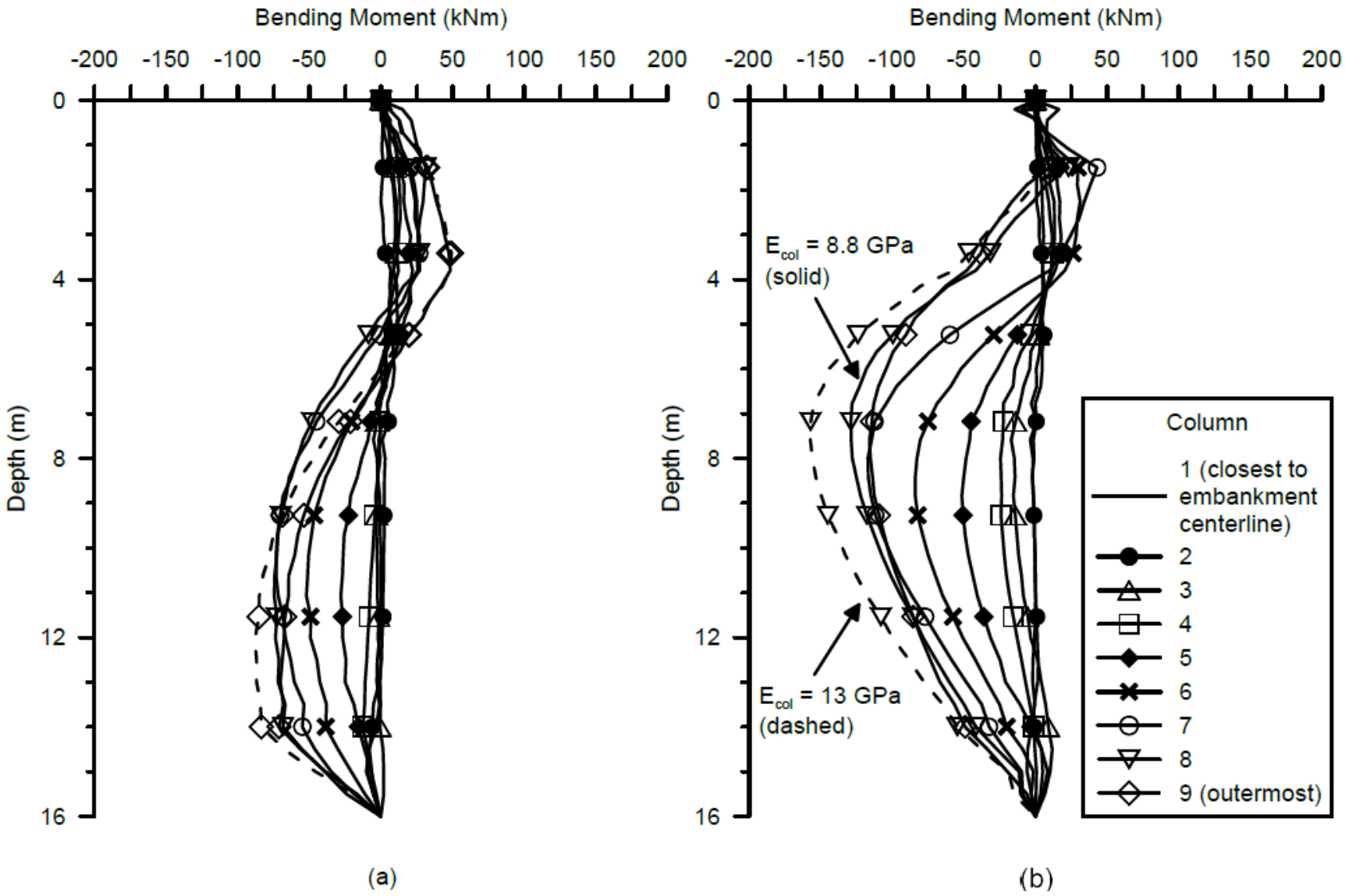

Figure 2-7. Column bending moment profiles calculated for a) undrained end-of-construction; and b) dissipated long-term. Calculations used orthotropic geogrid, E_{col} = 8.8 GPa, and $\kappa_{clays} = 0.1\lambda$, unless otherwise indicated.

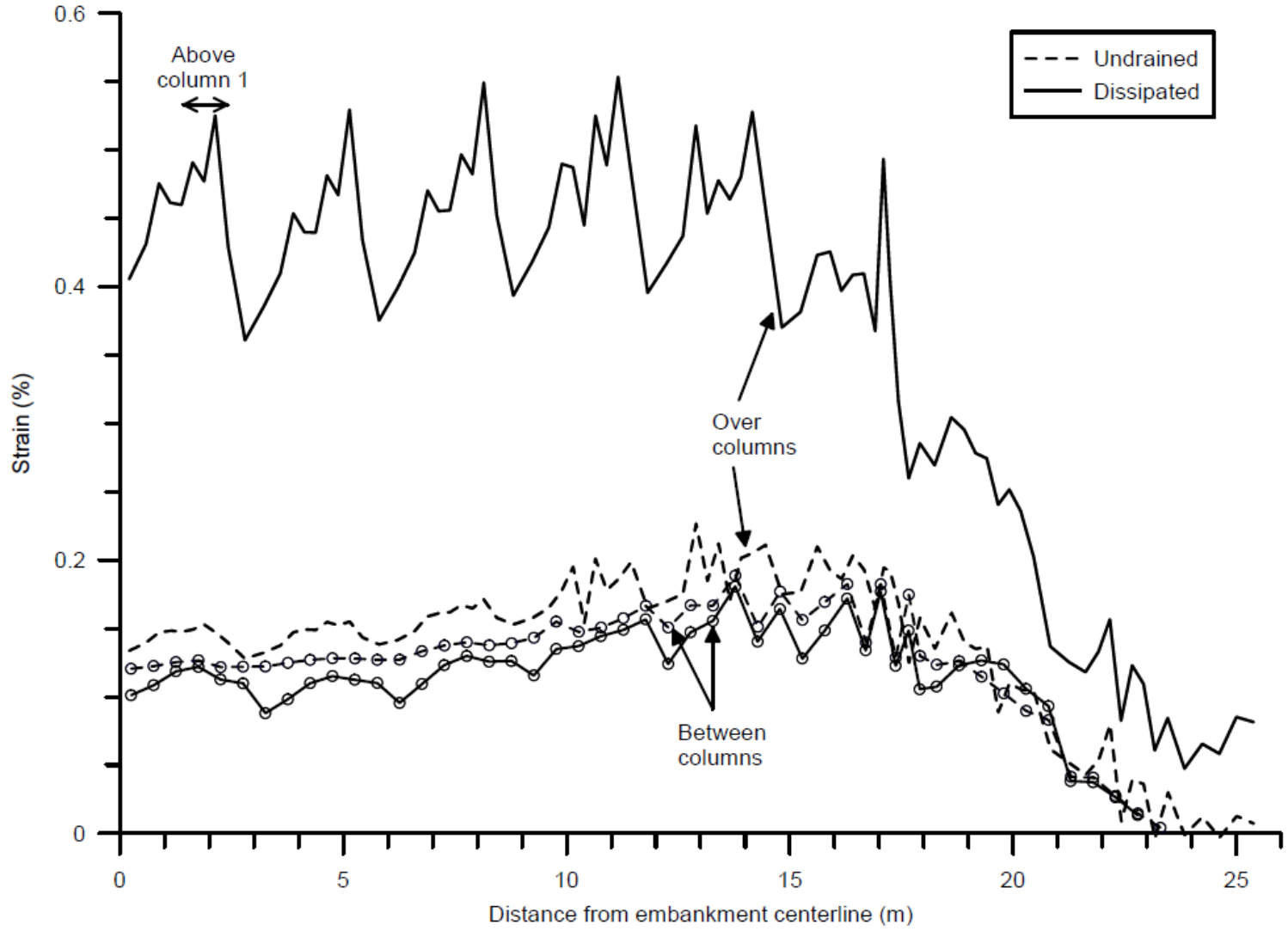

Figure 2-8. Transverse geogrid strain profiles calculated in half-embankment analysis using orthotropic geogrid, E_{col} = 8.8 GPa, and $\kappa_{clays} = 0.1\lambda$.

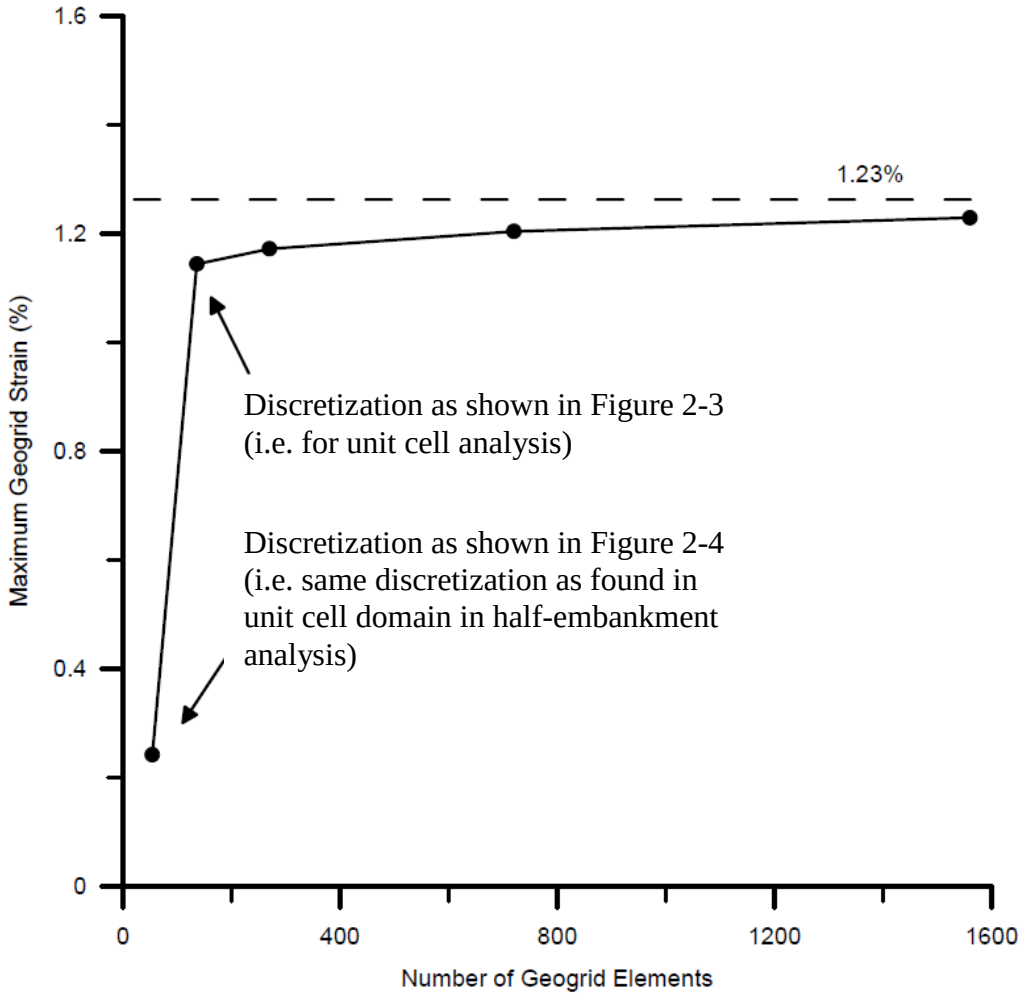

Figure 2-9. Maximum geogrid strain that develops under vertical load transfer effect vs. number of geogrid elements.

2.11. Electronic Supplement

This file supplements the technical paper, titled "Three-Dimensional Numerical Limiting Case Analyses of Lateral Spreading in a Column-Supported Embankment Case History." While the case history (Liu et al. 2007) was well-documented, some uncertainty remained in the selection of material parameters for numerical analysis. The technical paper describes the selection of parameters central to the numerical results discussion, while this supplementary file provides additional descriptions that would enhance the analysis reproducibility.

2.11.1. Unit Weights

Values of unit weights (γ) were assumed for the LTP gravel cushion, embankment fill, coarse-grained fill, and columns, as these were not provided by Liu et al. (2007). The LTP gravel was well-graded with a friction angle of 40°, and a γ of 21 kN/m^3 was estimated (NAVFAC 1986). The embankment fill γ of 18.3 kN/m^3 was selected to produce a total vertical pressure of 104 kPa from the embankment fill and LTP (Liu et al. 2007). Little was known about the foundation coarse-grained fill layer, and a γ of 20 kN/m^3 was assumed. The concrete annulus columns were modeled as a homogenous material with a volumetric average unit weight.

2.11.2. Poisson's Ratio

For all soils, the Poisson's ratio (ν) was modified to satisfy relationships among the effective friction angle (φ'), overconsolidation ratio (OCR), and the coefficient of lateral earth pressure at rest (K_0), using Equation 2.5 (Mayne and Kulhawy 1982) and Equation 2.6 (elastic relationship between ν and K_0). Values for the embankment fill and LTP gravel were rounded up to reflect the likely increase in lateral earth pressure due to compaction. The OCR of the clay layers were interpreted from vane shear data and the undrained shear strength ratio (Jamiolkowski 1985), as shown in Equation 2.7.

$$K_0 = (1 - sin\varphi')OCR^{sin\varphi'} \quad (2.5)$$

$$\nu = \frac{K_0}{1 + K_0} \quad (2.6)$$

$$s_u/\sigma'_v = 0.23 \cdot OCR^{0.8} \quad (2.7)$$

2.11.3. Column-Soil Interface Properties

Interface elements were placed at the column-soil contacts at the column head, toe, and shaft. Interface normal and shear stiffnesses were assigned a value of $1.5x10^{12}$ Pa/m, which is compatible with the adjacent zone stiffnesses to avoid numerical issues and excessive computation times. The interface elements along the pile shafts were assigned shear strengths determined according to the effective stress β-method for driven piles (Hannigan et al. 2016) because Liu et al. (2007) described the concrete annulus piles as displacement piles. β values of 0.8 and 0.25 were used for the interfaces with the coarse-grained fill and the clays, respectively. In the same order, the ratios of the interface friction angle to the soil friction angle (δ/φ) were chosen to be 0.8 and 0.67 (Potyondy 1961). The resulting shaft interface φ' are 22°, 20°, 16°, and 18°, in descending order into the foundation soil. At the column top, the interface φ' is 32°, which corresponds to δ/φ of 0.8. At the column toe, the interface φ' is 32°, which corresponds to δ/φ of 1 because the sandy silt is assumed to dominate the cross-sectional area of the annulus column. The lateral earth pressure coefficients, K, for conditions after column installation were then obtained from the β and δ values (Equation 2.8). These K values were assigned throughout the soil layers after column installation and were used to update lateral stresses from the in-situ at-rest condition.

$$\beta = K \cdot tan\delta \qquad (2.8)$$

2.11.4. Geogrid-LTP Interface Properties

Geogrid-LTP interface properties required material inputs but were not provided in the case history. To determine the appropriate input, interface normal and shear stiffness values were individually varied between $2x10^5$ to $2x10^7$ N/m (Eun et al. 2017; Liao et al. 2009), and the interface friction angle was varied between 30 to 40 degrees, which represented friction coefficients of 0.83 to 1 (Cancelli et al. 1992; Cazzuffi et al. 1993; Liu et al. 2009). The interface stiffness and the interface friction angle, within the ranges tested, were found to insignificantly impact vertical load distribution and settlement in the unit cell model. Interface normal and shear stiffnesses of $2x10^5$ N/m and a friction angle of 40° (equal to the friction angle of the LTP) were selected.

2.11.5. Foundation Compressibility

In the Modified Cam Clay formulation, soil compressibility is affected by preconsolidation pressure (p'_o), recompressibility (κ), and virgin compressibility (λ) (Wood 1990). In the numerical analysis of Liu et al. (2007) that supplemented documentation of the case history, the entire foundation was assumed to be normally consolidated, and calculated lateral displacements exceeded inclinometer measurements by 250%. The authors suspected that the foundation compressibility was overestimated. Thus, reasonable modifications were made to increase the foundation preconsolidation pressures and to decrease the κ.

The silty clay layer was assigned a preconsolidation pressure (σ'_p) increment of 10 kPa above the initial vertical effective stress (σ'_v) based on case history vane shear data. Vane shear data indicated an undrained shear strength ratio (USR) of 0.3 to 0.4, and a USR of 0.3 was selected because the undrained shear strength (S_u) tends to increase with strain rate, and in-situ tests are conducted much more quickly than the mobilization of shear strength in actual field failures (Duncan et al. 2014). This translated to an OCR of approximately 1.4 (Jamiolkowski 1985), and a σ'_p increment of 10 kPa to 15 kPa. The selection of a 10 kPa increment was based on the calibration of lateral displacements, as described later.

The sandy silt layer was assigned a σ'_p increment of 500 kPa above the initial σ'_v, as determined from unit cell drained load-share tests. The authors chose not to use the vane shear data to interpret the σ'_p for this layer because scatter in the USR of silts renders correlations unreliable (Duncan et al. 2014). The load-share test involved applying uniform vertical pressures of 674 kPa on the column and 49.5 kPa on the foundation soil. The 674 kPa was based on earth pressure cell measurements at E9 and E10 on column 2 at 125 days after construction (Figure 2-2 in technical paper). The 49.5 kPa represents the remaining embankment load that was applied on the subsoil, and this is a reasonable value that falls within the range of earth pressures measured on the subsoil at earth pressure cells E1 to E8. When the sandy silt was normally consolidated, the load-share test calculated column and subsoil settlements that unreasonably exceeded recordings. However, when a σ'_p increment of 500 kPa was adopted for the layer, the load-share test calculated column and subsoil settlements that were in good agreement with recordings at 125 days after construction. The option of maintaining the layer OCR at 1 and reducing the consolidation parameters was also

considered but judged unreasonable. To match settlements, a reduction factor of 6 was required for λ and κ as both parameters impact plastic strain increment calculations in virgin compression. Considering that the consolidation parameters were obtained from 1-D oedometer tests (Liu et al. 2007), it was judged more reasonable that the bearing layer was overconsolidated than to adjust both λ and κ.

Modifications to the σ'_p led to half-embankment calculations of the vertical stresses and settlements that were in reasonable agreement with measurements, but lateral displacements that were unreasonably large. The comparison of lateral displacements was made using end-of-construction inclinometer data at I1 (Figure 2-2 in technical paper) and two types of numerical analyses – dissipated and fully drained. The dissipated analysis, which proceeds after the undrained analysis by the dissipation of excess pore pressures, calculates deformations due to undrained distortions and consolidation. The fully drained analysis involves constructing the embankment without excess pore pressure development in the foundation, so it calculates deformations due to consolidation only. The inclinometer data at the end of construction reflect some undrained distortion and some consolidation that occurred during construction, so it should be smaller than the calculation for the dissipated analysis. It is uncertain how the calculation for the fully drained analysis compares to the inclinometer data, but it should be smaller than the calculation for the dissipated analysis. The authors judged that a suitable calibration could be provided if the end-of-construction inclinometer data were bracketed by the two calculations. However, this was found impossible by changing only the σ'_p within the established acceptable range. The inclinometer data was unreasonably exceeded by both the dissipated and fully drained calculations for all scenarios examined. This finding led to the reevaluation of κ, which affects both elastic and plastic deformations.

Liu et al. (2007) reported that λ and κ were obtained from 1-D oedometer tests. However, the authors noticed that for all clay layers the reported ratio of κ to λ was 0.2, which is at the upper end of the common range of 0.02 to 0.2 (Terzaghi et al. 1996). Given that the recompressibility index value is highly sensitive to soil disturbance and testing procedures (Terzaghi et al. 1996), it was impossible to reinterpret κ without access to original oedometer data or to find justification for the high κ values. Thus, the authors adopted κ of clays (κ_{clays}) equal to 0.1λ, a ratio at mid-range. After modifying κ_{clays}, calculated vertical stress distributions and settlements were in

reasonable agreement with measurements, and lateral displacements calculated from the dissipated and fully drained analyses bracketed inclinometer data. Note that using any σ'_p value within the established acceptable range for the silty clay layer calculated reasonable lateral displacements, but using an increment of 10 kPa provided the closest agreement to vertical load transfer measurements.

Notation

K = coefficient of lateral earth pressure;

K_0 = coefficient of lateral earth pressure at rest;

p'_o = preconsolidation pressure;

s_u = undrained shear strength;

β = Bjerrum-Burland beta coefficient;

γ = unit weight;

δ = interface friction angle;

κ = slope of recompression line;

κ_{clays} = slope of recompression line for clays;

λ = slope of virgin compression line;

ν = Poisson's ratio;

σ'_p = preconsolidation pressure;

σ'_v = effective vertical stress; and

φ' = effective friction angle.

References

Cancelli, A., Rimoldi, P., and Togni, S. (1992). "Frictional characteristics of geogrids by means of direct shear and pull-out tests." *Earth Reinforcement Practice*, 29-34.

Cazzuffi, D., Picarelli, L., Ricciuti, A., and Rimoldi, P. (1993). "Laboratory investigations on the shear strength of geogrid reinforced soils." *Geosynthetic Soil Reinforcement Testing Procedures*, 119-137. ASTM International.

Duncan, J. M., Wright, S. G., and Brandon, T. L. (2014). *Soil Strength and Slope Stability*. New Jersey: Wiley.

Eun, J., Gupta, R., and Zornberg, J. G. (2017). "Effect of Geogrid Geometry on Interface Resistance in a Pullout Test." In *Proc. Geotechnical Frontiers 2017*, 236-246. Reston, VA: American Society of Civil Engineers.

Hannigan, P. J., Rausche, F., Likins, G. E., Robinson, B. R., and Becker, M. L. (2016). *Design and Construction of Driven Pile Foundations*. U. S. Department of Transportation Federal Highway Administration.

Jamiolkowski, M., Ladd, C. C., Germaine, J. T., and Lancellotta, R. (1985). "New developments in field and laboratory testing of soils." In *Proc., 11th International Conference on Soil Mechanics and Foundation Engineering*, 57-153.

Liao, X., Ye, G., and Xu, C. (2009). "Friction and Passive Resistance of Geogrid in Pullout Tests." *Advances in Group Improvement*, 252-259. Reston, VA: American Society of Civil Engineers.

Liu, C., Ho, Y., and Huang, J. (2009). "Large scale direct shear tests of soil/PET-yarn geogrid interfaces." *Geotextiles and Geomembranes*, 27(1), 19-30.

Liu, H., Ng, C. W., and Fei, K. (2007). "Performance of a geogrid-reinforced and pile-supported highway embankment over soft clay: case study." *Journal of Geotechnical and Geoenvironmental Engineering*, 133(12), 1483-1493.

Mayne, P. W., and Kulhawy, F. H. (1982). "K_0-OCR Relationships in Soil." *Journal of the Soil Mechanics and Foundations Division*, 108(6), 851-872.

NAVFAC (1986). *Soil Mechanics Design Manual 7.01*. Alexandria, Virginia: U. S. Department of the Navy.

Potyondy, J. G. (1961). "Skin friction between various soils and construction materials." *Géotechnique*, 11(4), 339-353.

Terzaghi, K., Peck, R. B., and Mesri, G. (1996). *Soil Mechanics in Engineering Practice.* New York: Wiley.

Wood, D. M. (1990). *Soil Behaviour and Critical State Soil Mechanics*. Cambridge: Cambridge University Press.

CHAPTER 3. LATERAL THRUST DISTRIBUTION IN COLUMN-SUPPORTED EMBANKMENTS FOR LIMITING CASES OF LATERAL SPREADING

Zhanyu Huang[1], Katerina Ziotopoulou[2], George M. Filz[3]

[1] Graduate Research Assistant, The Charles E. Via Jr. Department of Civil and Environmental Engineering, Virginia Tech, Blacksburg, USA

[2] Assistant Professor, Department of Civil and Environmental Engineering, University of California, Davis, USA

[3] Professor, The Charles E. Via Jr. Department of Civil and Environmental Engineering, Virginia Tech, Blacksburg, USA

3.1. Abstract

Lateral spreading analysis of column-supported embankments (CSE) requires an understanding of the lateral thrust distribution, including the portion of thrust resisted by geosynthetic tension. Results from a three-dimensional (3D) numerical parametric study using a half-embankment domain and totaling 128 scenarios are presented in terms of the lateral thrust distribution. Forces examined include the lateral thrusts in the embankment and foundation soil, geosynthetic tension, and the base shear at depth, and these are presented for the limiting cases of lateral spreading (i.e. undrained end-of-construction and long-term dissipated). Results show that horizontal forces induced by embankment loading are significant in the embankment, foundation soil, and base shear beneath the columns, but the portion of lateral thrust carried by the geosynthetic is limited, although it increases with increasing geosynthetic stiffness. Results also indicate that lateral spreading in CSEs is more critical at the undrained end-of-construction condition than in the long-term condition after excess pore pressures have dissipated. Correlations for the thrust distribution at different limiting conditions and embankment locations (i.e. centerline, shoulder, and toe) are provided.

3.2. Introduction

Column-supported embankments (CSE) are constructed where project success is governed by time constraints. Unlike traditional methods of embankment construction on soft ground, such as staged fill placement with use of pre-fabricated vertical drains, CSEs can be rapidly constructed without consideration for excess pore pressure dissipation. The benefit of accelerated construction derives from the transfer of embankment and service loading to a competent stratum at depth using foundation columns (CSE schematic illustrated in Figure 3-1). Due to differences in stiffness and settlement of the subsoil and columns, vertical loads are transferred to columns through soil arching in the embankment and friction on the column-soil interfaces. Often, a load transfer platform (LTP) is included at the embankment base. The shear strength of the LTP facilitates soil arching, and geosynthetics may be included in the LTP as they can develop tension with vertical deflection and transfer additional loading to columns. Research about vertical load transfer in CSEs has flourished globally in the past few decades, advancing both fundamental understanding and related design procedures for practice (DGGT 2012; Sloan et al. 2014; BSI 2016; van Eekelen and Brugman 2016; Schaefer et al. 2017).

In the Schaefer et al. (2017) CSE design recommendations for U.S. practice, and with reference to the British Standards (BSI 2010), consideration is given to not only vertical load transfer and settlement but also lateral spreading via the ultimate limit state design of lateral sliding. Herein, lateral spreading is defined as the lateral displacements induced by lateral earth pressures in the embankment and foundation. If excessive, lateral spreading can lead to failure of the embankment, piled foundation, and/or geosynthetic reinforcement in the LTP. The design for lateral sliding has assumptions of the failure mechanism, and driving and resisting thrusts, including the geosynthetic tensile resistance. This paper discusses the current procedure for lateral sliding analysis and compares the lateral thrust distribution assumed in design to results from 128 CSE scenarios as obtained from a three-dimensional (3D) numerical parametric study, with the goal of advancing fundamental understanding of lateral spreading mechanics.

3.3. Design for Lateral Spreading

According to BSI (2016) and Schaefer et al. (2017), the ultimate limit state of lateral sliding considers failure of the CSE by sliding of the embankment fill over the foundation surface in

response to active lateral earth pressures in the embankment. The driving lateral thrust, P_{Lat}, is calculated using Equation (3.1), where K_a is the active lateral earth pressure coefficient, γ is the unit weight of the embankment soil, H_{emb} is the embankment height, and q is the surcharge pressure. A resisting lateral force, R_{ls}, is provided by the undrained shear strength (s_u) of the foundation soil mobilized over the length beneath the embankment slope (L_s), as shown in Equation (3.2). If a factor of safety of 1.5 is not achieved for the ratio of R_{ls} to P_{Lat}, then geosynthetic reinforcement is recommended in one of two ways (Schaefer et al. 2017): (1) using a single layer, the design tensile load is calculated as the sum of the demand from vertical load transfer and lateral sliding (P_{Lat}); or (2) using two layers, one biaxial layer carries the design tensile load from vertical load transfer, and a second uniaxial layer carries P_{Lat}. Method (2) is recommended by Schaefer et al. (2017) because both the properties of the geosynthetic and the tensile demand are direction dependent. The ultimate tensile strength of the geosynthetic is reduced by a safety factor of 1.5, as well as by factors accounting for durability, installation damage, and creep, to result in an allowable tensile strength that must equal or exceed the design tensile load.

$$P_{Lat} = K_a \left[\gamma \left(\frac{{H_{emb}}^2}{2}\right) + qH_{emb}\right] \qquad (3.1)$$

$$R_{ls} = L_s s_u \qquad (3.2)$$

The ultimate limit state of lateral sliding is framed in terms of failure in the embankment, and it thus neglects lateral earth pressures in the foundation. Only part of the embankment and service loading is carried by the columns, and the portion of vertical load carried by the subsoil between columns induces increases in lateral earth pressures in the foundation soil. The lateral earth pressures in both the embankment and foundation change with consolidation and development of soil arching. Thus, whether the embankment thrust should be calculated assuming an active condition, and how the geosynthetic responds in tension under the influence of a changing total lateral thrust, are uncertainties in the design of CSEs.

Limited research has been conducted to examine the CSE lateral thrust distribution. Farag (2008) measured the horizontal earth pressures in the embankment of a small-scale experimental CSE, but the resulting thrust was lower than the theoretical Rankine active thrust. Chen et al. (2016) examined the geosynthetic tension in a full-scale experimental CSE at the end of construction and before subsoil consolidation (undrained subsoil was modeled using water bags). They found the

tension highest at the centerline and near-zero at the shoulder, and concluded the results were affected by inadequate development length in the reinforcement. Questions remain for the thrust distribution in the embankment and geosynthetic for different stages of vertical load transfer.

3.4. Parametric Study using Undrained-Dissipated Analyses

Complexities associated with the CSE lateral thrust distribution require a computation method that can account for the effects of time on soil arching and foundation pore pressures. However, the analysis of deformation and pore pressure histories could be computationally expensive, depending on the size of the numerical domain and material properties. Huang et al. (2018) established that lateral spreading in CSEs can be instead analyzed using limiting cases, based on case history records of vertical earth pressure distributions and geosynthetic strains. The limiting case of undrained end-of-construction calculates the largest increment of earth pressure in the foundation. This is the result of limiting subsoil settlement and development of soil arching in the embankment under full embankment loading. The other limiting case of long-term dissipated pore pressures produces the largest geosynthetic strain and tension, as a result of increasing geosynthetic vertical deflection with subsoil consolidation. Both the foundation earth pressures (i.e. foundation thrust) and geosynthetic tension are quantities of interest in the analysis of CSE lateral thrust distribution.

The two limiting cases can be represented numerically using the undrained-dissipated approach, as described by Huang et al. (2019) and summarized here. This two-step approach computes an undrained end-of-construction state and a long-term dissipated state. An effective stress model is used to compute excess pore pressures in the clay during undrained embankment loading, resulting in an undrained end-of-construction state after the application of full embankment loading. All excess pore pressures are then dissipated. Deformations associated with the changes in effective stress are computed, resulting in the long-term dissipated state. The excess pore pressure dissipation stage also involves softening of select embankment zones to represent the loosening of fill during development of soil arching. One such loosened zone is shaded in Figure 3-1. These domed regions in the embankment above the subsoil have been observed in field-scale embankments and bench-scale tests to experience shear and decrease in normal stress and density with the redistribution of vertical loading (McGuire 2011; Sloan 2011). The geometry of the

loosened zone, in terms of an angle inclined from the vertical (α), can be determined using a correlation to the fill's effective friction angle (φ') (McGuire 2011). The properties of the loosened zones can be represented using reduced values of Young's modulus (E) and friction angle (φ') that were calibrated for a 3D embankment slice model using instrumented case history data (Huang et al. 2019). Settlements and vertical load distribution at the subgrade level computed using the dissipated analysis reached good agreement with long-term field recordings when 6 MPa and 30° were adopted for E and φ', respectively, to represent loosened fill. The same calibrated values for representing loosening in the embankment were adopted for the dissipated analysis of CSE scenarios in this parametric study.

3.5. Scope of Study

A parametric study totaling 128 scenarios was computed using a half-embankment domain in FLAC3D v.5.01 (Itasca 2012). An undrained end-of-construction and a long-term dissipated state was computed for each CSE scenario using the undrained-dissipated approach. Numerical parametric studies have been used to examine CSE system response under the change of individual parameters (Bhasi and Rajagopal 2014; Borges and Marques 2011; Chai et al. 2017; Farag 2008; Huang and Han 2010; Jennings and Naughton 2011; Liu and Rowe 2016; Mahdavi et al. 2016; Shrestha et al. 2015; Yapage and Liyanapathirana 2014; Zhuang and Wang 2015; Zhuang and Wang 2016). In this investigation, parameters were varied individually and in the multiple, as discussed subsequently.

This study used variations in fourteen (14) parameters that are all integral to CSE design. The range of parameter values are listed in Table 3-1, and values of design parameters were obtained from an experienced CSE designer (Collin, personal communication, 2018). Some of the examined variables are illustrated in the CSE schematic in Figure 3-1.

It was impossible to investigate all scenarios using the range of parameter values, and thus eight (8) base cases encompassing a wide range of conditions were selected (Table 3-2). Parameters were typically varied one at a time from the base case condition. Some scenarios varied from the base case by two (2) or three (3) parameters for examining different combinations of geosynthetic design at different embankment heights. Base case BC1 was recommended by Collin (personal communication, 2018); BC2 to BC5 were developed to investigate the CSE response for different

conditions of subgrade support and column area replacement ratio within the typical range of 2.5% to 10%; BC6 was designed to investigate edge instability in a tall embankment (i.e. instability downstream of outermost column); and BC7 and BC8 were marginal cases for investigating global instability, using very low column area replacement ratios. In addition, some analyses employed different combinations of parameters for investigating conditions of particular interest. The reader is directed to the supplemental data file (section 3.13 Electronic Supplement) for a complete list of investigated scenarios.

Some aspects of the model were kept constant as parameters were varied. Above the bearing layer, the foundation thickness was kept constant at 9.1 m (30 ft), such that the clay thickness varied between 6.4 m (21 ft) to 9.1 m (30 ft) depending on variations in the foundation fill thickness (H_{fill}). This range of clay thickness has been reported in several CSE case histories (Almeida et al. 2007; Bell et al. 1994; Holmberg 1978; Lai et al. 2006; Reid and Buchanan 1984) and was selected to avoid excessive computation time associated with a larger numerical domain. The groundwater table remained at a depth of 0.91 m (3 ft) from the foundation surface. The columns had properties corresponding to unreinforced concrete and a constant length of 9.1 m that extended to the bearing layer.

Results are presented in terms of the lateral thrust distribution:

1) The comparison of lateral thrust in the undrained end-of-construction condition versus the long-term dissipated condition.
2) The comparison of lateral thrust at different locations of the embankment in the transverse direction (i.e. centerline, shoulder, and toe, as annotated in Figure 3-1).
3) The comparison of thrust in the embankment versus thrust in the foundation;
4) The portion of lateral thrust resisted in the foundation at the embankment toe, by tension in the geosynthetic reinforcement, and by shear at the column base elevation (Figure 3-1).
5) The comparison of computed embankment lateral thrust to the theoretical active embankment thrust used in design (i.e. P_{Lat} from Equation 3.1).

The analysis of thrust at different embankment locations and pore pressure conditions represents an extension, as well as a point of comparison, to the analysis of driving thrust based on an active condition in the embankment. Select preliminary results from the parametric study were presented

in Huang et al. (2020). This paper presents the complete and detailed analysis of lateral thrust distribution in CSEs as synthesized from the same study.

3.6. Numerical Procedure

Constitutive models and material properties are listed in Table 3-3 for the soils and columns, and in Table 3-4 for the geosynthetic reinforcement. All soils, except for the clay, were modeled as linear elastic – perfectly plastic with the Mohr-Coulomb failure criterion. The clay was modeled with the Modified Cam Clay model. The columns were also modeled as linear elastic – perfectly plastic with the Mohr-Coulomb failure criterion, but including a tensile strength (σ_t) (ACI 2011; Pul et al. 2017; Schädlich and Schweiger 2014). The geosynthetic reinforcement was modeled using orthotropic linear elastic structural geogrid elements of the constant strain triangle type (Itasca 2013), which can sustain membrane stress but not bending. The orthotropic model is representative of biaxial geogrids, which have stiffness mainly in orthogonal directions. The geosynthetic reinforcement and columns interacted with surrounding zones through interfaces, whose properties are described in detail in section 3.13.1 (Electronic Supplement).

The embankment model geometry, discretization, and boundary conditions were selected to appropriately represent the physical domain of the problem while ensuring computational efficiency. The model consisted of a 3D half-embankment slice with zone discretization as illustrated in Figure 3-2. The half-embankment geometry is appropriate for analysis of lateral thrust distribution. The discretization consisted of a minimum of 34,000 grid points (locations of displacement calculation), and the lateral extent was four (4) times the embankment width and at least 13 times the embankment height. These quantities were determined from convergence studies conducted separately. Boundary conditions consisted of a free surface at the top, a pinned surface at the model base, and rollers on all other external surfaces.

Analyses were conducted using the large-strain mode in FLAC3D v.5.01 (Itasca 2012) and a loading sequence similar to the one reported in Huang et al. (2019). In-situ foundations stresses were assigned and mechanical equilibrium was established. Columns had the same density as the surrounding soils, and zones in the LTP and embankment fill were assigned null material properties. Column installation was then modeled by gradually increasing the column density while solving for equilibrium. This was followed by undrained embankment construction, wherein

drainage was disabled in the submerged foundation clay. The LTP and embankment were constructed in lifts, where zones were changed from null to Mohr-Coulomb materials and their density was gradually increased while solving for equilibrium. The construction of the final lift marked the undrained end-of-construction state. The subsequent dissipated analysis consisted of applying reduced parameter values of E and φ' in select embankment zones to represent the loosening of fill during development of soil arching (Figure 3-1, section view A-A′). Excess pore pressures were dissipated in one step. The model was solved for consolidation deformations and mechanical equilibrium for the long-term dissipated state.

3.7. Results and Discussion

The following discussion of the computed results focuses on the lateral thrust distribution in the embankment, geosynthetic, and foundation along vertical planes at the embankment centerline, shoulder, and toe (locations marked in Figure 3-1) for the two limiting cases (undrained end-of-construction and long-term dissipated). Herein, lateral thrust is defined differently from the active embankment thrust, P_{Lat}, from Equation 3.1, and the following definitions are provided for clarification:

Embankment thrust – the integration of the average total lateral stress at each zone elevation along a vertical plane from the foundation surface to the embankment surface.

Foundation thrust – the integration of the increment of lateral stress produced in the foundation (due to the increment of vertical loading in the subsoil between columns) at each zone elevation along a vertical plane from the column base elevation to the foundation surface.

Lateral thrust – the sum of the embankment and foundation thrusts, if the vertical plane examined is at the centerline or the shoulder, or only the foundation thrust, if the vertical plane is at the toe.

Geosynthetic tension – the tension in the transverse direction calculated by averaging the tension in geogrid elements closest to the vertical plane examined. Note that the vertical planes at the centerline and shoulder were mid-distance between columns, so the geosynthetic tension at these locations had no vertical component and were minimally influenced by column edge effects.

3.7.1. Comparison of Thrust in the Transverse Direction (Centerline, Shoulder, and Toe)

As shown in Figures 3-3a and 3-3b, the lateral thrust at the centerline in the dissipated condition is approximately half of that in the undrained condition, and this correlation is not significantly affected by the clay thickness for the range examined. Excess pore pressure dissipation directly reduces the total lateral thrust, and the associated clay consolidation transfers vertical loads from the clay to the columns and thereby also reduces the lateral thrust.

The thrusts at the shoulder and toe locations also decreases with excess pore pressure dissipation, and relative to the centerline thrust, they are smaller in magnitude, with a few exceptions (Figures 3-4a and 3-4b). The decrease in thrust with distance from the centerline was found in all scenarios in the undrained condition (Figure 3-4a), with thrusts at the shoulder and toe locations correlated at 82% and 47% of the centerline thrust, respectively. More variation was found for the dissipated condition. Although thrusts at the shoulder and toe locations are correlated at 89% and 56% of the centerline thrust (Figure 3-4b), 23 scenarios calculated the largest thrust at the shoulder and one scenario calculated the largest thrust at the toe. These scenarios have in common a wide distance from the outer edge of the outermost column to the embankment toe and/or large settlement at the shoulder relative to that at the centerline.

The trends in the relative magnitudes of thrust at the centerline, shoulder, and toe locations have several implications. In terms of movement, the general trend of decreasing lateral thrust with increase in distance from the centerline in the undrained condition is consistent with reduced lateral restraint at the edge and movement of the embankment away from the centerline. The magnitude of thrusts at the toe is smaller than at the shoulder and centerline, but the thrusts at the toe still represent a significant portion of resistance to the driving thrust in both the undrained and dissipated conditions, but more so in the dissipated condition. The scatter in correlation between the thrusts at the toe and centerline is significantly reduced when the data is grouped according to foundation preconsolidation pressure (σ'_p) and geosynthetic stiffness (J). As illustrated in Figures 3-5a to 3-5d for the preconsolidation pressure distribution shown in Case 1 of Figure 3-1, the thrust at the toe relative to the thrust at the centerline decreased with increasing J, indicating a redistribution of resisting thrust to the stiffer geosynthetics. However, the resisting foundation thrust at the toe remained significant for all geosynthetic conditions.

3.7.2. Geosynthetic Tension

Geosynthetic tension is examined at the embankment centerline and shoulder locations for different column ARR and geosynthetic stiffness (J) (Figures 3-6a to 3-6f). Results are exclusive to embankments with a height above the critical height, thus satisfying the serviceability limit for differential settlement. Each data set includes many parameter variations besides geosynthetic stiffness and column ARR, which produces scatter. Nevertheless, the trends and upper limits of the geosynthetic contribution to resisting lateral thrust can be compared.

For all cases of J and column ARR, the geosynthetic tension is higher in the dissipated condition (orange versus blue data points), and the upper limit in the ratio of geosynthetic tension to lateral thrust is approximately the same at the centerline and shoulder locations (dashed lines in plots on the left versus on the right). Geosynthetic tension is larger in the dissipated condition due to subsoil consolidation and increase in geosynthetic vertical deflection.

The upper limit in the ratio of geosynthetic tension to lateral thrust is more affected by J than location and column ARR. For typical column ARR and J = 300 kN/m, the geosynthetic resists at most 2% and 7% of the thrust in the undrained and dissipated conditions, respectively. Most scenarios calculated geosynthetic tensions much lower than the upper limits, indicating that for cases of practical importance, the geosynthetics that are typically used in the U. S. (Collin, personal communication, 2018) have limited utility in resisting lateral thrust. For typical column ARR and J = 8000 kN/m, the tensile resistance is increased respectively to 16% and 50%. The results in Figures 3-6a to 3-6f and Figures 3-5a to 3-5d correspond, both indicating more tension in the geosynthetic and less thrust in the foundation at the toe when using geosynthetics of greater stiffness.

3.7.3. Thrust Distribution in the Embankment and Foundation

Figure 3-7a to Figure 3-7d illustrate the embankment thrust versus the foundation thrust at the centerline and shoulder locations for the undrained and dissipated conditions. Due to scatter in the data resulting from the wide range of parameter values investigated, the following discussion of results centers on trends rather than correlations. In the undrained condition, the foundation thrust exceeds the embankment thrust at all locations across the embankment. The foundation thrusts are

larger in the undrained condition because the foundation supports the greatest increment of loading when settlement and soil arching are limited. In the dissipated condition, the embankment thrust increases in magnitude and the foundation thrust decreases in magnitude compared to the undrained condition. The embankment thrust exceeds the foundation thrust in a number of scenarios, particularly for the smallest column spacing (S_{col}) of 1.8 m (6 ft). This trend is explained by the development of soil arching and subsoil consolidation in the long-term dissipated condition. The development of arching results in larger lateral stresses in the embankment, while the simultaneous increase in differential settlement at the subgrade level facilitates vertical load transfer to columns and decreases the increment of loading in the subsoil. The ratio of embankment thrust to foundation thrust is larger for smaller S_{col} due to greater effectiveness in vertical load transfer to columns. Figure 3-7c and Figure 3-7d also show that the embankment thrust is smaller at the shoulder than at the centerline in the dissipated condition, likely due to effects of the embankment slope on arching.

The question of whether the embankment thrust can be appropriately represented by the design active thrust was investigated by comparing the expected P_{Lat} (Equation (3.1)) to the range of calculated embankment thrusts. Results are presented for scenarios with embankment heights of 3.0 m (10 ft), 4.6 m (15 ft), and 6.1 m (20 ft) and for the centerline and shoulder locations (Figure 3-8a and Figure 3-8b, respectively). In all cases, the calculated embankment thrust is larger than P_{Lat}, though the undrained case is closer, and cases with developing global instability in the undrained condition are the closest. The calculated embankment thrusts exceed P_{Lat} because full active conditions are generally not developed in the embankment. Embankment thrusts are larger in the dissipated condition due to the development of soil arching and increase in lateral stresses in the embankment, corresponding to trends in Figure 3-7a to Figure 3-7d.

3.7.4. Lateral Force Equilibrium

Free body diagrams illustrating horizontal force increments in the embankment, geosynthetic reinforcement, foundation, and shear at the column base elevation are provided for 3 scenarios in Figure 3-9. The scenarios represent different column ARR and geosynthetic design, with properties provided in Table 3-5 and summarized here: 1) scenario A is for a 3.0 m tall embankment using typical column ARR and 3 layers of geosynthetics with J = 300 kN/m; 2)

scenario B is for a 6.1 m tall embankment using typical column ARR and 2 layers of geosynthetics with J = 8000 kN/m; and 3) scenario C is for a 6.1 m tall embankment using low column ARR and 1 layer of geosynthetic with J = 8000 kN/m.

The following observations can be made for the lateral thrust distribution with reference to the free body diagrams in Figure 3-9. The shear at the column base elevation resists a significant portion of the driving thrust originating from the embankment and the foundation. During dissipation of excess pore water pressures, the total lateral thrust in the embankment and foundation at the centerline decreases, which is consistent with the trends shown in Figure 3-4. Both the base shear and lateral thrust at the toe decreases in response to the decrease in centerline thrust. The effect is particularly marked for Scenario C, which has low column ARR and less subgrade support (i.e. soft clay extended to foundation surface). Figure 3-9 shows that the geosynthetics in Scenario A provide negligible contribution to lateral force equilibrium. The geosynthetics represented in Scenario A are typical of those used in U.S. practice. The high stiffness geosynthetics represented in Scenarios B and C provide a larger contribution to satisfying lateral force equilibrium. Although the total geosynthetic stiffness for Scenario C is only half that of Scenario B, the geosynthetic reinforcement in Scenario C experiences larger tension in response to the larger lateral thrust at the centerline and shoulder.

3.8. Summary and Conclusions

Results from a three-dimensional (3D) numerical parametric study totaling 128 scenarios for column-supported embankments (CSE) were synthesized and presented in terms of the lateral thrust distribution. Driving and resisting thrusts for lateral spreading analysis of CSEs were examined and quantified in relative proportions: (1) the embankment thrust calculated by integrating total lateral stresses over the embankment height; (2) the foundation thrust calculated by integrating incremental lateral stresses from the column base elevation to the foundation surface; (3) the geosynthetic tension; and (4) the shear at the column base elevation (as required for analysis of lateral force equilibrium). Calculations were performed along vertical planes at the embankment centerline, shoulder, and toe, and for the limiting cases of lateral spreading (i.e. undrained end-of-construction and long-term dissipated).

Analyses of lateral thrust distribution in CSEs advanced fundamental understanding of lateral spreading mechanics through the following findings:

1) The driving thrust produced by the sum of embankment and foundation thrusts is resisted by the foundation thrust at the toe, geosynthetic tension, and base shear.
2) Pore pressure conditions affect the relative magnitudes of thrust. The foundation thrust is largest in the undrained condition and decreases with excess pore pressure dissipation. The embankment thrust is smallest in the undrained condition and increases with excess pore pressure dissipation and development of soil arching. The geosynthetic tension is smallest in the undrained condition and increases with excess pore pressure dissipation and vertical deflection. The base shear is largest in the undrained condition.
3) The foundation thrust contributes significantly to both the driving and resisting thrusts.
4) Geosynthetic tension increases with stiffness (J), and geosynthetics of greater stiffness resists a greater portion of the driving thrust.
5) The undrained condition may be most critical for lateral spreading:
    a. Lateral thrust is largest at the centerline and decreases in magnitude towards the toe, consistent with a system tendency to spread laterally away from the centerline.
    b. The embankment thrust is closest in value to the theoretical active thrust adopted for design, due to the limited development of soil arching and vertical load transfer to columns. The smallest calculated embankment thrusts were found for cases with developing global instability in the undrained condition.
    c. Both the geosynthetic tension and the portion of thrust resisted by the geosynthetic are smallest when vertical deflection is limited.
    d. The base shear is largest in the undrained condition, indicating the greatest likelihood of approaching the shear strength prior to consolidation.
6) The CSE lateral thrust distribution for the critical undrained condition can be estimated using the following correlations:
    a. The ratio of shoulder thrust to centerline thrust is approximately 80%.
    b. The ratio of thrust at the toe to centerline thrust is approximately 50%.
    c. The ratio of geosynthetic tension to centerline thrust depends on the geosynthetic stiffness (J). Using J = 300 kN/m, the ratio is at most 2%. Using J = 8000 kN/m,

the ratio is at most 16%. The maximum ratio of geosynthetic tension to thrust is approximately the same at the centerline and the shoulder.

d. Remaining driving thrust is resisted by base shear.

Future work could expand upon the correlations by investigating conditions outside the scope of this study. CSEs integrated with mechanically stabilized earth wall systems could produce the worst slope condition for lateral spreading. The effect of column length could also be investigated.

Another natural extension to the current work is to investigate the potential failure mechanisms in CSEs and to establish whether they occur in the undrained condition, as suggested by results from the current study. Failure analyses should incorporate tensile failure in the geogrid elements, such that the geosynthetic influence on load path can be examined in addition to its contribution to resisting thrust.

Notation

The following symbols are used in this chapter:

c' = effective cohesion;

d_{cap} = cap diameter;

d_{col} = column diameter;

E = Young's modulus;

$E_{reduced}$ = reduced Young's modulus adopted in loosened embankment zones;

e_1 = void ratio at reference pressure;

G = shear modulus;

H_{emb} = embankment height;

H_{fill} = foundation fill thickness;

H_{LTP} = load transfer platform height (i.e. thickness);

J = geosynthetic stiffness;

K_a = coefficient of active lateral earth pressure;

L_{emb} = shoulder-to-shoulder embankment width;

L_s = length of foundation beneath embankment slope;

M = slope of critical state line;

N_{col} = number of columns in half-embankment model relative to column group extent required to prevent edge instability;

N_{geo} = number of geosynthetic layers;

q = surcharge pressure loading;

R_{ls} = resisting thrust in the foundation based on undrained shear strength;

S_{col} = center-to-center column spacing;

s_u = undrained shear strength;

α = angle of shear failure surface from vertical;

γ = unit weight;

κ = slope of recompression line;

λ = slope of virgin compression line;

ν = Poisson's ratio;

σ_t = tensile strength;

σ'_p = preconsolidation pressure;

σ'_v = effective vertical stress;

φ' = effective friction angle;

φ'_{emb} = effective friction angle of embankment fill;

φ'_{fill} = effective friction angle of foundation fill; and

$\varphi'_{reduced}$ = reduced effective friction angle adopted in loosened embankment zones.

References

ACI (2011). "318-11: Building Code Requirements for Structural Concrete and Commentary." *Section 9.5.3.2*, American Concrete Institute, Farmington Hills, Michigan.

Almeida, M. S. S., Ehrlich, M., Spotti, A. P., and Marques, M. E. S. (2007). "Embankment supported on piles with biaxial geogrids." *Proceedings of the Institution of Civil Engineers - Geotechnical Engineering*, 160(4), 185-192.

Bell, A. L., Jenner, C., Maddison, J. D., and Vignoles, J. (1994). "Embankment Support using Geogrids with Vibro Concrete Columns." *Fifth International Conference on Geotextiles, Geomembranes and Related* Products, Singapore, 335-338.

Bhasi, A., and Rajagopal, K. (2014). "Geosynthetic-Reinforced Piled Embankments: Comparison of Numerical and Analytical Methods." *International Journal of Geomechanics*, 15(5), 04014074.

Borges, J. L., and Marques, D. O. (2011). "Geosynthetic-reinforced and jet grout column-supported embankments on soft soils: Numerical analysis and parametric study." *Computers and Geotechnics*, 38(7), 883-896.

BSI (2010). "BS 8006-1:2010 Code of practice for strengthened/reinforced soil and other fills." *Design of embankments with reinforced soil foundations on poor ground*, British Standards Institution, London.

BSI (2016). "BS 8006-1:2010+A1:2016 Code of practice for strengthened/reinforced soil and other fills." *Design of embankments with reinforced soil foundations on poor ground*, British Standards Institution, London.

Chai, J. C., Shrestha, S., Hino, T., and Uchikoshi, T. (2017). "Predicting bending failure of CDM columns under embankment loading." *Computers and Geotechnics*, 91, 169-178.

Chen, R. P., Wang, Y. W., Ye, X. W., Bian, X. C., and Dong, X. P. (2016). "Tensile force of geogrids embedded in pile-supported reinforced embankment: A full-scale experimental study." *Geotextiles and Geomembranes*, 44(2), 157-169.

Collin, J. G. (2018). Personal Communication.

DGGT (Deutsche Gesellschaft für Geotechnik) (2012). "Recommendations for Design and Analysis of Earth Structures Using Geosynthetic Reinforcements-EBGEO." John Wiley & Sons, New Yok.

Farag, G. S. F. (2008). " Lateral Spreading in Basal Reinforced Embankments Supported by Pile-Like Elements." Doctoral Dissertation, Institut für Geotechnik und Geohydraulik, University of Kassel.

Holmberg, S. (1978). "Bridge approaches on soft clay supported by embankment piles." *Geotechnical Engineering*, 10, 77-89.

Huang, J., and Han, J. (2010). "Two-dimensional parametric study of geosynthetic-reinforced column-supported embankments by coupled hydraulic and mechanical modeling." *Computers and Geotechnics*, 37(5), 638-648.

Huang, Z., Ziotopoulou, K., and Filz, G. M. (2018). "Numerical Predictions of Deformations in Geosynthetic-Reinforced Column-Supported Embankments: Validation of Manual Dissipation of Excess Pore Pressure Approach for Undrained and Drained Analyses." *IFCEE 2018: Innovations in Ground Improvement for Soils, Pavements, and Subgrades*, GSP 296, 327-336.

Huang, Z., Ziotopoulou, K., and Filz, G. M. (2019). "3D Numerical Limiting Case Analyses of Lateral Spreading in a Column-Supported Embankment " *Journal of Geotechnical and Geoenvironmental Engineering*, 145(11), 04019096.

Huang, Z., Ziotopoulou, K., and Filz, G. M. (2020). "Lateral Thrust Distribution in Column-Supported Embankments: A Parametric Study Via 3D Simulations." *ASCE Geo-Congress 2020*. (Accepted)

Itasca. 2012. FLAC3D, version 5.01, Minneapolis, MN.

Itasca (2013). *Structural Elements*, Itasca Consulting Group Inc., Minneapolis, Minnesota.

Jennings, K., and Naughton, P. J. (2011). "Lateral Deformation under the Side Slopes of Piled Embankments." *Geo-Frontiers 2011*, 142-151.

Lai, Y., Bergado, D., Lorenzo, G., and Duangchan, T. (2006). "Full-scale reinforced embankment on deep jet mixing improved ground." *Proceedings of the Institution of Civil Engineers-Ground Improvement*, 10(4), 153-164.

Liu, K. W., and Rowe, R. K. (2016). "Performance of reinforced, DMM column-supported embankment considering reinforcement viscosity and subsoil's decreasing hydraulic conductivity." *Computers and Geotechnics*, 71, 147-158.

Mahdavi, H., Fatahi, B., Khabbaz, H., Krzeminski, M., Santos, R., and Marix-Evans, M. (2016). "Three-Dimensional Simulation of a Load Transfer Mechanism for Frictional and End Bearing CMC Supported Embankments on Soft Soil." In *Proc., Geo-China 2016 Advances in Pavement Engineering and Ground Improvement*, 60-67. ASCE, Reston, VA.

McGuire, M. P. (2011). "Critical Height and Surface Deformation of Column-Supported Embankments." Doctoral Dissertation, Department of Civil and Environmental Engineering, Virginia Polytechnic Institute and State University.

Pul, S., Ghaffari, A., Öztekin, E., Hüsem, M., and Demir, S. (2017). "Experimental Determination of Cohesion and Internal Friction Angle on Conventional Concretes." *ACI Materials Journal*, 114(3), 407-416.

Reid, W. M., and Buchanan, N. W. (1984). "Bridge approach support piling." *Piling and Ground Treatment*, 267-274.

Schädlich, B., and Schweiger, H. (2014). "Internal report shotcrete model: Implementation validation and application of the shotcrete model." Plaxis, Delft.

Schaefer, V. R., Berg, R. R., Collin, J. G., Christopher, B. R., DiMaggio, J. A., Filz, G. M., Bruce, D. A., and Ayala, D. (2017). "Ground Modification Methods Reference Manual - Volume II." FHWA, Washington, D. C.

Shrestha, S., Chai, J. C., Bergado, D. T., Hino, T., and Kamo, Y. (2015). "3D FEM investigation on bending failure mechanism of column inclusion under embankment load." *Lowland Technology International*, 17(3), 157-166.

Sloan, J. A. (2011). "Column-Supported Embankments: Full-Scale Tests and Design Recommendations." Doctoral Dissertation, Department of Civil and Environmental Engineering, Virginia Tech.

Sloan, J. A., Filz, G. M., Collin, J. G., and Kumar, P. (2014). "Column-Supported Embankments: Field Tests and Design Recommendations (2nd Edition)." Virginia Tech Center for Geotechnical Practice and Research, Blacksburg, VA.

van Eekelen, S. J. M., and Brugman, M. H. A. (2016). *Design guideline basal reinforced piled embankments*, CRC Press, Boca Raton, FL.

Yapage, N. N. S., and Liyanapathirana, D. S. (2014). "A parametric study of geosynthetic-reinforced column-supported embankments." *Geosynthetics International*, 21(3), 213-232.

Zhuang, Y., and Wang, K. Y. (2015). "Three-dimensional behavior of biaxial geogrid in a piled embankment: numerical investigation." *Canadian Geotechnical Journal*, 52(10), 1629-1635.

Zhuang, Y., and Wang, K. Y. (2016). "Finite-Element Analysis on the Effect of Subsoil in Reinforced Piled Embankments and Comparison with Theoretical Method Predictions." *International Journal of Geomechanics*, 16(5), 04016011.

Tables

Table 3-1. Parameters and range of values investigated (*dependent variables are italicized).*

Parameter	Parameter Values
Embankment Height (H_{emb})	1.5, 3.0, 4.6, 6.1 m (5, 10, 15, 20 ft)
LTP Thickness (H_{LTP})	0.61, 0.91, 1.2 m (2, 3, 4 ft)
Foundation Fill Thickness (H_{fill})	0, 0.91, 1.8, 2.7 m (0, 3, 6, 9 ft)
Center-to-Center Column Spacing (S_{col})	1.8, 2.4, 3.0 m (6.0, 8.0, 10.0 ft)
Cap Diameter (d_{cap})	0.61, 0.91 m (24, 36 inches)
Column Diameter (d_{col})	0.36, 0.46, 0.61 m (14, 18, 24 inches)
Embankment Slope	3H:2V, 2H:1V
Shoulder-to-Shoulder Embankment Width (L_{emb})	10, 24, 40 m ($\pm$ 2 m) (32, 80, 128 ft)
Column Group Lateral Extent (N_{col})	-1, 0, +1, +2 number of columns relative to column lateral group extent required for preventing edge instability (BSI 2016)
Number of Geosynthetic Layers (N_{geo})	0, 1, 2, 3
Geosynthetic Stiffness (J)	300, 2000, 8000 kN/m (20500, 137000, 548000 lb/ft)
Embankment Fill Friction Angle (φ'_{emb})	34, 40, 50 degrees *Young's modulus, Poisson's ratio, and unit weight (values in Table 3)*
Foundation Preconsolidation Pressure (σ'_p)	Cases 1, 2, 3 (see Figure 1)
Service Loading (q)	0, 14 kPa (0, 300 psf)

Table 3-2. Base cases and corresponding parameter values.

Base Case	H_{emb} (m)	H_{LTP} (m)	H_{fill} (m)	S_{col} (m)	d_{cap} (m)	d_{col} (m)	Slope (H:V)	L_{emb} (m)	N_{col}	N_{geo}	J (kN/m)	φ'_{emb} (°)	σ'_p	q (kPa)
BC1	3.0	0.91	0.91	2.4	0.61	0.46	2:1	24	0	3	300	40	Case 2	0
BC2	3.0	0.91	2.7	1.8	0.61	0.61	2:1	24	0	0	-	40	Case 2	0
BC3	3.0	0.91	0	1.8	0.61	0.61	2:1	24	0	0	-	40	Case 1	0
BC4	4.6	0.91	2.7	3.0	0.61	0.61	2:1	24	0	0	-	40	Case 2	0
BC5	4.6	0.91	0	3.0	0.61	0.61	2:1	24	0	0	-	40	Case 1	0
BC6	6.1	0.91	0.91	1.8	0.61	0.61	2:1	22	0	2	8000	40	Case 2	0
BC7	4.6	0.91	0	3.0	0.36	0.36	3:2	25	0	0	-	40	Case 1	0
BC8	6.1	0.91	0	3.0	0.61	0.46	3:2	25	0	0	-	40	Case 1	0

Table 3-3. Material properties of soils and columns.

Material	γ (kN/m^3)	Model	φ' (°)	c' (kPa)	σ_t (kPa)	E (MPa)	ν	λ	κ	M	e_1
Embankment Fill											
Loose Sand	17.3	MC	35	0		17	0.30				
Dense Sand	18.9	MC	40	0		36	0.26				
Gravel	22.0	MC	50	0		120	0.20				
LTP (Gravel)	22.0	MC	50	0		120	0.20				
Foundation Fill	18.1	MC	37	0		24	0.28				
Clay	16.5	MCC					0.37	0.17	0.017	0.98	2.75
Bearing Sand	22.8	MC	45	0		43	0.23				
Concrete Column	23.6	MC	43	3700	1580	21,500	0.20				

Note: MC = Mohr-Coulomb; MCC = Modified Cam Clay; three different materials were investigated for the embankment fill and foundation fill; e_1 is the void ratio at a reference pressure of 0.048 kPa (1 psf); E = 6 MPa and φ' = 30° were applied to select embankment zones in the dissipated analyses to represent loosening of fill due to vertical load distribution.

Table 3-4. Material properties of geosynthetic reinforcement.

Model	J (kN/m)	ν	G (kPa)
Orthotropic Linear Elastic	300, 2000, 8000	0	1

Note: ν = 0 in both longitudinal and transverse directions.

Table 3-5. Parameter values for scenarios adopted in investigation of lateral force equilibrium (Figure 3-9).

H_{emb} (m)	H_{LTP} (m)	H_{fill} (m)	S_{col} (m)	d_{cap} (m)	d_{col} (m)	Slope (H:V)	L_{emb} (m)	N_{col}	N_{geo}	J (kN/m)	φ'_{emb} (°)	σ'_p	q (kPa)
Scenario A (BC1) – typical column ARR and lightweight geosynthetic													
3.0	0.91	0.91	2.4	0.61	0.46	2:1	24	0	3	300	40	Case 2	0
Scenario B – typical column ARR and heavyweight geosynthetic													
6.1	0.91	0.91	1.8	0.61	0.61	2:1	22	+2	2	8000	40	Case 2	0
Scenario C – low column ARR and heavyweight geosynthetic													
6.1	0.91	0	3.0	0.61	0.46	3:2	25	0	1	8000	40	Case 1	0

Figures

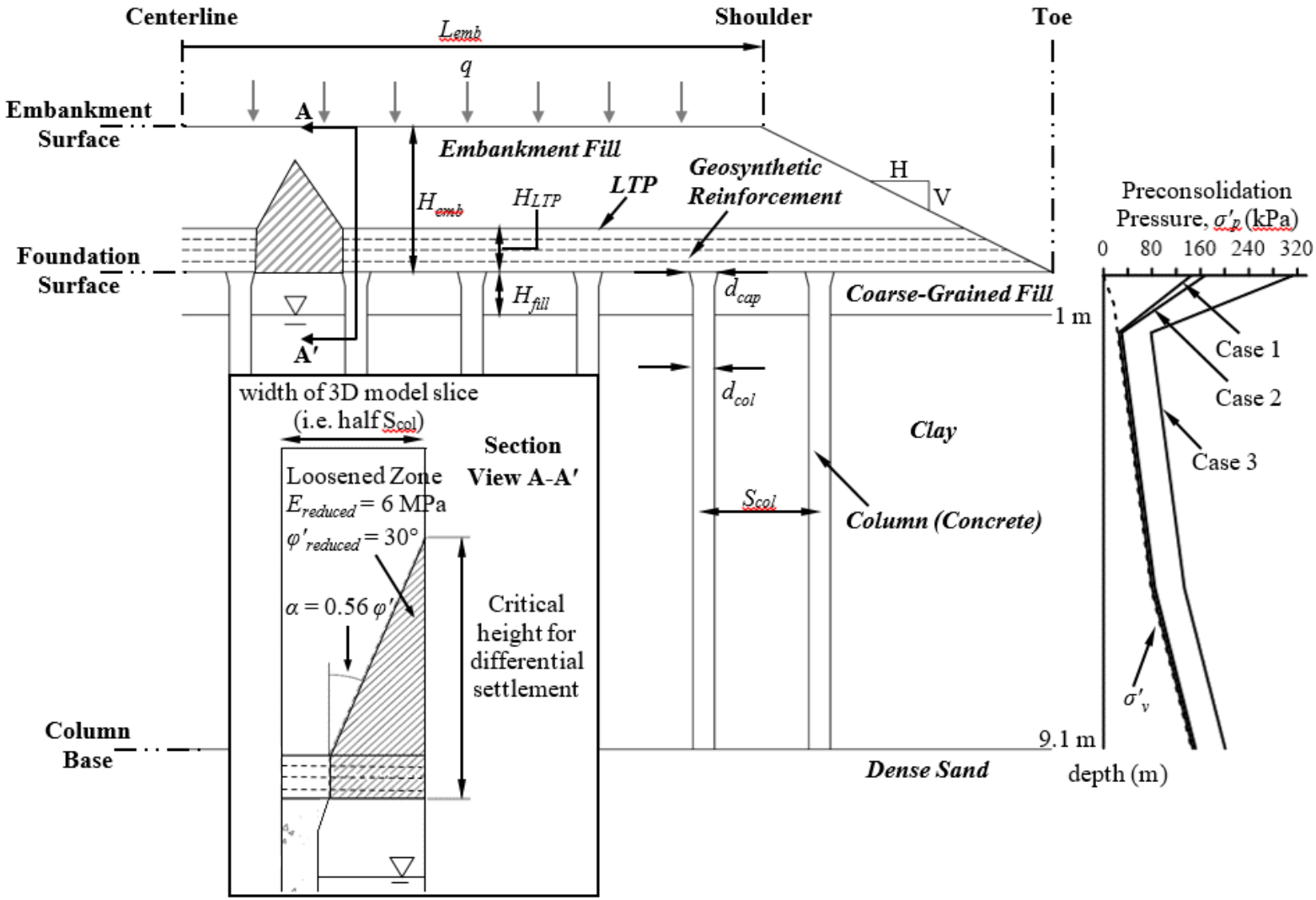

Figure 3-1. CSE schematic including geometry of loosened zones.

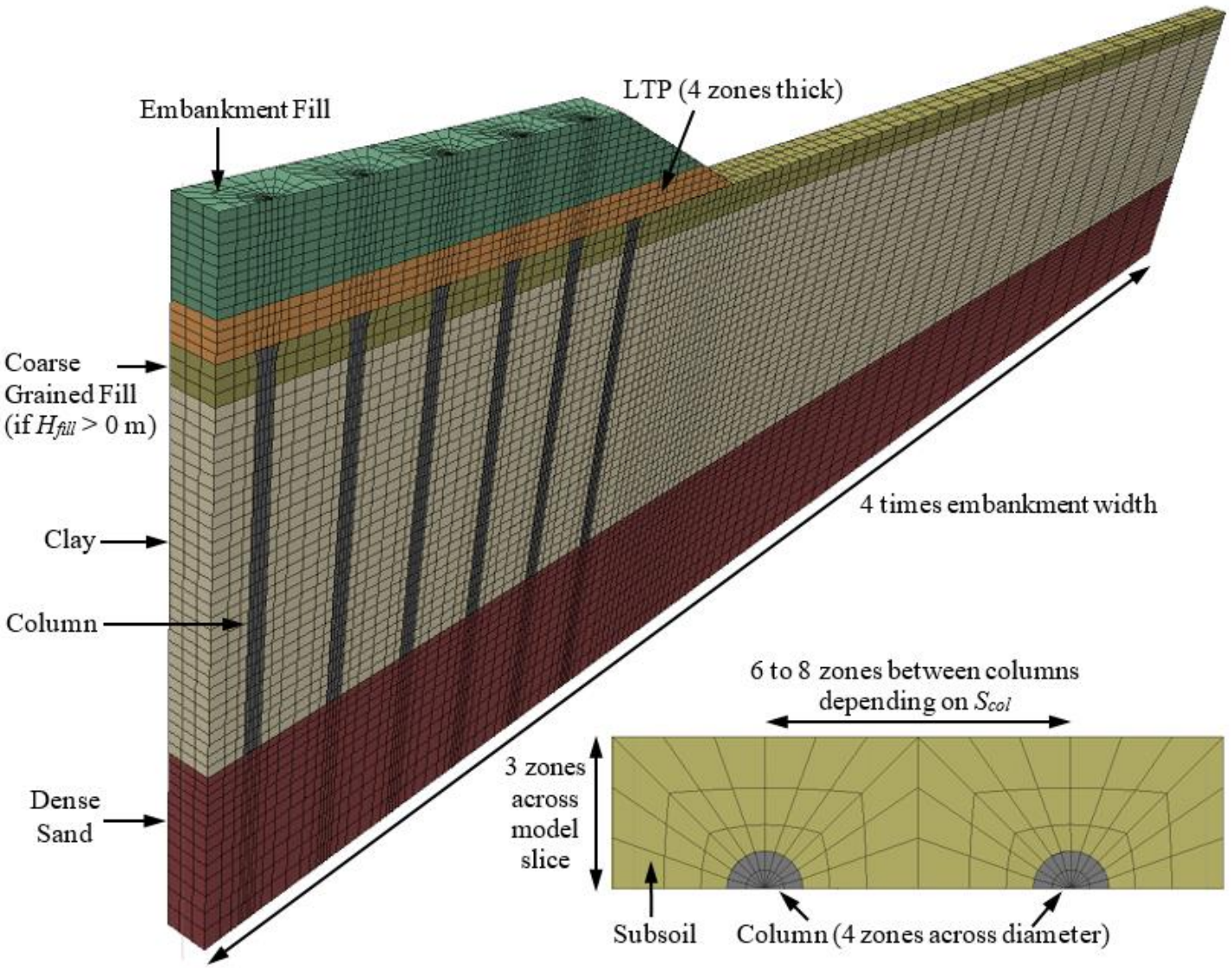

Figure 3-2. Model discretization.

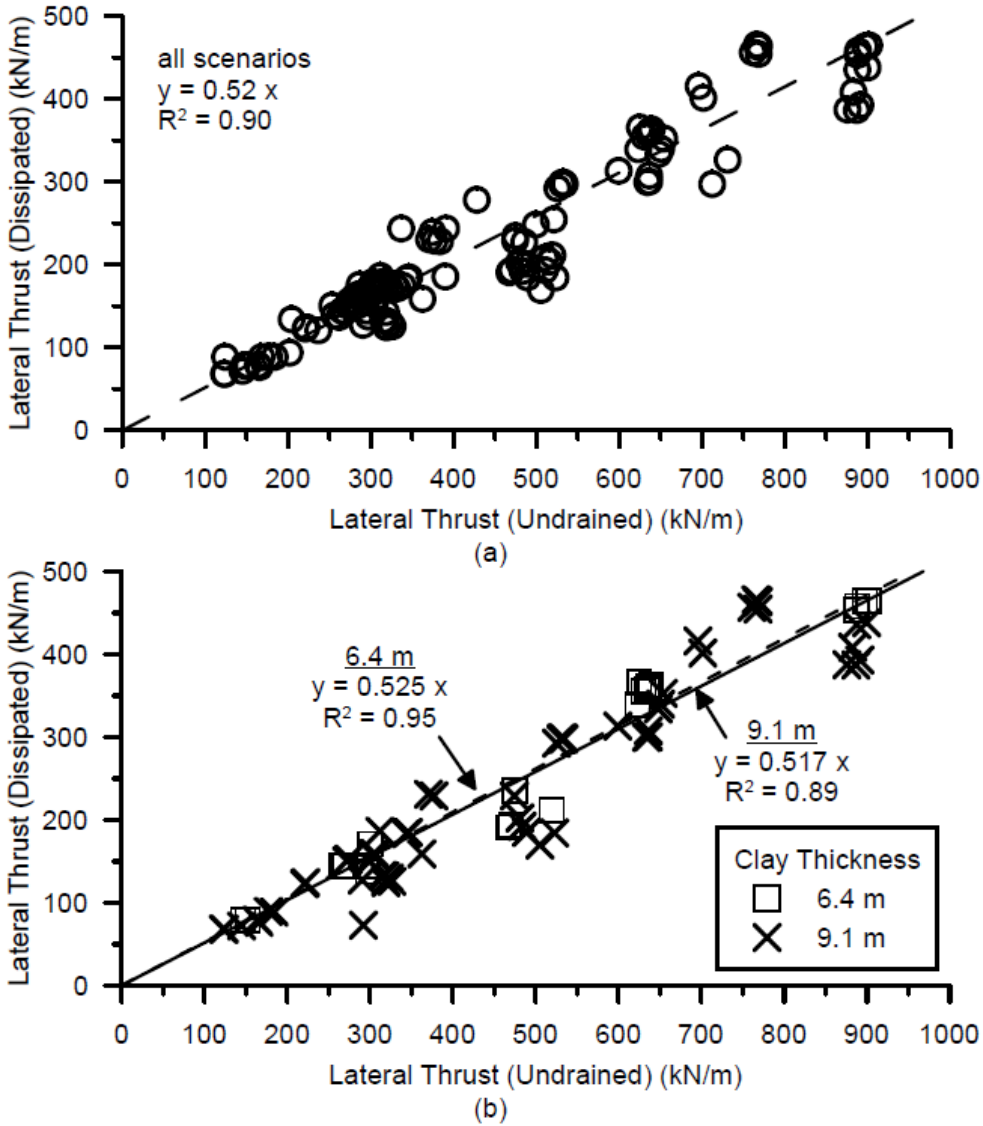

Figure 3-3. Lateral thrust at centerline in the dissipated vs. undrained conditions for a) all scenarios; and b) scenarios with clay thicknesses of 6.4 m and 9.1 m.

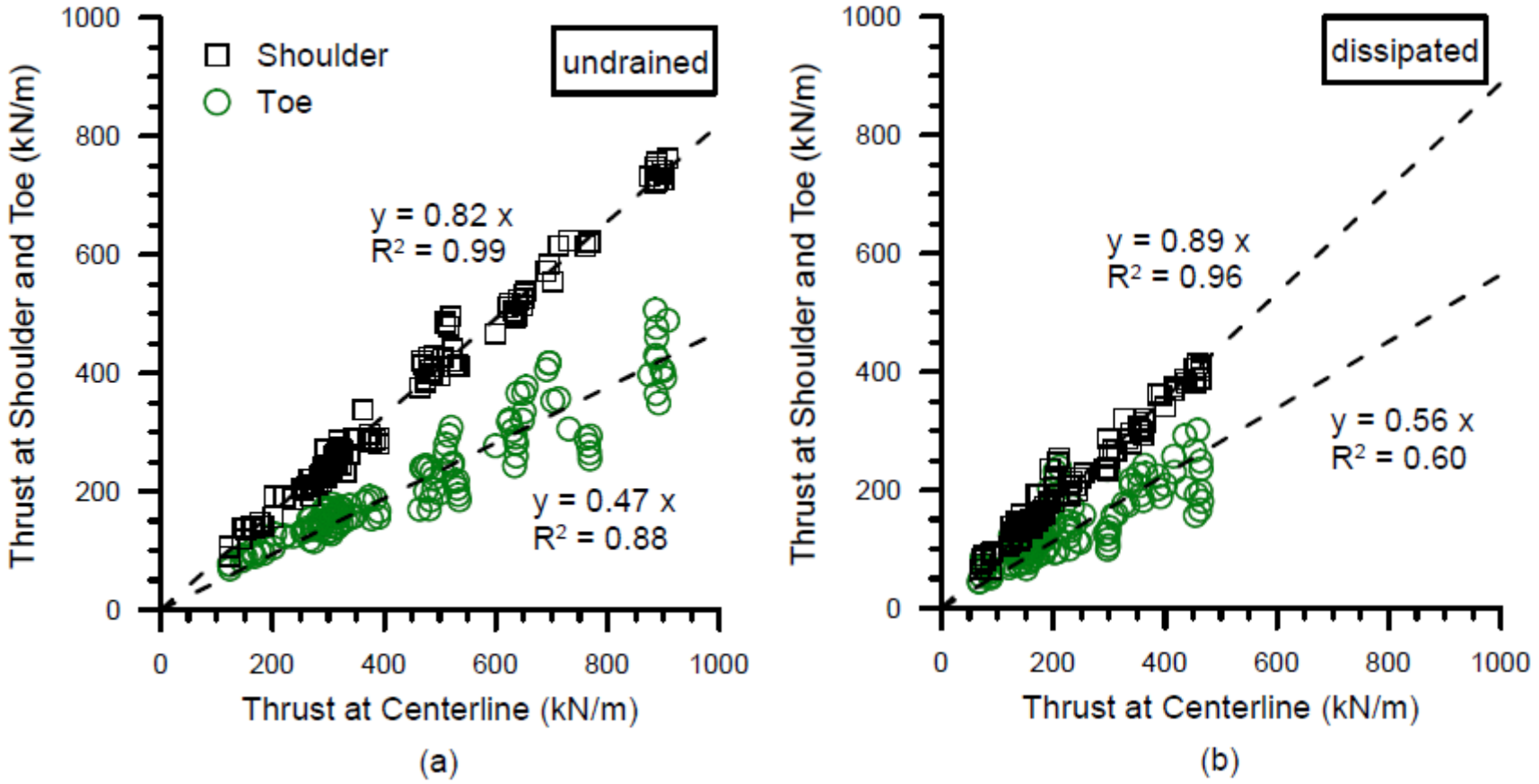

Figure 3-4. Lateral thrust at shoulder and toe locations vs. lateral thrust at centerline for a) undrained end-of-construction; and b) dissipated long-term.

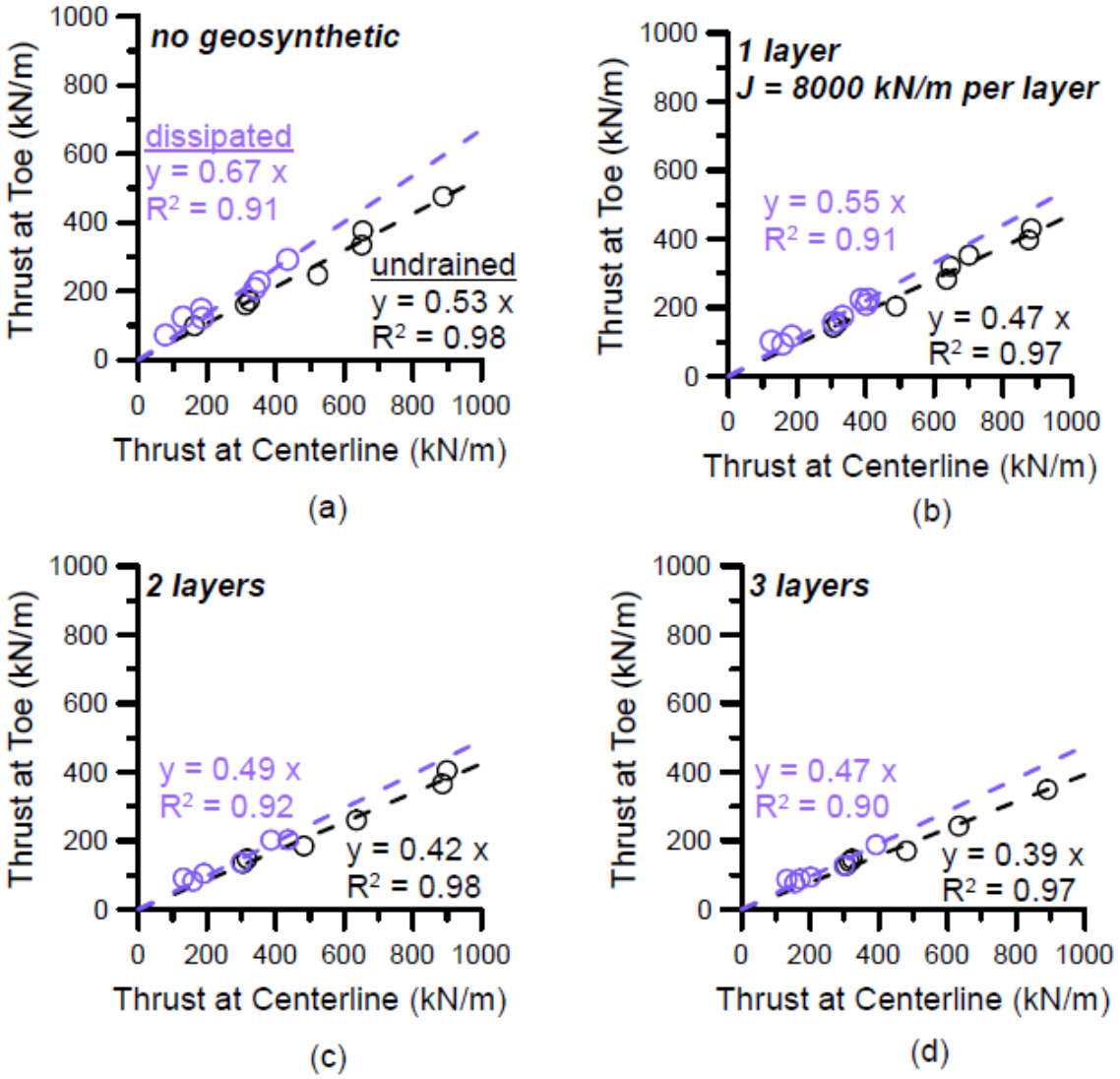

Figure 3-5. Thrust at toe vs. thrust at centerline in the undrained (in black) and dissipated (in purple) conditions for scenarios with Case 1 preconsolidation pressure using different number of geosynthetic layers (J = 8000 kN/m per layer)

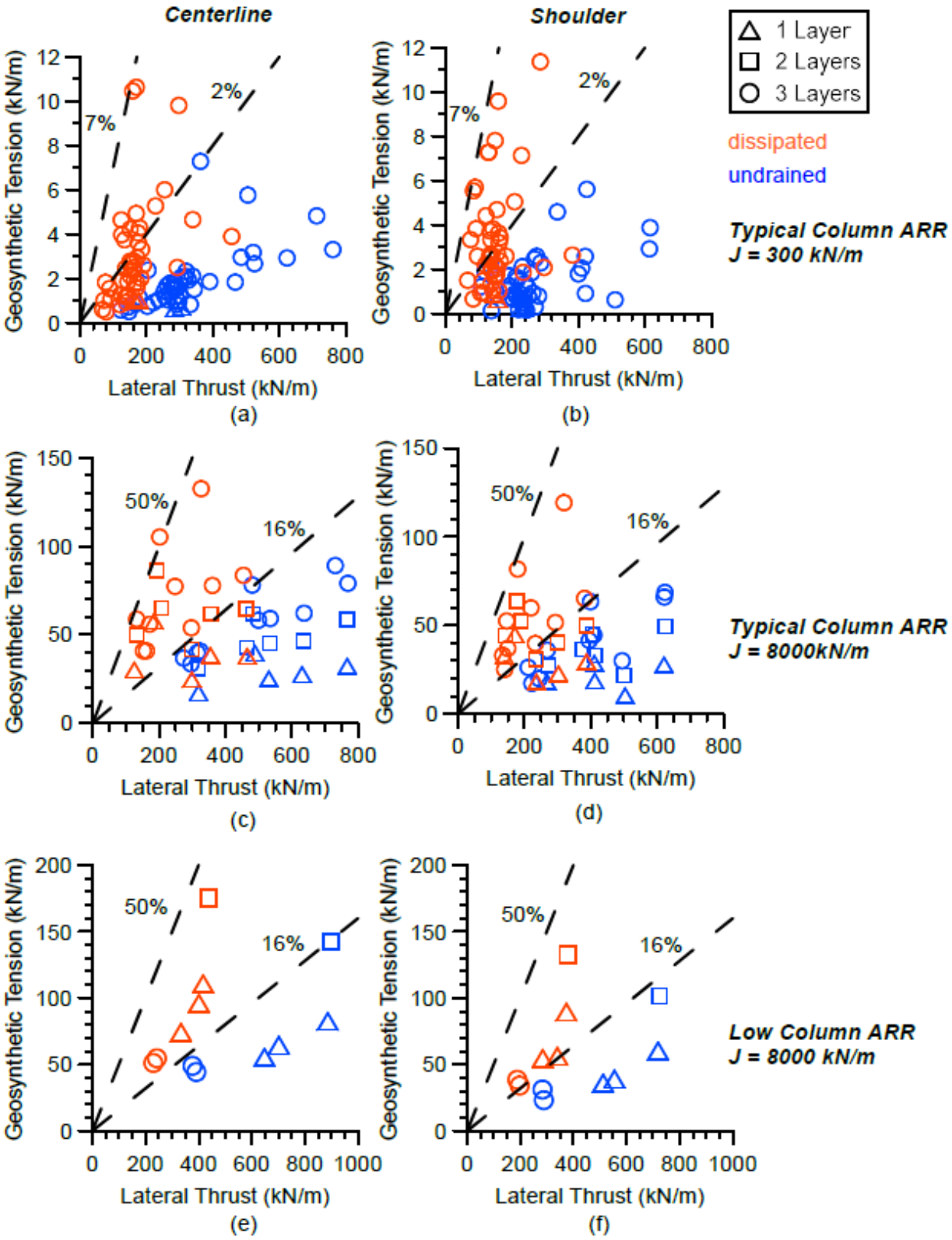

Figure 3-6. Geosynthetic resistance of lateral thrust at centerline and shoulder locations for different column area replacement ratios and geosynthetic stiffnesses.

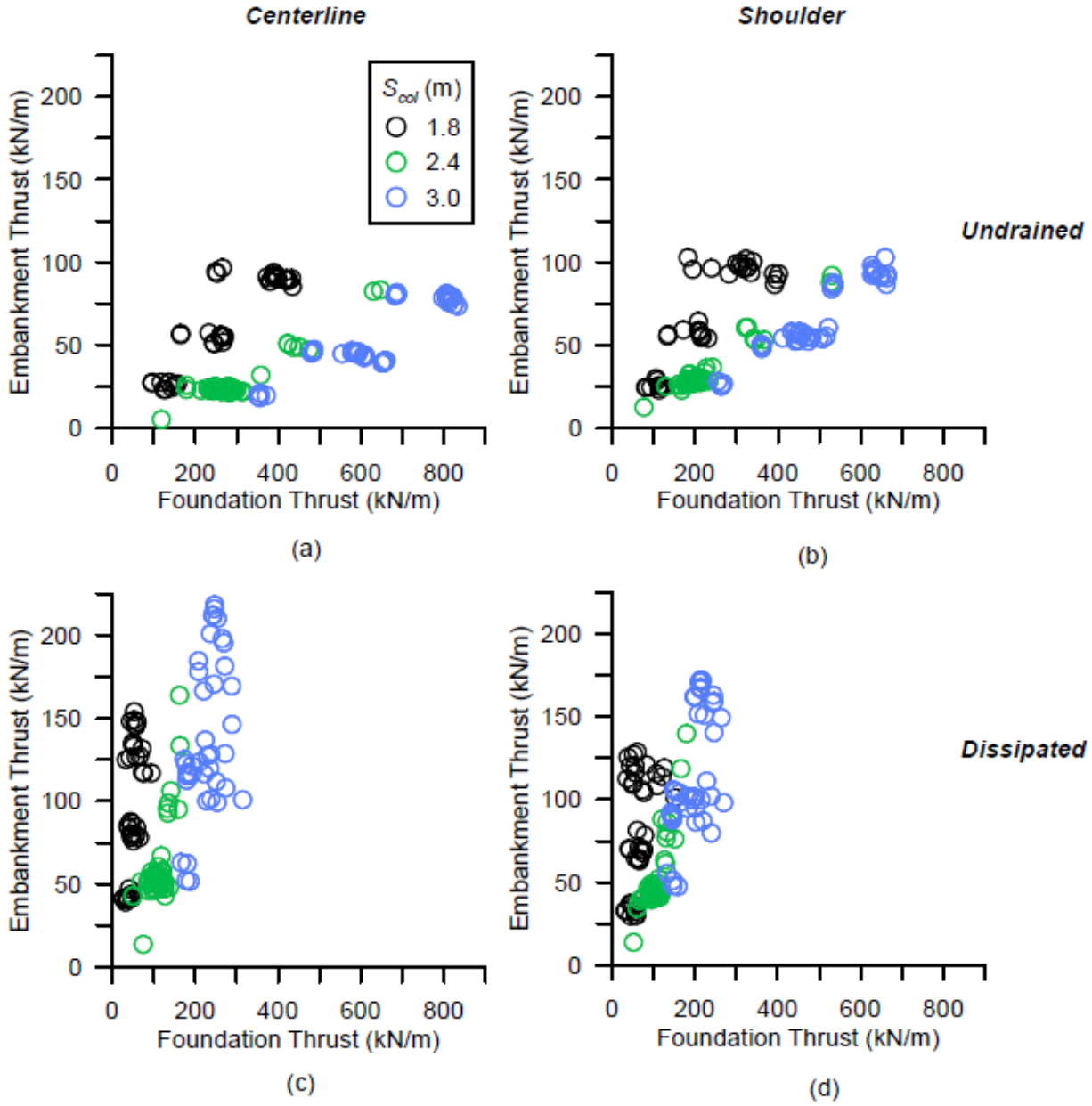

Figure 3-7. Embankment thrust vs. foundation thrust at different locations and limiting conditions.

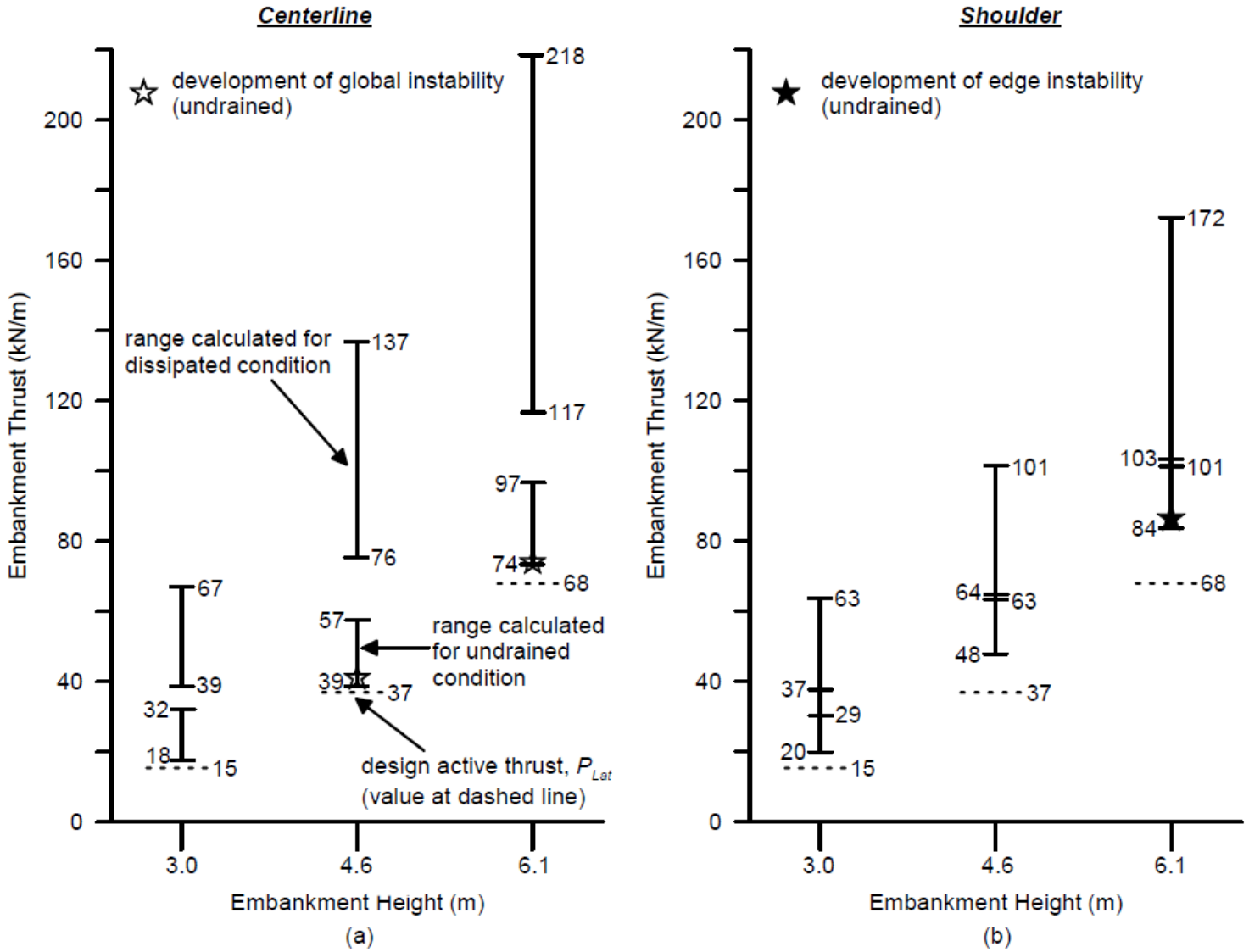

Figure 3-8. Comparison of calculated embankment lateral thrust vs. design active thrust for different embankment heights.

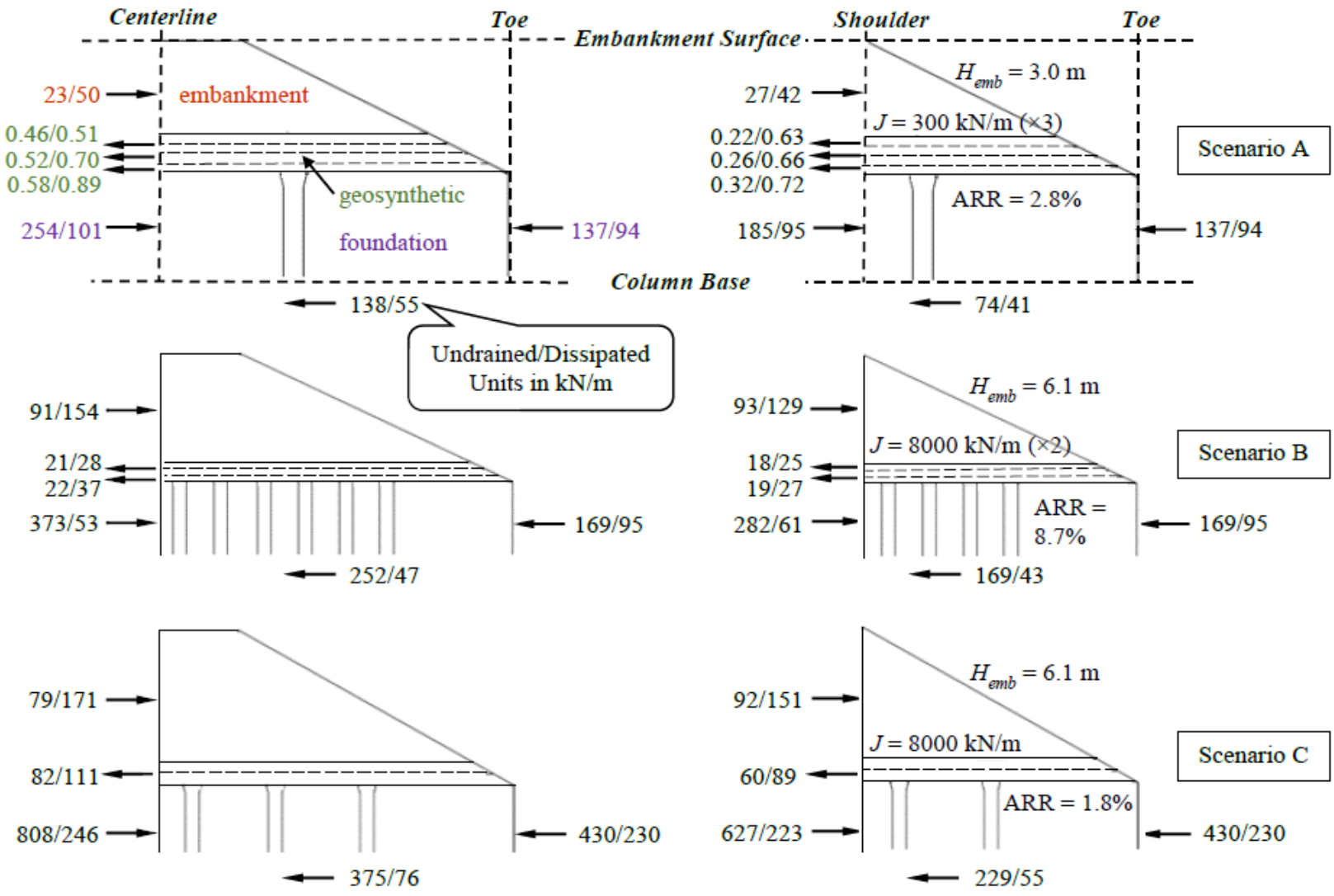

Figure 3-9. Free body diagrams of lateral thrust distribution (scenario geometries and material properties shown in Table 3-5); not to scale.

3.9. Electronic Supplement

The reader can find in this document: 1) details for the selection of column-soil and geogrid-soil interface properties used in the numerical models; and 2) a master list consisting of embankment geometries and site conditions for all column-supported embankment (CSE) scenarios investigated in the parametric study.

3.9.1. Selection of Soil-Structure Interface Properties

Column zones interacted with surrounding soils through interface elements that were installed at the column top, shaft, and base. The normal and shear stiffness values of the interfaces were 10 times the apparent stiffness of adjacent zones (Itasca 2013) to avoid excessive computation times. The interface shear strength was selected assuming rough concrete. The ratios of the interface effective friction angle to the adjacent soil effective friction angle (δ'/φ') for coarse-grained soils and clay were 0.98 and 0.95, respectively, using values from Potyondy (1961).

Geogrid elements had the following properties at the interface. The friction angle was 50°, or the same as the gravel load transfer platform (LTP), representing a friction coefficient of 1 (Cancelli et al. 1992; Cazzuffi et al. 1993; Liu et al. 2009). Both the normal and shear stiffness values were $2x10^6$ N/m (Eun et al. 2017; Liao et al. 2009).

3.9.2. Scenario Geometries and Site Conditions

The parametric study investigated 128 CSE scenarios, in which columns were all assigned properties assuming unreinforced concrete. Scenario geometries and site conditions are listed in Table 3-6. The table is organized by base cases (BC), where parameters are typically varied one at time from the base case condition. Some scenarios represent conditions of interest using different combinations of parameters.

Table 3-6. Master list of scenario geometries and site conditions.

Base Case	H_{emb} (m)	H_{LTP} (m)	H_{fill} (m)	S_{col} (m)	d_{cap} (m)	d_{col} (m)	*Slope* (H:V)	L_{emb} (m)	N_{col}	N_{geo}	J (kN/m)	φ'_{emb} (°)	σ'_p	q (kPa)
BC1	3.0	0.91	0.91	2.4	0.61	0.46	2:1	24	0	3	300	40	Case 2	0
		0												
		1.8												
		2.7												
				1.8										
				3.0										
												34		
												50		
						0.36								
						0.61								
					0.46									
					0.91									
													Case 1	
													Case 3	
							3:2							
		0.61												
		1.2												
										2				
										1				
										0				
								10						
								39						
	1.5													
	4.6													
	6.1													
											2000			
											8000			

Note: blank cells contain values corresponding to the base case.

Table 3-6. Master list of scenario geometries and site conditions (continued).

Base Case	H_{emb} (m)	H_{LTP} (m)	H_{fill} (m)	S_{col} (m)	d_{cap} (m)	d_{col} (m)	*Slope* (H:V)	L_{emb} (m)	N_{col}	N_{geo}	J (kN/m)	φ'_{emb} (°)	σ'_p	q (kPa)
BC1	3.0	0.91	0.91	2.4	0.61	0.46	2:1	24	0	3	300	40	Case 2	0
									-1					
									+1					
														14
					0.46					1				
					0.46								Case 1	
	4.6				0.46									
				2.7	0.46									
	4.6										8000			
	6.1										8000			
				3.0							8000			
			0								8000			
											8000		Case 1	
									-1		8000			
BC2	3.0	0.91	2.7	1.8	0.61	0.61	2:1	24	0	0	-	40	Case 2	0
										3	300			
	4.6													
	4.6									3	300			
	6.1													
	6.1									3	300			
BC3	3.0	0.91	0	1.8	0.61	0.61	2:1	24	0	0	-	40	Case 1	0
										3	300			
	4.6													
	4.6									3	300			
	4.6									1	8000			
	4.6									2	8000			

Note: blank cells contain values corresponding to the base case.

Table 3-6. Master list of scenario geometries and site conditions (continued).

Base Case	H_{emb} (m)	H_{LTP} (m)	H_{fill} (m)	S_{col} (m)	d_{cap} (m)	d_{col} (m)	*Slope* (H:V)	L_{emb} (m)	N_{col}	N_{geo}	J (kN/m)	φ'_{emb} (°)	σ'_p	q (kPa)
BC3	3.0	0.91	0	1.8	0.61	0.61	2:1	24	0	0	-	40	Case 1	0
	4.6									3	8000			
	6.1													
	6.1								+2	3	300			
	6.1								+2	1	8000			
	6.1								+2	2	8000			
	6.1								+2	3	8000			
	6.1							10	+2	3	300			
						0.46							Case 2	
						0.46				3	300		Case 2	
										3	300		Case 2	
	4.6									3	300		Case 2	
													Case 3	
										3	300		Case 3	
	4.6												Case 3	
	4.6									3	300		Case 3	
	6.1												Case 3	
	6.1									3	300		Case 3	
BC4	4.6	0.91	2.7	3.0	0.61	0.61	2:1	24	0	0	-	40	Case 2	0
										3	300			
										1	8000			
										2	8000			
										3	8000			
	6.1													
	6.1									1	8000			
	6.1									2	8000			
	6.1									3	8000			
							3:2			1	8000			

Note: blank cells contain values corresponding to the base case.

Table 3-6. Master list of scenario geometries and site conditions (continued).

Base Case	H_{emb} (m)	H_{LTP} (m)	H_{fill} (m)	S_{col} (m)	d_{cap} (m)	d_{col} (m)	*Slope* (H:V)	L_{emb} (m)	N_{col}	N_{geo}	J (kN/m)	φ'_{emb} (°)	σ'_p	q (kPa)
BC5	4.6	0.91	0	3.0	0.61	0.61	2:1	24	0	0	-	40	Case 1	0
										1	8000			
										2	8000			
										3	8000			
	6.1													
	6.1									1	8000			
	6.1									2	8000			
	6.1									3	8000			
	3.0					0.46				3	8000			
	3.0			2.4		0.46								
	3.0			2.4		0.46				1	8000			
	3.0			2.4		0.46				2	8000			
	3.0			2.4		0.46				3	8000			
				2.4		0.46				1	8000			
						0.46				3	300		Case 2	
										1	8000		Case 2	
													Case 3	
										1	8000		Case 3	
										2	8000		Case 3	
										3	8000		Case 3	
										3	300		Case 3	
	6.1									1	8000		Case 3	
	6.1									2	8000		Case 3	
	6.1									3	8000		Case 3	
	6.1									3	300		Case 3	
BC6	6.1	0.91	0.91	1.8	0.61	0.61	2:1	22	0	2	8000	40	Case 2	0
									+1					
									+2					

Note: blank cells contain values corresponding to the base case.

Table 3-6. Master list of scenario geometries and site conditions (continued).

Base Case	H_{emb} (m)	H_{LTP} (m)	H_{fill} (m)	S_{col} (m)	d_{cap} (m)	d_{col} (m)	*Slope* (H:V)	L_{emb} (m)	N_{col}	N_{geo}	J (kN/m)	φ'_{emb} (°)	σ'_p	q (kPa)
BC6	6.1	0.91	0.91	1.8	0.61	0.61	2:1	22	0	2	8000	40	Case 2	0
			2.7											
							3:2							
										1				
										0	-			
BC7	4.6	0.91	0	3.0	0.36	0.36	3:2	25	0	0	-	40	Case 1	0
										1	300			
										1	2000			
										1	8000			
	6.1									1	2000			
BC8	6.1	0.91	0	3.0	0.61	0.46	3:2	25	0	0	-	40	Case 1	0
										1	8000			
										2	8000			
	4.6													
	4.6									1	300			
	4.6									1	8000			
Others														
	3.0	0.91	0.91	2.4	0.61	0.61	2:1	24	0	3	300	40	Case 3	0
	3.0	0.91	0.91	1.8	0.61	0.61	2:1	24	0	2	8000	40	Case 2	0
	3.0	0.91	2.7	2.4	0.61	0.61	2:1	24	0	0	-	40	Case 2	0
	3.0	0.91	2.7	2.4	0.61	0.61	2:1	24	0	3	300	40	Case 2	0
	4.6	0.91	2.7	2.4	0.61	0.61	2:1	24	0	0	-	40	Case 2	0
	4.6	0.91	0.91	1.8	0.61	0.61	2:1	24	0	2	8000	40	Case 2	0
	4.6	0.91	0	1.8	0.61	0.61	2:1	22	0	2	8000	40	Case 1	0

Note: blank cells contain values corresponding to the base case.

References

Cancelli, A., Rimoldi, P., and Togni, S. (1992). "Frictional characteristics of geogrids by means of direct shear and pull-out tests." *Earth Reinforcement Practice*, 29-34.

Cazzuffi, D., Picarelli, L., Ricciuti, A., and Rimoldi, P. (1993). "Laboratory investigations on the shear strength of geogrid reinforced soils." *Geosynthetic Soil Reinforcement Testing Procedures*, 119-137. ASTM International.

Eun, J., Gupta, R., and Zornberg, J. G. (2017). "Effect of Geogrid Geometry on Interface Resistance in a Pullout Test." In *Proc. Geotechnical Frontiers 2017*, 236-246. Reston, VA: American Society of Civil Engineers.

Liao, X., Ye, G., and Xu, C. (2009). "Friction and Passive Resistance of Geogrid in Pullout Tests." *Advances in Group Improvement*, 252-259. Reston, VA: American Society of Civil Engineers.

Liu, C., Ho, Y., and Huang, J. (2009). "Large scale direct shear tests of soil/PET-yarn geogrid interfaces." *Geotextiles and Geomembranes*, 27(1), 19-30.

Potyondy, J. G. (1961). "Skin friction between various soils and construction materials." *Géotechnique*, 11(4), 339-353.

CHAPTER 4. 3D NUMERICAL FAILURE ANALYSES OF COLUMN-SUPPORTED EMBANKMENTS: FAILURE HEIGHTS, FAILURE MODES, AND DEFORMATIONS

Zhanyu Huang[1], Katerina Ziotopoulou[2], George M. Filz[3]

[1] Graduate Research Assistant, The Charles E. Via Jr. Department of Civil and Environmental Engineering, Virginia Tech, Blacksburg, USA

[2] Assistant Professor, Department of Civil and Environmental Engineering, University of California, Davis, USA

[3] Professor, The Charles E. Via Jr. Department of Civil and Environmental Engineering, Virginia Tech, Blacksburg, USA

4.1. Abstract

The failure height, failure mode, and deformations were investigated for eight column-supported embankment (CSE) scenarios using three-dimensional (3D) numerical analyses. Embankment stability was evaluated for the limiting conditions at undrained end-of-construction and after long-term dissipation of excess pore water pressures. The numerical model included representations of flexural tensile failure in the concrete columns and tensile failure in the geosynthetic reinforcement. Scenarios consisted of a base case with typical concrete column design, five single-parameter variations using base case conditions, and two multi-parameter variations using base case conditions. The undrained condition was the most critical, and two failure modes were found: (1) multi-surface shearing in the embankment coupled with bending failure of columns and near circular shear failure in the clay and (2) multi-surface shearing in the embankment coupled with bending failure of columns and shearing in the upper portion of the soft foundation clay. Both failure modes were accompanied by rupture of the geosynthetic when included in the load transfer platform. Soil-column interactions were complex, and many columns failed in bending at lower embankment heights than those that produced collapse. The failure height increased with increases in the geosynthetic tensile capacity and clay foundation strength.

4.2. Introduction

Column-supported embankments (CSEs) have been used more frequently in recent decades for construction on soft soils. With appropriate design, CSEs can enable accelerated construction and high performance through the transfer of embankment and service loads to a competent stratum at depth via stiff foundation columns. Often, a load transfer platform (LTP) is constructed at the embankment base, and it consists of quality coarse-grained fill reinforced with one or more layers of geosynthetic. The load transfer mechanism occurs by the simultaneous soil arching in the embankment, differential settlement in the foundation, frictional resistance on the column shafts, and membrane action in the geosynthetic.

Design of CSEs requires evaluation of stability, as is necessary for all embankments. In the recommendations by Schaefer et al. (2017) for CSE design in the U.S., and with reference to the British standard (BSI 2010), consideration must be given to the ultimate limit states of embankment lateral sliding and global instability. Embankment lateral sliding is assumed to occur by the embankment mass sliding over the foundation with the concurrent mobilization of an active condition in the embankment. Geosynthetic reinforcement is recommended if the embankment active thrust cannot be resisted by the foundation undrained shear strength (s_u) mobilized over the slope length by a safety factor of 1.5. Global instability is assumed to occur by shear failure through the embankment and column foundation. The conventional limit equilibrium method (LEM) is recommended for evaluation of global instability, in which case both the geosynthetic and columns are included in the analysis.

Fundamental to CSE stability evaluation is understanding all possible failure modes, but there is, in fact, limited understanding of the failure modes that can occur in CSEs designed using unreinforced concrete columns and geosynthetics in the LTP. Investigations of CSE failure modes have been performed using centrifuge tests and numerical analyses, but these were predominantly for embankments supported by columns or elements installed using the deep mixing method (Adams 2011; Chai et al. 2017; Inagaki et al. 2002; Jamsawang et al. 2015; Kitazume and Maruyama 2007; Navin 2005; Shrestha et al. 2015; Yapage et al. 2013; Zhang et al. 2014), for which the column properties and design differ from unreinforced concrete columns. A fundamental difference is that concrete columns are typically installed using isolated columns at low area replacement ratios (ARR) of 2.5% to 10% (Collin, personal communication, 2018). Unreinforced

concrete has limited tensile strength, and such columns are more likely to fail in bending rather than shear (King et al. 2018; Huang et al. 2019). Zhang et al. (2012) reported a CSE centrifuge model using columns consisting of cement, fly ash, and gravel that failed under a combined mechanism of shearing through the soft soil, cracking of columns near the embankment toe, and failure of the material representing the geosynthetic. Questions remain regarding (1) the various possible CSE failure modes involving failure of both the concrete columns and geosynthetic reinforcement and (2) the design parameters that influence stability, including the specific geosynthetic contribution. This study was motivated by both issues.

4.3. Scope of Study

CSE failure modes were investigated using three-dimensional (3D) finite difference analyses in the commercial software FLAC3D v.5.01 (Itasca 2012). The analyses are computationally intensive, and consideration was given to the (1) stability metric, (2) limiting conditions and corresponding numerical approach with regards to pore pressures, (3) material modeling, and (4) scenarios.

The selected stability metric is the embankment failure height. The failure height is relatable to practice. In addition, increasing the embankment height is judged less computationally intensive than the iterative shear strength reduction approach (Griffiths and Lane 1999) to determine values of safety factor.

The limiting conditions for analysis were undrained end-of-construction and long-term dissipated, as concluded based on CSE case history data (Huang et al. 2019). The embankments were constructed in lifts in the undrained condition with excess pore water pressure development in the clay, followed by dissipation of excess pore pressures and consolidation. Equilibrium was computed for an undrained end-of-construction state and a long-term dissipated state at different embankment heights. The failure height was interpreted as the one at which equilibrium could not be established and deformations continually increased.

Columns and geosynthetic reinforcement were each assigned a failure criterion. Column zones were modeled using the Mohr-Coulomb failure criterion with a tensile cutoff. Orthotropic linear

elastic geogrid elements (Itasca 2013) were removed from the unit cell between columns in which the geogrid tensile strain exceeded 10%.

A total of eight (8) scenarios were investigated, and comparisons were made for the failure height, failure mode, lateral toe displacement, and centerline surface settlement. The scenarios consisted of a base case and seven parametric variations using base case conditions (Table 4-1). The parameters for variation are important for CSE design and site characterization: the center-to-center column spacing (S_{col}), column diameter (d_{col}), geosynthetic stiffness (J), and the clay's undrained shear strength (s_u). Figure 4-1 illustrates a schematic of the base case, whose geometry and site conditions were selected to produce failure at an embankment height of about 6 m. The base case includes the following features:

1) The columns had properties of unreinforced concrete, as produced during construction of vibro-concrete columns, and an area replacement ratio (ARR) of 2.8%. This ARR is in the lower range for typical CSE applications. Columns were installed in a square array, using S_{col} of 2.4 m (8 ft) and d_{col} of 0.46 m (1.5 ft) (Collin, personal communication, 2018).
2) A layer of geosynthetic was included, using J of 438 kN/m (30,000 lb/ft) in both the longitudinal and transverse directions.
3) The clay was assigned properties corresponding to an s_u of 4.8 kPa (100 psf) at the layer top, and with s_u increasing with depth at a rate of 1.66 kPa/m (10.6 psf/ft) corresponding to a preconsolidation pressure profile that is at a constant increment above the vertical effective stress. This low s_u profile reflects the realistic and potentially challenging construction conditions for some CSEs, as reported in case histories (Zanzinger and Gartung 2002; Plomteux and Lacazedieu 2007).
4) The clay was overlain by a layer of loose, coarse-grained fill, similar to what sometimes exists at CSE construction sites. The fill thickness was 0.91 m (3 ft).

The other scenarios were related to the base case as follows. The column spacing (S_{col}) was increased in Scenario 1, the column diameter (d_{col}) was decreased in Scenario 2, and no geosynthetic was used in Scenario 3. The three changes from the base case to create Scenarios 1 through 3 were applied simultaneously to produce Scenario 4. The geosynthetic stiffness (J) was increased in Scenario 5, and the undrained strength (s_u) of the clay was increased in Scenario 6.

The two changes from the base case to create Scenarios 5 and 6 were applied simultaneously to produce Scenario 7. Thus, the base case and Scenarios 1 through 4 can be readily compared, as can the base case and Scenarios 5 through 7.

4.4. Numerical Procedure

Numerical analyses were conducted using FLAC3D v.5.01 (Itasca 2012) in large strain mode. The following sections describe the rationale and procedure behind various aspects of the numerical model, including the undrained-dissipated approach for analyzing limiting conditions, the selection of constitutive models and material properties, the numerical domain and boundary conditions, and the loading sequence.

4.4.1. Undrained-Dissipated Analyses

Investigation of CSE failure modes in a computationally efficient manner required analysis of limiting conditions rather than histories of deformations and pore pressures. The undrained-dissipated approach was selected for calculating an undrained end-of-construction state and a long-term state after dissipation of all excess pore water pressures. These are the two limiting conditions for lateral spreading analysis, as synthesized using CSE case history data (Huang et al. 2019). Field measurements show that vertical pressures in the foundation soil decrease with consolidation, indicating an ongoing development of soil arching at end-of-construction. This can be represented numerically as a limiting condition, in which an undrained analysis of embankment construction limits the subsoil consolidation and soil arching, and produces the maximum increments of vertical and lateral earth pressure in the foundation soil. Field measurements also show the increase in geosynthetic strain with the increase in vertical load transfer to columns and subsoil settlement. This can be represented also as a limiting condition, in which full dissipation of excess pore pressures leads to consolidation and development of geosynthetic strains with the increase in vertical deflection. The long-term dissipated condition is of interest to failure analyses because tensile failure of the geosynthetic could be accompanied by a reduction in the lateral restraint provided by the geosynthetic and an increase in loading on the foundation soil.

Previous work adopting the undrained-dissipated approach includes a validation of the method (Huang et al. 2018), an example application in CSE lateral spreading analysis (Huang et al. 2019),

and a parametric study investigating the effect of design parameters on lateral thrust distribution in CSEs (Huang et al., manuscript, 2019). First, the method of excess pore pressure dissipation and computed consolidation deformations were validated using benchmark solutions (Huang et al. 2018). Benchmarks consisted of one-dimensional consolidation as well as consolidation with lateral drainage for which a fully coupled analysis was performed for comparison. The undrained-dissipated approach was then adopted for the analysis of a CSE case history using a 3D half-embankment domain (Huang et al. 2019). The numerical model was calibrated such that the system response at the undrained end-of-construction and long-term dissipated conditions was in agreement with instrumented case history data. Lastly, the approach using calibrated values was adopted in a 3D numerical parametric study that employed the half-embankment domain and totaled 128 scenarios (Huang et al., manuscript, 2019). Results from the parametric study indicate that the undrained-dissipated approach is appropriate for failure analyses of CSEs. A number of scenarios with marginal conditions (i.e. very low column ARR) was found to approach global instability at undrained end-of-construction. Geosynthetic strains were found to maximize in the long-term dissipated condition for all scenarios. However, the aforementioned studies were limited by the adoption of purely elastic geogrid elements for which the influence of geosynthetic tensile failure on load path could not be examined. In addition, there was uncertainty regarding failure modes because collapse was not initiated in any scenario. The present study overcomes these limitations by adopting a failure criterion for the geosynthetic and by increasing the embankment height until embankment collapse occurred. Furthermore, failure is examined for a range of column ARR.

The undrained-dissipated approach was implemented in the current study as follows. The embankment was constructed in the undrained condition, in which foundation drainage was disabled and an effective stress model was used to calculate excess pore pressures in the clay. The embankment was constructed in lifts of 0.6 m (2 ft) up to a height of 3.0 m (10 ft), then in lifts of 0.3 m (1 ft) to achieve heights above 3.0 m. For scenarios in which the embankment was expected to be very tall, 0.6 m lifts were used throughout construction. The model was solved for equilibrium and an undrained end-of-construction state after construction of every lift. Following undrained loading, pore pressures were returned to the hydrostatic condition, and the model was solved for consolidation and a long-term dissipated state. The first dissipated analysis was conducted at an embankment height (H_{emb}) of 3.0 m (10 ft), which is above the estimated critical

height (H_{crit}) for differential settlement (McGuire 2011) based on the least conservative column arrangement used in the eight scenarios. Subsequent dissipated analyses were conducted for every 0.6 m (2 ft) or 1.2 m (4 ft) increase in embankment height above H_{emb} = 3.0 m.

The dissipated analyses involved applying calibrated values of Young's modulus (E) and effective friction angle (φ') in select embankment zones above the subsoil between columns (Figure 4-1, shaded embankment regions). As observed in bench-scale and full-scale CSEs (McGuire 2011; Sloan 2011), fill in a limited region above the subsoil between columns became very loose during differential settlement at the embankment base due to shearing and decrease in normal stresses. The geometry of the loosened zones was established using a correlation to the fill's φ', which was formulated using data from bench-scale CSEs for sands with a range of relative densities prior to differential settlement (McGuire 2011). The properties of the loosened zones were determined from calibration of a 3D numerical embankment slice model using case history data for vertical load transfer and settlement at the subgrade level (Huang et al. 2019).

4.4.2. Soil Properties

Constitutive models selected for the soils and their input properties are listed in Table 4-2. All coarse-grained soils were represented as linear elastic and perfectly plastic with the Mohr-Coulomb failure criterion. The clay was modeled with Modified Cam Clay. An undrained shear strength (s_u) was selected for the clay at the layer top, and the corresponding preconsolidation pressure (p'_o) was determined using Equation (4.1) (Wood 1990). The preconsolidation pressure profile was then selected to be linearly increasing with depth at a constant increment above the effective vertical stress.

$$s_u = \frac{M}{2} \exp\left[\frac{(\Gamma - v_\lambda)}{\lambda} + ln\left(p'_o\right) - \left(\frac{\kappa}{\lambda}\right) ln\left(\frac{p'_o}{p'_i}\right)\right] \qquad (4.1)$$

4.4.3. Column Properties

Unreinforced concrete columns were modeled using the linear elastic – perfectly plastic Mohr Coulomb failure criterion with a tensile cutoff, whose properties were determined as follows, with reference to Figure 4-2:

1) The concrete was assumed to have an unconfined compressive strength (f'_c) of 17 MPa (2500 psi), which is typical for vibro-concrete columns (SHRP2 2012).
2) The flexural tensile strength (f'_r) was 2.6 MPa (375 psi), estimated using Equation (4.2) for normal weight concrete as a function of f'_c in U.S. customary units (ACI 2011).

$$f'_r = 7.5\sqrt{f'_c} \qquad (4.2)$$

3) Points A and B were used in generating the portion of the failure envelope that defined the friction angle (φ) and the cohesion intercept (c). Point A was on the larger stress circle representing the unconfined compression test (f'_c). Point B used a normal stress (σ) of f'_r and a shear stress (τ) that was half of f'_r. Point B was selected over a point on the smaller stress circle representing the flexural tension test so that failure in tension would be calculated before failure in shear. The resulting φ of 43° and c of 3.7 MPa are within the range of reported values (Schädlich and Schweiger 2014; Pul et al. 2017).
4) The tensile strength (σ_t) was assigned a reduced value of 1.6 MPa compared to f'_r. This was to account for the difference in the maximum tension calculated at zone centroids for a highly refined discretization of a single column and for a more practical discretization that could be incorporated in the half-embankment models. The isolated column with a highly refined discretization and $\sigma_t = f'_r$ was simply supported at the ends and subjected to a uniformly distributed line load. The magnitude of the line load was increased until flexural tensile failure occurred. Then the same failure load was applied to an isolated column with the same zone discretization as used in the current study, and flexural failure occurred when σ_t was reduced to 1.6 MPa.
5) Brittle behavior was modeled by reducing σ_t to zero after tensile failure.

Interface elements were applied at the column top, shaft, and base. Rough interfaces were assumed, using 0.98 and 0.95 for the ratio of interface friction angle to soil friction angle for coarse-grained soils and clay, respectively (Potyondy 1961). Interface normal and shear stiffnesses were assigned values equal to ten times the apparent stiffness of adjacent zones (Itasca 2013).

4.4.4. Geosynthetic Properties

Properties of the geosynthetic reinforcement are listed in Table 4-3. Biaxial geogrids were modeled using orthotropic linear elastic structural geogrid elements of the constant strain triangle type

(Itasca 2013). The geogrid elements can sustain membrane stress but not bending, and they can develop tension under out-of-plane deformation when computed in large-strain mode. Stiffnesses typical of biaxial geogrids were selected (Tensar International Corporation 2015; INOVA Geosynthetics 2017; Huesker 2019). The Poisson's ratio (v) was 0 (Zhuang and Wang 2015). A small shear modulus (G) was assigned (Huang et al. 2019). There is uncertainty in the shear modulus of geosynthetics (Santacruz Reyes 2016), so a small value was selected to contrast between isotropic and orthotropic behavior. At the geogrid-soil interfaces, the friction angle was the same as the surrounding LTP (Cancelli et al. 1992; Cazzuffi et al. 1993; Liu et al. 2009), and the normal and shear stiffness values were 2×10^6 N/m (Eun et al. 2017; Liao et al. 2009).

Failure of the geosynthetic reinforcement was manually implemented. When the transverse geosynthetic strain (ε_{trans}) in a unit cell reached 10%, tensile failure was assumed, and geogrid elements within the unit cell were removed. The ε_{trans} was determined by summing the strain from the lateral spreading effect (ε_{lat}) and the strain from the vertical load transfer effect (ε_{vert}) (Equation 4.3). The ε_{lat} value was calculated as the ratio of the change in center-to-center column spacing (ΔS_{col}) in the transverse direction to the column clear span prior to deformation, which is the design S_{col} reduced by the edge length (a) of an equivalent square column cross-section (Equation 4.4). This approach assumes that the geosynthetic did not slide appreciably at locations above the columns. The ε_{vert} value was calculated according to the Parabolic method using the geosynthetic vertical deflection (d) (Equation 4.5). The Parabolic method has been adopted in a number of design recommendations for calculating the geosynthetic strain under vertical deflection (Sloan et al. 2014; BSI 2016; Schaefer et al. 2017). The authors chose to estimate ε_{trans} using established design methods rather than to rely on values automatically calculated in the geogrid elements because geosynthetic strains are highest above column edges (Ariyarathne et al. 2013; Han and Gabr 2002; Huang and Han 2009; Huang et al. 2019; Zhuang and Wang 2015), and numerical calculation of this local strain effect is influenced by zone discretization (Huang et al. 2019).

$$\varepsilon_{trans} = \varepsilon_{lat} + \varepsilon_{vert} \qquad (4.3)$$

$$\varepsilon_{lat} = \frac{\Delta S_{col}}{S_{col} - a} \qquad (4.4)$$

$$\varepsilon_{vert} = \frac{8d^2}{3(S_{col} + \Delta S_{col} - a)^2} \qquad (4.5)$$

4.4.5. Numerical Domain and Boundary Conditions

A 3D half-embankment slice geometry was adopted (Figure 4-1), with the following numerical domain and boundary conditions. The centerline-to-toe width was kept constant at 37.5 m (123 ft) for all scenarios. The embankment was constructed at a slope of 1.5H:1V up to a maximum height of 12.8 m (42 ft), which was reported by Zhang et al. (2016) to be the tallest CSE ever constructed. The lateral extent was four (4) times the centerline-to-toe width and 12 times the maximum embankment height (Huang et al. 2019). The centerline-to-shoulder width was selected to prevent effects of the centerline boundary on failure mechanisms near the slope. The column group did not extend beyond the embankment toe, but it did extend as close as possible to the embankment toe to avoid edge instability. Boundary conditions consisted of pins at the model base below the strong bearing layer, a free surface at the top, and rollers on all other external surfaces.

4.4.6. Loading Sequence

A loading sequence similar to the one described by Huang et al. (2019) was adopted in the current study, as follows:

1) In-situ stresses were assigned to foundation soils and columns, which had the same density as the surrounding soils. Null material properties were assigned to zones in the LTP and embankment fill. Mechanical equilibrium was computed, and the resulting displacements were very small.
2) Column installation was simulated by gradually increasing the column density while solving for mechanical equilibrium. The small displacements calculated during this step were zeroed after column installation.
3) The embankment was constructed with the foundation clay in an undrained condition by disabling drainage in the submerged clay. The zone material model of the LTP and embankment fill was changed to Mohr-Coulomb. The embankment was constructed in lifts as previously described, where each lift was applied by gradually increasing the density while solving for equilibrium.

4) In the dissipated analysis, reduced material parameters (E and φ') representing loosening of fill were applied to select embankment zones at the same time as excess pore pressures were dissipated in one step. The model was solved for consolidation and mechanical equilibrium. The result was the long-term dissipated state.

4.5. Results and Discussion

Results are provided for the embankment failure height, failure mode, and deformations. The discussion regarding failure heights and failure modes refers to the undrained calculation, as embankment stability was found to be most critical at undrained end-of-construction. Embankment deformations are discussed for both the undrained and dissipated conditions.

4.5.1. Embankment Failure Height

Scenario failure heights (H_{fail}) are listed in Table 4-1. Herein, effects of the different scenarios on the calculated H_{fail} are presented first and then followed by a discussion. The failure height was affected by all parameters investigated, as shown by comparing Scenarios 1 to 7 with the base case. Scenario 1 with larger S_{col} calculated a decrease in H_{fail} of 0.6 m. Scenario 2 with smaller d_{col} calculated a slight increase in H_{fail} of 0.3 m. Scenario 3 with the geogrid excluded calculated a decrease in H_{fail} of 0.6 m. Scenario 4, which resulted from the simultaneous change in the three parameters that created Scenarios 1 to 3 from the base case, calculated a decrease in H_{fail} of 2.1 m. The H_{fail} for Scenario 4 was most influenced by S_{col} and geosynthetic tensile capacity, which is correlated to geosynthetic stiffness (J) because rupture was assumed to occur at 10% strain. Scenario 5 with greater geosynthetic J (and tensile capacity) calculated an increase in H_{fail} of 2.4 m. Scenario 6 with greater s_u calculated an increase in H_{fail} of 6.1 m. Scenario 7, which resulted from the simultaneous change in the two parameters that created Scenarios 5 and 6 from the base case, was constructed to a maximum height of 12.8 m without failing, and this was mostly due to the influence of the clay's s_u.

Scenario 2 calculated a slightly greater H_{fail} than the base case even though a smaller d_{col} was used. This is because embankment failure initiated after geosynthetic failure, which was defined by ε_{trans} exceeding 10% in any unit cell between two columns, and the distribution of ε_{trans} differed for Scenario 2 and the base case. At H_{emb} = 6.1 m, the base case failed after ε_{trans} exceeded 10%

in the unit cell between the 12th and 13th columns from the centerline. At the same height, Scenario 2 also calculated a large ε_{trans} of 9.2% in the same unit cell, as well as large ε_{trans} in other unit cells, though none exceeded 10%. After the H_{emb} increased to 6.3 m, Scenario 2 failed following geosynthetic rupture between the 11th and 12th columns from the centerline. Thus, the slight increase in H_{fail} in Scenario 2 relative to the base case was due to a slight change in the overall system response from a change in d_{col}, and not because d_{col} had a significant influence on the failure height.

4.5.2. Failure Modes

Scenario failure modes are listed in Table 4-1. Two failure modes were observed for the undrained condition: (1) multi-surface shearing in the embankment coupled with column bending failure and near-circular shear failure in the clay (mode A), which occurred for Scenarios 1 and 4; and (2) multi-surface shearing in the embankment coupled with column bending failure and sliding within the top portion of the clay (mode B), which occurred for the base case and Scenarios 2, 3, 5, and 6. Other failure modes may be possible for CSE configurations outside the current scope of study. The sequences leading to failure are described in the following sections.

4.5.2.1. Multi-Surface Shearing in the Embankment Coupled with Column Bending Failure and Near-Circular Shear Failure in the Clay

This failure mode was found in Scenarios 1 and 4, in which the column ARRs were low (1.8% and 1.1%, respectively). Notable features for the failure mode include:

1) Column bending failure that initiated in the outermost column and retrogressively developed towards inner columns. A retrogressive direction indicates a direction of growth uphill (Duncan et al. 2014).
2) Greater movement in clay than in columns near the embankment toe after column bending failure.
3) Both progressive and retrogressive propagation of shear strains in the embankment and clay. A progressive direction indicates a direction of growth downhill (Duncan et al. 2014).
4) Development of multiple shear bands in the embankment that converged to form a near-circular failure surface in the clay.

Figure 4-3 illustrates the shear strain contours and exaggerated deformations for Scenario 4 at failure height and with increasing deformations. The number of shear bands in the embankment increased with displacement. The number of columns failing in flexural tension also increased. The columns were supporting axial compressive loads, but the bending moments were sufficient to produce tensile failure on the column cross-section. Shear strains developed both progressively and retrogressively, as annotated using arrows at locations A1 and A2, B1 and B2, and C1 and C2, which are corresponding locations in line and between columns, respectively.

Figure 4-4 illustrates the lateral displacements of the columns and subsoil in between columns at an elevation corresponding to the top of the clay layer for Scenario 4. The lateral displacements in the three columns nearest to the embankment toe increased as the embankment height increased. The lateral displacements were largest for the column closest to the toe (labeled 1). At the same distance from the toe, the soil between columns displaced more than the columns. Figure 4-4 also shows the embankment height at which each column first experienced tensile failure due to column bending. The column closest to the embankment toe experienced bending failure at an embankment height of 1.2 m, which is much less than the height of 4 m at which a collapse mechanism developed.

A difference in the failure sequence between Scenarios 1 and 4 is that Scenario 4 included a layer of geosynthetic reinforcement, and collapse occurred post tensile failure of the geosynthetic.

4.5.2.2. Multi-Surface Shearing in the Embankment Coupled with Column Bending Failure and Shearing in the Top Portion of the Clay

This failure mode was found in the base case and Scenarios 2, 3, 5 and 6, which all had a column ARR of 2.8%. Notable features common to all affected scenarios include:

1) Extensive column bending failure that initiated in the outermost column and retrogressively developed towards inner columns.
2) Greater lateral displacements in clay than in columns beneath the embankment slope, with the exception of the outermost column, which experienced lateral displacements similar to the subsoil (i.e. the outermost column was pushed laterally along with the soil).
3) Both progressive and retrogressive propagation of shear strains in the embankment and clay.

4) Development of multiple sets of complementary shear bands in the embankment.
5) Development of high shear strains in the upper portion of the clay.
6) Collapse following tensile failure of the geosynthetic, when geosynthetic was included in analysis.

Figure 4-5 illustrates shear strain contours and exaggerated deformations for the base case at increasing embankment heights up to the failure height of 6.1 m. The increase in embankment height resulted in the increasing development of high shear strain regions in the embankment involving multiple sets of complementary shear bands. The increase in embankment height resulted also in the increasing development of high shear strains at the top of the clay. When the embankment reached a height of 6.1 m, the geosynthetic failed in tension between columns 4 and 5, and collapse was initiated. Column flexural tensile failure due to bending moments was calculated in the seven (7) columns closest to the embankment toe, and the exaggerated deformations indicate column failure by bending.

Figure 4-6a to Figure 4-6e show lateral displacements of columns and subsoil in between columns at an elevation corresponding to the top of the clay layer. Lateral displacements were larger closer to the embankment toe (i.e. location 1), and relative movement of the subsoil and columns differed by location. The column closest to the embankment toe (labeled 1) had similar displacements as the subsoil, indicating it was pushed outwards along with the subsoil (Figure 4-6a). Columns 2, 3, and 4 displaced less compared to the subsoil (Figure 4-6b to Figure 4-6d). Columns 1 to 4 were towards the toe from location where the geosynthetic failed. Column 5 had similar lateral displacements as the subsoil (Figure 4-6e), as was also the case for inner columns closer to the centerline.

Retrogressive failure of the columns occurred with the increase in embankment loading, as illustrated by the dash-dot lines in Figure 4-6a to Figure 4-6d for the base case. Columns 1 and 2 failed in flexural tension at an H_{emb} of 1.2 m (4 ft) and 3.0 m (10 ft), respectively. At H_{emb} = 3.0 m, the soil and column lateral movements were approximately the same. A further increase in embankment height led to greater movement in the clay than in the columns and flexural tensile failure of inner columns. Columns 3 and 4 failed at H_{emb} = 4.5 m and 4.9 m, respectively, when lateral displacements in the clay were already greater than in the columns (Figure 4-6c and Figure

4-6d). By H_{fail} = 6.1 m, the seven (7) columns closest to the embankment toe had failed in flexure, though lateral movement in columns 5, 6 and 7 were about the same as in the subsoil. Column flexural tensile failure was also calculated at the elevation corresponding to the contact between the bottom of the clay and the underlying bearing layer. However, it was unlikely the column failure at depth influenced the failure mechanism at the top of the clay layer and in the embankment.

Figure 4-7 illustrates shear strain contours and exaggerated deformations for the base case at failure height with increasing displacements. The increase in displacements resulted in the development of additional shear bands in the embankment as well as an increase in the number of columns that failed in flexural tension due to bending. There were multiple regions in the embankment and foundation with high shear strains and for which shear strains propagated both progressively and retrogressively.

4.5.3. Deformations

The embankment lateral toe displacement in the undrained and dissipated conditions are illustrated in Figure 4-8a and Figure 4-8b, which include embankment deformations up to but excluding failure. The figures show that the lateral toe displacement in the undrained and dissipated conditions were similar, as was also reported in Huang et al. (2019). By placing a geosynthetic with J = 439 kN/m, lateral displacements decreased (base case vs. Scenario 3), and by increasing the geosynthetic J from 439 kN/m to 1459 kN/m, lateral displacements also decreased (Scenario 5 vs. base case).

The total settlement at centerline for the dissipated condition is illustrated in Figure 4-8c. Settlements that occur with excess pore pressure dissipation impact serviceability, and thus they are more important than settlements that occur in the undrained condition prior to consolidation. Figure 4-8c illustrates that for Scenarios 1 to 3, in which each scenario represents a single-parameter change from the base case, the total settlement at any embankment height was influenced by the geosynthetic (Scenario 3), d_{col} (Scenario 2), and S_{col} (Scenario 1) in increasing order of magnitude. Scenario 4, which represents a simultaneous change from the base case in all three parameters, calculated the largest total settlements primarily due to the influence of d_{col} and S_{col}. The total settlement as influenced by geosynthetic J and s_u are illustrated in the comparison

of Scenarios 5 and 6 with the base case. The increase in s_u in Scenario 6 more effectively reduced settlements at any given embankment height. Scenario 7, which represents a simultaneous increase in s_u and J from the base case, calculated the smallest settlements largely due to the influence of s_u.

Figure 4-8a to Figure 4-8c show that the geosynthetic failed in tension in the dissipated condition for embankment heights below the failure height reached during undrained embankment placement. For example, Scenario 1 calculated geosynthetic tensile failure in the undrained condition at an embankment height (H_{emb}) of 5.5 m, and the embankment failed following geosynthetic rupture. During dissipation of excess pore pressures, the geosynthetic failed in tension starting at a H_{emb} of 4.9 m, but the embankment did not collapse. The dissipated analysis was not performed with the embankment placed to 5.5 m because the embankment had already collapsed during undrained loading.

4.5.4. Implications for Design

The geosynthetic influenced both ultimate and serviceability limit states, as determined by comparing the base case (J = 439 kN/m) with Scenario 3 (no geogrid) and Scenario 5 (J = 1459 kN/m), which are scenarios that differ by only the geosynthetic. The geosynthetic influenced the ultimate limit state because it influenced the failure height. Increasing the geosynthetic stiffness (and thus the tensile capacity) increased the failure height (H_{fail}), as shown in Table 4-1 by comparing the base case with Scenario 3, and by comparing Scenario 5 with the base case. The geosynthetic influenced serviceability limit states by reducing lateral displacements and total settlements (Figure 4-8a to Figure 4-8c). Using J = 1459 kN/m (Scenario 5) was more effective in reducing deformations than using J = 439 kN/m (base case).

The geosynthetic improved system ductility, as shown by pre-failure lateral toe displacements in Figure 4-8a. The pre-failure lateral toe displacement is 0.56 m for the base case (J = 439 kN/m) and 0.32 m for Scenario 3 (no geogrid). All scenarios that included geosynthetic reinforcement calculated greater lateral displacements prior to failure than scenarios that did not include geosynthetic reinforcement, even for cases with the same failure height (Scenario 1 versus Scenario 3). These results indicate that inclusion of geosynthetic in design can prevent sudden and catastrophic failures.

The two failure modes found in the current study suggest that the LEM may be inappropriate for evaluating the stability of CSEs supported by unreinforced concrete columns. Calculated failure modes involved complex soil-column interactions and flexural tensile failure in the columns – mechanisms that differ from assumptions of shear strength mobilization, particularly in the unreinforced concrete columns. The LEM also cannot calculate factors of safety for failure occurring on multiple surfaces, but both CSE failure modes occurred by multi-surface shearing in the embankment. Future investigations should use the LEM to calculate factors of safety for CSEs at the failure height to determine whether and to what extent the LEM would be applicable for evaluating CSE stability.

4.6. Summary and Conclusions

The failure height, failure mode, and deformations were computed for eight (8) column-supported embankment (CSE) scenarios using the three-dimensional (3D) finite difference method. The eight scenarios included a base case using typical concrete column design with an area replacement ratio of 2.8%, five single-parameter variations using base case conditions, and two cases with variations in multiple parameters that produced significantly worse and better performance than the base case. Each CSE was incrementally increased in height in the undrained condition with excess pore water pressure development in the clay, followed by dissipation of excess pore pressures, such that the stability was evaluated at different heights both at the undrained end-of-construction and the long-term dissipated conditions. Column properties represented unreinforced concrete, and a Mohr-Coulomb failure criterion was adopted to permit flexural tensile failure in the columns. The geosynthetic reinforcement was modeled using orthotropic linear elastic geogrid elements, whose tensile failure was manually implemented. The transverse geosynthetic strain was calculated for each unit cell bridging columns, and when the strain reached 10%, geogrid elements in the unit cell were removed.

Key findings are as follows:

1) CSE stability was most critical at the undrained end-of-construction condition.
2) Two CSE failure modes were found for the undrained condition:
    a. Mode A involved multi-surface shearing in the embankment coupled with column bending failure and near-circular shear failure through the clay. Failure of columns

initiated closest to the embankment toe and retrogressed towards inner columns with increasing embankment height. As columns failed in bending, lateral displacements in the clay exceeded lateral displacements in the columns.

b. Mode B involved multi-surface shearing in the embankment coupled with column bending failure and shearing within the top portion of the clay. Soil-column interactions were complex, and failure of columns retrogressed towards inner columns. With the increase in embankment height, columns near the embankment toe failed early in construction, followed by clay lateral displacements exceeding those of columns and degradation of inner columns with increasing clay displacement.

3) Where the geosynthetic was present, collapse in the undrained condition occurred after geosynthetic rupture.
4) Geosynthetic rupture in the dissipated condition did not lead to CSE failure.
5) The geosynthetic contributed to both ultimate and serviceability limit states. It allowed construction of taller embankments as well as reduced lateral toe displacements and total settlements at centerline.
6) The geosynthetic increased the system's overall ductility and allowed for greater deformations before failure.
7) Increasing the undrained shear strength of the clay by 9.6 kPa (200 psf) increased the embankment failure height by 6.1 m.
8) The analyses indicate that a CSE could be constructed to a height of 12.8 m (42 ft) without failing for the following conditions: a center-to-center column spacing of 2.4 m (8 ft), a column diameter of 0.46 m (1.5 ft), a layer of geosynthetic with stiffness of 1459 kN/m (100,000 lb/ft) and rupture at 10% strain, and foundation conditions consisting of 0.9 m (3 ft) of existing loose fill overlying 15 m (50 ft) of soft clay with an undrained shear strength of 14.4 kPa (300 psf) at the top and increasing with depth at a rate of 1.7 kPa/m (11 psf/ft).

Results indicate that the limit equilibrium method (LEM) is inappropriate for evaluating stability of CSEs under conditions like those considered here. The calculated failure modes involved column flexural tensile failure and complex column-soil interactions, and this is inconsistent with the assumption of shear failure in the LEM. In addition, the factor of safety calculated using the LEM is for a single critical slip surface, whereas 3D numerical analyses calculated shearing on

multiple surfaces in the embankment. Alternative simplified approaches for CSE stability evaluation should be explored until 3D numerical analyses are used more routinely in practice.

Notation

The following symbols are used in this chapter:

a = edge length of square column cross-section;

c = cohesion;

c' = effective cohesion;

d = vertical deflection of geosynthetic reinforcement;

d_{col} = column diameter;

E = Young's modulus;

e_1 = void ratio at reference pressure;

f'_c = unconfined compressive strength;

f'_r = flexural tensile strength (modulus of rupture);

G = shear modulus;

H_{crit} = critical height;

H_{emb} = embankment height;

H_{fail} = embankment failure height;

J = geosynthetic stiffness (in longitudinal and transverse directions);

M = slope of critical state line;

p'_i = initial mean effective stress;

p'_o = preconsolidation pressure;

S_{col} = center-to-center column spacing;

s_u = undrained shear strength;

α = angle of shear failure surface from vertical;

Γ = specific volume at unit mean effective stress on critical state line;

γ = unit weight;

ΔS_{col} = change in center-to-center column spacing;

ε_{lat} = unit cell transverse strain in geogrid due to lateral spreading;

ε_{trans} = unit cell transverse strain in geogrid;

ε_{vert} = unit cell transverse strain in geogrid due to vertical deflection;

κ = slope of recompression line;

λ = slope of virgin compression line;

ν = Poisson's ratio;

σ = normal stress;

σ_t = tensile strength;

τ = shear stress;

υ_λ = specific volume at unit mean effective stress on normal compression line;

φ = friction angle; and

φ' = effective friction angle.

References

ACI (2011). "318-11: Building Code Requirements for Structural Concrete and Commentary." *Section 9.5.3.2*, American Concrete Institute, Farmington Hills, Michigan.

Adams, T. E. (2011). "Stability of Levees and Floodwalls Supported by Deep-Mixed Shear Walls: Five Case Studies in the New Orleans Area." Doctor of Philosophy, Department of Civil and Environmental Engineering, Virginia Polytechnic Institute and State University.

Ariyarathne, P., Liyanapathirana, D. S., and Leo, C. J. (2013). "Effect of geosynthetic creep on reinforced pile-supported embankment systems." *Geosynthetics International*, 20(6), 421-435.

BSI (2010). "BS 8006-1:2010 Code of practice for strengthened/reinforced soils and other fills." *Design of embankments with reinforced soil foundations on poor ground*, British Standards Institution, London.

BSI (2016). "BS 8006-1:2010+A1:2016 Code of practice for strengthened/reinforced soils and other fills." *Design of embankments with reinforced soil foundations on poor ground*, British Standards Institution, London.

Cancelli, A., Rimoldi, P., and Togni, S. "Frictional characteristics of geogrids by means of direct shear and pull-out tests." *Proc., International Symposium on Earth Reinforcement Practice*, 29-34.

Cazzuffi, D., Picarelli, L., Ricciuti, A., and Rimoldi, P. (1993). "Laboratory investigations on the shear strength of geogrid reinforced soils." *Geosynthetic Soil Reinforcement Testing Procedures*, ASTM International, 119-137.

Chai, J. C., Shrestha, S., Hino, T., and Uchikoshi, T. (2017). "Predicting bending failure of CDM columns under embankment loading." *Computers and Geotechnics*, 91, 169-178.

Tensar International Corporation (2015). "Product Specification Tensar Biaxial Geogrid." <https://www.tensarcorp.com/Systems-and-Products/Tensar-Biaxial-BX-geogrids>. (2015).

Duncan, J. M., Wright, S. G., and Brandon, T. L. (2014). *Soil Strength and Slope Stability*, Wiley, New Jersey.

Eun, J., Gupta, R., and Zornberg, J. G. (2017). "Effect of Geogrid Geometry on Interface Resistance in a Pullout Test." *Geotechnical Frontiers 2017*, Orlando, Florida, 236-246.

Griffiths, D. V., and Lane, P. A. (1999). "Slope stability analysis by finite elements." *Géotechnique*, 49(3), 387-403.

Han, J., and Gabr, M. A. (2002). "Numerical Analysis of Geosynthetic-Reinforced and Pile-Supported Earth Platforms over Soft Soil." *Journal of Geotechnical and Geoenvironmental Engineering*, 128(1), 44-53.

Huang, J., and Han, J. (2009). "3D coupled mechanical and hydraulic modeling of a geosynthetic-reinforced deep mixed column-supported embankment." *Geotextiles and Geomembranes*, 27(4), 272-280.

Huang, Z., Ziotopoulou, K., and Filz, G. M. (2018). "Numerical Predictions of Deformations in Geosynthetic-Reinforced Column-Supported Embankments: Validation of Manual Dissipation of Excess Pore Pressure Approach for Undrained and Drained Analyses." *IFCEE 2018: Innovations in Ground Improvement for Soils, Pavements, and Subgrades*, GSP 296, 327-336.

Huang, Z., Ziotopoulou, K., and Filz, G. M. (2019). "3D Numerical Limiting Case Analyses of Lateral Spreading in a Column-Supported Embankment " *Journal of Geotechnical and Geoenvironmental Engineering*, 145(11), 04019096.

Huesker (2019). "Product Overview." <https://www.huesker.us/fileadmin/Media/Brochures/US/Product_Overview_Geosynthetics_GB.pdf>. (2019).

Inagaki, M., T., A., Yamamoto, M., Nozu, M., Yanagawa, Y., and Li, L. (2012). "Behavior of cement deep mixing columns under road embankment." *Proc., Physical modeling in Geotechnics: ICPMG'02*, 967-972.

INOVA Geosynthetics (2017). "Geoter® F Range High Strength Reinforcement Geocomposites." <http://www.inova-geo.com/high-strength-reinforcement.html>. (2019).

Itasca. 2012. FLAC3D, version 5.01, Minneapolis, MN.

Itasca (2013). *FLAC3D Theory and Background*, Itasca Consulting Group Inc., Minneapolis, Minnesota.

Itasca (2013). *Structural Elements*, Itasca Consulting Group Inc., Minneapolis, Minnesota.

Jamsawang, P., Voottipruex, P., Boathong, P., Mairaing, W., and Horpibulsuk, S. (2015). "Three-dimensional numerical investigation on lateral movement and factor of safety of slopes stabilized with deep cement mixing column rows." *Engineering Geology*, 188, 159-167.

King, J. D., Bouazza, A., Gniel, J. R., Rowe, R. K., and Bui, H. H. (2018). "Geosynthetic reinforced column supported embankments and the role of ground improvement installation effects." *Canadian Geotechnical Journal*, 55, 792-809.

Kitazume, M., and Maruyama, K. (2007). "Centrifuge model tests on deep mixing column failure under embankment loading." *Advances in Deep Foundations*, Kikuchi, Otani, Kimura, and Morikawa, eds., Taylor & Francis Group, London, 379-383.

Liao, X., Ye, G., and Xu, C. (2009). "Friction and Passive Resistance of Geogrid in Pullout Tests." *Advances in Ground Improvement: Research to Practice in the United States and China*, 252-259.

Liu, C., Ho, Y., and Huang, J. (2009). "Large scale direct shear tests of soil/PET-yarn geogrid interfaces." *Geotextiles and Geomembranes*, 27(1), 19-30.

McGuire, M. P. (2011). "Critical Height and Surface Deformation of Column-Supported Embankments." Doctoral Dissertation, Department of Civil and Environmental Engineering, Virginia Polytechnic Institute and State University.

Navin, M. P. (2005). "Stability of Embankments Founded on Soft Soil Improved with Deep-Mixing-Method Columns." Doctor of Philosophy, Department of Civil and Environmental Engineering, Virginia Polytechnic Institute and State University, Blacksburg, Virginia.

Plomteux, C., and Lacazedieu, M. (2007). "Embankment construction on extremely soft soils using controlled modulus columns for Highway 2000 project in Jamaica." *16th Southeast Asian Geotechnical Conference*, K. Yee, O. T. Aun, T. W. Hui, and C. S. Fatt, eds. Kuala Lumpur, 533-539.

Potyondy, J. G. (1961). "Skin friction between various soils and construction materials." *Geotechnique*, 11(4), 339-353.

Pul, S., Ghaffari, A., Öztekin, E., Hüsem, M., and Demir, S. (2017). "Experimental Determination of Cohesion and Internal Friction Angle on Conventional Concretes." *ACI Materials Journal*, 114(3), 407-416.

Santacruz Reyes, K. J. (2016). "Geosynthetic Reinforced Soil: Numerical and Mathematical Analysis of Laboratory Triaxial Compression Tests." Ph.D. Dissertation, Department of Civil and Environmental Engineering, Virginia Polytechnic Institute and State University.

Schädlich, B., and Schweiger, H. (2014). "Internal report shotcrete model: Implementation validation and application of the shotcrete model." Plaxis, Delft.

Schaefer, V. R., Berg, R. R., Collin, J. G., Christopher, B. R., DiMaggio, J. A., Filz, G. M., Bruce, D. A., and Ayala, D. (2017). "Ground Modification Methods Reference Manual - Volume II." FHWA, Washington, D. C.

Shrestha, S., Chai, J. C., Bergado, D. T., Hino, T., and Kamo, Y. (2015). "3D FEM investigation on bending failure mechanism of column inclusion under embankment load." *Lowland Technology International*, 17(3), 157-166.

SHRP2 (2012). "Column-Supported Embankments." <http://www.GeoTechTools.org>.

Sloan, J. A. (2011). "Column-Supported Embankments: Full-Scale Tests and Design Recommendations." Doctoral Dissertation, Department of Civil and Environmental Engineering, Virginia Tech.

Sloan, J. A., Filz, G. M., Collin, J. G., and Kumar, P. (2014). "Column-Supported Embankments: Field Tests and Design Recommendations (2nd Edition)." Virginia Tech Center for Geotechnical Practice and Research, Blacksburg, VA.

Wood, D. M. (1990). *Soil Behaviour and Critical State Soil Mechanics*, Cambridge University Press, Cambridge.

Yapage, N. N. S., Liyanapathirana, D. S., Poulos, H. G., Kelly, R. B., and Leo, C. J. (2013). "Analytical Solutions to Evaluate Bending Failure of Column Supported Embankments." *International Journal of Engineering and Technology*, 502-507.

Zanzinger, H., and Gartung, E. (2002). "Performance of a geogrid reinforced railway embankment on piles." *7th ICG*, Delmas, Gourc, and Girard, eds., Swets & Zeitlinger, Lisse, 381-386.

Zhang, C., Jiang, G., Liu, X., and Buzzi, O. (2016). "Arching in geogrid-reinforced pile-supported embankments over silty clay of medium compressibility: Field data and analytical solution." *Computers and Geotechnics*, 77, 11-25.

Zhang, J. S., Guo, C., and Xiao, S. W. (2012). "Analysis of Effect of CFG Pile Composite Foundation Pile Spacing on Embankment Stability Based on Centrifugal Model Tests." *Applied Mechanics and Materials*, 178, 1641-1648.

Zhang, Z., Han, J., and Ye, G. (2014). "Numerical Analysis of Failure Modes of Deep Mixed Column-Supported Embankments on Soft Soils." *ASCE Ground Improvement and Geosynthetics*, GSP 238, 78-87.

Zhuang, Y., and Wang, K. Y. (2015). "Three-dimensional behavior of biaxial geogrid in a piled embankment: numerical investigation." *Canadian Geotechnical Journal*, 52(10), 1629-1635.

Tables

Table 4-1. Scenario parameters and ultimate limit state.

Scenario	Parameters				Ultimate Limit State		
	S_{col} (m)	d_{col} (m)	J (kN/m)	s_u (kPa)	H_{fail} (m)	Critical Condition	Failure Mode
base case	2.4	0.46	438	4.8	6.1	undrained	B – Multi-surface shearing in the embankment coupled with column bending failure and shearing in the top portion of the clay (Figure 4-5)
1	3.0				5.5	undrained	A – Multi-surface shearing in the embankment coupled with column bending failure and near-circular shear failure in the clay (Figure 4-3)
2		0.36			6.4	undrained	B
3			0 (no geogrid)		5.5	undrained	B
4	3.0	0.36	0 (no geogrid)		4.0	undrained	A
5			1459		8.5	undrained	B
6				14.4	12.2	undrained	B
7			1459	14.4	(>12.8)	N/A	The embankment was constructed to an upper bound height of 12.8 m without failing.

Note: Blank cells contain values corresponding to the base case; s_u is for top of clay layer.

Table 4-2. Material properties of soils and columns.

Material	γ (kN/m^3)	Model	φ' (°)	c' (MPa)	σ_t (MPa)	E (MPa)	ν	λ	κ	M	e_1
Embankment Fill (Sand)	18.9	MC	37, 30[a]	0		24, 6[a]	0.28				
LTP (Gravel)	21.2	MC	40, 30[a]	0		36, 6[a]	0.26				
Foundation Fill (Sand)	18.1	MC	34	0		14	0.31				
Clay	16.5	MCC					0.37	0.17	0.017	0.98	2.57
Bearing Sand	22.8	MC	45	0		72	0.23				
Concrete Column	23.6	MC	43	3.7	1.6	21,500	0.20				

Note: MC = Mohr-Coulomb; MCC = Modified Cam Clay; e_1 is the void ratio at a reference pressure of 0.048 kPa (1 psf).
[a] Reduced material property values adopted for loosened zones in the dissipated analyses.

Table 4-3. Material properties of geosynthetic reinforcement.

Model	J (kN/m)	ν	G (kPa)
Orthotropic Linear Elastic	438, 1459	0	1

Note: J and ν apply to both longitudinal and transverse directions.

Figures

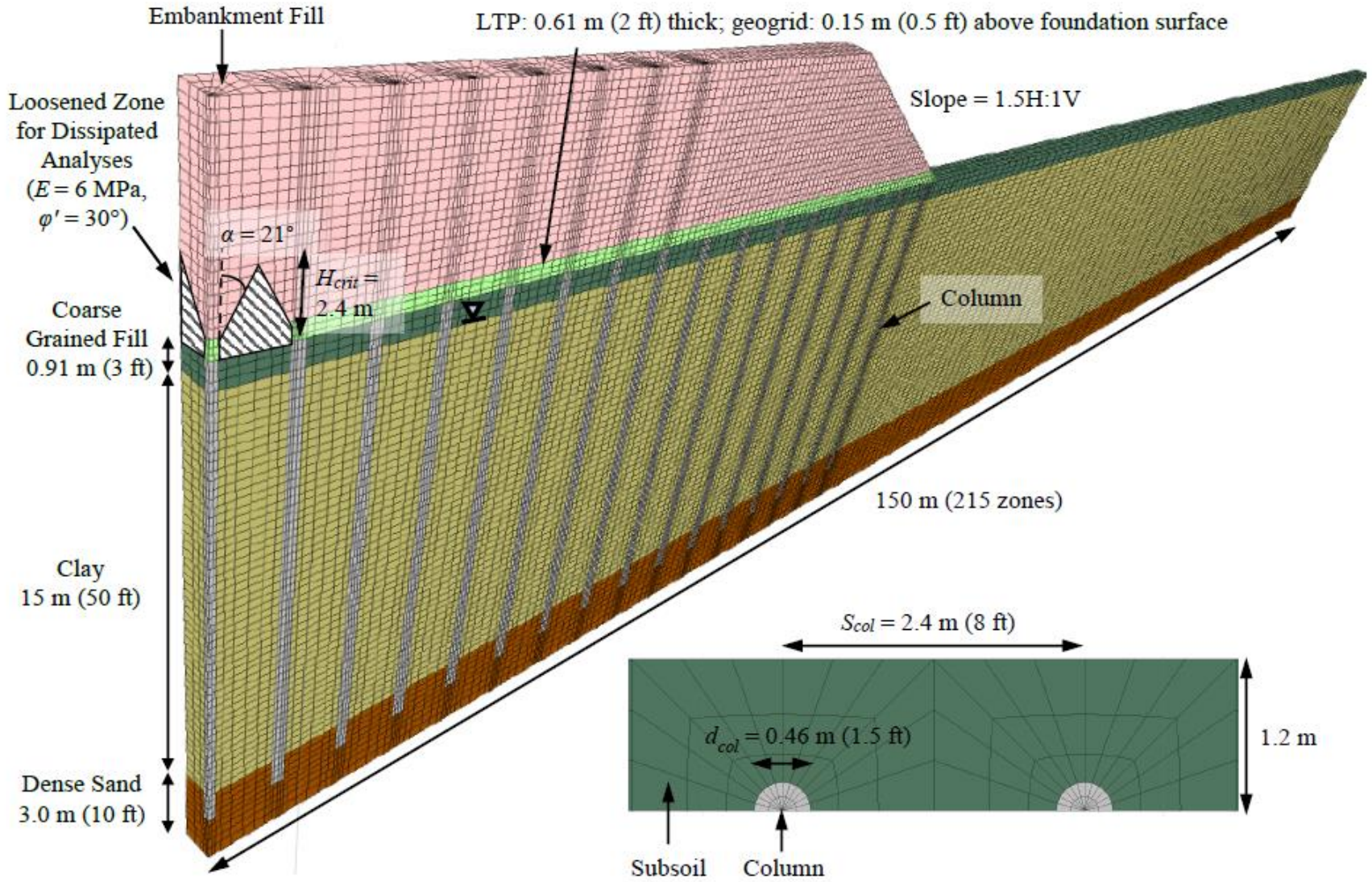

Figure 4-1. Schematic of base case CSE.

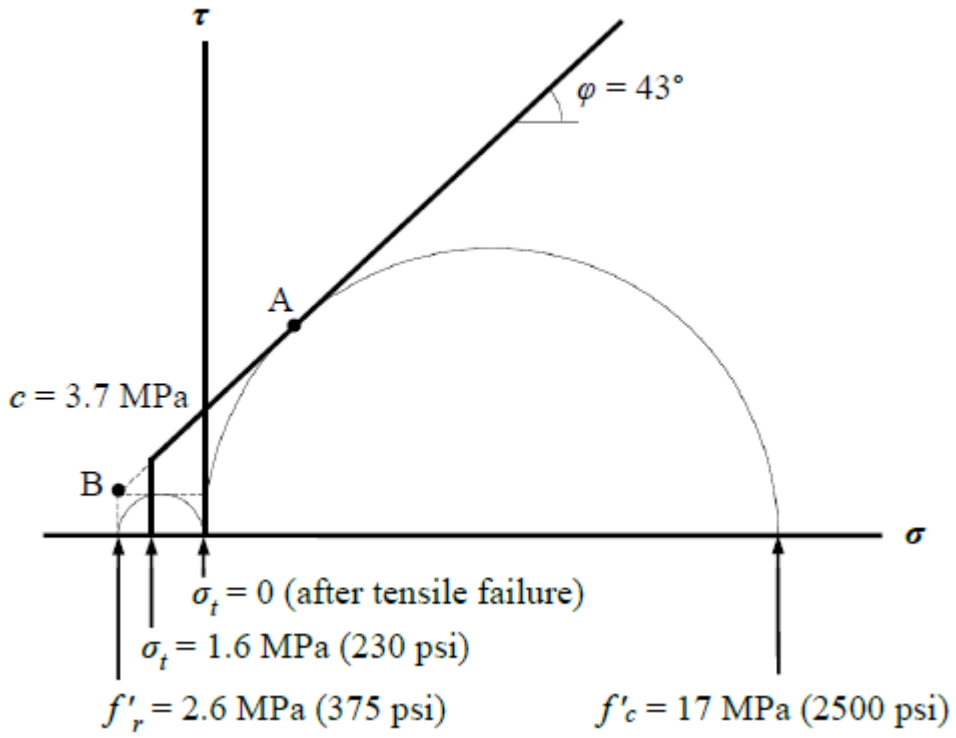

Figure 4-2. Failure envelope of unreinforced concrete as adopted for columns.

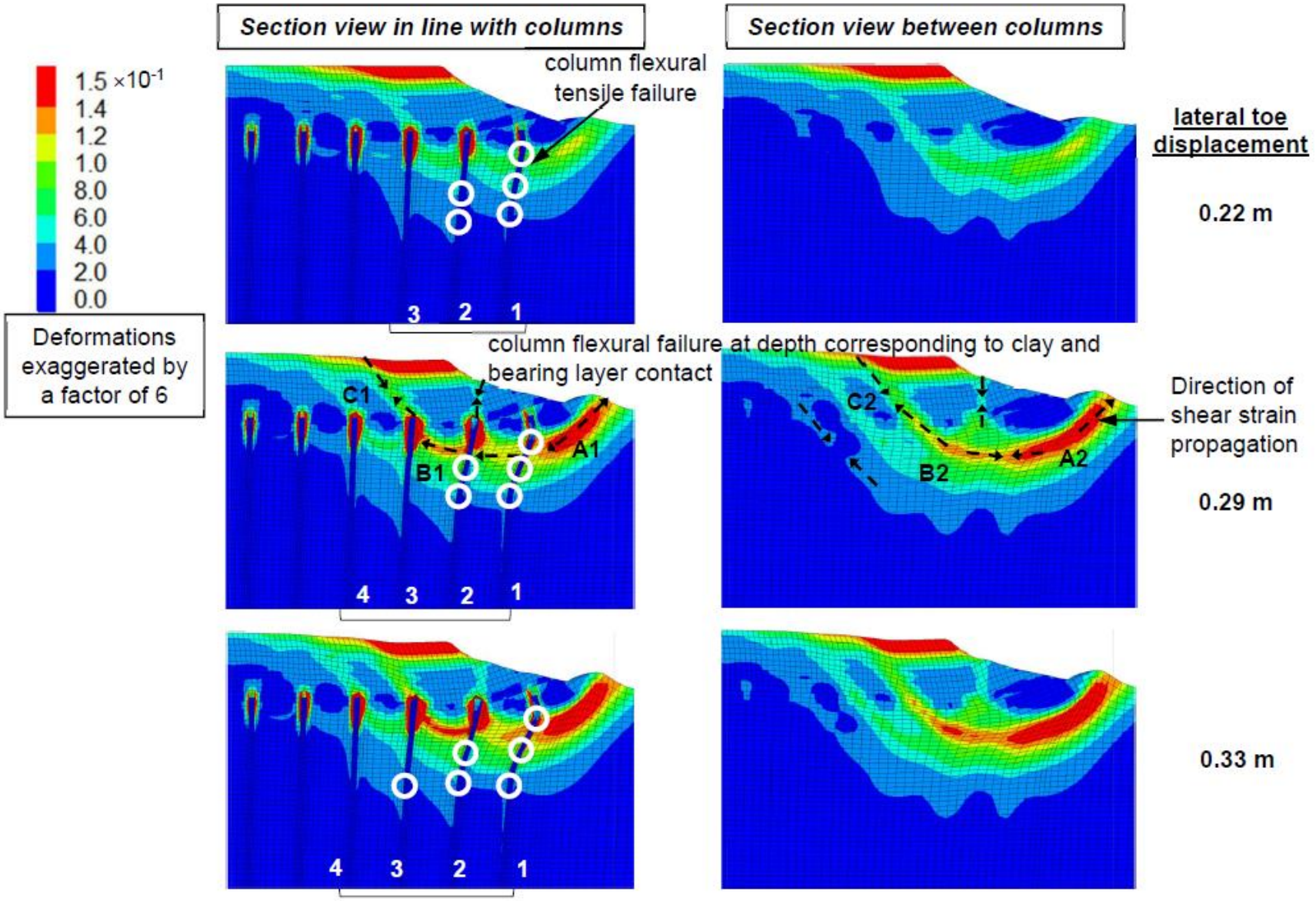

Figure 4-3. Propagation of failure in Scenario 4 at H_{fail} = 4.0 m via shear strain contours and exaggerated deformations.

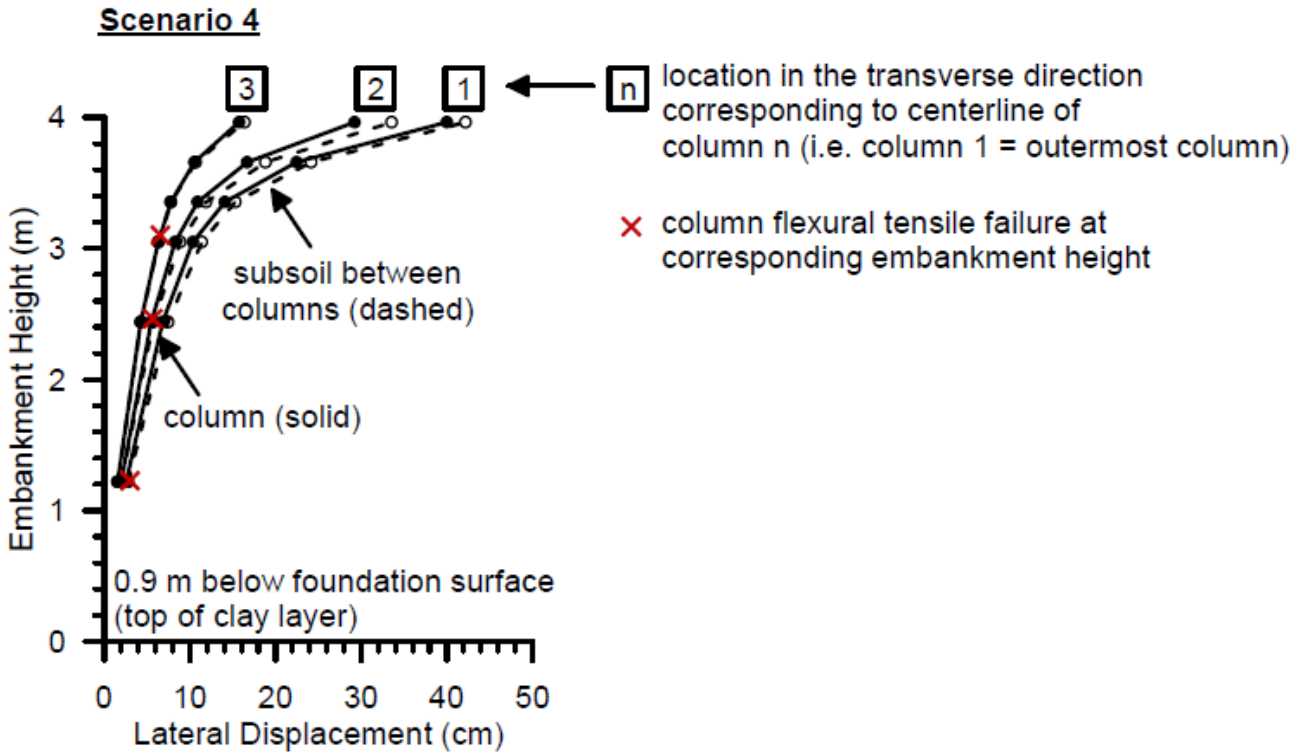

Figure 4-4. Scenario 4 lateral displacements in columns and in subsoil between columns for embankment heights up to and including failure height.

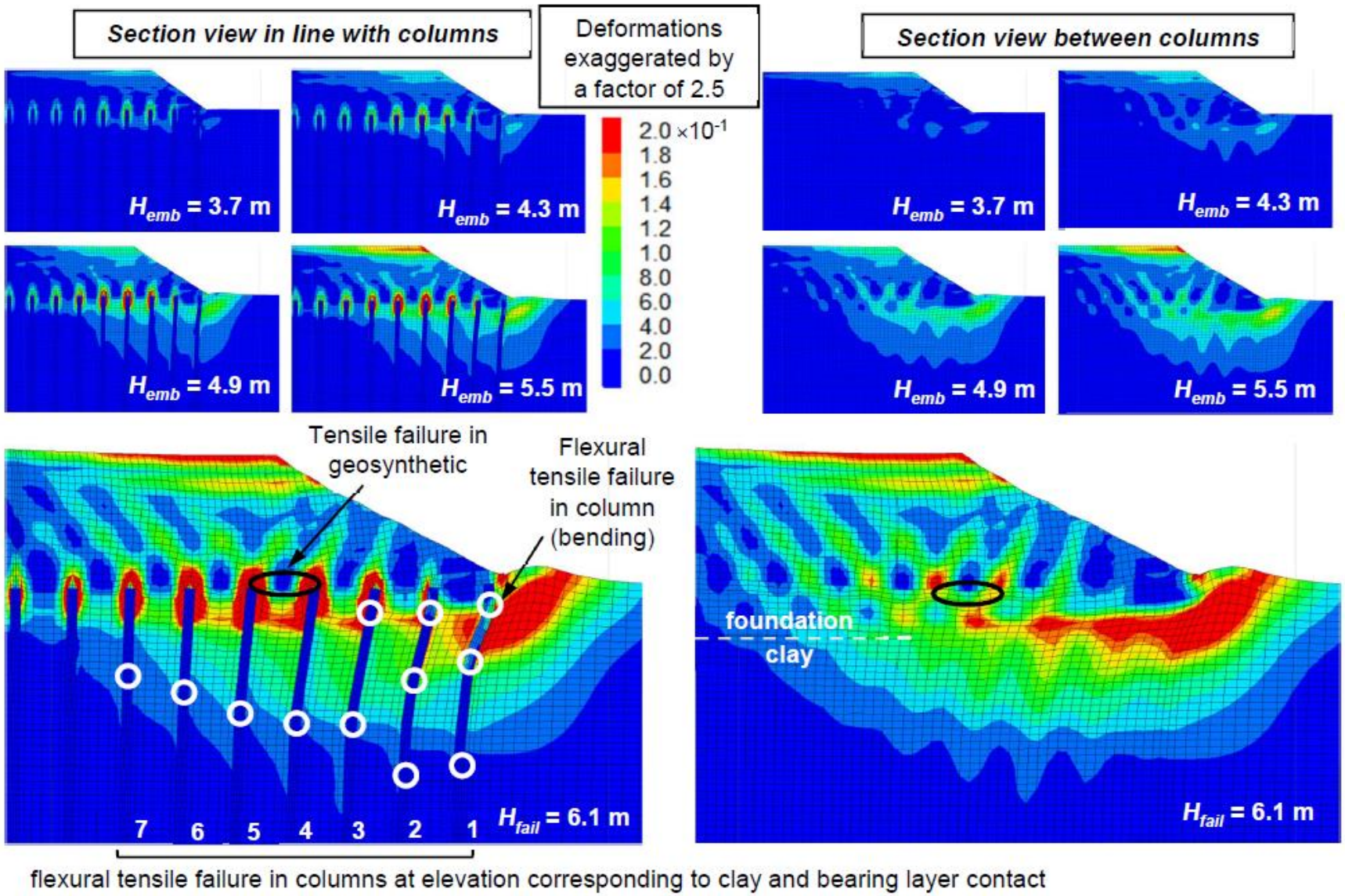

Figure 4-5. Shear strain contours and exaggerated deformations for the base case at increasing embankment heights.

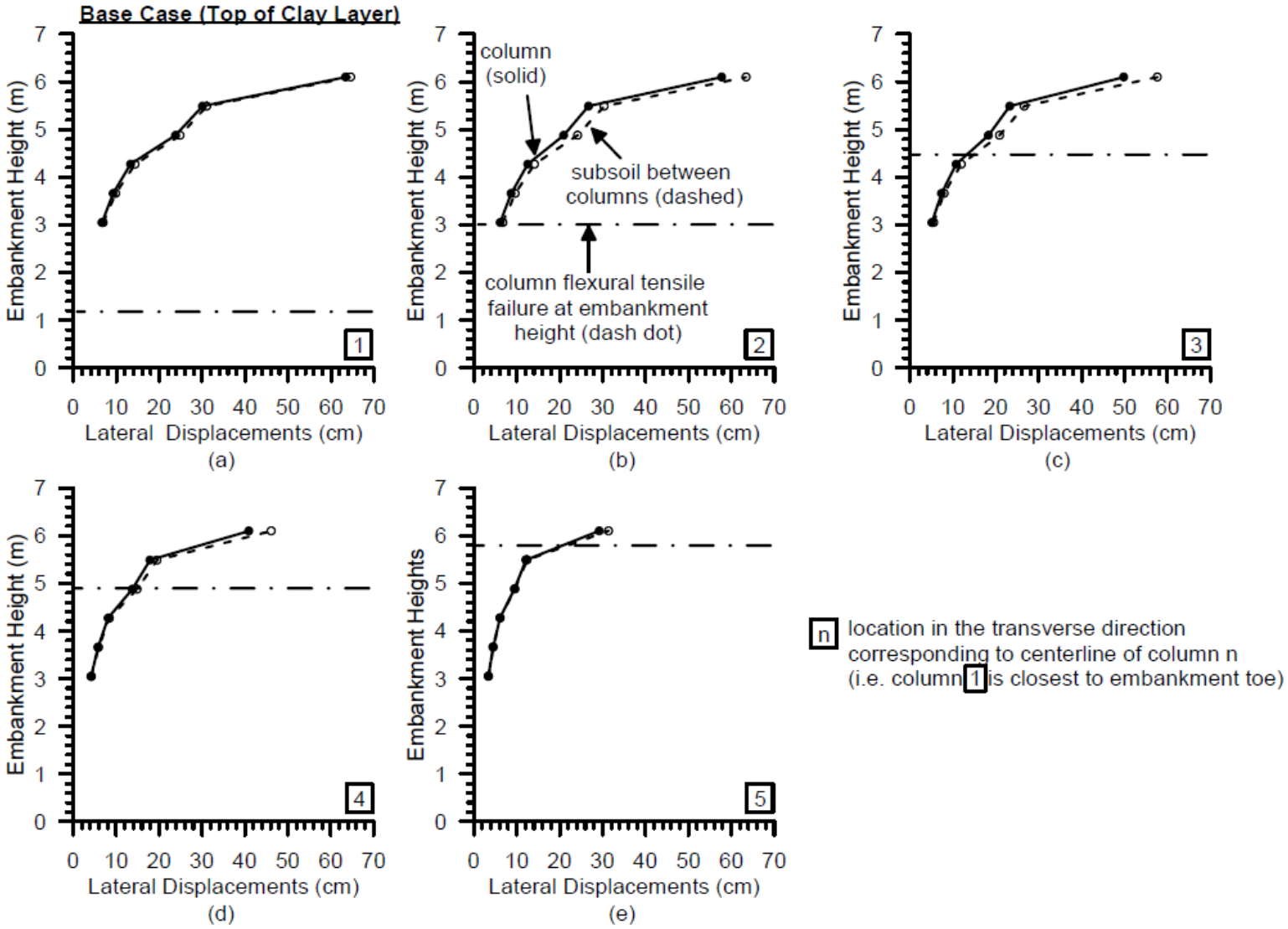

Figure 4-6. Base case lateral displacements in columns and in subsoil between columns for embankment heights up to and including failure height.

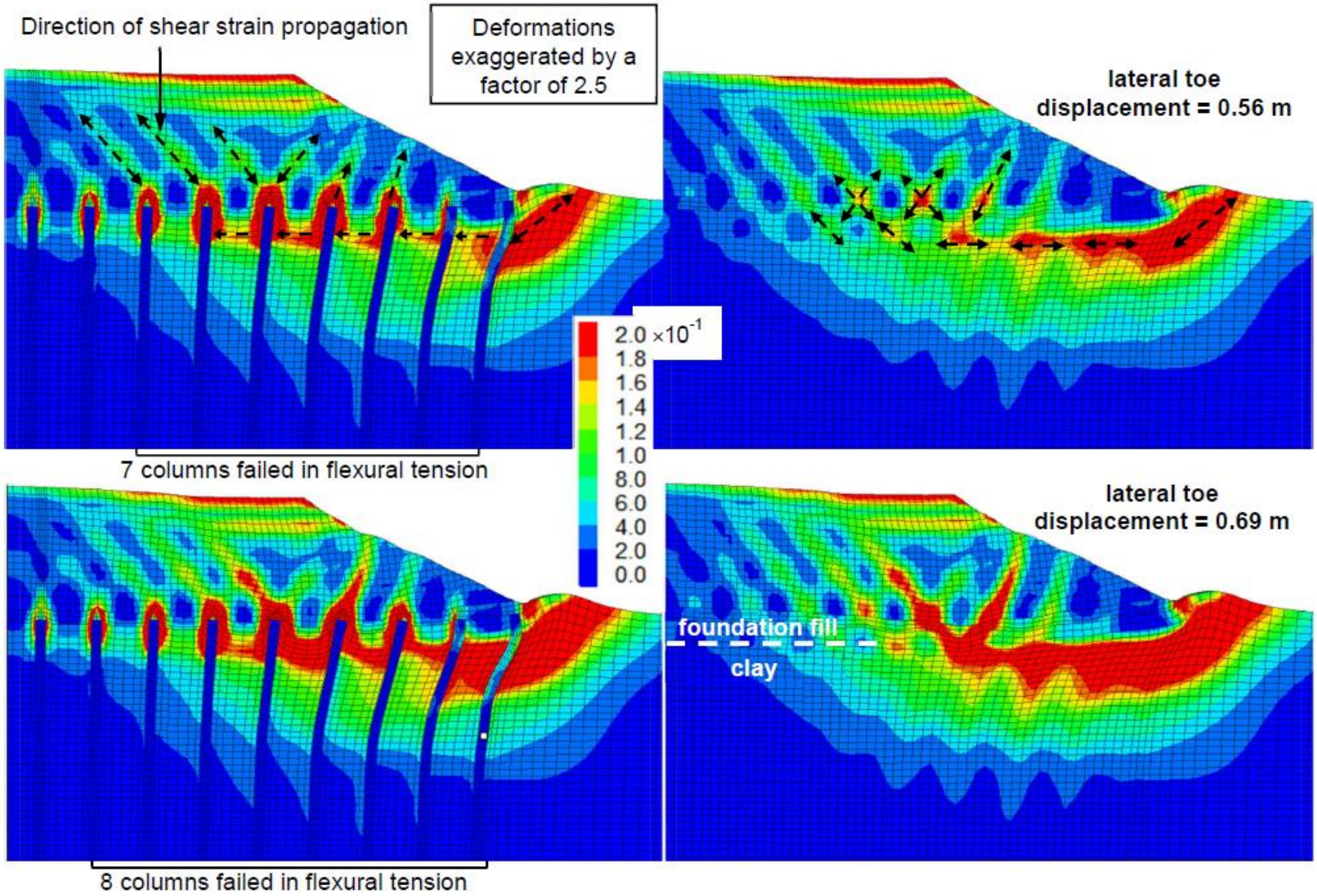

Figure 4-7. Shear strain contours and exaggerated deformations for base case at H_{fail} = 6.1 m showing propagation of shear strains.

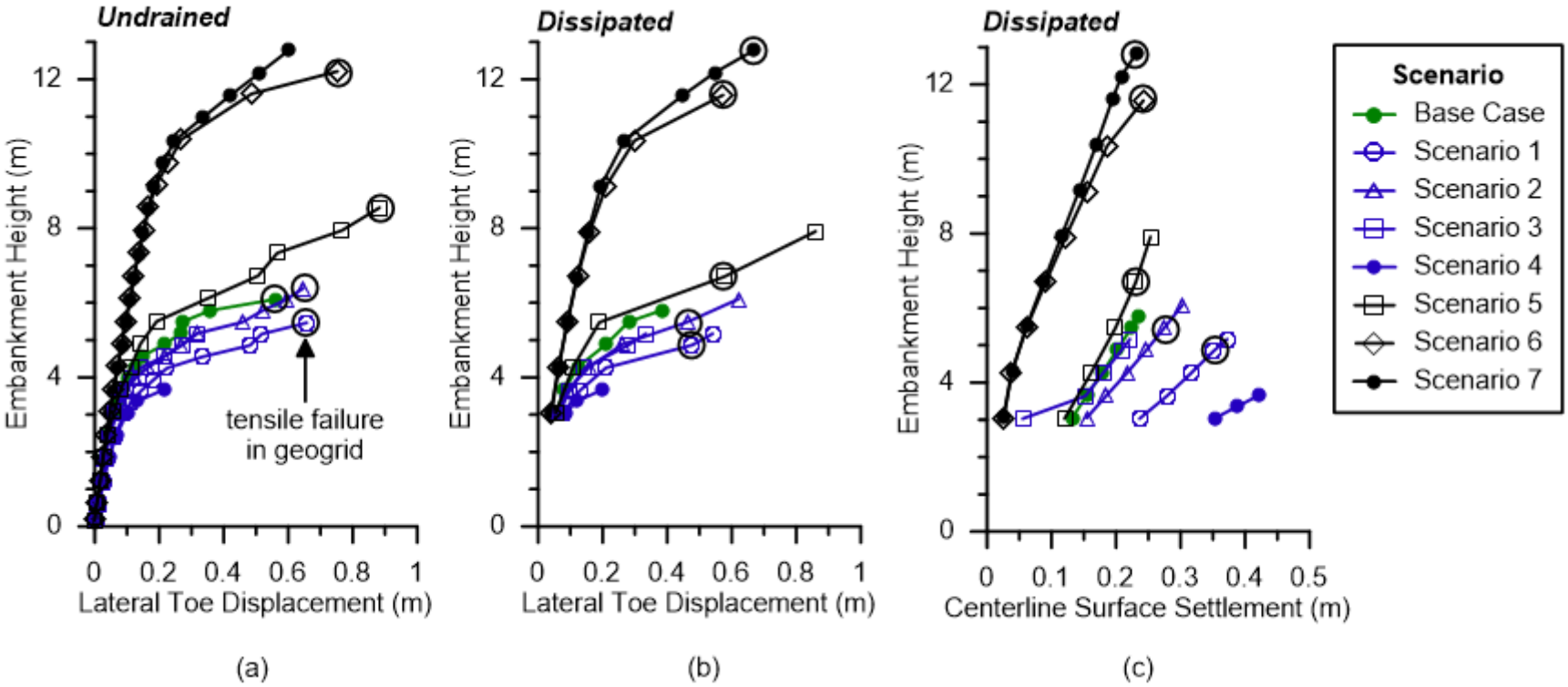

Figure 4-8. Embankment height versus pre-failure deformations in terms of a) lateral toe displacement in the undrained condition; lateral toe displacement in the dissipated condition; and c) centerline surface settlement in the dissipated condition.

CHAPTER 5. SUMMARY, CONCLUSIONS, AND DESIGN GUIDANCE

Lateral spreading of column-supported embankments (CSEs) was investigated using the finite difference method in three-dimensional numerical analyses. The research was motivated by uncertainties in CSE design, specifically concerning resistance to lateral loads provided by geosynthetic reinforcement in the load transfer platform (LTP) and by unreinforced concrete columns, e.g. vibro-concrete columns, which are frequently used for embankment support. Details include the distribution of lateral loads in the embankment and foundation, the combined effects of vertical load transfer and lateral spreading on geosynthetic tension, the bending moments in the concrete columns, and the CSE failure modes involving column bending failure and geosynthetic tensile failure.

The research consisted of five main components:

1) Unit validation studies were conducted to understand and validate the response of individual components within the larger embankment model. These studies include comparison with benchmark solutions to validate consolidation deformations calculated using an "undrained-dissipated" approach, in which a load was applied to a saturated clay soil without drainage, and then the resulting excess pore water pressures were dissipated. Good agreement was reached for cases of one-dimensional consolidation and consolidation under load of limited lateral extent.
2) The numerical modeling procedures were calibrated using CSE case history recordings as documented by Liu et al. (2007), using both unit cell and half-embankment model geometries. The undrained-dissipated approach was adopted for analyzing the response at the end of construction and after long-term dissipation of excess pore water pressures. The unit cell model was applied first for the calibration of vertical load transfer in terms of settlements and vertical load distribution at the subgrade level. Softening of select embankment zones was found to be necessary for modeling the long-term behavior of soil arching, in which fill above the subsoil between columns experiences shear strains, decreases in normal stress, and loosening. The geometry of these loosened zones was related to the effective friction angle (φ') of the fill, using a relationship developed from

bench-scale CSEs (McGuire 2011). The properties of the loosened zones were calibrated by simultaneously reducing the Young's modulus (E) and φ' until differential settlements and vertical load distribution at the subgrade level were in agreement with long-term case history recordings. The same calibrated property values and geometry of loosened zones were applied to all subsequent calculations of the long-term dissipated condition. Following unit cell analyses, the half-embankment geometry was employed, and recompression indices of the clay layers were calibrated to match inclinometer measurements at the embankment toe. The calibrated half-embankment model was in good agreement with Liu et al. (2007) case history recordings in terms of vertical load distribution, settlements, and lateral displacements. The half-embankment model was then used for additional analyses of lateral earth pressures in the foundation, geosynthetic strains, and column bending moments.

3) A parametric study was conducted to examine the lateral thrust distribution in 128 CSE scenarios involving a variety of conditions. For each scenario, the undrained end-of-construction state and the long-term dissipated state were computed. The lateral thrust distribution in the embankment, foundation, and geosynthetic were examined for each state at different embankment locations (i.e., on vertical planes at the centerline, shoulder, and toe). Correlations for thrust magnitude were obtained.
4) Substructure analyses using refined discretization were performed to analyze local strain effects in the geosynthetic, specifically above column edges where the largest strains occur. The goal was to investigate the coupling effect of vertical load transfer and lateral spreading on geosynthetic tension and strain. The study was limited by mesh zone geometry errors, which resulted from zones undergoing significant distortions under the large strains that were computed.
5) Failure analyses were conducted for eight scenarios involving a base case, five single-parameter variations from the base case conditions, and two multi-parameter variations from the base case conditions. In each scenario, the embankment height was gradually increased until failure was calculated in either the undrained or dissipated condition. Comparisons were made for the constructible embankment height, lateral toe displacement, and centerline surface settlement. Descriptions were provided for the different failure mechanisms.

The numerical analyses led to the following advances in understanding CSE lateral spreading mechanics:

1) The critical condition for lateral spreading analysis is undrained end-of-construction.
    a. When CSE system collapse occurs, it happens during undrained conditions, before dissipation of excess pore pressures. This was established by analyzing each scenario at increasing embankment heights, first computing the deformations in the undrained condition and then with excess pore pressures dissipated for each embankment height. Many scenarios experienced CSE system collapse as the embankment height increased under undrained conditions. In no case did an embankment that was stable under undrained conditions become unstable as a result of dissipating excess pore pressures, even when consolidation of the foundation soils increased vertical deflection in the geosynthetic and produced rupture of the geosynthetic.
    b. Lateral thrust in CSEs is distributed among the embankment, foundation, and geosynthetic. Compared to the dissipated condition, the undrained condition showed the following: (1) larger magnitudes of driving thrust, which resulted from larger incremental lateral earth pressures in the foundation; (2) larger mobilization of passive earth pressures in the foundation at the embankment toe; (3) larger mobilization of shear stresses at the top of the bearing stratum; and (4) smaller mobilization of resisting geosynthetic tension.
    c. The lateral thrust in the embankment from the numerical analyses was generally larger than the value determined from Rankine lateral earth pressure theory. The embankment thrust from the numerical analyses most closely approached the Rankine value for marginally stable cases in the undrained condition.
    d. In the undrained condition, total lateral thrust decreases in magnitude with increasing distance from the centerline, commensurate with a system tendency to laterally displace away from the centerline.
2) Two failure modes were found for the undrained condition:
    a. In mode A, multiple shear bands develop in the embankment, and they converge into a near-circular failure surface in the clay.

b. In mode B, multiple complementary sets of shear bands develop in the embankment, and high shear strains develop in the upper portion of the clay.
c. Modes A and B have the following characteristics in common: (1) embankment collapse occurs following geosynthetic rupture; (2) column bending failure initiates in the outermost column and retrogresses to inner columns; and (3) shear strains propagate progressively and retrogressively in the embankment and foundation soils.

3) Unreinforced concrete columns using typical designs failed in bending (i.e., flexural tension) for most cases examined. Columns closer to the embankment toe failed at embankments heights that were much lower than produced CSE system collapse. This occurred because outer columns sustain the largest bending moments but the smallest axial compression under embankment loading. However, columns that failed in bending were still capable of supporting vertical embankment loads.
4) Geosynthetic reinforcement allows for construction of taller embankments. The contribution is greater for geosynthetics with larger tensile capacities.
5) Geosynthetic inclusion increases system ductility.
6) Geosynthetic strain is largest in the dissipated condition but geosynthetic rupture in the dissipated condition does not lead to collapse.
7) Geosynthetic contribution to mitigating lateral spreading is a function of geosynthetic stiffness:
    a. Higher stiffness geosynthetics can resist a larger percentage of lateral thrust through development of tension. One to three layers of geosynthetics with stiffness of 300 kN/m per layer resisted at most 2% and 7% of the total driving thrust in the undrained and dissipated conditions, respectively, whereas the corresponding distributions in geosynthetics with stiffness of 8000 kN/m per layer were 16% and 50%.
    b. Higher stiffness geosynthetics are more effective for reducing lateral displacements.
8) The undrained shear strength of the clay foundation soil significantly impacts embankment failure height.

Although a simplified design procedure was not developed, the following guidance is provided based on findings from this research:

1) Calculation of column bending moments does not appear to be necessary. Unreinforced concrete columns can be expected to fail in flexural tension even when using typical column designs for embankment heights much lower than the failure height. The columns that failed in bending were still capable of supporting vertical loads.
2) Because geosynthetic tensile rupture in the long-term condition (after excess pore pressure dissipation) does not produce collapse of the CSE system, it does not appear necessary to combine the effects of vertical load transfer and lateral spreading to design the geosynthetic for the purpose of preventing CSE system collapse.
3) Inclusion of geosynthetic in CSE design improves system ductility and contributes to preventing sudden and catastrophic failures during rapid embankment construction.
4) Some guidance that may be useful to CSE designers is provided regarding lateral thrust distribution (Figures 3-3a and 3-3b, Figures 3-4a and 3-4b, and Figures 3-6a to 3-6f), embankment failure heights (Table 4-1), and deformations (Figures 4-8a to 4-8c).
5) Global stability of CSEs constructed using unreinforced concrete columns should not be evaluated using conventional limit equilibrium analyses of slope stability with the shear strength of the concrete represented by area-weighted averaging. Soil-column interactions are complex and columns fail in bending rather than shear. In addition, failure modes entail shearing on multiple surfaces in the embankment rather than shearing on a single critical surface.

Further research on CSEs is recommending in the following areas:

1) A comprehensive suite of conventional limit equilibrium slope stability analyses should be performed for the CSE scenarios in this research that resulted in system collapse. Such analyses would demonstrate quantitatively the extent to which limit equilibrium stability analyses can overstate the factor of safety against collapse of CSEs supported on unreinforced concrete columns. Such research could be extended to consider other column types.
2) A practical and comprehensive design procedure should be developed for CSEs supported on unreinforced concrete columns. Such a procedure should provide quantitative guidance

regarding the effects of geosynthetic reinforcement on decreasing system deformations and increasing the embankment height that would cause system collapse.

3) Guidance for CSEs with vertical faces provided by mechanically stabilized earth (MSE) walls should be developed. CSEs with MSE walls are used in practice, and they are expected to have lower collapse heights than the embankments with sloped faces that were considered in this research.
4) Although the technique used in this research to represent the combined effect of consolidation settlement and lateral spreading on geosynthetic strains is considered safe, it would be informative to pursue detailed numerical analyses of localized strain effects where the geosynthetic passes over the top of columns. The discrete element method and the material point method are approaches that could be considered in light of the large deformations that occur over short distances in this region. Higher order geogrid elements could also be considered.

APPENDIX A. UNIT VALIDATIONS

The lateral spreading analysis of column-supported embankments (CSE) using three-dimensional (3D) numerical modeling requires construction of a relative large and complex half-embankment model. This model should at a minimum capture effects of soil arching, subsoil consolidation, undrained distortions, and interactions of the soil with geosynthetic reinforcements and columns. An understanding of the numerical procedure and model behavior is required prior to the assembly of a large and complex numerical model. Numerical results should be validated using analytical or benchmark solutions where available. Unit validation studies serve these purposes by targeting the analysis of specific model behaviors using relatively small numerical domains.

A total of 26 unit validation studies were conducted. These are broadly categorized, as follows.

- Behavior of geosynthetic reinforcement and its interactions with soil
- Column-soil interactions via interface elements
- Structural pile elements (Itasca 2013)
- Constitutive models and behavior under different loading paths
- Consolidation (APPENDIX B)

The following sections describe the individual unit validation studies, including the rationale, procedure, and numerical results.

A.1. Geosynthetic Reinforcement

Geosynthetic reinforcement is included in CSE design to increase vertical load transfer to columns and to resist lateral spreading. Mechanisms of interest include its participation in the membrane effect, where tension develops under out-of-plane loading, as well as its participation in resisting lateral thrust. Under the coupling of vertical and lateral loads, the geosynthetic may fail in tension, resulting in an increase of load transferred to the weak subsoil.

Geosynthetic reinforcement was modeled using geogrid structural elements of the Constant Strain Triangle (Itasca 2013) type. These elements can sustain membrane stress but not bending. Each element has three nodes, with two translational degrees-of-freedom per node and rigid attachment

in the direction normal to the element plane. Interactions with the soil is modeled using Coulomb frictional springs at the nodes. The elements are linear elastic, and both the isotropic and orthotropic models were investigated. The latter is representative of biaxial geogrids, which have stiffness mainly in orthogonal directions.

The numerical representation of geosynthetic reinforcement was validated for its response under out-of-plane deformation, its frictional resistance at the geogrid-soil interface, and its stress-strain response when assigned properties of orthotropic linear elasticity.

A.1.1. Deformation and Tension under Out-of-Plane Loading

Validation of the geosynthetic response under out-of-plane loading involved two steps. The first step was to determine the minimum element discretization required to obtain calculation convergence. The second step was to compare numerical calculations to analytical solutions.

For determining the required discretization, a 10 m by 10 m geogrid was subjected to an out-of-plane uniform pressure of 100 Pa. Analyses were conducted in FLAC3D large-strain mode, which was required for the development of tension under out-of-plane loading. The geogrid was isotropic linear elastic and had properties as tabulated below. Edges were pinned. Three discretizations of increasing refinement were investigated.

Table A-1. Geogrid properties used in out-of-plane loading test.

Young's Modulus (*E*)	**Poisson's Ratio (*v*)**	**Thickness (m)**	**Density (kg/m^3)**
5.745x10^8 Pa	0.25	0.00254	0.65

Initial findings indicate that displacements and tensions were relatively insensitive to discretization, as shown in the following table. Thus, subsequent unit validations used a geogrid discretization of 20 by 20 elements or 2 elements per 1 m of distance.

Table A-2. Geosynthetic deflection and tension under self-weight and out-of-plane uniform pressure (total pressure of 100.0162 Pa)

	Geogrid Element Discretization		
	10 x 10	**20 x 20**	**40 x 40**
Maximum Deflection (m)	0.2617	0.2615	0.2611
Tension at Center (Pa)	1.142×10^6	1.132×10^6	1.132×10^6

The calculated geogrid response under out-of-plane loading was compared to the analytical solution provided in Young and Budynas (2001). This solution is for large deflection of plates, where the deflection needs to be greater than half the plate thickness. For the case of a circular plate without flexural stiffness, subjected to a uniform distributed load, and with edges held, the following equations were used to approximate the deflection and the tension at the plate center:

$$\frac{q\alpha^4}{Et^4} = K_1 \frac{y}{t} + K_2 (\frac{y}{t})^3 \qquad \text{(A.1)}$$

$$\frac{\sigma\alpha^2}{Et^2} = K_3 \frac{y}{t} + K_4 (\frac{y}{t})^2 \qquad \text{(A.2)}$$

Where,

E = elastic modulus = 5.745×10^8 Pa

K_1 = 0.0

K_2 = 3.44

K_3 = 0.0

K_4 = 0.965

q = pressure = 100.0162 Pa

t = plate thickness = 0.00254 m

y = maximum deflection

α = plate outer radius = 5 m

σ = plate stress (bending and diaphragm, where diaphragm stress is 0 without flexural stiffness)

The formulation does not account for effects of the Poisson's ratio (v), but reasonable agreement between the numerical and analytical solutions was obtained when v = 0.3 was used (i.e. steel), as tabulated below.

Table A-3. Geosynthetic deflection and tension under out-of-plane pressure: comparison with Young and Budynas (2001) using ν = 0.3.

	Young and Budynas (2002)	**Numerical**	**Difference (%)**
Maximum Deflection (m)	0.232	0.233	0.430
Tension at Center (Pa)	1.19 x 10^6	1.16 x 10^6	-2.61

The analytical solution for an elastic catenary (Irvine 1981) was also used for validating the geosynthetic response under out-of-plane loading. An elastic catenary is an elastic cable that deflects under its own weight. Using Irvine's (1981) solution, the horizontal and vertical reactions at the two cable ends were first calculated (Equation A.3), then the cable tension (Equation A.4), and finally the vertical displacement at any point along the cable (Equation A.5).

$$\sinh\left(\frac{Wl}{2HL_o} - \frac{W}{2EA_o}\right) = \frac{W}{2H} \qquad \text{(A.3)}$$

$$T(s) = \{H^2 + (V - W\frac{s}{L_o})^2\}^{1/2} \qquad \text{(A.4)}$$

$$z(s) = \frac{Ws}{EA_o}\left(\frac{V}{W} - \frac{s}{2L_o}\right) + \frac{HL_o}{W}\left[\left\{1 + (\frac{V}{H})^2\right\}^{\frac{1}{2}} - \left\{1 + \left(\frac{V - \frac{Ws}{L_o}}{H}\right)^2\right\}^{\frac{1}{2}}\right] \qquad \text{(A.5)}$$

Where,

A_o = unit cross-sectional area of the unstrained profile = 0.00254 m^2

E = elastic modulus = 5.745 x 10^8 Pa

H = horizontal reaction at the two cable ends resting at the same elevation

L_o = unstrained cable length = 10 m

l = cable span = 10 m

V = vertical reaction at the two cable ends resting at the same elevation

W = cable weight = 0.16 N/m

s = unstrained distance from one cable end

z = vertical displacement

The elastic catenary was simulated using a plane strain geogrid model, which had dimensions of 10 m by 100 m, a ν = 0, and was loaded under gravity to result in deflection under its own weight. The length of the geogrid (i.e. 100 m) was determined using a convergence study. Agreement with the analytical solution was obtained, as shown below.

Table A-4. Geosynthetic deflection and tension under out-of-plane pressure: comparison with analytical solution for the elastic catenary (Irvine 1981).

	Irvine (1981)	**Numerical**	**Difference (%)**
Maximum Deflection (m)	0.0173	0.0174	0.564
Tension (N)	11.7	11.6	-0.566

In summary, the numerical response of the geosynthetic reinforcement under out-of-plane loading was validated against two analytical solutions and reached agreement with both.

A.1.2. Frictional Response of Geosynthetic-Soil Interface

A geosynthetic pull-out test was conducted to verify that the force required to cause slip at the geosynthetic-soil interface is equal to the interface shear resistance. As the geogrid elements were formulated to interact with adjacent soil zones at only one face, there was concern that the interface shear resistance was equal to only half the expected resistance. For the unit validation, the geogrid was wedged between two soil blocks and was pulled using two approaches (described below). A schematic of the pull-out test is illustrated.

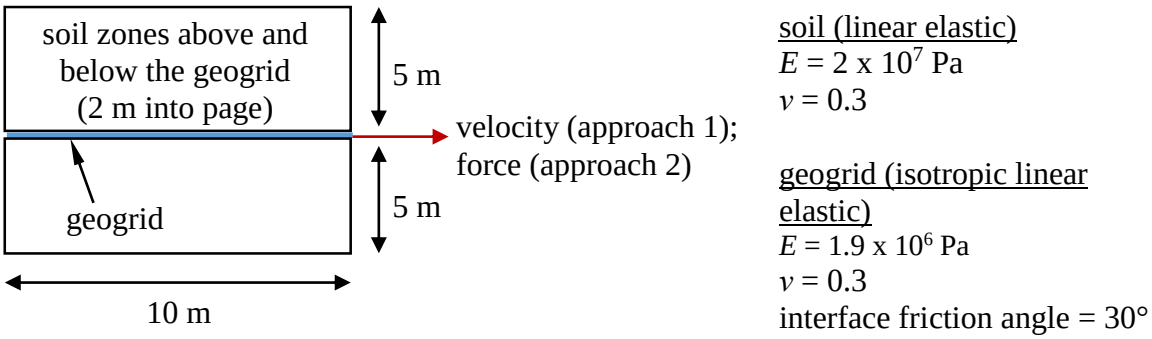

Figure A-1. Schematic of geogrid pull-out test.

Boundary conditions were as follows. The geogrid was free to move as no boundary conditions were imposed. Large-strain mode was employed to facilitate sliding of the geogrid. Soil zones were imposed with rollers on all external faces.

Two pull-out approaches were tested. The first approach was strain-controlled and was used to validate interface shear stresses. Loading consisted of initializing a compressive normal stress of 100 Pa in all soil zones and turning off gravity to discount the soil weight. A constant velocity of 1×10^{-6} m/s was applied at all geogrid nodes. The shear stress in a coupling spring at mid-geogrid

was tracked. The expected shear stress under 100 Pa normal stress was 57.7 Pa, and the shear stress in the spring was 56.0 Pa. There was some variation in the spring shear stress across the geogrid, especially at the edges, but the majority of the springs had shear stresses in the range of 55 Pa to 60 Pa. The second pull-out approach was stress-controlled and was used to validate the pull-out force. A force was applied at all nodes on one edge of the geogrid. The pull-out force represented one that initiated slip along the entirety of the geogrid-soil interface. Under 100 Pa confining stress, the expected pull-out force was 2309 N, which accounted for shear resistance on two interfaces. The pull-out force that facilitated geogrid movement in the numerical model was approximately 1135 N or about half the expected.

In summary, shear stresses at the geosynthetic-soil interface were calculated correctly, but the interaction was limited to only one interface.

A.1.3. Orthotropic Linear Elasticity

The orthotropic linear elastic model is applicable for modeling biaxial geogrids, which have stiffness mainly in orthogonal directions. Under plane stress conditions (e.g. membrane loading), the orthotropic stress-strain response has the following formulation:

$$\begin{Bmatrix} \sigma_x \\ \sigma_y \\ \tau_{xy} \end{Bmatrix} = \begin{bmatrix} c_{11} & c_{12} & 0 \\ & c_{22} & 0 \\ sym. & & G \end{bmatrix} \begin{Bmatrix} \epsilon_x \\ \epsilon_y \\ \gamma_{xy} \end{Bmatrix} \qquad \text{(A.6)}$$

$$c_{12} = \frac{E_y \nu_x}{1-\nu_x \nu_y} = \frac{E_x \nu_y}{1-\nu_x \nu_y} \qquad \text{(A.7)}$$

$$c_{11} = \frac{E_x}{1-\nu_x \nu_y} \qquad \text{(A.8)}$$

$$c_{22} = \frac{E_y}{1-\nu_x \nu_y} \qquad \text{(A.9)}$$

Where,

E_x, E_y = Young's modulus in the direction as indicated by the subscript

G = shear modulus

γ_{xy} = shear strain

ϵ_x, ϵ_y = strain due to normal stress in the direction as indicated by the subscript

ν_x, ν_y = Poisson's ratio in the direction as indicated by the subscript

σ_x, σ_y = normal stress in the direction as indicated by the subscript

τ_{xy} = shear stress

A series of studies was conducted to validate the stress-strain response of the orthotropic linear elastic geogrid implementation in FLAC3D. The geogrid had dimensions of 1 m by 1 m and 4 elements spanning orthogonal directions. Geogrid properties and study results are tabulated below. Note that geogrid properties were modeled after the biaxial geogrid, BX1500 (Tensar International Corporation 2015), but there was uncertainty in the shear modulus, G. Santacruz Reyes (2016) reached the same conclusion regarding shear moduli of geosynthetics but found that the parameter insignificantly impacted the calculated response of reinforced soils subjected to triaxial loading. For the purpose of unit validation, G was assumed to be 1/3 of the average Young's modulus.

Table A-5. Properties of orthotropic linear elastic geogrid elements as adopted in unit validation studies

Stiffness in Machine Direction, J_x (kN/m)	**Stiffness in Cross Machine Direction, J_y (kN/m)**	**Thickness (m)**	**Poisson's Ratio in Machine Direction, ν_x**	***G* (kPa)**
425	500	0.002	0.3	77000

Table A-6. Stress-strain validation of orthotropic linear elastic geogrid elements

Validation Test	Boundary and Loading Conditions	Results
Pull geogrid in x-direction, check stress in x-direction and c_{11}.	Rollers were placed on one edge perpendicular to the x-direction and on both edges perpendicular to the y-direction. A constant x-velocity was applied to nodes on the free edge to pull the geogrid.	At ϵ_x = 0.01, ϵ_y = 0: σ_x = 2.38 x 10^6 Pa $c_{11} = \sigma_x/\epsilon_x$ = 2.38 x 10^8 Pa (correct)
Pull geogrid in y-direction, check stress in y-direction and c_{22}.	Rollers were placed on one edge perpendicular to the y-direction and on both edges perpendicular to the x-direction. A constant y-velocity was applied to nodes on the free edge to pull the geogrid.	At ϵ_y = 0.01, ϵ_x = 0: σ_y = 2.80 x 10^6 Pa $c_{22} = \sigma_y/\epsilon_y$ = 2.80 x 10^8 Pa (correct)
Pull geogrid in both x- and y-directions in equal magnitudes, check stresses in both directions and c_{12}.	Constant velocities were applied on all edges until reaching pre-determined strains.	At $\epsilon_x = \epsilon_y$ = 0.01: σ_x = 3.22 x 10^6 Pa σ_y = 3.64 x 10^6 Pa $c_{12} = \sigma_x/\epsilon_x - c_{11}$ $= \sigma_y/\epsilon_y - c_{22}$ = 8.39 x 10^7 Pa (correct)
Investigate the influence of G on the tension developed during out-of-place loading.	Pins were applied on all boundaries. A uniform pressure of 10 kPa was applied on the geogrid.	At G = 10000 kPa: Maximum membrane stress = 5.21 x 10^6 Pa Maximum deflection = 0.0879 m At G = 77000 kPa: Maximum membrane stress = 5.41 x 10^6 Pa Maximum deflection = 0.0869 m At G = 200000 kPa: Maximum membrane stress = 5.96 x 10^6 Pa Maximum deflection = 0.0850 m

Using a smaller shear modulus resulted in a smaller membrane stress and a larger deflection, as expected, and the variation was small for the range of moduli investigated. Results also point to conservatism in vertical load transfer analysis if the orthotropic geogrid were modeled using a very low shear modulus.

The last unit validation study involving the orthotropic linear elastic geogrid elements was to compare the stress-strain response for an orthotropic geogrid assigned equivalent isotropic properties with calculations using the isotropic formulation. Reported CSE case history values were used (Liu et al. 2007): J = 1180 kN/m and ν = 0.3. A shear modulus (G) was calculated using Equation A.10. The validation study involved applying pins at all edges and a uniform pressure of 40 kPa on the geogrid. Agreement between the two geogrid formulations was obtained for the membrane stress and deflection, as shown in Table A-7.

$$G = \frac{E}{2(1+\nu)} \qquad \text{(A.10)}$$

Table A-7. Comparison of out-of-plane loading response using orthotropic geogrid with isotropic properties and isotropic geogrid

	Maximum Membrane Stress (Pa)	**Maximum Deflection (m)**
Orthotropic formulation with isotropic properties	6.95 x 10^6	0.104
Isotropic formulation	6.95 x 10^6	0.104

In summary, the stress-strain response of orthotropic linear elastic geogrid elements was validated. As there was uncertainty in the shear modulus, the parameter was varied to examine its effect on the geogrid response under out-of-plane loading. A small shear modulus may be adopted for orthotropic geogrid elements for conservative analysis of vertical load transfer.

A.2. Interface Elements for Column-Soil Interactions

Interface elements can be used to represent planes of slip and separation. Mechanisms that involve slip and that are of interest to lateral spreading analysis of CSEs include soft soil extrusion around columns and column-soil differential settlement. Thus, numerical models adopted in the research have included interface elements on the column shaft. Interface elements were also included at column tops and bases due to geometric constraints in zone construction.

A broad overview of the FLAC3D v.5.01 interface element formulation (Itasca 2013) is provided, as follows. Interface elements are one-sided, and the zone surface over which they wrap can interact with any other zone surface that comes into contact. Contact takes places at interface

nodes, and there are three nodes per interface element. Nodal contact is characterized by the Coulomb shear-strength criterion and by normal and shear stiffnesses.

Interface elements were validated through two studies: (1) as slip was expected at the column-soil interface, the interface shear strength was validated; (2) the behavior of interface slip around corners and zone edges was investigated.

A.2.1. Interface Shear Strength

To validate the Coulomb shear strength criterion of interface elements, a cylinder consisting of linear elastic zones and wrapped by 1560 interface elements on the shaft was pushed out from surrounding linear elastic zones, akin to removing a plug. The cylinder was 1 m in length, 0.5 m in diameter, and 1.57 m^2 in shaft area. Shaft interface elements had a cohesion of 100 Pa, such that 157 N was the expected load to initiate pushout. Rollers were applied on all external surfaces of zones surrounding the cylinder to prevent displacement. All zones were initialized with 100 Pa of confining pressure, and this normal stress was not expected to influence the cohesion-only interface shear strength. A velocity of gradually increasing magnitude was applied at grid points on one end of the cylinder. At initiation of cylinder movement, the unbalanced forces at the aforementioned grid points were summed to obtain the pushout load, which was 149 N. The 5% underestimate was likely due to the reduction in contact surface area as the cylinder moved during large-strain mode. In summary, the calculated pushout load was in reasonable agreement with the expected pushout load.

A.2.2. Interface Slip Around Zone Edges

A column wrapped by interface elements on the shaft was pushed laterally into surrounding soil. The purpose of this unit validation was to investigate whether interface elements can enable slip around edges and lateral flow of soil around columns. A model schematic is shown in Figure A-2. The zone discretization was relatively coarse, and the column circumference was polygonal rather than circular, with vertical edges around which the soil zones had to slip.

Material properties are listed in Table A-8. Soil zones were assigned the Modified Cam Clay model. Column zones were assigned the linear elastic model with properties representing concrete.

Interface elements were assigned values of normal and shear stiffnesses equal to ten (10) times the apparent stiffness of adjacent soil zones (Itasca 2013). Interfaces had a low friction angle of 10°.

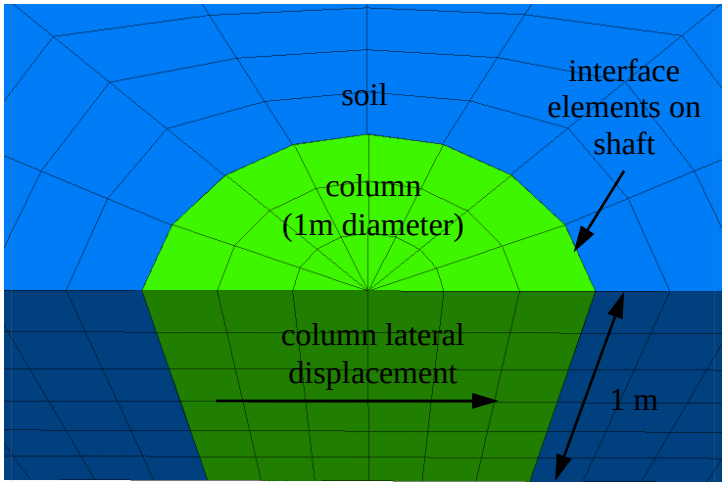

Figure A-2. Model schematic of column lateral load test

Table A-8. Material model and properties for column and soil in column lateral load test

	Constitutive Model	***λ***	***κ***	***M***	**Preconsolidation pressure**	***ν***	***E* (GPa)**
Soil	Modified Cam Clay	0.06	0.012	1.2	Normally consolidated	0.35	-
Column	Linear Elastic	-	-	-	-	0.2	20

Where,

E = Young's modulus

M = slope of critical state line

κ = slope of recompression line

λ = slope of virgin compression line

ν = Poisson's ratio

Boundary and loading conditions were as follows. Rollers were applied on all external surfaces. Gravity was turned off, and all zones were initialized to a confining pressure of 10 kPa. A constant velocity of 1×10^{-7} m/s was applied on all column grid points, and the column was displaced laterally by 14 mm. Large-strain mode was adopted.

Figures below illustrate the slippage of soil around column edges and the differences in lateral displacement between the two materials. These figures point to relative movement, where interface locking did not occur.

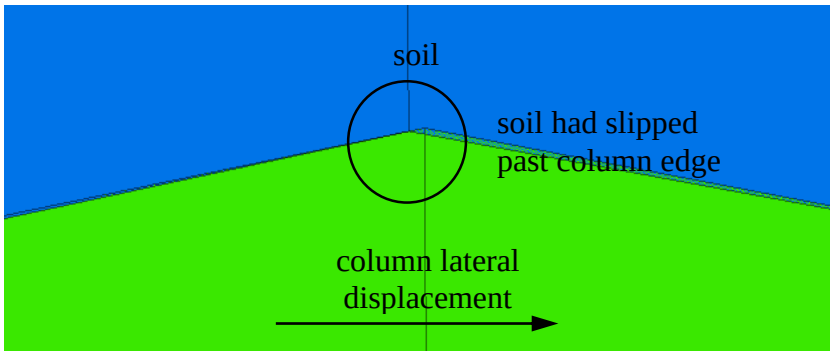

Figure A-3. Soil slippage around column edge (i.e. along shaft) after column lateral displacement.

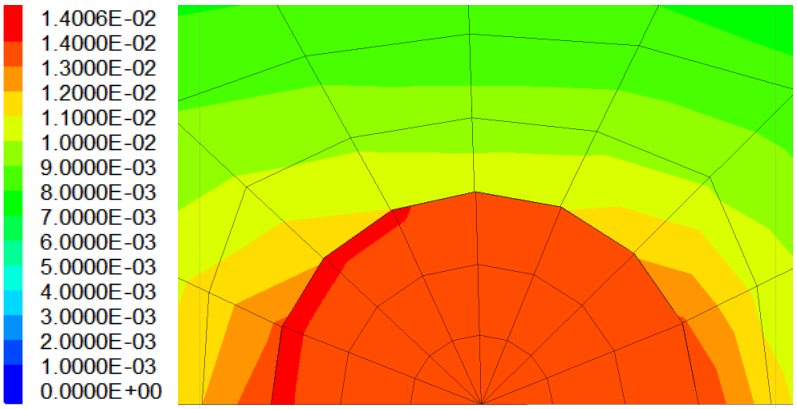

Figure A-4. Lateral displacement contours of laterally loaded column and surrounding soil.

A.3. Pile Elements

Structural pile elements (Itasca 2013) were adopted for the analysis of column tensile stresses. Under the combination of axial loads and bending moments, tensile stresses can develop in columns and lead to flexural failure of columns types weak in tension (e.g. unreinforced concrete). Structural pile elements have the capability of automatically calculating axial loads and bending moments under different conditions of loading and displacement. The procedure for calculating column tensile stresses using structural pile elements consisted of (1) exporting displacements calculated along the centerline of column zones in the half-embankment model, (2) imposing the

displacements on corresponding isolated structural pile elements (i.e. not surrounded by zones), (3) solving for mechanical equilibrium in the pile elements (i.e. solving for the axial loads and bending moments), and (4) summing stresses from axial loading and bending at different elevations along the column for calculating the outer fiber stress profile. While stresses can also be extrapolated from the centroid of column zones in a half-embankment model, the aforementioned procedure using structural pile elements is preferred as it does not require extrapolation.

A broad overview of the structural pile element formulation is provided, as follows. Each pile element consists of a linear segment with uniform cross-sectional properties and two end nodes. Properties of the pile elements are linear elastic, with options to include a plastic moment capacity and rockbolt logic (e.g. tensile failure strain, axial tensile yield strength, shear coupling springs, confining stress). Pile elements can be joined at the nodes to form a column. The nodes are locations for applying boundary conditions, such as loads and displacements. Each node has 12 degrees-of-freedom. Pile elements can interact with grid points on zones through nodal coupling springs, but this capability was not utilized in the research.

Axial loads and bending moments automatically calculated by structural pile elements were validated using two different loading conditions in a 10 m long, weightless pile consisting of 50 pile elements and 51 nodes. For the first loading condition, the pile was fixed at one end and left free at the other (i.e. cantilever), and was applied with a uniformly distributed lateral load of 100 kN/m. For the second loading condition, the pile had the same boundary conditions as in the first, but was applied with a lateral point load of 1 kN at the free end. Calculated maximum displacements and bending moments were compared to analytical solutions (Table A-9). Equations A.11 and A.12 are the analytical solutions for the maximum displacement (δ_{max}) and bending moment (M_{max}) in a cantilever beam (length, L) subjected to a uniformly distributed loading (W). Equations A.13 and A.14 are the analytical solutions for the maximum displacement and bending moment in a cantilever beam subjected for a point load (P). Note that results were relatively insensitive to the pile element discretization in the range of 10 to 100 pile elements.

$$\delta_{max} = \frac{WL^4}{8EI} \quad \text{(A.11)}$$

$$M_{max} = \frac{WL^2}{2} \quad \text{(A.12)}$$

$$\delta_{max} = \frac{PL^3}{3EI} \quad \text{(A.13)}$$

$$M_{max} = PL \quad \text{(A.14)}$$

Where,

E = Young's modulus

I = second moment of inertia

Table A-9. Comparison of pile element calculations to analytical solutions

		Analytical	**Numerical (pile element)**	**Percent Difference (%)**
Uniformly distributed load applied on cantilever	δ_{max} (m)	0.85	0.0849	0.12
	M_{max} (Nm)	5 x 10^6	4.9996 x 10^6	0.02
Point load applied on cantilever	δ_{max} (m)	2.26 x 10^{-4}	2.2634 x 10^{-4}	0.15
	M_{max} (Nm)	1 x 10^4	1 x 10^4	0

Displacements and bending moments calculated in structural pile elements were in good agreement with analytical solutions.

A.4. Constitutive Models

Unit validations were conducted for three constitutive models by numerically simulating laboratory tests that apply different loading paths. The constitutive models were (1) isotropic linear elasticity, (2) Modified Cam Clay; and (3) Isotropic linear elasticity with Mohr-Coulomb failure criterion (perfectly plastic with non-associated flow rule).

The following sections discuss each model with respect to its formulation, the materials and behaviors represented, and the different loading paths subjected to study.

A.4.1. Isotropic Linear Elasticity

The isotropic linear elastic model was adopted for modeling the unreinforced concrete columns in the lateral spreading analysis of a CSE case history (Huang et al. 2019). There was uncertainty as to whether the columns would fail in flexural tension under lateral earth pressures, so the relatively simple linear elastic model was adopted for the preliminary analysis of column lateral response.

The formulation of the linear elastic model has its basis in Hooke's law, which states that a force is required to displace a spring by some distance at a linear relationship to its stiffness. Linear elasticity relates the stress (σ) as a linear function of strain (ϵ) (Equation A.15), and isotropy dictates that the same properties apply in all directions. Furthermore, a purely linearly elastic material cannot fail, and strains are reversible in unload-reload.

$$\sigma = E\epsilon \quad \text{(A.15)}$$

The linear elastic model is characterized by the Young's modulus (E), bulk modulus (K), shear modulus (G), and the Poisson's ratio (ν). Only two of the parameters are needed for the material model input, and the remaining parameters can be determined as a function of the parameters whose values are defined. For example, given inputs for E and ν, K and G can be calculated using the following relationships.

$$K = \frac{E}{3(1-2\nu)} \quad \text{(A.16)}$$

$$G = \frac{E}{2(1+\nu)} \quad \text{(A.17)}$$

For validating the linear elastic constitutive model, a group of linear elastic brick zones forming a weightless cube was tested in isotropically consolidated drained (ICD) triaxial compression. The loading path in this test is representative of that in columns under soil confinement and axial compression from embankment loading. The cube had an edge length of 1 m and a discretization consisting of 4 zones of equal size along all edges. The material properties were representative of concrete, using E = 20 GPa and ν = 0.2.

The loading sequence of the ICD triaxial compression simulation was as follows. Grid points on all external surfaces were applied with a velocity of equal magnitude until a compressive strain of 0.001 was reached in the vertical (z) and horizontal (x and y) directions. An isotropic compressive stress was generated after this first loading stage. The velocities were then freed, and an isotropic compressive stress equal to that generated by the first stage of loading was applied on all external faces to maintain equilibrium. Next, deviatoric loading was simulated by applying a velocity in the z-direction on the external horizontal faces until an additional vertical strain of 0.001 was reached. In this second loading stage, horizontal strains were incurred. The following tables show the comparison of the computed and expected stresses and strains resulting from the strain-controlled ICD test.

Table A-10. All-around compressive stress in linear elastic zones under strain-controlled isotropic compression (compressive stresses are positive)

	σ_{xx} (Pa)		σ_{yy} (Pa)		σ_{zz} (Pa)	
	Expected	Computed	Expected	Computed	Expected	Computed
Isotropic compression	$3.33\text{x}10^7$	$3.33\text{x}10^7$	$3.33\text{x}10^7$	$3.33\text{x}10^7$	$3.33\text{x}10^7$	$3.33\text{x}10^7$

Under isotropic compression,

$$\sigma_{ij}\,[Pa] = KI_\epsilon\delta_{ij} = (1.11\times10^{10}\,Pa)(0.001+0.001+0.001)\begin{bmatrix}1&0&0\\0&1&0\\0&0&1\end{bmatrix}$$

$$= \begin{bmatrix}3.33\times10^7 & 0 & 0\\ 0 & 3.33\times10^7 & 0\\ 0 & 0 & 3.33\times10^7\end{bmatrix}[Pa]$$

Under deviatoric compression, the known variables were the vertical strain, ϵ_{zz} = 0.002, and horizontal stresses, $\sigma_{xx} = \sigma_{yy} = 3.33\times10^7 Pa$. The unknown variables were the vertical stress, σ_{zz}, and horizontal strains, ϵ_{xx} and ϵ_{yy}, and these were calculated as follows:

$$\sigma_{ij} = KI_\epsilon\delta_{ij} + 2GE_{ij} = KI_\epsilon\delta_{ij} + 2G(\epsilon_{ij} - \frac{I_\epsilon}{3}\delta_{ij})$$

$$\sigma_{xx} = K(2\epsilon_{xx}+\epsilon_{zz}) + 2G\left(\epsilon_{xx} - \frac{(2\epsilon_{xx}+\epsilon_{zz})}{3}\right)$$

$$3.33\times10^7 Pa = 1.1110^{10}(2\epsilon_{xx}+0.002) + 2(8.33\times10^9)\left(\epsilon_{xx} - \frac{(2\epsilon_{xx}+0.002)}{3}\right)$$

$$\epsilon_{xx} = \epsilon_{yy} = 0.0008$$

$$\sigma_{zz} = K(2\epsilon_{xx}+\epsilon_{zz}) + 2G\left(\epsilon_{zz} - \frac{(2\epsilon_{xx}+\epsilon_{zz})}{3}\right) = 5.33\times10^7 Pa$$

Table A-11. Deviatoric stress and horizontal strains in linear elastic zones under strain controlled deviatoric loading (compressive stresses and strains are positive)

	σ_{zz} (Pa)		ϵ_{xx} (Pa)		ϵ_{yy} (Pa)	
	Expected	Computed	Expected	Computed	Expected	Computed
Deviatoric compression	$5.33\text{x}10^7$	$5.33\text{x}10^7$	0.0008	0.0008	0.0008	0.0008

A.4.2. Modified Cam Clay

The Modified Cam Clay model was originally described in the literature by Roscoe and Burland (1968). It is a volumetric hardening model with associated flow. This model was selected for to represent the clay for its (1) relative simplicity, where the elliptical yield surface is controlled by the mean effective stress, deviatoric stress, preconsolidation pressure, and the slope of the critical state line, (2) ability to model the consolidation behavior of clay by linking the change in specific volume to the change in logarithm of mean effective stress using parameters obtained from 1-D consolidation tests, and (3) closed yield surface (i.e. capped) for estimating plastic strains.

As an elastic-plastic model, the Modified Cam Clay is defined by elastic properties, a yield surface, a plastic potential, and a hardening rule. The elastic properties are defined by the recoverable volumetric and shear strains that occur as a result of changes in mean effective stress and deviator stress, as shown in Equations A.18 and A.19, respectively. The yield surface is defined by the equation of an ellipse (Equation A.20), which also defines the plastic potential function given the condition of normality in associated flow. Lastly, the hardening rule results in the expansion of the yield surface at constant shape and by a linear relationship between specific volume and logarithm of mean effective stress in isotropic virgin compression (Equation A.21).

$$\delta\varepsilon_p^{\mathrm{e}} = \frac{\kappa}{\nu}\left(\frac{\delta p'}{p'}\right) \qquad \text{(A.18)}$$

$$\delta\varepsilon_q^{\mathrm{e}} = \frac{\delta q}{3\mathrm{G}} \qquad \text{(A.19)}$$

$$g = f = q^2 - M^2\left[p'\left(p'_o - p'\right)\right] = 0 \qquad \text{(A.20)}$$

$$\frac{\delta p'_o}{\delta\varepsilon_p^{\mathrm{p}}} = \frac{\nu p'_o}{\lambda-\kappa} \qquad \text{(A.21)}$$

Where,

f = yield function

G = shear modulus

g = plastic potential function

M = slope of critical state line

p' = mean effective stress

p'_o = preconsolidation pressure

q = deviator stress

$\delta p'$ = change in mean effective stress

$\delta p'_o$ = change in preconsolidation pressure

δq = change in deviatoric stress

$\delta \varepsilon_p^{\mathrm{e}}$ = elastic volumetric strain increment

$\delta \varepsilon_p^{\mathrm{p}}$ = plastic volumetric strain increment

$\delta \varepsilon_q^{\mathrm{e}}$ = elastic shear strain increment

κ = slope of the recompression line

λ = slope of virgin compression line

ν = Poisson's ratio

Stress-strain response of the Modified Cam Clay model was validated by simulating laboratory tests representing the likely loading paths in clay under embankment loading. The tests were the undrained triaxial compression, undrained direct simple shear, and undrained triaxial extension. In all simulations, samples were anisotropically consolidated prior to undrained shear. The validation of consolidation deformations calculated using the Modified Cam Clay model are presented in APPENDIX B.

Anisotropically Consolidated Undrained Triaxial Compression

This unit validation was designed to verify (1) the undrained shear strength (s_u) of a sample for known values of specific volume (v), critical state friction angle (ϕ'_{cs}), confining stresses, and

preconsolidation pressure, (2) the effective stress path (p'-q), and (3) the pore pressure at failure (u_f). Validations were conducted for normally consolidated, lightly overconsolidated (i.e. OCR < 2,) and heavily overconsolidated (OCR > 2) samples.

The numerical procedure for the anisotropically consolidated undrained (ACU) triaxial tests was as follows. A 1 ft^3 (0.0283 m^3) sample consisting of brick type soil zones was constructed in the cubic geometry, with 4 zones of equal size spanning every edge, totaling 64 zones. The soil zones were assigned material property values for λ, κ, M, and specific volume at unit pressure (v_1), as shown in Table A-12. Note that the expected s_u for the normally consolidated, lightly overconsolidated, and heavily overconsolidated samples were 88 psf, 100 psf, and 300 psf, respectively. In-situ effective stresses were initialized in the soil zones at the same time as external confining stresses were applied. Pore pressures were zero. This initial state was computed for mechanical equilibrium and represented anisotropic consolidation. Initial effective stresses and specific volumes are listed in Table A-13. Good agreement was reached between the expected and computed specific volumes. The next stage was the undrained deviatoric loading. Strain-controlled compression was applied in the form of fixing velocities at gridpoints on the two external horizontal surfaces. Pore pressures were enabled to freely develop at all gridpoints. Deviatoric compression was applied until failure, at which point the p'-q stress path reached the critical state line and ceased to change.

Table A-12. Modified Cam Clay properties adopted in ACU triaxial compression simulations.

$\boldsymbol{\lambda}$	$\boldsymbol{\kappa}$	$\boldsymbol{M}$	$\boldsymbol{v_1}$
0.173	0.0173	0.984	3.57

Table A-13. Initial effective stresses in samples in ACU triaxial compression simulations.

	$\boldsymbol{\sigma'_v}$ **(psf)**	**OCR**	$\boldsymbol{K_0}$	$\boldsymbol{\sigma'_h}$ **(psf)**	$\boldsymbol{p'_i}$ **(psf)**	$\boldsymbol{q_i}$ **(psf)**	$\boldsymbol{v}$	
							Computed	Expected
Normally Consolidated	345	1	0.577	199	248	146	2.56	2.56
Lightly Overconsolidated	345	1.18	0.619	225	265	120	2.54	2.54
Heavily Overconsolidated	345	3.85	1.02	352	350	7	2.35	2.35

Results for the s_u and u_f are shown in Table A-14. The expected s_u was analytically determined using Equation A.22 (Wood 1990). The calculated s_u was interpreted as 50% of the calculated

deviator stress at failure. The expected u_f is the difference in the mean total stress at failure and the mean effective stress at failure, and was calculated using Equations A.23 to A.25. The calculated u_f was read from grid points. Note that the calculated results were extracted from one of the interior zones in the 64-zone sample. Results show good agreement between the expected and calculated values of s_u and u_f.

Table A-14. Expected versus calculated S_u and u_f for ACU triaxial compression using Modified Cam Clay formulation.

	s_u			u_f		
	Expected (psf)	Calculated (psf)	Percent Difference (%)	Expected (psf)	Calculated (psf)	Percent Difference (%)
Normally Consolidated	88	86	2.3	79.1	81.7	3.23
Lightly Overconsolidated	100	100	negligible	88.4	87.4	1.14
Heavily Overconsolidated	300	301[a], 300[b]	0.333	-57.4	-57.1	0.524

[a] Peak s_u.
[b] s_u at critical state.

$$s_u = \frac{M}{2}\exp\left[\frac{(\Gamma - v_1)}{\lambda} + \ln\left(p'_o\right) - \left(\frac{\kappa}{\lambda}\right)\ln\left(\frac{p'_o}{p'_i}\right)\right] \qquad \text{(A.22)}$$

$$u_f = \frac{\Delta q_f}{3} + p'_i - p'_f \quad \text{(A.23)}$$

$$\Delta q_f = 2S_u - q_i \qquad \text{(A.24)}$$

$$p'_f = \frac{2S_u}{M} \qquad \text{(A.25)}$$

Where,

p'_f = mean effective stress at failure

p'_i = initial mean effective stress

q_i = initial deviator stress

Δq_f = total change in deviator stress at failure

Γ = specific volume at unit pressure on critical state line

The shapes of the p'-q paths are as expected. Note that the p'-q path for the normally consolidated sample (Figure A-5a) has a vertical portion, which is characteristic of overconsolidated samples and not normally consolidated samples. The discrepancy is due to numerical difficulties in calculating an initial mean effective stress state that perfectly satisfies the yield criterion without rounding errors.

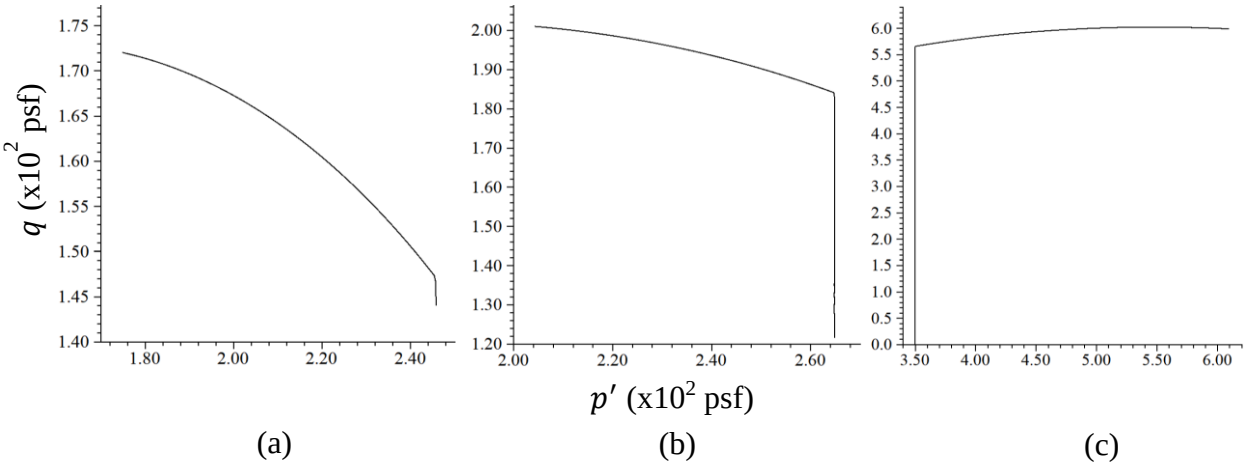

Figure A-5. Calculated p'-q stress path in ACU triaxial compression simulation for a sample that was a) normally consolidated; b) lightly overconsolidated; and c) heavily overconsolidated.

Anisotropically Consolidated Direct Simple Shear

Three soil samples with the same material properties as in the ACU triaxial compression simulations were tested in direct simple shear. In theory, this loading path involves an increase in shear strain and zero strains in the vertical and lateral directions. The numerical procedure was as follows. Initially, 1 ft^3 volume of soil was constructed in the cubic geometry using 64 brick zones of equal size, but the geometry was modified to consist of a single cubic zone. The change was made such that reasonable pore pressures could be generated, as described later. In-situ effective stresses were initialized at the same time as external confining stresses were applied, resulting in anisotropic consolidation. In undrained shear, pore pressures were enabled to freely develop at all grid points, and a constant lateral velocity of $0.5x10^{-8}$ ft/step was applied at grid points on the top external surface. Rollers prevented lateral movement in the direction orthogonal to the applied velocities as well as prevented change in sample height. Each simulation was conducted until the p'-q stress path ceased to change.

Results for the s_u, u_f, p-q stress path, and p'-q stress path are provided in the following table. The calculated s_u was interpreted in the same way as in the ACU triaxial compression simulation. When the soil sample was constructed using 64 brick zones, there was variation in pore pressures throughout the sample ranging from negative to positive values in both the normally consolidated and overconsolidated samples. The pore pressure in one of the interior zones oscillated between negative and positive values with the increase in shear strain. This pore pressure response was likely the result of variations in the specific volume across zones. Velocities at grid points bordering interior zones were found to be non-zero in the vertical and lateral directions. This finding led to the adoption of a single-zone model, where the constraint of zero vertical and lateral strains was imposed. In the single-zone model, excess pore pressures remained at nil throughout the simulation, and the p-q and p'-q stress paths were equivalent.

Table A-15. Expected versus calculated s_u for ACU direct simple shear simulation using Modified Cam Clay formulation.

	Expected (psf)	**Calculated (psf)**	**Percent Difference (%)**
Normally Consolidated	88	86	2.3
Lightly Overconsolidated	100	100	negligible
Heavily Overconsolidated	300	301[a], 300[b]	0.333

[a] Peak s_u.
[b] s_u at critical state.

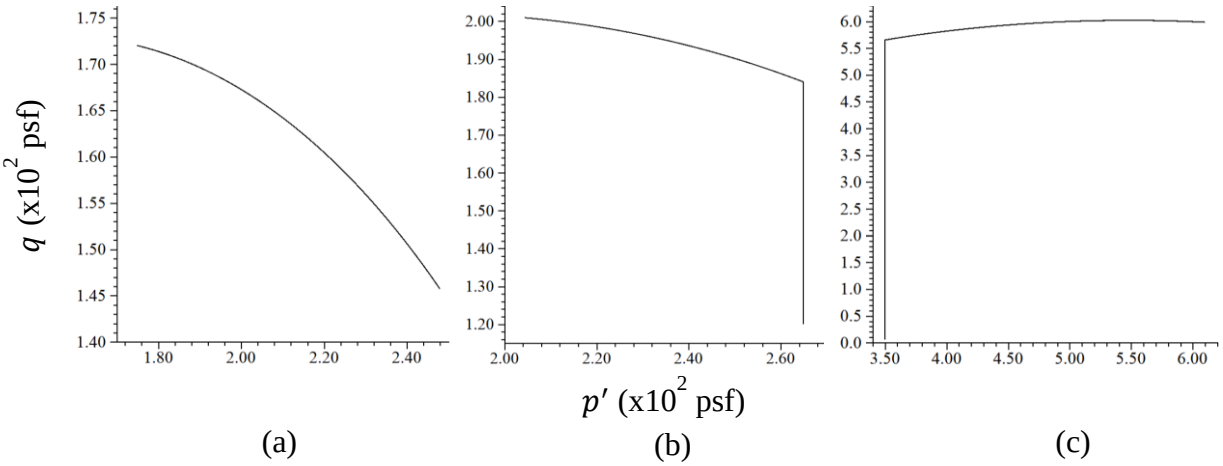

Figure A-6. Calculated p'-q stress path in ACU direct simple shear simulation for a sample that was a) normally consolidated; b) lightly overconsolidated; and c) heavily overconsolidated.

Anisotropically Consolidated Undrained Triaxial Extension

The undrained triaxial extension test involves soil shear failure through the increase in total lateral stresses. This loading path may be found in soil zones near the embankment toe (i.e. where a failure surface daylights). Simulations of the ACU triaxial extension test were conducted using the same geometry, material properties, and procedure as in the simulations for ACU triaxial compression. The only difference was that the strain controlled deviatoric loading involved applying velocities in the orthogonal lateral directions as opposed to the vertical direction. The samples contracted laterally and extended vertically under constant volume.

Results are presented below for the s_u, u_f, p-q stress path, and p'-q stress path. Good agreement was reached between the expected and calculated values of s_u. The expected u_f was the difference between the expected p_f and p'_f. The p_f was determined using the 3V:2H slope of the total stress path in triaxial extension, and the p'_f was found on the critical state line. The effective stress paths as illustrated below show a similarity to the previous tests, with the only exception being the initial decrease in q at constant p' in the normally consolidated and lightly overconsolidated samples. The lateral consolidation stress in these samples was lower than the vertical consolidation stress, thus, the stress path decreased in q and moved towards an isotropic stress state before increasing in q.

Table A-16. Expected versus calculated s_u and u_f for ACU triaxial extension simulation using Modified Cam Clay formulation.

	s_u			u_f		
	Expected (psf)	Calculated (psf)	Percent Difference (%)	Expected (psf)	Calculated (psf)	Percent Difference (%)
Normally Consolidated	88	86	2.3	283	285	0.704
Lightly Overconsolidated	100	100	negligible	275	274	0.364
Heavily Overconsolidated	300	301[a], 300[b]	0.333	135	135	negligible

[a] Peak s_u.
[b] s_u at critical state.

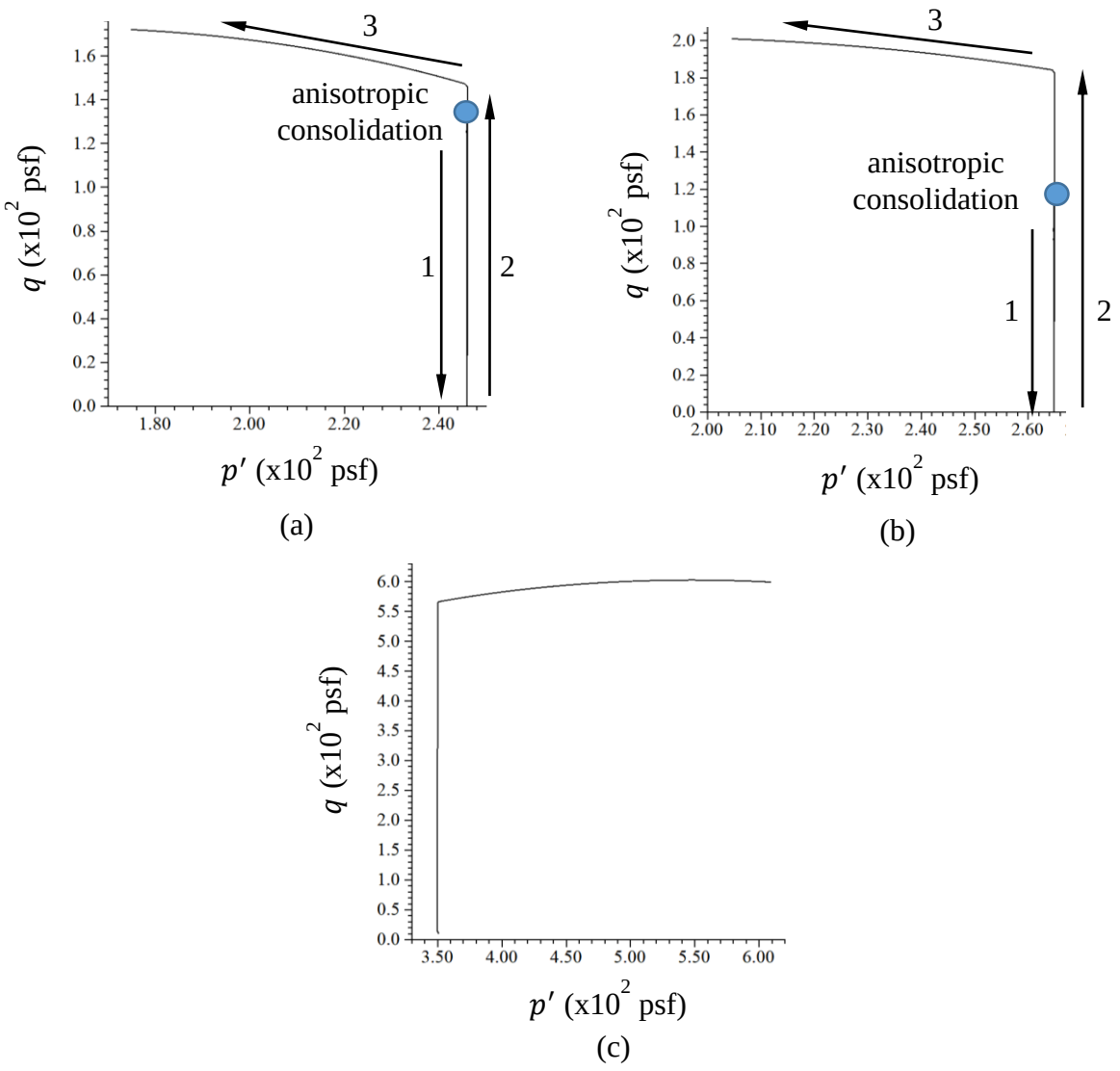

Figure A-7. Calculated p'-q stress path in ACU triaxial extension simulation for a sample that was a) normally consolidated; b) lightly overconsolidated; and c) heavily overconsolidated.

A.4.3. Isotropic Linear Elasticity with Mohr-Coulomb Failure Criterion

The Mohr-Coulomb failure criterion has its origins in a scientific paper written by Coulomb in 1772. Coulomb observed that materials such as soil, wood, stone, and masonry derived their strengths from cohesion and friction, and proposed a two-dimensional failure criterion that relates the normal stress to the shear strength as a function of these two parameters (c and ϕ) (Davis and Selvadurai 2002), as shown in Equation A.26. Implementation of the Mohr-Coulomb failure

criterion extends to three dimensions in FLA3D v.5.01. The elastic response is isotropic linear elastic, the same as that described in Section A.4.1. At failure, stresses are defined by the shear yield function, f^s (Equation A.27), and the tensile yield function, f^t (Equation A.28). The shear flow is defined by the non-associated flow rule in Equation A.29, which is a function of the dilation angle (ψ) that describes the volume change in soil during shear. The tensile flow is defined by the associated flow rule in Equation A.30. Note that stresses are negative in compression. The Mohr-Coulomb failure criterion is perfectly plastic.

$$\tau = c + \sigma tan\phi \qquad \text{(A.26)}$$

$$f^s = 0 = \sigma_1 - \sigma_3 \left(\frac{1+sin\phi}{1-sin\phi}\right) + 2c\sqrt{\frac{1+sin\phi}{1-sin\phi}} \qquad \text{(A.27)}$$

$$f^t = 0 = \sigma_3 - \sigma_t \qquad \text{(A.28)}$$

$$g^s = \sigma_1 - \sigma_3 \left(\frac{1+sin\psi}{1-sin\psi}\right) \qquad \text{(A.29)}$$

$$g^t = -\sigma_3 \qquad \text{(A.30)}$$

Soil zones assigned the Mohr-Coulomb failure criterion were anisotropically consolidated and then loaded in the undrained condition in three different loading paths: triaxial compression, direct simple shear, and triaxial extension. Material properties are shown in Table A-17. The initial consolidation stresses were σ'_v = 345 psf and σ'_h = 152 psf (K_0 = 0.44 for OCR = 1). Numerical procedures for the different tests were the same as those previously described. Results are presented below in terms of the s_u, u_f, and the p'-q stress path. Note that for triaxial compression and triaxial extension, failure falls on a line defined by the slope, M, and passing through the origin of p-q space, as shown in Equations A.31 and A.32, respectively. Calculated s_u, u_f, and p'-q stress paths were as expected for the three loading paths, as shown in Table A-18 and Figure A-8.

Table A-17. Material properties for the isotropic linear elastic Mohr-Coulomb failure criterion as adopted in laboratory test simulations.

E (psf)	ν	c' (psf)	ϕ' (°)	ψ (°)	σ_t (psf)
300,000	0.31	0	34	0	0

$$M = \frac{6sin\phi'}{3-sin\phi'} \quad \text{(A.31)}$$

$$M = \frac{6sin\phi'}{3+sin\phi'} \quad \text{(A.32)}$$

Table A-18. Expected versus calculated s_u and u_f from laboratory test simulations using the isotropic linear elastic Mohr-Coulomb failure criterion.

	s_u			u_f		
	Expected (psf)	Calculated (psf)	Percent Difference (%)	Expected (psf)	Calculated (psf)	Percent Difference (%)
ACU Triaxial Compression	149	149	negligible	34.9	34.8	0.287
ACU Direct Simple Shear	N/A	130	N/A	N/A	0	N/A
ACU Triaxial Extension	102	102	negligible	265	264	0.378

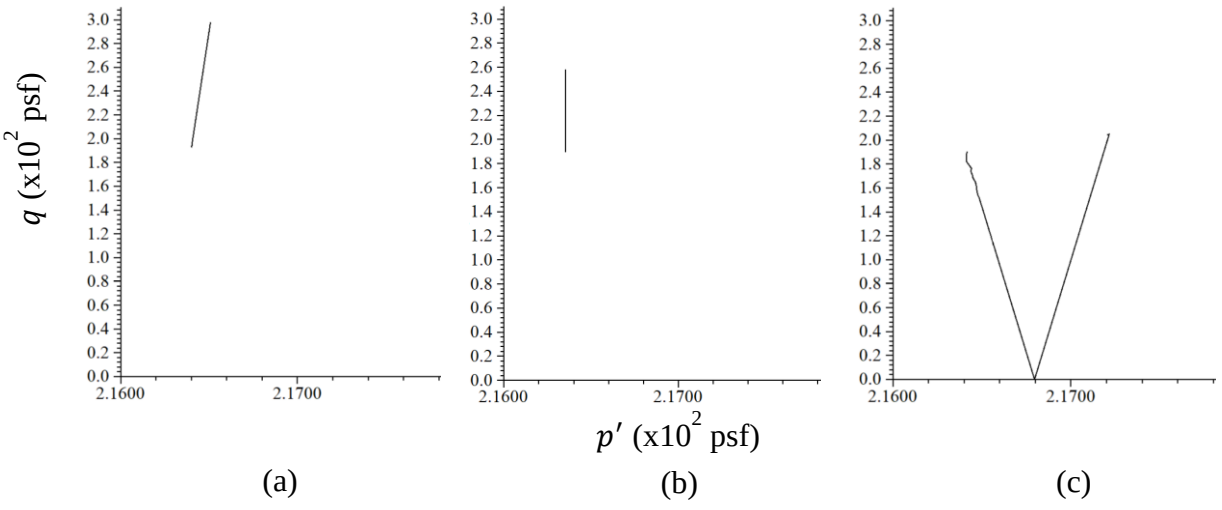

Figure A-8. Calculated p'-q stress path for Mohr-Coulomb material subjected to ACU a) triaxial compression; b) direct simple shear; and c) triaxial extension.

References

Tensar International Corportation (2015). "Product Specification Tensar Biaxial Geogrid." <https://www.tensarcorp.com/Systems-and-Products/Tensar-Biaxial-BX-geogrids>. (2015).

Davis, R. O., and Selvadurai, A. P. S. (2002). *Plasticity and Geomechanics*, Cambridge University Press, Cambridge.

Huang, Z., Ziotopoulou, K., and Filz, G. M. (2019). "Three-Dimensional Numerical Limiting Case Analyses of Lateral Spreading in a Column-Supported Embankment Case History." *Journal of Geotechnical and Geoenvironmental Engineering*, 145(11), 04019096.

Irvine, H. M. (1981). *Cable Structures*, The MIT Press, Cambridge, Massachusetts.

Itasca (2013). *FLAC3D Theory and Background*, Itasca Consulting Group Inc., Minneapolis, Minnesota.

Itasca (2013). *Structural Elements*, Itasca Consulting Group Inc., Minneapolis, Minnesota.

Liu, H., Ng, C. W., and Fei, K. (2007). "Performance of a geogrid-reinforced and pile-supported highway embankment over soft clay: case study." *Journal of Geotechnical and Geoenvironmental Engineering*, 133(12), 1483-1493.

Roscoe, K. H., and Burland, J. B. (1968). "On the generalised stress-strain behaviour of 'wet' clay." *Engineering Plasticity*, J. Heyman, and F. A. Leckie, eds., Cambridge University Press, Cambridge.

Santacruz Reyes, K. J. (2016). "Geosynthetic Reinforced Soil: Numerical and Mathematical Analysis of Laboratory Triaxial Compression Tests." Doctor of Philosophy, Department of Civil and Environmental Engineering, Virginia Tech, Blacksburg, VA.

Wood, D. M. (1990). *Soil Behaviour and Critical State Soil Mechanics*, Cambridge University Press, Cambridge.

Young, W. C., and Budynas, R. G. (2001). *Roark's Formulas for Stress and Strain*, McGraw Hill Professional.

APPENDIX B. NUMERICAL PREDICTIONS OF DEFORMATIONS IN GEOSYNTHETIC-REINFORCED COLUMN-SUPPORTED EMBANKMENTS: VALIDATION OF MANUAL DISSIPATION OF EXCESS PORE PRESSURE APPROACH FOR UNDRAINED AND DRAINED ANALYSES

Huang, Z., Ziotopoulou, K., and Filz, G. M. (2018). "Numerical Predictions of Deformations in Geosynthetic-Reinforced Column-Supported Embankments: Validation of Manual Dissipation of Excess Pore Pressure Approach for Undrained and Drained Analyses." *IFCEE 2018: Innovations in Ground Improvement for Soils, Pavements, and Subgrades, GSP 296*, 327-336.

B.1. Abstract

Deformations in geosynthetic-reinforced column-supported embankments (GRCSE) can be calculated by performing fully-coupled consolidation analyses, which, depending on the system properties and the size of the numerical domain, can be computationally intensive and time consuming. In this paper, an alternative approach for numerically analyzing deformations in GRCSEs is presented. This approach captures the complex time-dependent deformations in the GRCSE through manual dissipation of excess pore pressures, where deformations are computed for known pore pressure distributions. Two validation examples were analyzed using the finite difference method as implemented in the computer program FLAC3D. They show that this alternative approach is computationally faster than fully-coupled analyses and provides comparable deformation results. This approach is adopted for the analysis of a GRCSE case history. Excess pore pressures developed in an undrained end-of-construction analysis are manually dissipated to solve for deformations in a drained long-term analysis. Numerical results are shown to envelope measured case history recordings in terms of settlement and vertical pressures on the subsoil and on the columns.

B.2. Introduction

Stresses and deformations in a GRCSE evolve with time, depending on the system properties and the embankment construction rate. Time dependent components include development of soil arching within the embankment fill, development of geosynthetic reinforcement strains within the load transfer platform (LTP), and consolidation of the soft foundation soil. The simultaneous occurrence of these processes justifies application of fully coupled fluid-mechanical analyses for the GRCSE (Bhasi and Rajagopal 2014; Borges and Marques 2011; Huang and Han 2009; Huang and Han 2010; Liu and Rowe 2016; Rowe and Liu 2015; Yapage et al. 2014; Zhuang and Wang 2016). While this analysis method is correct, it can also be difficult to perform as well as costly in computation time, depending on the system properties and the size of the numerical domain.

Evidence from case histories suggests that analysis of displacements (lateral spreading) in a GRCSE may not require a fully coupled analysis. Foundation lateral earth pressures, which directly influence the reinforcement tension and column bending moments, may be critical during or at the end of construction. In this period, case history recordings have shown that soil arching may not

fully develop in the embankment fill, and the subsoil between columns must support more load than if arching had fully developed (Briançon and Simon 2012; Chen et al. 2009; Chen et al. 2013; Habib et al. 2002; Oh and Shin 2007; Shang et al. 2016; Xu et al. 2015; Zhou et al. 2016; Zhuang and Cui 2016). Case histories with longer recording periods have also found that reinforcement strains and foundation lateral deformations can increase after embankment construction is complete (Briançon and Simon 2012; Hong and Hong 2017; Lai et al. 2006; Liu et al. 2012; Shang et al. 2016; Wang et al. 2014; Zhang et al. 2015; Zhou et al. 2016). This evidence suggests that the limiting cases to examine for lateral spreading design are undrained end-of-construction and drained long-term.

In this paper, a manual pore pressure dissipation approach is presented as an alternative to a fully coupled analysis, and the two limiting cases are examined. Following the validation of deformations against two consolidation examples, the approach is applied to the analysis of a selected case history to demonstrate its applicability in reasonably enveloping measurements.

B.3. Numerical Procedure and Validation

The steps in the manual pore pressure dissipation approach for calculating consolidation deformations are: 1) assignment of initial excess pore pressures; 2) manual prescription of reduced pore pressures; and 3) computation of deformations for the given pore pressure distribution and changes in effective stresses. Using the finite difference method as implemented in FLAC3D version 5.01 (Itasca Consulting Group Inc. 2012), these three steps are all conducted in the fluid configuration mode in which mechanical deformations and fluid flow can interact. In Step 1, the development of initial excess pore pressures is simulated by applying the load and allowing excess pore pressures to develop without fluid flow. This models undrained, short-term behavior that requires mechanical deformation calculations but not fluid flow calculations. A realistic fluid bulk modulus (i.e., $2x10^9$ Pa for water) is assigned for pore pressures to develop in response to the embankment load. In Step 2, a reduced pore pressure distribution is prescribed in fluid calculation mode (mechanical calculations turned off), wherein the pore pressure at every grid point is assigned a value associated with a later stage in consolidation. The pore pressure at each grid point is applied with a condition of fixity. In Step 3, the mechanical calculation is performed (without fluid flow calculation) to determine the deformations associated with the changes in pore pressures

and effective stresses. Applying the condition of fixity in Step 2 as well as setting the fluid bulk modulus to zero in Step 3 prevent the assigned pore pressures from changing during calculations. The resulting deformations represent those found at that later stage in consolidation.

The 3-step procedure would represent the calculation of long-term drained deformations starting from an initial undrained state if the pore pressures assigned in Step 2 were for the hydrostatic condition. Likewise, gradual dissipation of excess pore pressures could be modeled if steps 2 and 3 were repeated using gradually reduced pore pressure distributions.

Provided below are two validation examples of the manual pore pressure dissipation approach as applied to clay consolidating under applied loading. The deformations at different stages of consolidation calculated by the manual pore pressure dissipation approach are compared to those calculated by a benchmark solution.

B.3.1. Validation Example 1: 1-D Consolidation of a Lightly Overconsolidated Clay

In this example, a 5 m thick clay deposit is loaded instantaneously by a vertical load of 54 kPa. Prior to consolidation loading, an additional overburden of 54 kPa was applied to prevent numerical instability near the surface (low effective stress). The clay is lightly overconsolidated (OCR = 1.2) under the overburden stresses. The groundwater table is at the clay surface. The soil deposit was modeled as a 3-D column discretized uniformly in all directions, with 250 zones over the soil deposit thickness (in the direction of loading), and 4 zones in the orthogonal directions. Roller boundary conditions were applied on the model sides. The vertical load was applied gradually in the undrained condition, so that a uniform excess pore pressure distribution of 54 kPa developed in the soil. The clay was modeled as a Modified Cam Clay (MCC) material, and properties are provided in Table B-1.

Table B-1. Properties of lightly overconsolidated clay in Validation Example 1

Unit Weight (kN/m^3)	**M**	**λ**	**κ**	**Void Ratio**	**Poisson's Ratio**	**c_v (m^2/s)**	**c_{vr} (m^2/s)**
15.2	1.12	0.242	0.055	1.0	0.36	$1.2x10^{-8}$	$5.2x10^{-7}$

Pore pressure distributions at various stages of consolidation were imported into the FLAC3D model from an equivalent non-linear model constructed in the finite difference software, Settle3D version 4.008 (Rocscience Inc. 2017). This was to provide a validation basis for the settlements

calculated by the manual pore pressure dissipation approach. Note that the pore pressure distributions were prescribed in successive stages to result in a cumulative settlement. A comparison of the degree of consolidation (percent ratio of the current total settlement to the ultimate settlement) at various times after loading is provided in Table B-2. The results demonstrate a good agreement and the validity of the manual pore pressure dissipation approach for calculating settlements in 1-D consolidation.

Table B-2. Degree of consolidation (Us) of lightly overconsolidated clay in Validation Example 1 under 1-D consolidation at various times after loading

Time after Loading	**U_s (%) Calculated by FLAC3D Manual Dissipation of Pore Pressures**	**U_s (%) Calculated by Settle3D**
1 year	21.4	20.7
10 years	51.2	54.7
50 years	89.0	92.6

B.3.2. Validation Example 2: Consolidation of Normally Consolidated Clay under Vertical Load of Limited Lateral Extent

In this example, a 4 m wide strip load of 10 kPa is applied instantaneously on a 10 m thick normally consolidated clay deposit. The groundwater table is at the soil surface. The soil was modeled by a 3-D slice with a thickness of a single zone (plane strain condition). Only half of the strip load was modeled, and the soil was extended 20 m in the lateral direction. The model was uniformly discretized in all directions, with 20 zones over the soil thickness and 40 zones in the lateral direction. Boundary conditions and the undrained loading procedure were identical to Example 1. An overburden of 10 kPa was applied prior to the application of the strip load to prevent numerical instability. MCC material properties are provided in Table B-3.

Table B-3. Properties of normally consolidated clay in Validation Example 2

Unit Weight (kN/m^3)	**M**	**λ**	**κ**	**Void Ratio**	**Poisson's Ratio**	**c_v (m^2/s)**
18.0	0.9	0.3	0.06	0.8	0.35	2.8×10^{-7}

Pore pressure distributions at various stages of consolidation calculated using the FLAC3D coupled fast-flow solution were prescribed in the manual pore pressure dissipation approach as a basis of comparison. Similar to Example 1, the pore pressures were prescribed in successive stages to result in cumulative deformations. A comparison of vertical and lateral deformations calculated

by the two approaches is reported in Table B-4. A comparison of vertical and lateral deformation contours at 115 days after undrained loading is illustrated in Figures B-1 and B-2, respectively.

Note that the reported coupled analysis results were from calculations using a fluid relaxation coefficient of $1x10^{-7}$, a time step of 10 seconds, and 100 mechanical substeps. These parameters produced converging results for the coupled analyses. When a larger time step and/or a larger fluid relaxation coefficient was used, the pore pressures from the coupled analyses were not accurate, and the manual approach using these pore pressures provided deformation predictions that diverged from the coupled analyses predictions. Thus, accuracy of the deformations calculated by the manual pore pressure dissipation approach depends on the accuracy of the assigned pore pressure distribution. Fortunately, this would not be an issue in the drained analysis of the GRCSE because the pore pressure distribution would be hydrostatic.

A comparison of computation times showed that the manual pore pressure dissipation approach was faster compared to the coupled analysis. For the computation of deformations up to 115 days after loading, the manual approach was almost instantaneous, while the coupled analysis took 20 minutes on an Intel i7-6700 CPU @ 3.40 GHz and 32 GB RAM. The time required to conduct the coupled analysis was in fact several times longer given the multiple iterations required to arrive at convergence of pore pressures as a function of the time step and the fluid relaxation coefficient.

Table B-4. Vertical and lateral deformations of normally consolidated clay in Validation Example 2 under vertical loading of limited lateral extent at various times after loading

	FLAC3D Manual Dissipation of Pore Pressures	**FLAC3D Coupled Fast-Flow Solution**
Time after loading = 11.5 days		
Maximum Settlement (m)	0.0829	0.0829
Maximum Heave (m)	0.0104	0.0104
Maximum Lateral Displacement (m)	0.0212	0.0212
Time after loading = 115 days		
Maximum Settlement (m)	0.133	0.134
Maximum Heave (m)	0.0108	0.0109
Maximum Lateral Displacement (m)	0.0212	0.0212

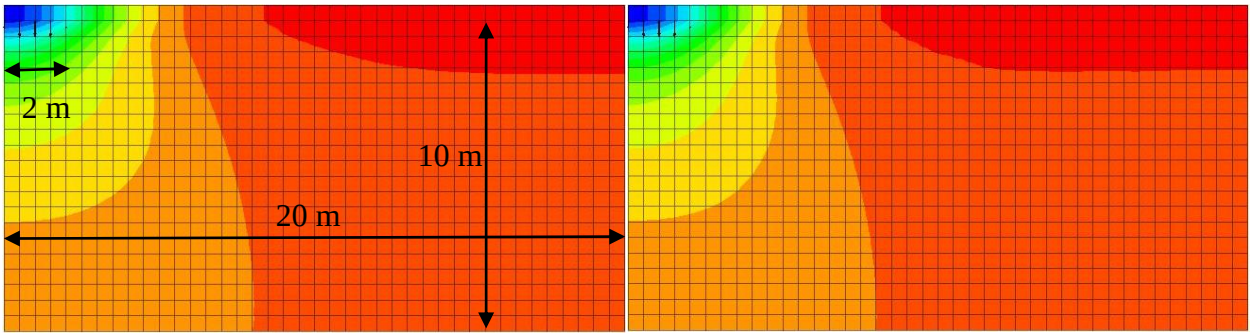

(1a) (1b)

Figure B-1. Vertical deformation contours at 115 days after loading for normally consolidated clay in Validation Example 2, as calculated by a) FLAC3D manual pore pressure dissipation approach; b) FLAC3D coupled fast-flow solution

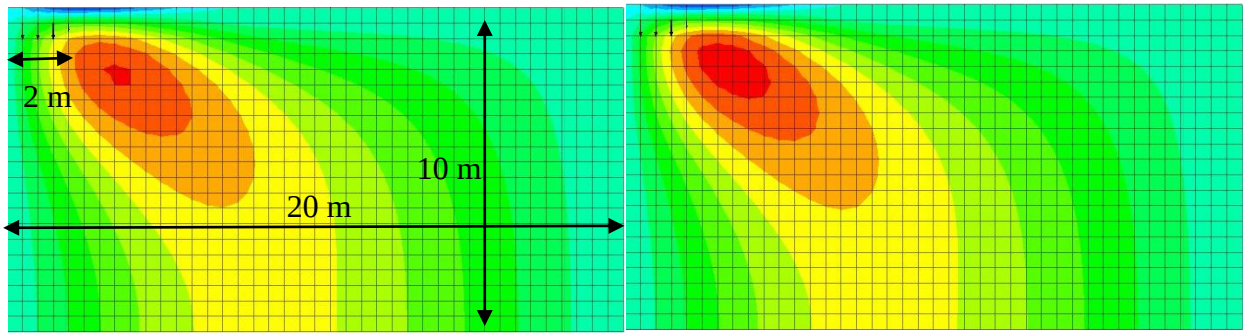

(2a) (2b)

Figure B-2. Lateral deformation contours at 115 days after loading for normally consolidated clay in Validation Example 2, as calculated by a) FLAC3D manual pore pressure dissipation approach; b) FLAC3D coupled fast-flow solution

B.3.3. Stress Path Dependency

For a non-linear, inelastic material, how different is the final deformation going directly from an undrained to a drained state versus gradual consolidation? Further validations showed that for the previous two examples, the deformations calculated using the manual pore pressure dissipation method did not appear significantly sensitive to the stress path, though larger deformations could be expected due to nonlinearity. As shown in Table B-5, the deformations at the final stage were not significantly influenced by the number of stages it took to reach the end point. In other words, if pore pressures were prescribed for times ‘A,’ ‘B,’ and ‘C,’ and the deformations were successively calculated for each stage (i.e. going from times ‘A’ to ‘B’ to ‘C’), then the resulting deformations at time ‘C’ would not significantly differ from those calculated going from times ‘A’ to ‘C’ directly.

The effect of nonlinearity was observed for Validation Example 1 (Table B-5). Immediately stepping from the undrained loading stage to 50 years after loading resulted in a slightly higher degree of consolidation (i.e. larger settlements) compared to calculations with intermediate stages (i.e. 89.9% vs. 89.0%). However, the result was still reasonable when compared to the Settle3D benchmark solution (i.e. 92.6%). This means that the resulting drained deformations in a GRCSE should not significantly vary whether the excess pore pressures developed during the undrained analysis were manually dissipated in one or multiple steps.

Table B-5. Manual pore pressure dissipation: comparison of deformations with and without intermediate stages for Validation Examples 1 and 2

	Without Intermediate Stages	**With Intermediate Stages**
Validation Example 1: Undrained Loading Stage to 50 years after Loading		
Degree of Consolidation (%)	89.9	89.0 (Table B-2)
Validation Example 2: Undrained Loading Stage to 115 days after Loading		
Maximum Settlement (m)	0.133	0.133 (Table B-4)
Maximum Heave (m)	0.0108	0.0108 (Table B-4)
Maximum Lateral Displacement (m)	0.0212	0.0212 (Table B-4)

A commonality between the two validation examples is the monotonic loading, which may have been the reason that stress path dependency did not significantly influence the deformation response. Embankment loading is also monotonic, and the manual pore pressure dissipation approach should be applicable for calculating the soft soil deformation response.

B.4. Case History

The manual pore pressure dissipation approach is applied to the analysis of a GRCSE case history documented by Liu et al. (2007). The embankment was monitored up to 125 days after construction, at which time the degree of consolidation was estimated at 70% (Liu et al. 2007). Undrained end-of-construction and drained long-term analyses were performed using FLAC3D. The model description and comparison of numerical calculations with case history recordings are provided below.

B.4.1. Description of FLAC3D Unit Embankment Model

A unit embankment model consisting of a quarter column cross-section was constructed. The unit embankment is a reasonable representation of the actual system given that the case history

recordings were taken near the embankment center, 17 m from the crest. The soil stratigraphy and model discretization are illustrated in Figure B-3. The groundwater table was at a depth of 1.5 m. Roller boundary conditions were applied to the model sides.

The embankment fill, LTP, and coarse-grained fill were modeled as Mohr-Coulomb materials, the column was linear elastic, and the clay and sandy silt layers were MCC materials. Material parameters followed those listed in Liu et al. (2007) for the most part, though some modifications were made. The concrete column (a concrete annulus encasing soil) was assigned a combined Young's Modulus of 8.8 GPa rather than the original 20 GPa. It was also assumed to be a homogenous material with a volumetric average density of 2092 kg/m^3. The clay and sandy silt layers were assigned preconsolidation pressures of 10 kPa and 120 kPa higher than the insitu vertical effective stresses, respectively, such that the layers were all lightly overconsolidated rather than normally consolidated as assumed in Liu et al. (2007). This was a reasonable change given the natural geological processes that could occur. It also helped calculations to better match plate load test results.

Interface elements were assigned along the column shaft and at the two ends of the column. The column-soil interface friction angle was 0.9 of the drained friction angle of the adjacent soil (Potyondy 1961). The interface normal and shear stiffness values were selected to achieve numerical convergence. Interface properties were validated through a numerical static load test that provided good agreement with the field static load test.

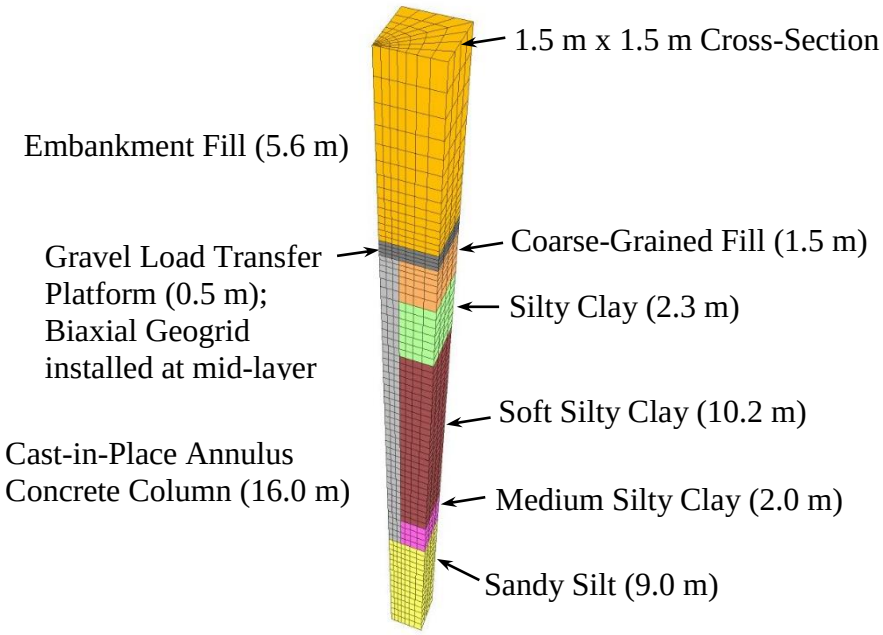

Figure B-3. FLAC3D unit embankment

The biaxial geogrid was modeled with geogrid elements of isotropic linear elastic properties, with a stiffness of 1180 kN/m and a Poisson's ratio of 0.3 (Liu et al. 2007). The numerical analyses were conducted in the large-strain mode so that the geogrid could develop tension under out-of-plane deformation.

Before construction, insitu vertical and lateral stresses in the ground were assigned, and the column density was initialized to that of the surrounding ground. The column was then installed by increasing its density to 2092 kg/m^3 under drained conditions, and lateral stresses in the ground were increased according to the effective stress β-method (Hannigan et al. 2016). The model was solved for mechanical equilibrium. Displacements resulting from stress initialization and column installation were zeroed.

The LTP and embankment fill loads were applied next by gradually increasing their densities while excess pore pressures freely developed in the clay and sandy silt layers. The model was solved for equilibrium, providing results for the undrained end-of-construction analysis. Finally, excess pore pressures in the foundation were manually dissipated by prescribing the hydrostatic pore pressure distribution. The model was again solved for equilibrium, providing results for the drained long-term analysis of the GRCSE.

B.4.2. Comparison of Undrained and Drained Analysis Results to Case History Recordings

Table B-6 summarizes the case history recordings and the corresponding numerical predictions for both the undrained end-of-construction and drained long-term analyses. The undrained analysis overestimated the pressure on the subsoil while it underestimated the pressure on the column. It also underestimated the settlement of the column and the subsoil. These results are as expected given the limited relative subsoil settlement and vertical load transfer to columns that could occur when drainage was not allowed. Given that some consolidation and dissipation of excess pore pressures would have occurred during embankment construction, the numerical calculation for the pressure on subsoil assuming zero consolidation was larger than measured.

Compared to the undrained end-of-construction scenario, the drained long-term analysis resulted in a decrease in the pressure on the subsoil, an increase in the pressure on the column, and an increase in the settlement of both subsoil and column. These results reflect the increase in vertical load transfer to the column as a result of greater differential settlement between subsoil and column. The current numerical model underestimates the differential settlement and overestimates the settlement of the column (i.e. sandy silt layer). A reason could be that the response of the LTP and the embankment fill is less compliant in the numerical model than it is in the field where large strains and differential settlement take place. This is likely a limitation of the current constitutive model for modeling behavior under large strains, and is to be addressed in future works.

Table B-6. Liu et al. (2007) case history recordings vs. undrained end-of-construction and drained long-term analyses

	Case History Measured (End of Construction)	**FLAC3D Undrained**
Pressure on Subsoil between Columns (kPa)	31-56	77-78
Pressure on Column (kPa)	552-584	419
Total Settlement of Subsoil between Columns (mm)	63	12-13
Total Settlement of Column (mm)	14	2
	Case History Measured (125 days after Construction)	**FLAC3D Drained**
Pressure on Subsoil between Columns (kPa)	40-60	47-51
Pressure on Column (kPa)	674	756
Total Settlement of Subsoil between Columns (mm)	87	71-73
Total Settlement of Column (mm)	19	30

B.5. Conclusion

The manual pore pressure dissipation approach was validated for predicting consolidation deformations for two examples using FLAC3D. It has only been validated for cases of monotonic loading, and may not be applicable for problems involving unloading and reloading. The manual pore pressure dissipation approach was adopted for the undrained end-of-construction and long-term drained analyses of a GRCSE case history, where excess pore pressures developed in undrained embankment loading were manually decreased to the hydrostatic condition for calculation of long-term deformations. The undrained analysis predicted a reasonable upper bound for the vertical pressure acting on the subsoil. This approach can be extended to a half-embankment analysis, where the vertical and lateral earth pressures predicted in the undrained condition can be used to calculate the column bending moments and to investigate the geosynthetic response to lateral spreading.

References

Bhasi, A., and Rajagopal, K. (2014). "Geosynthetic-Reinforced Piled Embankments: Comparison of Numerical and Analytical Methods." *International Journal of Geomechanics*, 15(5), 04014074.

Borges, J. L., and Marques, D. O. (2011). "Geosynthetic-reinforced and jet grout column-supported embankments on soft soils: Numerical analysis and parametric study." *Computers and Geotechnics*, 38(7), 883-896.

Briançon, L., and Simon, B. (2012). "Performance of Pile-Supported Embankment over Soft Soil: Full-Scale Experiment." *Journal of Geotechnical and Geoenvironmental Engineering*, 138(4), 551-561.

Briançon, L., and Simon, B. (2017). "Pile-supported embankment over soft soil for a high-speed line." *Geosynthetics International*, 24(3), 293-305.

BSI (2010). "BS 8006-1:2010 Code of practice for strengthened/reinforced soil and other fills." *Design of embankments with reinforced soil foundations on poor ground*, British Standards Institution.

BSI (2016). "BS 8006-1:2010+A1:2016 Code of practice for strengthened/reinforced soil and other fills." *Design of embankments with reinforced soil foundations on poor ground*, British Standards Institution.

Chai, J. C., Shrestha, S., Hino, T., and Uchikoshi, T. (2017). "Predicting bending failure of CDM columns under embankment loading." *Computers and Geotechnics*, 91, 169-178.

Chen, R., Xu, Z., Chen, Y., Ling, D., and Zhu, B. (2009). "Field tests on pile-supported embankments over soft ground." *Journal of Geotechnical and Geoenvironmental Engineering*, 136(6), 777-785.

Chen, R. P., Wang, Y. W., Ye, X. W., Bian, X. C., and Dong, X. P. (2016). "Tensile force of geogrids embedded in pile-supported reinforced embankment: A full-scale experimental study." *Geotextiles and Geomembranes*, 44(2), 157-169.

Chen, Y., Qi, C., Xu, H., and Ng, C. W. W. (2013). "Field Test Research on Embankment Supported by Plastic Tube Cast-in-place Concrete Piles." *Geotechnical and Geological Engineering*, 31(4), 1359-1368.

Collin, J. G. (2018). Personal Communication.

CUR226 (2016). "Design guideline basal reinforced piled embankments. Revision of the design guideline CUR226." CRC Press.

Demerdash, M. A. (1996). "An experimental study of piled embankments incorporating geosynthetic basal reinforcement." Doctoral Dissertation, University of Newcastle-Upon-Tyne.

FHWA (2017). "American Association of State Highway and Transportation Officials (AASHTO) Unites States Department of Transportation Federal Highway Administration (FHWA) 2002 Scanning Project Innovative Technology for Accelerated Construction of Bridge and Embankment Foundations Preliminary Summary Report." <https://www.fhwa.dot.gov/engineering/geotech/research/bescan.cfm#4>. (June, 2017).

Habib, H., Brugman, M., and Uijting, B. (2002). "Widening of Road N247 founded on a geogrid reinforced mattress on piles." *7th Int. Conf. on Geosynthetics*, Swets & Zeitlinger Nice, France, 369-372.

Hannigan, P. J., Rausche, F., Likins, G. E., Robinson, B. R., and Becker, M. L. (2016). "Design and Construction of Driven Pile Foundations." U. S. D. o. T. F. H. Administration, ed.

Hong, W. P., and Hong, S. (2017). "Piled embankment to prevent damage to pipe buried in soft grounds undergoing lateral flow." *Marine Georesources & Geotechnology*, 35(5), 719-729.

Huang, J., and Han, J. (2009). "3D coupled mechanical and hydraulic modeling of a geosynthetic-reinforced deep mixed column-supported embankment." *Geotextiles and Geomembranes*, 27(4), 272-280.

Huang, J., and Han, J. (2010). "Two-dimensional parametric study of geosynthetic-reinforced column-supported embankments by coupled hydraulic and mechanical modeling." *Computers and Geotechnics*, 37(5), 638-648.

Inc., R. 2017. Settle3D, version 4.008, Toronto, Canada.

Itasca. 2012. FLAC3D, version 5.01, Minneapolis, MN.

Itasca (2013). *Structural Elements*, Itasca Consulting Group Inc., Minneapolis, Minnesota.

Jamsawang, P., Yoobanpot, N., Thanasisathit, N., Voottipruex, P., and Jongpradist, P. (2016). "Three-dimensional numerical analysis of a DCM column-supported highway embankment." *Computers and Geotechnics*, 72, 42-56.

Kitazume, M., and Maruyama, K. (2006). "External stability of group column type deep mixing improved ground under embankment loading." *Soils and Foundations*, 46(3), 323-340.

Kitazume, M., and Maruyama, K. (2007). "Internal Stability of Group Column Type Deep Mixing Improved Ground under Embankment Loading." *Soils and Foundations*, 47(3), 437-455.

Lai, Y., Bergado, D., Lorenzo, G., and Duangchan, T. (2006). "Full-scale reinforced embankment on deep jet mixing improved ground." *Proceedings of the Institution of Civil Engineers-Ground Improvement*, 10(4), 153-164.

Liu, H., Ng, C. W., and Fei, K. (2007). "Performance of a geogrid-reinforced and pile-supported highway embankment over soft clay: case study." *Journal of Geotechnical and Geoenvironmental Engineering*, 133(12), 1483-1493.

Liu, K. W., and Rowe, R. K. (2016). "Performance of reinforced, DMM column-supported embankment considering reinforcement viscosity and subsoil's decreasing hydraulic conductivity." *Computers and Geotechnics*, 71, 147-158.

Liu, S., Du, Y., Yi, Y., and Puppala, A. J. (2012). "Field Investigations on Performance of T-Shaped Deep Mixed Soil Cement Column–Supported Embankments over Soft Ground." *Journal of Geotechnical and Geoenvironmental Engineering*, 138(6), 718-727.

Oh, Y. I., and Shin, E. C. (2007). "Reinforcement and Arching Effect of Geogrid-Reinforced and Pile-Supported Embankment on Marine Soft Ground." *Marine Georesources & Geotechnology*, 25(2), 97-118.

Potyondy, J. G. (1961). "Skin friction between various soils and construction materials." *Geotechnique*, 11(4), 339-353.

Rowe, R. K., and Liu, K.-W. (2015). "Three-dimensional finite element modelling of a full-scale geosynthetic-reinforced, pile-supported embankment." *Canadian Geotechnical Journal*, 52(12), 2041-2054.

Schaefer, V. R., Berg, R. R., Collin, J. G., Christopher, B. R., DiMaggio, J. A., Filz, G. M., Bruce, D. A., and Ayala, D. (2017). "Ground Modification Methods Reference Manual - Volume II." FHWA, ed.Washington, D. C.

Shang, Y., Xu, L., Xu, Y., Li, Y., and Ou, N. (2016). "Field Test Study on a Short Pile-net Composite Foundation over Gravel Clay for High-Speed Railways." *Journal of Engineering Science & Technology Review*, 9(3).

SHRP2 (2012). "Column-Supported Embankments." <http://www.GeoTechTools.org>.

Wang, Y., Song, W., Zou, C., and Yang, K. (2014). "Field tests on performance of geosynthetic-reinforced and pile-supported embankment in highway expansion project." *Project Planning and Project Success: The 25% Solution*, 287-292.

Xu, C., Song, S., and Han, J. (2015). "Scaled model tests on influence factors of full geosynthetic-reinforced pile-supported embankments." *Geosynthetics International*, 23(2), 140-153.

Yapage, N. N. S., Liyanapathirana, D. S., Kelly, R. B., Poulos, H. G., and Leo, C. J. (2014). "Numerical Modeling of an Embankment over Soft Ground Improved with Deep Cement Mixed Columns: Case History." *Journal of Geotechnical and Geoenvironmental Engineering*, 140(11), 04014062.

Yu, Y., Bathurst, R. J., and Damians, I. P. (2016). "Modified unit cell approach for modelling geosynthetic-reinforced column-supported embankments." *Geotextiles and Geomembranes*, 44(3), 332-343.

Zanzinger, H., Gartung, E., and LGA (2002). "Performance of a geogrid reinforced railway embankment on piles." *7th ICG*, Delmas, Gourc, and Girard, eds., 381-386.

Zhang, J., Zheng, J., Zhao, D., and Chen, S. (2015). "Field study on performance of new technique of geosynthetic-reinforced and pile-supported embankment at bridge approach." *Science China Technological Sciences*, 59(1), 162-174.

Zheng, G., Jiang, Y., Han, J., and Liu, Y.-F. (2011). "Performance of Cement-Fly Ash-Gravel Pile-Supported High-Speed Railway Embankments over Soft Marine Clay." *Marine Georesources & Geotechnology*, 29(2), 145-161.

Zhou, M., Liu, H., Chen, Y., and Hu, Y. (2016). "First application of cast-in-place concrete large-diameter pipe (PCC) pile-reinforced railway foundation: a field study." *Canadian Geotechnical Journal*, 53(4), 708-716.

Zhuang, Y., and Cui, X. (2016). "Case Studies of Reinforced Piled High-Speed Railway Embankment over Soft Soils." *International Journal of Geomechanics*, 16(2), 06015005.

Zhuang, Y., and Wang, K. Y. (2016). "Finite-Element Analysis on the Effect of Subsoil in Reinforced Piled Embankments and Comparison with Theoretical Method Predictions." *International Journal of Geomechanics*, 16(5), 04016011.

APPENDIX C. SUBSTRUCTURE ANALYSES

Substructure analyses investigate specific phenomena as found in large systems through the adoption of smaller and highly refined models. Substructure analyses were adopted for the analysis of geosynthetic tensions and strains that develop under the combined effects of vertical load transfer and lateral spreading. Refinement in zone discretization was required for the analysis of local strain effects above column edges. The substructure consisted of a unit cell model that extended vertically from the embankment surface to the neutral plane of settlement in the foundation (Figure C-1). As the analysis was meant to target the geosynthetic, discretization was highly refined in the geogrid elements and neighboring zones in the load transfer platform (LTP), gradually coarsening with distance from the area of interest. The required discretization was determined using a convergence study, as described later. Such refinement would have resulted in excessive computation times if implemented in the larger 3D half-embankment slice geometry.

Findings from the substructure analyses were limited by challenges in large deformations and illegal zone geometry. Computations used large strain mode, as required for the geosynthetic to develop tension under out-of-plane deformation. In locations of very large deformation, such as around the column edge where the soil settles relative to the column, the zone geometry was significantly deformed, leading to poor mesh quality that stopped computations altogether. To facilitate large movements and to prevent significant straining of the zones, interface elements were installed in the embankment. Unfortunately, the issue of bad zone geometry persisted.

The rest of APPENDIX C describes the convergence study used to determine the zone discretization, the different interface element configurations that were tested to try and overcome the zone geometry issue, and the lessons learned based on the challenges encountered. All discussion refers to the CSE design as shown in Figure C-1. This design was selected for substructure analysis because it had a typical column area replacement ratio of 2.8%, and because the long-term geosynthetic strain was estimated to be in the working range of 3% to 4%.

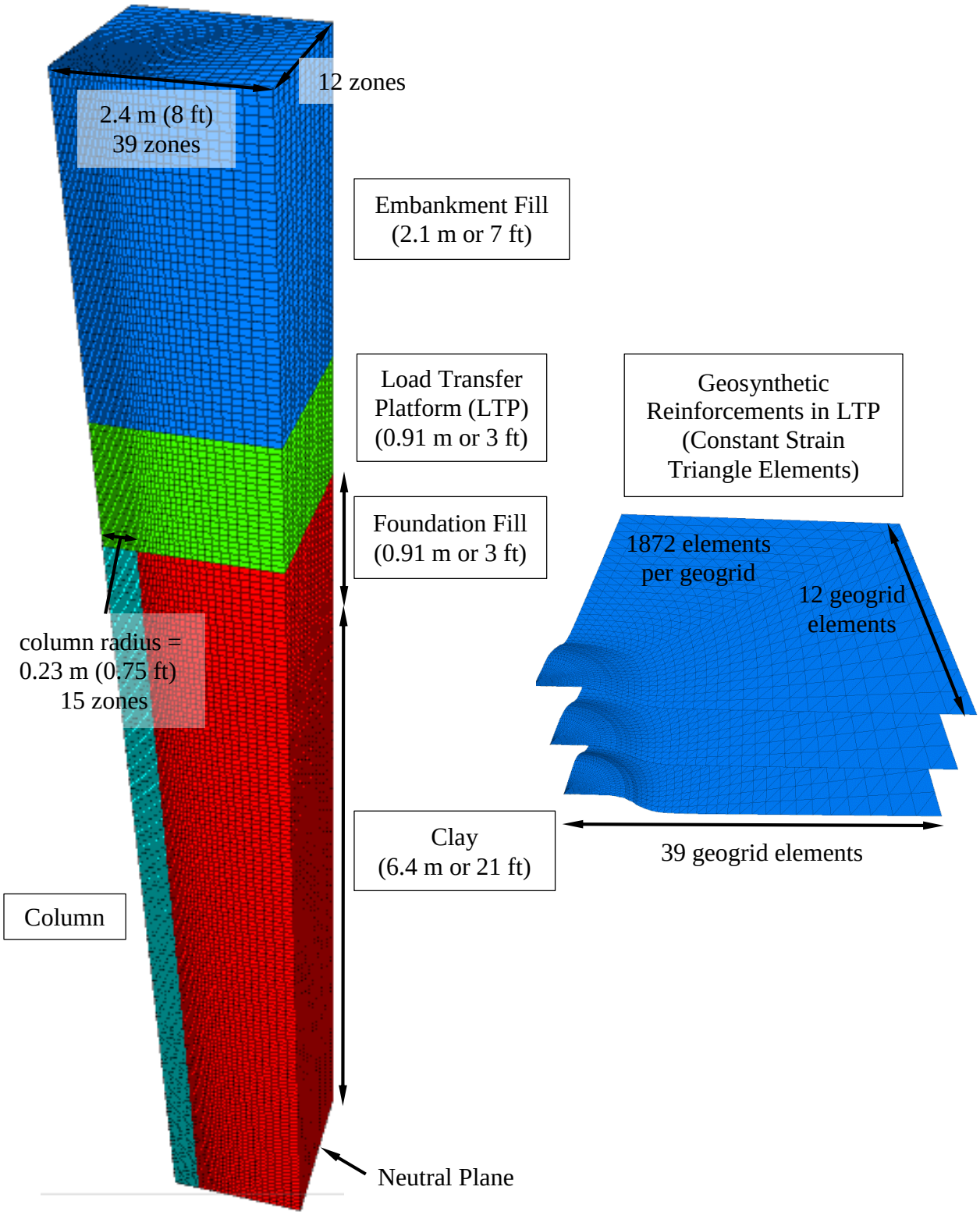

Figure C-1. Substructure model in unit cell geometry with highly refined discretization.

C.1. Discretization for Substructure Analysis

For the analysis of local strain effects in the geosynthetic above columns edges, discretization of the geosynthetic and neighboring LTP zones were gradually refined until convergence was established for the maximum tensions above the column edge. Orthotropic linear elastic geogrid elements were used. These elements were of the constant strain triangle (CST) type with two (2) translational degrees of freedom per node (Itasca 2013). An alternative to refining the discretization was to use higher order geogrid elements, which were considered to have a better potential of calculating non-linear distributions of tension at a coarser discretization. This was not an option in FLAC3D v.5.01, and the only other alternative was to use the CST hybrid plane-stress element (Cook 1987), in which an extra rotational degree of freedom was included per node. The CST hybrid element was found to be ill behaved in the CSE model using the same geogrid properties as adopted for the CST elements.

Convergence studies used to establish the zone discretization adopted the following loading sequence. Prior to embankment construction, foundation in-situ stresses were assigned in both the soils and the columns, which had the same density as adjacent soils. Column installation was modeled by increasing density while solving for mechanical equilibrium. Zones in the embankment were assigned null material properties. Accumulated displacements were zeroed. The embankment was constructed in five (5) lifts under a fully drained condition. This was the loading path with the fastest computation time and in which the zone geometry was relatively well behaved. Select embankment zones were softened during lift construction to represent the loosening of fill during vertical load redistribution.

The substructure model was gradually increased in discretization in the geogrid as well as in the zones throughout the model. Refinement in both was necessary because the geosynthetic vertical deflection occurs simultaneously with the differential settlement in the embankment and subgrade. Discretization was increasingly refined until the maximum tension in the longitudinal and transverse directions (i.e. above the column edge) converged. Figure C-2 illustrates the maximum geogrid tension in the longitudinal and transverse directions with the increase in the number of elements per geogrid. The tensions converged when 3040 elements were used per geogrid, but to reduce computation time, preliminary analyses were conducted using 1872 elements per geogrid. The refined model with 1872 elements per geogrid is shown in Figure C-1.

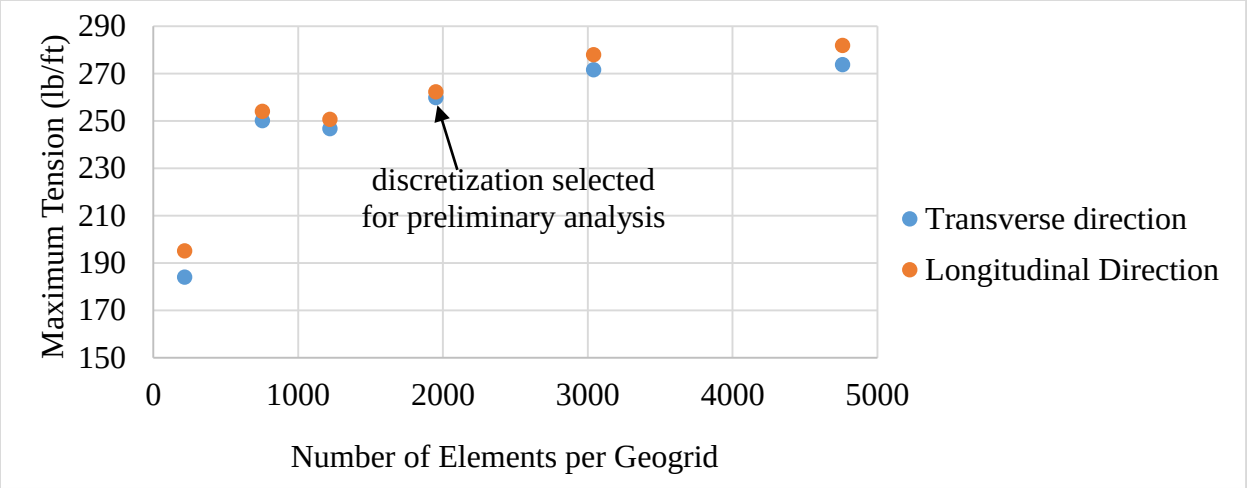

Figure C-2. Convergence of geosynthetic tension with increase in discretization.

C.2. Large Deformations and Illegal Zone Geometry

The substructure model when adopted for undrained-dissipated analyses resulted in illegal zone geometry errors. Zones around the column edge deformed significantly during vertical load distribution and differential settlement, and the problem was worse for greater refinement in discretization. As shown in Figure C-3, LTP zones immediately above the column moved radially outward under high vertical load concentration, while LTP and subsoil zones around the column edge settled relative to the column. Modeling large local deformations such as the one illustrated represents a challenge for continuum analysis.

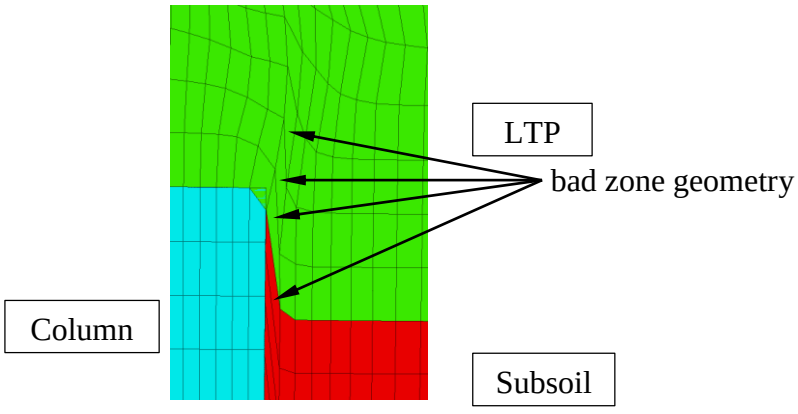

Figure C-3. Significant deformation in zones due to vertical load distribution and differential settlement.

To facilitate shearing in the column edge vicinity, and thus to overcome the issue of illegal zone geometry, interface elements were installed in the embankment. Three interface geometries of increasing complexity were tested, as illustrated in Figures C-4a to Figure C-4c. Illegal zone geometry was calculated in all three cases, because interface elements that were installed vertically and horizontally could not fully facilitate shearing that occurred on planes of differing orientation. To install interface elements on the corresponding planes of shearing would be overwhelmingly difficult.

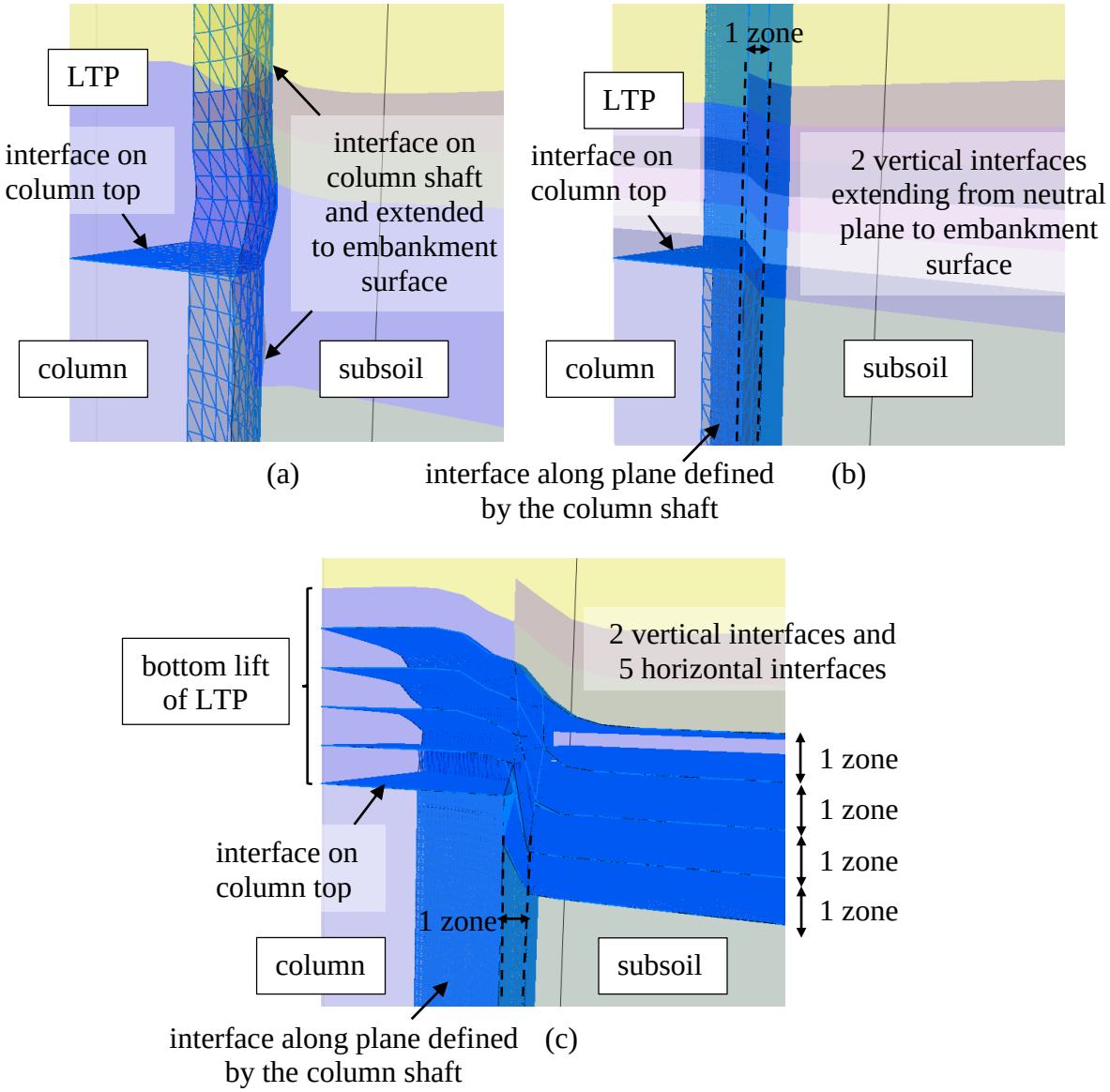

Figure C-4. Interface geometries that were tested to facilitate slip around column edge and to prevent significant distortion of zones.

There was evidence that the substructure analysis might be unnecessarily complex considering the numerical procedure inherently introduced errors in the calculation of geosynthetic tension. The geosynthetic shape under vertical deflection shows a sharp drop above the column edge and is relatively flat above the subsoil (Figure C-5), whereas the expected deformed geometry is more similar to a dish with smooth curvature. The sharp drop above the column edge was likely a byproduct of the adopted method of zone softening (i.e. reducing E and φ' of select embankment zones). Peak strains were likely overestimated. Thus, it was concluded that the method of zone softening produced geosynthetic strains that were unreliable for refined analysis, but the approach was still valid for the calculation of long-term deformations and load distributions.

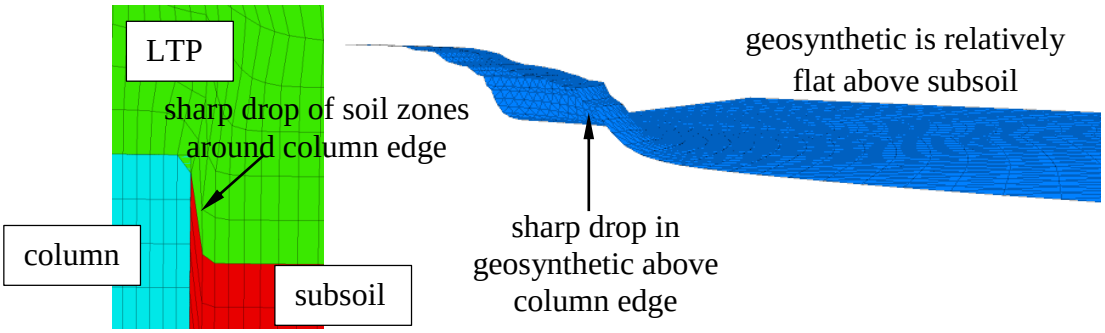

Figure C-5. Deformed shapes of soil at subgrade level and geosynthetic reinforcement under vertical loading and differential settlement.

C.3. Lessons Learned

Several lessons were learned from the substructure analyses:

1) Peak geosynthetic tensions and strains converged using only very refined discretization.
2) Use of interface elements to facilitate movement in zones around the column edge did not prevent illegal zone geometry because the planes of shear did not correspond to the planes of interface installation. It would be very challenging to install interface elements along expected planes of deformation.
3) The long-term dissipated analysis using calibrated values of E and φ' to represent zone softening resulted in the overestimate of peak geosynthetic strains.
4) Calculation of differential settlements and soil arching is challenging using the continuum technique. Alternative numerical techniques, such as the discrete element method and material points method, should be explored, as should higher order geogrid elements.

References

Cook, R. D. (1987). "A plane hybrid element with rotational dof and adjustable stiffness." *International Journal for Numerical Methods in Engineering*, 24(8), 1499-1508.

Itasca (2013). *Structural Elements*, Itasca Consulting Group Inc., Minneapolis, Minnesota.